

Abstract

TOPTAN, AYSEUR. A Novel Approach to Improve Transient Fuel Performance Modeling in Multi-Physics Calculations. (Under the direction of Maria N. Avramova and David J. Kropaczek).

A current challenge in multi-physics simulations is the being computational expense required for whole core calculations during cycle depletion and transient applications. The complexity arises from fuel performance modeling due to the multi-disciplinary and multi-scale modeling paradigm of material behavior, and not practicality with today's computing capabilities. This study attempted to improve fuel temperature predictions for whole-core calculations, which was achieved under two major parts.

In the first part, the study focused on isolating a modernized version of COBRA-TF (CTF)'s fuel performance capabilities to be used as a standalone capability. This new capability, CTF-Fuel, was successfully constructed to interface CTF's fuel performance modeling capabilities for simulation of the steady state and transient thermal response of an Light Water Reactor (LWR) fuel rod. This capability provides flexibility for its use in multi-physics calculations of the US Department of Energy (DOE) funded Consortium for Advanced Simulation of Light Water Reactors (CASL)'s Virtual Environment for Reactor Applications–Core Simulator (VERA-CS). New modeling options were added to investigate the fuel thermal conductivity degradation of LWR oxide fuels and radial fuel deformation. Work performed in this study improved the thermal modeling capabilities of both CTF and CTFFuel. The models were integrated in the code according to the CASL coding guidelines.

In the second part, the gap conductance modeling was improved according to kinetic theory and a conventional form of the gap conductance model was proposed with enhanced prediction considering its practical use in today's nuclear applications. Large uncertainties in the gap conductance model exist primarily due to inaccurate estimation of either mechanical or thermal aspects of the gap. Accurate simulation of the gap between nuclear fuel and cladding is crucial due to its pronounced effect on the thermo–mechanical performance of nuclear fuel rods. Heat transfer across the gap heavily impacts the fuel temperatures, particularly Doppler temperature feedback which is critical for reactor stability of LWRs. The motivation of this research originated from the necessity of better understanding the physics to reduce these large uncertainties in the gap conductance calculations and to yield more accurate estimation of fuel temperatures. An overview of the theoretical considerations and the underlying assumptions of gap conductance modeling were provided in addition to the traditional modeling approaches in nuclear fuel performance codes. Deficiencies of traditional approaches were discussed. The models were generalized to curvilinear coordinates and for diatomic/polyatomic gases due to

their incorrect use in the nuclear fuel performance codes. The expressions were made consistent with kinetic theory to be more representative of real world data. The fill gas thermal conductivity was updated to include its dependence on rod internal pressure, which is presently ignored in the nuclear fuel performance codes. This study confirmed that the pressure dependence is important when the initial fill gas is not helium or is replaced by lower-conductivity gaseous fission products during the reactor's operation. In parallel, a conventional gap conductance model in nuclear applications was optimized for uranium dioxide-Zircaloy interfaces using available experimental data at high pressures for the single- and multi-component gases. The model conventionally used in nuclear fuel performance codes to conduct heat across the fuel-cladding gap is a modified version of the Ross-Stoute model. The model was modified in nuclear applications to include gap distance in the formulation, which introduced additional uncertainty as the model parameters were not adjusted after the modification. In this study, this conventional model was optimized for uranium dioxide-Zircaloy interfaces using available experimental data in the literature for single- and multi-component gases. Then, overall uncertainty in the gap conductance was quantified by performing uncertainty propagation. The validation results confirmed that the proposed model results in a larger gap conductance with significantly reduced error. To demonstrate predictions with the improved gap heat transfer modeling in nuclear applications, a finite-element based nuclear fuel performance code, Bison is utilized. The simulation results indicated that the proposed model resulted in a significant reduction of fuel centerline temperatures due to the higher gap conductance estimates with the proposed model.

© Copyright 2019 by Aysenur Toptan

All Rights Reserved

A Novel Approach to Improve Transient Fuel Performance Modeling in Multi-Physics
Calculations

by
Aysenur Toptan

A dissertation submitted to the Graduate Faculty of
North Carolina State University
in partial fulfillment of the
requirements for the Degree of
Doctor of Philosophy

Nuclear Engineering

Raleigh, North Carolina

2019

APPROVED BY:

Kostadin Ivanov

Jia Hou

Maria N. Avramova
Co-chair of Advisory Committee

David J. Kropaczek
Co-chair of Advisory Committee

Technical Consultants:

Robert K. Salko

Kevin Clarno

Dedication

This dissertation is dedicated to my parents.

Biography

Aysenur Toptan entered the doctoral program in nuclear engineering at North Carolina State University (NCSSU) in 2015. Her doctoral study has been sponsored by the DOE funded CASL to conduct research on gap conductance theory and applications for nuclear industry to improve fuel temperature predictions in multi-physics calculations. The author has several publications as numerous conference papers and technical reports. She currently has six published works in peer-reviewed journals at the present.

- A Toptan, K A Gamble, and others, *Validation of the Bisons enhanced heat transfer modeling across the fuel-cladding gap*. (to be published)
- A Toptan, D J Kropaczek, M N Avramova, *Gap conductance modeling II: Optimized model for uranium dioxide-Zircaloy interfaces*, J Nuclear Engineering and Design. (submitted, NED-D-19-00145)
- A Toptan, D J Kropaczek, M N Avramova, *Gap conductance modeling I: Theoretical considerations on the model for single- and multi-component gases*, J Nuclear Engineering and Design. (submitted, NED-D-19-00144)
- A Toptan, D J Kropaczek, M N Avramova, *On the validity of dilute gas assumption for gap conductance calculations in nuclear fuel performance codes*, J Nuclear Engineering and Design. (submitted, NED-D-19-00052)
- A Toptan, R K Salko, M N Avramova, K Clarno, D J Kropaczek, *A new fuel modeling capability, CTFFuel, with a case study on the fuel thermal conductivity degradation*, J Nuclear Engineering and Design 341 (2019) 248–258. doi: 10.1016/j.nucengdes.2018.11.010
- A Toptan, N Porter, R K Salko, M N Avramova, *Implementation and assessment of wall friction models for LWR core analysis*, Annals of Nuclear Energy 115 (2018) 565–572. doi: 10.1016/j.anucene.2018.02.022
- T Worosz, M Bernard, R Kong, A Toptan, S Kim, and C Hoxie, *Sensitivity studies on the multi-sensor conductivity probe measurement technique for two-phase flows*, J Nuclear Engineering and Design 310 (2016) 552-563. doi: 10.1016/j.nucengdes.2016.10.046

Acknowledgments

The author would like to express her profound and sincere gratitude to Professors Maria N Avramova and David J Kropaczek for their support throughout this process and genuine kindness. The author was privileged to work with Professor David J Kropaczek who shared the excitement of scientific curiosity and is very thankful for his unwavering enthusiasm in development of the author's critical thinking in science, and his enlightening guidance how to be '*a good scientist and a good human*'. Also, special thanks to the author's mentor at Oak Ridge National Laboratory (ORNL), Robert K Salko for his willingness to share his knowledge, positive attitude and readiness to discuss any aspects of the author's research. The author's sincere appreciation extends to Kevin Clarno of ORNL, Richard Williamson and Jason Hales of Idaho National Laboratory (INL), who provided the author opportunities to join their teams, and who gave access to the laboratory and research facilities. The author would like to acknowledge Jess Gehin of INL for his kindness and unconditional support. In addition, the author would like to thank her fellow colleagues, Kyle Gamble, especially Taylor S Blyth and Nathan W Porter for their collaboration, proofreading, and many invaluable discussions. The author is thankful to the rest of thesis committee, her professors and colleagues whose guidance and encouragement, over many years and in many places, contributed to her profession. The author would also thank to Hermine Kabbendjian for her support and prompt help in administrative process at NCSU.

The author expresses her gratefulness to her family and beloved friends. In particular, Zineb Aly for her absolute love, encouragement, support in addition to her honest and objective feedbacks in any conditions at any time. The author respects her how she stands for her moral values and how she follows her enthusiasm to feed her scientific curiosity beyond materialistic bounds. Also, special thanks to Alp Tezbaşaran who have helped the author to interpret the world from a different perspective and to provide objective feedbacks. Lastly, the author's cat, Zeytin has been a real joy for the last two years and is a real proof that the knowledge can be in any forms of any living beings.

This research could not have been completed without the financial support from the Consortium for Advanced Simulation of Light Water Reactors (<http://www.cas1.gov>), an Energy Innovation Hub (<http://www.energy.gov/hubs>) for Modeling and Simulation of Nuclear Reactors under US Department of Energy Contract No. DE-AC05-00OR22725.

"Fakat devam ediyor bizimkisi, sevmek, düşünmek ve anlamakta devam ediyor kafam, . . ."

Nazım Hikmet Ran.

Table of Contents

List of Tables	viii
List of Figures	ix
List of Algorithms	xv
List of Symbols	xvi
Chapter 1 Introduction	1
Chapter 2 Verification, Validation, Uncertainty Quantification	6
2.1 Software Quality Assurance	7
2.2 Code Verification	8
2.3 Solution Verification	9
2.4 Validation	10
2.5 Uncertainty Quantification and Sensitivity Analysis	10
2.6 Parameter Estimation Methods	11
2.6.1 Frequentist Inference	12
2.6.2 Bayesian Inference	12
2.7 Metrics	13
2.8 Chapter Summary	16
Chapter 3 Fuel Modeling Capability, CTFFuel	17
3.1 CTFFuel	18
3.1.1 CTF's Conduction Model	19
3.1.2 CTF's Dynamic Gap Conductance Model	22
3.2 Code Structure	25
3.3 Chapter Summary	27
Chapter 4 Fuel Thermal Conductivity Degradation	28
4.1 Background	29
4.2 Order-of-accuracy tests	33
4.2.1 Exact Solution to the Mathematical Model	33
4.2.2 Results & Discussion	34
4.3 Code Comparison	34
4.3.1 Results & Discussion	38
4.4 Chapter Summary	40
Chapter 5 Sensitivity Analysis and Uncertainty Quantification	41
5.1 Sensitivity Analysis	41
5.1.1 Fuel Temperature Predictions	41
5.1.2 Radial Power Distribution and Fuel Thermal Conductivity	44
5.2 Uncertainty Quantification	44

5.2.1	Procedure	46
5.2.2	Results & Discussion	47
5.3	Chapter Summary	49
Chapter 6	Fill Gas Thermal Conductivity	50
6.1	Single-Component Gas Thermal Conductivity	50
6.2	Multi-Component Gas Thermal Conductivity	53
6.3	Gas Density	57
6.4	Case Study	59
6.5	Chapter Summary	63
Chapter 7	Gap Conductance Theory	64
7.1	Fill Gas Conductance	65
7.1.1	Temperature Jump Distance	68
7.1.2	Thermal Accommodation Coefficient	75
7.2	Solid Contact Conductance	76
7.3	Thermal Radiation	78
7.4	Chapter Summary	79
Chapter 8	Optimized Gap Conductance Model for UO₂-Zircaloy Interfaces	80
8.1	Modeling	81
8.2	Methods	83
8.2.1	Experimental Data	84
8.2.2	Calibration	84
8.2.3	Uncertainty Quantification	85
8.3	Results & Discussion	85
8.3.1	No Contact Results & Discussion	85
8.3.2	Contact Results & Discussion	87
8.4	Chapter Summary	90
Chapter 9	Thermal Behavior Assessment in Bison	93
9.1	Gap Conductance Modeling in Bison	93
9.2	Separate Effects Validation	96
9.2.1	Bison Model Description	96
9.2.2	Results & Discussion	98
9.3	Integral Effects Assessment	99
9.3.1	Results & Discussion	100
9.4	Chapter Summary	110
Chapter 10	Concluding Remarks	111
References	114
Appendices	134
Appendix A	Fuel Radial Deformation Models	135
Appendix B	RIA Transient	144

Appendix C	Radial Power Distribution	148
Appendix D	CTF's Friction Factor Correlations	153

List of Tables

Table 2.1	Verification assessment classifications and descriptions [1, 2].	9
Table 2.2	DRAM Statistics.	13
Table 4.1	The empirical coefficients for the generalized burnup-dependent model. . .	31
Table 4.2	Description of the steady state fuel rod test cases, generated based on FRAPCON-4.0 [3]	37
Table 4.3	Overall code comparison results in terms of RMSE	40
Table 5.1	Selected uncertainty bounds for the uniform distribution	43
Table 5.2	Thermal conductivity options	44
Table 5.3	Selected input uncertainties [4, 5].	47
Table 6.1	The parameters from Tournier and El-Genk [6] for selected rare gases. The critical parameters are denoted by the subscript <i>c</i>	53
Table 6.2	Fuel centerline predictions between the traditional and new approaches are summarized in terms of the metrics for the selected IFA rods.	62
Table 7.1	Molal specific heat capacities and degrees of freedom for a number of gases at near room temperature [7]. The specific heat at constant pressure is related by $c_P = c_V + R_g$	67
Table 8.1	Non-contact results for the gap conductance, h_{gap} for helium in Figure 8.3.	86
Table 8.2	Validation results for the gap conductance, h_{gap} for the single-component gases, multi-component gases, and combined data.	92
Table 9.1	Overview of the fuel centerline temperature experimental data for Bison integral effects validation, from Williamson et al. [8].	100
Table 9.2	Results for the fuel centerline temperatures for the rod average burnup of [0, 30 MWd/kgU].	104
Table 9.3	Results for the volume averaged fuel temperatures for the rod average burnup of [0, 30 MWd/kgU].	104
Table 9.4	Results for the volume-averaged fuel temperatures for the rod average burnup of [0, 30 MWd/kgU].	107
Table A.1	Fuel thermal expansion models	136
Table B.1	List of fuel rod cases used from FRAPTRAN-1.5 integral assessment [9]. .	145

List of Figures

Figure 1.1	Schematic illustration of the complex phenomena and behavioral evolution and their interactions, which must be incorporated in modeling fuel rod behavior, as reproduced from Olander and Motta [10], after Rashid et al. [11] and Olander [12].	2
Figure 1.2	Schematic illustration of coupling in VERA-CS. The neutronics code require fuel temperature estimates from the fuel performance code and fluid conditions from the thermal-hydraulics code in the coupling.	3
Figure 2.1	Simplified view of the model verification and validation process [13]. The dashed lines represent the assessment activities. The solid lines represent the modeling and simulation activities.	7
Figure 2.2	Schematic illustration of Dakota-to-code coupling.	11
Figure 3.1	Schematic illustration of how CTFFuel interfaces CTF’s fuel rod model. Shaded areas represent solid and fluid domains with corresponding calculations. The dashed rectangle represents shared subroutines between the codes.	18
Figure 3.2	Schematic of CTF’s radial meshing (not to scale).	20
Figure 3.3	CTFFuel’s single pin nodalization.	26
Figure 4.1	Comparison of thermal conductivity of 95% theoretical density (TD) fuel with different correlations	32
Figure 4.2	Solution verification with the thermal conductivity model	35
Figure 4.3	Solution and code verification with the constant thermal conductivity	36
Figure 4.4	Design of the code comparison. Manually and dynamically calculated parameters are represented, respectively, by dashed and solid lines.	38
Figure 4.5	CTFFuel vs. FRAPCON-4.0 fuel centerline temperature predictions. CTFFuel uses the old thermal conductivity model (left column) and the new burnup-dependent thermal conductivity model (right column). Note that FRAPCON-4.0 uses the burnup-dependent thermal conductivity model (modified version of the the Nuclear Fuel Industries (NFI) model for UO ₂ and UO ₂ +Gd ₂ O ₃ fuels; the Duriez/modified NFI for MOX fuels).	39
Figure 5.1	Morris results of mean (blue) and standard deviation (orange)	42
Figure 5.2	Correlation coefficients from the random sampling study	43
Figure 5.3	Difference in the centerline temperature for a given radial power shape and uniform power profile vs. percent power change at the centerline $r = 0$	45
Figure 5.4	Centerline temperature predictions and measurements for IFA681 rods. Grey shaded areas on the plots represent two standard deviations around the quantified mean temperatures, while dashed lines signify the 95% percentile that is calculated based on Wilks’ formula.	48
Figure 5.5	Prediction results with mean and nominal predictions.	49

Figure 6.1	The dynamic viscosity (upper plot) and thermal conductivity (lower plot) of the dilute inert gases based on the closure relations given by Tournier and El-Genk [6].	52
Figure 6.2	Comparison of predicted and measured thermal conductivity using the literature data up to 30 MPa. Tabulated validation metrics belong to the predictions with $\lambda(T, P)$ given in Eq. 6.1. Note that MATPRO-11 correlations with the assumption of $\lambda(T, P) \approx \lambda^0(T)$ are only added for visual comparison.	54
Figure 6.3	Reduced-state plot of thermal conductivity for the selected inert gases according to the critical parameters from Tournier and El-Genk [6]. . . .	55
Figure 6.4	Comparison of predicted and measured gas thermal conductivity using the literature data up to 30 MPa. The thermal conductivities of binary and ternary gas mixtures are calculated according to Eq. 6.1. Consistent legend is used in both figures (left plot: the low-pressure; right plot: the high-pressure).	57
Figure 6.5	The reduced second and third virial coefficients, $B_{2,r}$ and $B_{3,r}$ vs. the reduced temperature, θ for Xe, Kr, Ar and Ne (upper plot). The second virial coefficient for He as a function of temperature (lower plot), where its third virial coefficient is neglected due to its dilute gas behavior. The closure relations are calibrated based on the literature data by Tournier and El-Genk [6].	58
Figure 6.6	Comparison of predicted and measured density using the literature high-pressure data up to 30 MPa. The data are from Kestin et al. [14], Michels [15], Rosenbaum [16], and Sengers[17].	59
Figure 6.7	Thermal conductivities of (a) He–Kr–Xe and (b) Ar–Kr–Xe ternary mixtures at varied gas temperatures and rod internal pressures.	61
Figure 6.8	(a) Measured and predicted centerline temperature for IFA432 Rod 1 with UO_2 fuel at lower thermocouple position (burnup=45 MWd/kgU, cold radial gap=114 μm , rod internal pressure= 0.2 to 4.2 MPa, open gap), and (b) gas composition with respect to time.	62
Figure 6.9	Measured and predicted centerline temperature for IFA681 Rod 6 UO_2 +8% Gd_2O_3 fuel. (burnup=13 MWd/kgU, cold radial gap=85 μm , rod internal pressure= 2.2 to 4.3 MPa, open gap). The gas mixture is composed of 50% He and 50% Ar.	63
Figure 7.1	Two block geometry (left to right; plane, cylinder, and sphere). The gap distance is referred to the distance between two solid blocks.	65
Figure 7.2	The fill gas conductance in the continuum flow with respect to the pressure for (a) the single-component gases, (b) the gas mixtures of helium with the gaseous fission products, and (c) the gas mixtures of argon with the gaseous fission products. The gas compositions are arbitrarily chosen. The fill gas temperature is set to 300 K (left column) and 900 K (right column). The plane geometry is chosen and $(g_1 + g_2) \approx 2g$. The gap distance is set to 100 μm , while $r_1 = 0.005\text{m}$	69

Figure 7.3	The fill gas conductance in the continuum flow with respect to the pressure for (a) the single-component gases, (b) the gas mixtures of helium with the gaseous fission products, and (c) the gas mixtures of argon with the gaseous fission products. The gas compositions are arbitrarily chosen. The fill gas temperature is set to 300 K (left column) and 900 K (right column). The plane geometry is chosen and $(g_1 + g_2) \approx 2g$. The gap distance is set to 100 μm , while $r_1 = 0.005\text{m}$	70
Figure 7.4	The fill gas conductance in the free-molecular flow with respect to the pressure for (a) the single-component gases, (b) the gas mixtures of helium with the gaseous fission products, and (c) the gas mixtures of argon with the gaseous fission products. The gas compositions are arbitrarily chosen. The fill gas temperature is set to 300 K (left column) and 900 K (right column). The plane geometry is chosen and $(g_1 + g_2) \approx 2g$. The gap distance is set to 100 μm , while $r_1 = 0.005\text{m}$	71
Figure 7.5	Schematic illustration of the temperature jump distance [18].	72
Figure 7.6	Temperature jump distance comparison at various gas pressures and temperatures for: (a) helium, (b) argon, (c) krypton, and (d) xenon.	73
Figure 7.7	Temperature jump distance comparison at various gas pressures and temperatures for the gas mixtures of helium (left column) and argon (right column) with the gaseous fission products. The gas compositions are arbitrarily chosen.	74
Figure 7.8	The thermal accommodation coefficient of the selected inert gases using the improved model (Eq. 7.14) and the traditional approach by Lanning and Hahn [19] for He and Xe for 500–1000 K according to Ullman data [20]. Note that the mass of the solid is set to a very large value (i.e., $M_s = 1 \times 10^5 \text{ g/mol}$) in the calibration. Experimental data are extracted from Song and Yovanovich [21].	76
Figure 8.1	Schematic illustration of gap between two solid bodies along with equivalent circuit for the system (not to scale).	82
Figure 8.2	Schematic illustration of analysis including model optimization and uncertainty quantification to estimate uncertainty of the computational model.	83
Figure 8.3	Model fit for helium at (a) 289 K, and (b) 673 K using the calibrated model (—) with $\hat{\theta} = \{-2.406 \pm 0.496, 0\}$ and $\hat{\sigma} = 8069.009 \text{ W/m}^2\text{-K}$, the Ross-Stoute model (---), the modified Ross-Stoute model (---), and analytically derived expression (.....) with $\theta = \{-1, 0\}$. The grey areas in the plot correspond to $\pm\hat{\sigma}_M$ around the mean (■) and 95% confidence interval (▬). The data are from Garnier and Begej [22].	86
Figure 8.4	Model fit for helium at (a) 283 K, (b) 466 K, and (c) 673 K using the calibrated model (—) with $\hat{\theta} = \{1.807 \pm 0.566, 168.754 \pm 13.552\}$ and $\hat{\sigma} = 11208.501 \text{ W/m}^2\text{-K}$, the Ross-Stoute model (---), and the modified Ross-Stoute model (---). The grey areas in the plot correspond to $\pm\hat{\sigma}_M$ around the mean (■) and 95% confidence interval (▬). The data are from Garnier and Begej [22].	88

Figure 8.5	Model fit for argon at (a) 283 K, and (b) 473 K using the calibrated model (—) with $\hat{\theta} = \{0.140 \pm 0.121, -0.277 \pm 5.468\}$ and $\hat{\sigma} = 463.261$ W/m ² -K, the Ross-Stoute model (---), and the modified Ross-Stoute model (---). The grey areas in the plot correspond to $\pm\hat{\sigma}_M$ around the mean (■) and 95% confidence interval (▬). The data are from Garnier and Begej [22].	89
Figure 8.6	Model fit for He(51.79%):Ar(48.21%) gas pair at (a) 283 K and (b) 473 K using the calibrated model (—) with $\hat{\theta} = \{0.914 \pm 0.082, 29.377 \pm 3.361\}$ and $\hat{\sigma} = 521.531$ W/m ² -K, the Ross-Stoute model (---), and the modified Ross-Stoute model (---). The grey areas in the plot correspond to $\pm\hat{\sigma}_M$ around the mean (■) and 95% confidence interval (▬). The data are from Garnier and Begej [22].	90
Figure 8.7	Relative gap conductance difference for helium, argon, and a binary mixture of helium and argon at 283–473 K between the experimental data and predictions from (a) the Ross-Stoute model, (b) the modified Ross-Stoute model, and (c) the calibrated model with $\hat{\theta} = \{0.605 \pm 0.096, 14.522 \pm 7.896\}$ and $\hat{\sigma} = 4754.568$ W/m ² -K. The data are from Garnier and Begej [22].	91
Figure 9.1	Gap conductance comparison at various temperatures and pressures for (a) helium only, (b) argon only, and (c) a binary mixture of helium and argon using the newly implemented model, Eq. 9.2 (—), the original Ross-Stoute model, Eq. 8.1 (---), and Bison’s default model, Eq. 9.1 (---). Temperature jump distance, accommodation coefficient, and the gas thermal conductivity are calculated based on the expressions given in [23]. The shaded areas (▬) represent the initial rod internal pressure ranges from 0.3 to 3.45 MPa in LWRs [24]. The experimental data are from Garnier & Begej [22] and represented with $\pm 1\sigma$ data uncertainty (■). The applied load is 1300 N/m ² . The gap thickness is 5.9 μ m.	95
Figure 9.2	Configuration of the measurement points, regenerated from Garnier and Begej [25]. Upper plate and bottom plate faces only at those 19 points. Therefore, the data are measured at 19 points including the center point.	96
Figure 9.3	Schematic illustration of the geometry constructed for Bison simulations (not to scale). d_i denotes the i -th local gap distance between the sample plates, and is varied for $i = 1, 19$ including all measurement points.	97
Figure 9.4	Schematic of the automated benchmark. Darker gray boxes represent the gold files for each surface configuration that includes local gap distances, and the experimental conditions/data.	98
Figure 9.5	Gap conductance comparison of the Bison predictions against the experimental data. Open gap configuration. Hand calculations (HC) are presented for Eq. 9.2 to confirm that the computational model setup is done correctly set in the code. The fill gas thermal conductivity is computed from the models as in the code.	99
Figure 9.6	The average linear heat rate histories for (a) the Halden Instrumented Fuel Assembly (IFA)-515.10 irradiation and (b) the Halden IFA-562 irradiation.	100

Figure 9.7	Fuel centerline temperature differences using Bison’s original model and the proposed model with respect to the rod average burnup for (a) the Halden IFA-515.10 irradiation and (b) the Halden IFA-562 irradiation.	102
Figure 9.8	Comparison of the fuel centerline temperature predictions using Bison’s original model and the proposed model for the burnup range of [0, 30 MWd/kgU].	103
Figure 9.9	KS-test comparison cumulative fraction plot of the fuel centerline temperature predictions using Bison’s original model and the proposed model for the burnup range of [0, 30 MWd/kgU].	103
Figure 9.10	Volume averaged fuel temperature differences using Bison’s original model and the proposed model with respect to the rod average burnup for (a) the Halden IFA-515.10 irradiation and (b) the Halden IFA-562 irradiation.	105
Figure 9.11	Comparison of the volume averaged fuel temperature predictions using Bison’s original model and the proposed model for the burnup range of [0, 30 MWd/kgU].	106
Figure 9.12	KS-test comparison cumulative fraction plot of the volume averaged fuel temperature predictions using Bison’s original model and the proposed model for the burnup range of [0, 30 MWd/kgU].	106
Figure 9.13	NEA temperature differences using Bison’s original model and the proposed model with respect to the rod average burnup for (a) the Halden IFA-515.10 irradiation and (b) the Halden IFA-562 irradiation.	108
Figure 9.14	Comparison of the NEA temperature predictions using Bison’s original model and the proposed model for the burnup range of [0, 30 MWd/kgU].	109
Figure 9.15	KS-test comparison cumulative fraction plot of the NEA temperature predictions using Bison’s original model and the proposed model for the burnup range of [0, 30 MWd/kgU].	109
Figure A.1	Model comparison to experimental data for fuel thermal expansion model with respect to temperature for (a) UO ₂ fuel and (b) PuO ₂ fuel. The data are extracted from Material Property Correlations [26] that include the experimental data for UO ₂ fuel [27, 28, 29, 30, 31, 32, 33] and PuO ₂ fuel [34, 35].	137
Figure A.2	Model comparison for the fractional volume change due to the solid fission products with respect to temperature.	139
Figure A.3	Model comparison for the fractional volume change due to the gaseous fission products with respect to temperature at various burnups using (a) MATPRO-11 model and (b) FRAPCON model.	139
Figure A.4	Model comparison for the fractional volume change due to irradiation-induced densification with respect to the burnup at various temperatures and resintering densities using Eq. A.15.	141
Figure A.5	Model comparison for the fractional volume change due to irradiation-induced densification with respect to the burnup at various temperatures and resintering densities using Eq. A.16.	142

Figure A.6	Model comparison for the fractional volume change due to fuel relocation with respect to the burnup at various linear heat rates using (a) the FRAPCON-4.0 model and (b) the ESCORE model.	143
Figure B.1	Schematic illustration of the fuel rod behavior during a reactivity initiated accident (RIA) transient [36].	145
Figure B.2	Illustration of the code comparison between CTFFuel and FRAPTRAN-1.5 for assessment of RIA transient behaviors.	146
Figure C.1	Contour plots of the radial power distribution as a function of the rod average burnup and the normalized radius for various Gd concentrations.	149
Figure C.2	Evolution of the radial power profile as the fuel burns out for various Gd concentrations.	150
Figure D.1	Three-by-three rod bundle geometry with coolant-centered (left) and rod-centered (right) subchannels.	156
Figure D.2	Comparison of different friction models as coded in CTF. All four options limit to the Hagen-Poiseuille equation for low Reynolds numbers. For the Churchill and Zigrang correlations, the roughness effect is displayed as two extreme values, which are labeled in the figure. Note that the McAdams and Churchill correlations in the code are actually modified versions of their respective namesakes.	157

List of Algorithms

1	The Delayed Rejection Adaptive Metropolis [37, 38].	14
2	The Delayed Rejection [37, 38]	14
3	Two-Sample Kolmogorov–Smirnov Test [39]	16

List of Symbols

Greek Letters

α	thermal accommodation coefficient	
η	the angle between the velocity vector of the incident gas atom and the line joining the centers of the spheres at impact	
γ	($= c_P/c_V$), the ratio of specific heats	
$\hat{\rho}$	($= 1/V$), molar density	
Λ	($= \frac{2\lambda_1\lambda_2}{\lambda_1+\lambda_2}$), harmonic mean of the thermal conductivities of surrounding solids	(W/m-K)
λ	thermal conductivity	(W/m-K)
μ	dynamic viscosity	(Pa.s)
μ	mean	
μ	ratio of the mass of incident gas atom to the mass of the other stationary solid atom	
ν	degrees of freedom	
Φ	two-phase multiplier	
Φ_{ij}	the empirical expression that is proportional to the ratio of translational to fictitious conductivity characterizing the interaction between unlike molecules	
π	posterior density	
π_0	prior density	
Ψ_λ	excess thermal conductivity	(W/m-K)
Ψ_{ij}	empirical expression that is a function of thermal conductivities, Sutherland constants, temperature, and molecular weights of the constituents	
ρ	density	(kg/m ³)
σ	standard deviation	
σ^2	variance estimate	
σ_{SB}	the Stefan-Boltzmann constant	(5.67×10^{-8} W/m ² K ⁴)
ε	emissivity	
χ	Jacobian matrix	
θ	coefficient matrix	
ξ	surface roughness	(m)

Nondimensional Numbers

Kn	Knudsen number
Re	Reynolds number

Roman Letters

Δt	time increment
\dot{q}	internal heat generation rate
\hat{F}	empirical distribution function of the i -th sample
\mathbf{R}	residual matrix
\mathbf{V}	covariance matrix
\mathbf{v}	observations
\mathbf{y}	predictions

a	accommodation coefficient / parameter of the Morse potential	
A_{ij}^*, B_{ij}^*	inter-molecular potential functions	
$B_i(T)$	i -th virial coefficient	
Bu	burnup	(MWd/kgU)
c_P	specific heat capacity	(J/mol-K)
D	the Kolmogorov-Smirnov statistic	
d	Euclidian distance	
d	distance	(m)
d_M	Manhattan distance	
E_D	formation energy of a defect	
f	Darcy friction factor	
G	mass flux of the field of interest	
g	temperature jump distance	(m)
H	hardness	(N/m ²)
h	bandwidth parameter	
h	heat transfer coefficient	(W/m ² -K)
K	Kernel function	
k_B	the Boltzmann constant	(1.38×10 ⁻²³ J/K)
l	mean free path	(m)
M	molecular weight	
m	mass	
n	number of constituents in mixture	
P	pressure	(Pa)
q	quantity of interest	
R	thermal resistance	
R^2	coefficient of determination	
R_g	gas constant	(8.314 J/mol-K)
R_{molten}	fraction of the molten fuel	
SS_q	sum of squares	
T	temperature	(K)
V	volume	(m ³)
V^*	(= $R_g T_c / P_c$), characteristic molar volume	
W	load	(N/m ²)
x	mole fraction	
Z	compressibility factor	
Subscripts / Superscripts		
0	dilute gas	
c	pseudo-critical / critical	
ci	clad inner	
cl	fuel centerline	
co	clad outer	

<i>D</i>	Doppler
<i>fs</i>	fuel surface
<i>g</i>	fill gas
<i>h</i>	hydraulic
<i>l</i>	liquid
<i>m</i>	mixture / harmonic mean
<i>r</i>	reduced / radiation
<i>s</i>	solid contact
<i>SNTR</i>	sintering
<i>v</i>	vapor
<i>w</i>	wall

List of Acronyms

AM	Adaptive Metropolis
BWR	boiling water reactor
CASL	Consortium for Advanced Simulation of Light Water Reactors
CDF	cumulative (or empirical) distribution function
COBRA-TF	Coolant Boiling in Rod Arrays–Two Fluid
DOE	US Department of Energy
DR	Delayed Rejection
DRAM	Delayed Rejection Adaptive Metropolis
FRACAS	Fuel Rod and Cladding Analysis Subcode
CTF	a modernized version of COBRA-TF
EPRI	Electric Power Research Institute
IFA	Instrumented Fuel Assembly
IETs	integral effects validation tests
INL	Idaho National Laboratory
ITU	Institute for Transuranium Elements
KDE	kernel–density estimation
KS	Kolmogorov–Smirnov
LWR	Light Water Reactor
MH	Metropolis–Hastings
MPD	modified pulse design
MLD	modified longitudinal design
MCMC	Markov Chain Monte Carlo
MOOSE	Multiphysics Object Oriented Simulation Environment
NEAMS	Nuclear Energy Advanced Modeling and Simulation
NCSU	North Carolina State University
NEA	Nuclear Energy Agency

NFI Nuclear Fuel Industries
NRC US Nuclear Regulatory Commission
NSRR Nuclear Safety Research Reactor
OECD Organisation for Economic Co-operation and Development
ORNL Oak Ridge National Laboratory
PDF probability density function
PNNL Pacific Northwest National Laboratory
PWR pressurized water reactor
RIA reactivity initiated accident
RMSE root-mean-square error
SA sensitivity analysis
SETs separate effects validation tests
SNL Sandia National Laboratories
SRQ system response quantity
SQA software quality assurance
TD theoretical density
UQ uncertainty quantification
VERA-CS Virtual Environment for Reactor Applications–Core Simulator
VVUQ verification, validation, and uncertainty quantification

CHAPTER

1

INTRODUCTION

Nuclear reactor technology has been utilized since 1960s to supply the demand of energy through sustainable energy production. This led efforts to improve the current nuclear reactor designs and to resolve materials' problems to provide promising features in terms of economics, efficiency, safety, proliferation resistance, waste production, and the safe aging of the materials. However, new problems arise due to increased radiation damage, corrosion, and so on, as the nuclear utilities seek to extract as much energy from the fuel as possible. They increase the capacity factor by applying principal methods (e.g., extended burnup, power uprates, and longer refueling cycle), and other cost-reduction measures to remain competitive due to electricity deregulation [10]. At this stage, computational tools serve promising features with increasing capabilities of high performance computing resources to improve operations of the power plants; however, this is not an easy task. It is expected that those tools can explicitly incorporate all relevant physical mechanisms controlling fuel rod behavior. Figure 1.1 shows the illustration of the complex phenomena and behavioral evolution and their interactions, which must be incorporated in modeling fuel rod behavior. Important requirements for the fuel rod modeling are to produce thermal energy, and maintain the necessary structural integrity to retain fission products. This is important as the fuel rod cladding serves as a defense in depth physical barrier. Based on the US Nuclear Regulatory Commission (NRC), the defense in depth is an approach to design and operate nuclear facilities that prevents and mitigates accidents that release radiation or hazardous materials.

In the last decade, the US Department of Energy (DOE) has supported the use and adoption of high-fidelity multi-physics modeling and simulation tools such as Consortium for Advanced Simulation of Light Water Reactors (CASL) and Nuclear Energy Advanced Modeling and Simulation (NEAMS) programs. These multi-physics calculations couple neutronics codes with fuel performance and thermal-hydraulics codes to understand the best-estimate system response of the nuclear reactors through science-based modeling and simulation technology for

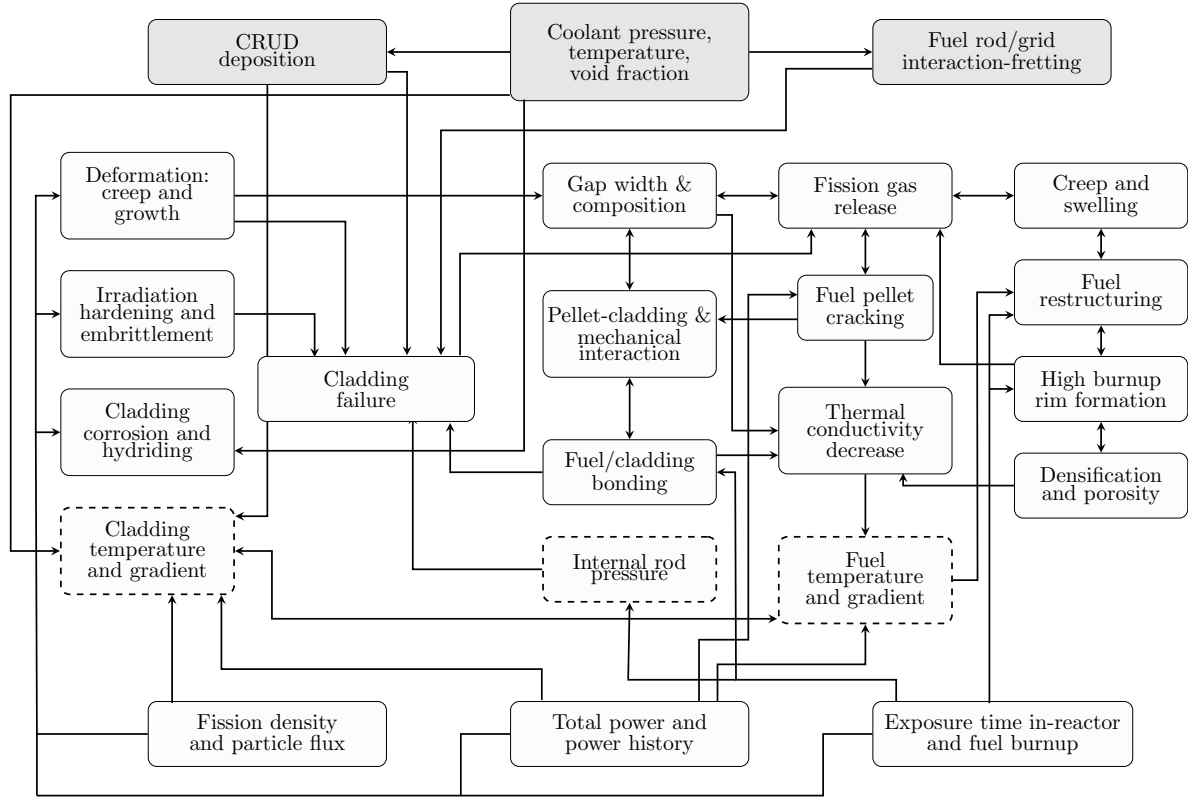


Figure 1.1: Schematic illustration of the complex phenomena and behavioral evolution and their interactions, which must be incorporated in modeling fuel rod behavior, as reproduced from Olander and Motta [10], after Rashid et al. [11] and Olander [12].

the nuclear energy industry. The aim is to provide predictive capabilities to the vendors for design and performance improvements, reactor operator support analyses, licensing safety analyses, safe methods of burnup extension, and decrease the time necessary for development and qualification of new materials. CASL's Virtual Environment for Reactor Applications–Core Simulator (VERA-CS) [40] is a good example where the neutronics code MPACT [41], the thermal-hydraulic subchannel code a modernized version of COBRA-TF (CTF) [42] and the fuel performance code Bison [43] are coupled, as illustrated in Figure 1.2.

A current challenge in multi-physics simulations is being too computationally expensive for whole core calculations during cycle depletion and transient applications. The complexity arises from fuel performance modeling due to the multi-disciplinary and multi-scale modeling paradigm of material behavior (Figure 1.1), and impracticality of today's computing capabilities. For example, the fuel performance code Bison in VERA-CS requires a substantial amount of run time to model each pin separately in the assembly. The first attempt was to replace Bison calculations in VERA-CS with pre-generated fuel temperature tables, which introduced a bias in the coupled calculations. The second attempt was the use of CTF's original simplified fuel rod model instead of the pre-generated tables, which allowed for simultaneously modeling

the whole core on both the assembly and the pin level. With considerations related to the computational time, it is intended to have simple improvements to allow for better predictions in the subchannel/system codes such as the addition of correlations to better predict the material properties or to utilize pre-generated gap conductance tables from fuel performance codes. In this manner, a better dynamic behavior can be observed.

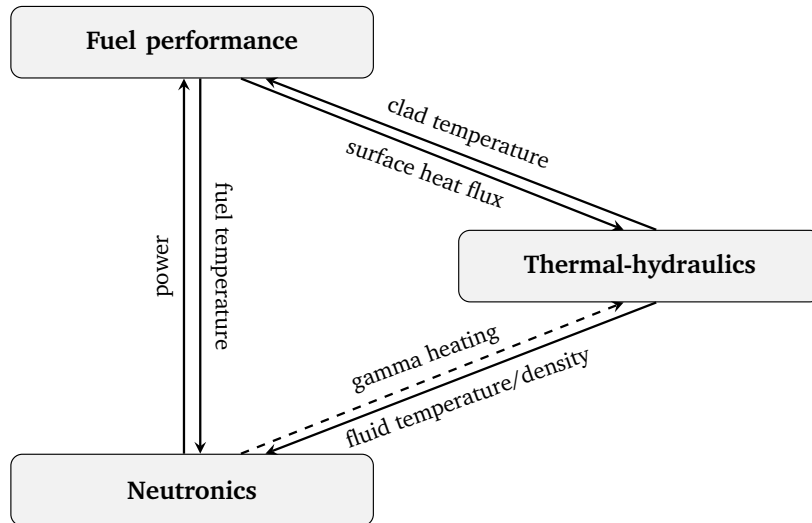


Figure 1.2: Schematic illustration of coupling in VERA-CS. The neutronics code require fuel temperature estimates from the fuel performance code and fluid conditions from the thermal-hydraulics code in the coupling.

Some of the well-known fuel performance codes in the nuclear industry are: FRAPCON (steady state) & FRAPTRAN (transient) by the NRC and Pacific Northwest National Laboratory (PNNL) [44, 45]; TRANSURANUS by the Institute for Transuranium Elements (ITU) [46]; FALCON by the Electric Power Research Institute (EPRI) [47]; and Bison by Idaho National Laboratory (INL) [48]. This list can be expanded with the inclusion of industry codes. Essentially, the codes differ according to their coupled thermal-mechanical fuel performance calculations in multi dimensions. Typically, a single pin is modeled in the fuel performance codes. The codes contain simplified neutronics models to compute radial power and burnup distributions during their fuel performance calculations.

This study aims to improve fuel temperature predictions, which is achieved under two major parts. In the first part, the study focuses on isolating the fuel performance capabilities of CTF to be used in a standalone capability and integrating new modeling options to investigate the fuel thermal conductivity degradation of Light Water Reactor (LWR) oxide fuels and fuel radial deformation. In the second part, gap conductance modeling is improved according to kinetic theory, and a conventional form of the gap conductance model is proposed with enhanced prediction considering its practical use in today’s nuclear applications. Accurate simulation

of the gap between the nuclear fuel and the cladding is crucial due to its pronounced effect on the thermo-mechanical performance of nuclear fuel rods. Heat transfer across the gap heavily impacts fuel temperatures, particularly Doppler temperature feedback which is critical for reactor stability in LWRs.

Chapter 2 outlines verification, validation, and uncertainty quantification (VVUQ) methods for *software quality assurance (SQA)* which is the process of detecting unintentional coding mistakes in software. The application of modern software quality assurance, verification, and validation methods is increasingly becoming a focus of code development in nuclear engineering.

Chapter 3 provides an overview of this fuel modeling capability, CTFFuel, and a brief description of methodology to construct the code the framework of CTFFuel. This chapter summarizes the code's structure in addition to model updates and their integration into the code.

Chapter 4 introduces additional modeling options that account for burnup dependency of the fuel thermal conductivity. This is to improve CTF's temperature predictions by adding new fuel thermal conductivity models that account for the irradiation effects at the macroscopic scale with a reduced number of parameters such as burnup and content of the additives such as plutonium and gadolinium. Previous versions of CTF incorporated a temperature-dependent fuel thermal conductivity model, but in reality, fuel thermal conductivity is affected by fission product buildup and radiation damage. This results in a degradation of fuel thermal conductivity and a corresponding increase in fuel temperature due to the impaired heat transfer in the fuel. Accounting for the irradiation effects on the fuel thermal conductivity is particularly important for correct estimation of the fuel temperature predictions. This is required to calculate correct thermal feedback effects.

Chapter 5 describes sensitivity and uncertainty quantification studies on the fuel temperature predictions for the selected physical phenomena. The fuel temperature predictions are found to be the most sensitive to heat transfer across the gap given representative uncertainty bounds for selected parameters in nuclear conditions. The motivation of second part in this research is originated from the necessity of better understanding of the physics to reduce these large uncertainties in the gap conductance calculations and to yield more accurate estimation of fuel temperatures. Large uncertainties in the gap conductance model exist primarily due to inaccurate estimation of either mechanical or thermal aspects of the gap.

Chapter 6 attempts to examine the validity of the temperature-dependent fill gas thermal conductivity assumption in nuclear fuel rod gap calculations. The gap between fuel and cladding is initially pressurized to prevent unstable thermal behavior and to maintain cladding integrity. In LWRs, this initial pressure ranges from 0.3 to 3.45 MPa [24], and tends to increase throughout the life of the reactor due to phenomena such as expansion/contraction of the fuel and cladding and fission gas release. In some cases, the rod internal pressure approaches the external pressure or exceeds it. Presently, nuclear performance codes use thermal conductivity correlations from the Handbook of Material Properties [49] for inert gases of interest. The correlations are only temperature-dependent and are calibrated to experimental data at pressures below atmospheric pressure [50, 51]. However, the thermal conductivity of all gases increases with pressure, though the extent of this dependence varies depending upon the pressure. Therefore, the use of these models in nuclear applications, particularly in gap conductance calculations is questionable.

Chapter 7 describes improved gap conductance theory according to kinetic theory with

an extensive literature review. Deficiencies of the traditional approaches in gap conductance modeling are discussed for today's nuclear fuel performance codes. Corrections are made in the expressions of the gap conductance models to be more representative of the real world data.

Chapter 8 proposes a new gap conductance model for uranium dioxide-Zircaloy interfaces to be used instead of the model conventionally used in today's nuclear fuel performance codes. The model conventionally used to conduct heat across the fuel-to-cladding gap is a modified version of the Ross-Stoute model [52]. The model is modified in nuclear applications to include gap distance in the formulation, which introduces additional uncertainty as the model parameters were not adjusted after the modification. In this study, this conventional model is optimized for uranium dioxide-Zircaloy interfaces using available experimental data in the literature for single- and multi-component gases. Then, overall uncertainty in the gap conductance is quantified by performing uncertainty propagation.

Chapter 9 demonstrates predictions with the improved gap heat transfer modeling in nuclear applications using a finite-element based, DOE funded nuclear fuel performance code, Bison.

Chapter 10 presents the concluding remarks and primary contributions of this research.

CHAPTER

2

VERIFICATION, VALIDATION, UNCERTAINTY QUANTIFICATION

The application of modern software quality assurance, verification, and validation methods is increasingly becoming a focus of code development in nuclear engineering. *SQA* is the process of detecting unintentional coding mistakes in software. Once the code quality is established, verification is used to ensure that the mathematical model is working as intended. The *verification* is the process of assessing a code’s capability to accurately model mathematical problems, which can be simply described as “solving the equations right”. This is performed in two ways: code verification and solution verification (Table 2.1). Next, the *validation* is the process of assessing a code’s capability to accurately model physical problems, which can be simply described as “solving the right equations”. The application of these software development procedures is crucial to the development of computational tools that are free of coding mistakes and that accurately represent reality (Figure 2.1). To identify sources of uncertainties in a scientific computing code, the *uncertainty quantification (UQ)* and *sensitivity analysis (SA)* help the code and model developers to understand how thoroughly the uncertainties and sensitivities are characterized and propagated. SA is the process to understand how simulation results depend on all input parameters, assumptions, or mathematical models in the analysis, which informs the user about the most important factors in uncertain results. Meanwhile, UQ allows for users to quantify how accurately a mathematical model describes the physical problems in both computational and real world applications. An extensive set of literature is available for more information on SQA, verification, and validation [53, 54, 55, 56, 57, 58, 59]. Lastly, parameter estimation methods are described in this chapter. Parameter estimation (or model calibration) is the process of using observations—either synthetic or experimental data—to es-

timate the parameters of the computational model and to estimate the associated parameter uncertainties.

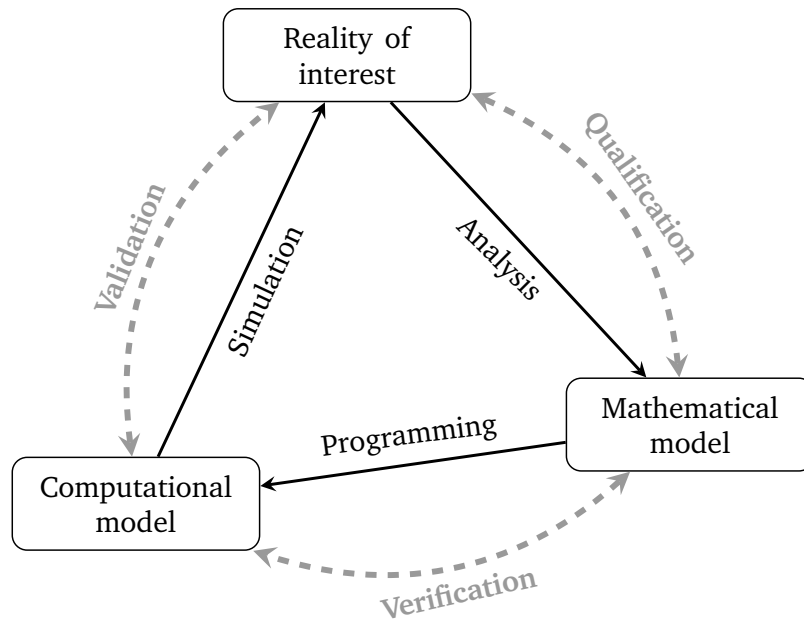


Figure 2.1: Simplified view of the model verification and validation process [13]. The dashed lines represent the assessment activities. The solid lines represent the modeling and simulation activities.

2.1 Software Quality Assurance

SQA is the process of detecting unintentional coding mistakes in software. After the initial coding, it is important to ensure that the new code capabilities function as expected, are free of coding mistakes, and are dynamically tested to prevent regression. To address this part of SQA, three types of defect tests are used [2, 60, 61, 62]: (i) the *unit tests* verify the execution of a single function or subroutine and prove that the tested section of the code is free of mistakes; (ii) the *component tests* compare a specific submodel or algorithm to expected output, showing that an overall model is running as expected; and (iii) the *system tests* address the whole code, which indicates that a new model is properly integrated into the overall code structure. Note that a selection of the above tests is integrated into the code's *testing harness* and is run periodically to ensure that the code capabilities are protected [63]. These tests contribute to the *code coverage* that is defined as the tested percentage of code components as well as their interactions [64].

2.2 Code Verification

Code verification is the process to assess a code's capability for accurate representation of the underlying mathematical model and to assess correctness of the code. This allows for users to address both the correctness of the chosen numerical algorithm and the correct implementation of that algorithm into the code. The criteria that are used for the code verification can be listed (from the least to the most rigorous) as: simple tests, code comparisons, discretization error evaluation, convergence tests, and order-of-accuracy tests.

Simple tests The simple tests are used as a part of the code verification process. The tests do not require an exact solution to the mathematical model and are directly applied to the numerical solution. For example, the *symmetry tests* are implemented to check if the code produces a symmetric solution for a given symmetric geometry, initial and boundary conditions. Another example is the inclusion of *conservation tests* to ensure that the mass, momentum, and/or energy are conserved.

Code comparisons The code comparison is a common approach to test correctness of the code; however, agreement between the two codes does not imply that either code is correct. Additionally, it is useful to improve a code's credibility on prediction of a specific model with the reference codes prediction. The comparison helps to understand differences between the two codes when similar mathematical models under controlled conditions are used in both codes. A more detailed discussion can be found on the code comparison principles in the literature [65].

Discretization error evaluation The discretization error is defined as error in the discrete solution relative to the exact solution of the mathematical model. Its evaluation is an approach to quantitatively assess the error between the numerical solution and an exact solution of the mathematical model using a single spatial mesh and/or time step. Note that this requires an intuitive reasoning of the error if it is sufficiently small.

Convergence tests The convergence test is the process of assessing a code's capability to accurately demonstrate that the observed convergence of the discretization error matches the mathematically-derived convergence. The code verification is performed by calculating the observed order of accuracy and comparing it to an analytically derived exact solution of the underlying mathematical model.

Order-of-accuracy tests The order-of-accuracy test is the process to assess the convergence of the numerical scheme and to assess reduction of the discretization error as the mesh is refined relative to the mathematically-derived exact solution. The formal order of accuracy is evaluated from a truncation error analysis of the numerical scheme. The observed order of accuracy is evaluated from the systematic mesh refinement once the exact solution of the mathematical model exists.

2.3 Solution Verification

It is often necessary to calculate the observed order of accuracy by comparing the results from successive refinements of the solution domain since exact solutions are generally difficult for systems which solve coupled differential equations. This is referred as *solution verification* and it attempts to address whether a given simulation of a mathematical model is sufficiently accurate for its intended use and to assess confidence in the computed results. This includes accuracy of the simulation, accuracy of the simulation inputs, and accuracy of the simulation outputs. This process is important for the quantification of the numerical accuracy of the simulation for two main reasons: to quantify the total uncertainty in a simulation prediction and to establish the numerical accuracy of a simulation for model validation purposes. The aspects of the solution verification can be listed as: (i) verification of input data (e.g., input files, mesh, material properties, boundary and initial conditions); (ii) verification of post-processing tools (e.g., automation of post-processing steps to prevent any possible human errors); and (iii) numerical error estimation (e.g., round-off error, statistical sampling error, iterative error, discretization error) [2].

Table 2.1: Verification assessment classifications and descriptions [1, 2].

Classification		Focus	Responsibility	Methods
Code Verification	Software Quality Assurance	Reliability and robustness of the software	Code developer & Model developer	Configuration management, static & dynamic testing, formal analysis, etc.
	Numerical Algorithm Verification	Correctness of the numerical algorithms in the code	Model developer	Analytical solutions, benchmark problems, manufactured solutions, conservation tests, iterative convergence tests, symmetry tests, etc.
Solution Verification	Numerical Error Estimation	Estimation of the numerical accuracy of a given solution to the governing equations	Model developer	Grid convergence, time convergence, etc.

2.4 Validation

Validation is the process of assessing a code’s capability to accurately model physical problems, which can simply be described as “solving the right equations”. It is important to ensure that the code is capable of accurately modeling real-world problems. To address this, two types of validation tests are often performed: (i) the *separate effects validation tests (SETs)* which are aimed at evaluating a code’s capability to model a single physical phenomenon; and (ii) the *integral effects validation tests (IETs)* to investigate a system’s overall response to a model which involves many phenomena. An extensive set of literature is available for more information on the validation [2, 66, 67].

2.5 Uncertainty Quantification and Sensitivity Analysis

The UQ is an important process to quantify how accurately a mathematical model describes the physical problems in both computational and real world applications. Uncertainty can be classified into two distinct meanings [2, 68, 67]: (i) the *aleatory (or statistical) uncertainty* due to the probabilistic variability; and (ii) the *epistemic (or systematic) uncertainty* due to lack of data and knowledge. The uncertainty can enter the mathematical models and data in many ways. Sources of the uncertainty can be listed as follows [69]:

- the *parameter uncertainty* due to unknown model parameters,
- the *parametric variability* due to variability of input variables of the computational model,
- the *structural uncertainty* due to the lack of underlying physics, known as the model bias or discrepancy,
- the *algorithmic uncertainty* due to numerical errors or approximations during integration of the computational model,
- the *experimental uncertainty* due to the variability of experimental measurements, and
- the *interpolation uncertainty* due to the lack of data or use of the computational model out of its applicability range.

The SA is the process to understand how simulation results depend on all input parameters, assumptions, or mathematical models in the analysis, which informs the user about the most important factors in uncertain results. It can be either local or global [53]: (i) the *local SA* aims to determine how outputs locally change as a function of varying input parameters, which is a common approach to use local SA for system design and optimization; and (ii) the *global SA* aims to determine which input parameters contribute most variability and determine the conditions to reduce the epistemic uncertainties due to poorly understood multi-physics phenomena. In this study, three sensitivity methods are used: the *parameter study* to show how input parameters influence the response variables; the *Morris screening* to study interactions of input parameters; and the *random sampling* to study linear relationships between input parameters.

In this study, a statistical black-box uncertainty propagation method is employed using the Dakota toolkit that is being developed at Sandia National Laboratories (SNL). The toolkit contains algorithms for optimization with gradient and nongradient-based methods; uncertainty

quantification with sampling, reliability, and stochastic expansion methods; parameter estimation with nonlinear least squares methods; and sensitivity/variance analysis with design of experiments and parameter study methods [70]. A Dakota to any user code coupling scheme is illustrated in Figure 2.2, which is used for both SA and UQ.

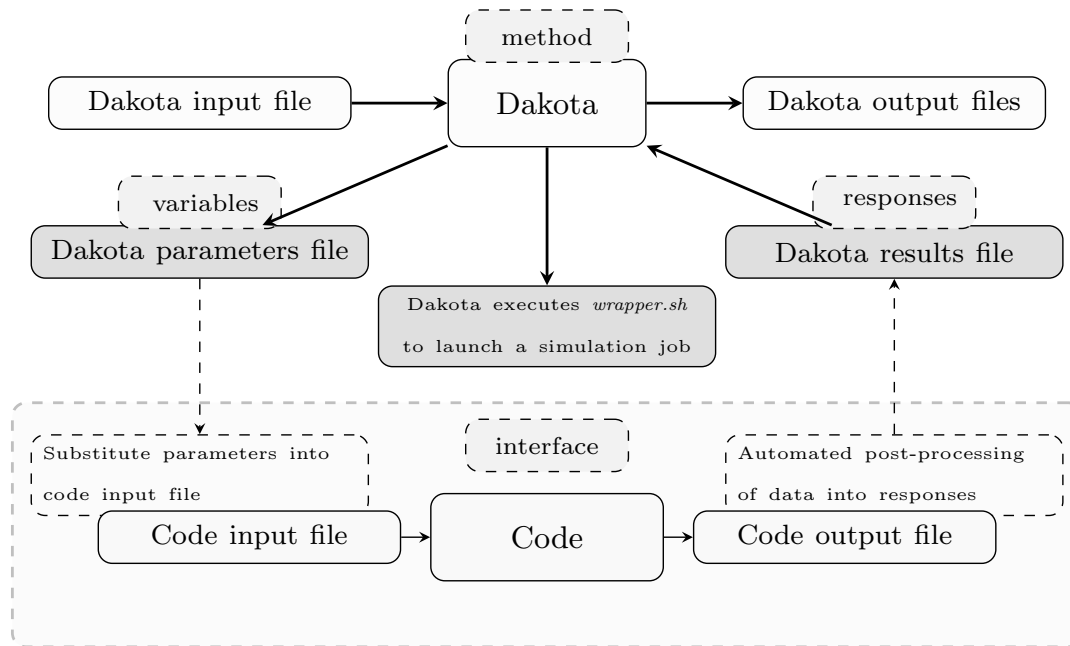


Figure 2.2: Schematic illustration of Dakota-to-code coupling.

2.6 Parameter Estimation Methods

Calibration is the process of using observations—either synthetic or experimental data—to estimate the parameters of the computational model. There are several parameter estimation methods available in literature. In this study, Frequentist and Bayesian estimation methods are used. The Frequentist view of probability is the frequency of occurrence as

$$P(A) = \frac{n}{N}, \quad (2.1)$$

for n times event A occurs in N . The Bayesian view of probability is a measure of the plausibility of an event given incomplete knowledge, where Bayes' rule simply expresses the likelihood of

an event A occurring that event B as

$$P(A | B) = \frac{P(B | A)P(A)}{P(B)}, \quad (2.2)$$

for events A and B with $P(B) \neq 0$. The Frequentist inference does not require a prior and is less computationally intensive as compared to the Bayesian inference, which can be computationally intensive due to integration over many dimensions.

2.6.1 Frequentist Inference

The principle is to estimate model parameters $\boldsymbol{\theta} = \{\theta_i\}_{i=1}^p$ by minimizing the differences between observations $\mathbf{v} = \{v_i\}_{i=1}^n$ and predictions $\mathbf{y} = \{y_i\}_{i=1}^n$, where predictions are made according to the model function $f(\boldsymbol{\theta})$. Note that this is performed by minimizing the function using the downhill simplex algorithm [71].

$$\hat{\boldsymbol{\theta}} = \underset{\boldsymbol{\theta}}{\operatorname{argmin}} \sum_i^n [v_i - y_i]^2. \quad (2.3)$$

The sensitivity matrix, $\boldsymbol{\chi}$ of the model function is calculated numerically and used to estimate the covariance of parameter matrix $\boldsymbol{\theta}$ [72]. The covariance matrix \mathbf{V} can be estimated from

$$\hat{\mathbf{V}} = \hat{\sigma}^2 \left[\hat{\boldsymbol{\chi}}^T(\hat{\boldsymbol{\theta}}) \hat{\boldsymbol{\chi}}(\hat{\boldsymbol{\theta}}) \right]^{-1}, \quad (2.4)$$

where

$$\hat{\chi}_{ij} = \partial f_i(\hat{\boldsymbol{\theta}}) / \partial \theta_j,$$

$$\hat{\sigma}^2 = \frac{1}{(n-p)} \mathbf{R}^T \mathbf{R}, \text{ variance estimate, and}$$

\mathbf{R} = residual matrix between the observations and the predictions.

2.6.2 Bayesian Inference

The motivation in statistical inference is to draw conclusions about a phenomenon based on observed data, $\mathbf{v} = \{v_i\}_{i=1}^n$. The interpretation of probability is subjective and updated with the new data set. In parameter estimation, the parameters, $\boldsymbol{\theta} = \{\theta_i\}_{i=1}^n$ are described as densities. With Bayes' relation, the posterior distribution can be calculated in terms of likelihood, prior, and the normalization constant which is not solvable analytically. Therefore, its evaluation typically requires high dimensional integration using the numerical methods. In this manner, stochastic or deterministic approximations can be used, which may be computationally intensive.

$$\pi(\boldsymbol{\theta} | \mathbf{v}) = \frac{p(\mathbf{v} | \boldsymbol{\theta}) \pi_0(\boldsymbol{\theta})}{p_{\mathbf{v}}(\mathbf{v})} = \frac{\pi(\mathbf{v} | \boldsymbol{\theta}) \pi_0(\boldsymbol{\theta})}{\int_{R^p} \pi(\mathbf{v} | \boldsymbol{\theta}) \pi_0(\boldsymbol{\theta}) d\boldsymbol{\theta}}, \quad (2.5)$$

where

$\pi(\boldsymbol{\theta} \mid \mathbf{v})$ = the posterior density that is the conditional distribution of unknown parameters for a given observed data, and
 $\pi_0(\boldsymbol{\theta})$ = the prior distribution that quantifies prior knowledge of the parameters.

The Delayed Rejection Adaptive Metropolis

The Delayed Rejection Adaptive Metropolis (DRAM) [37] is one of the Markov Chain Monte Carlo (MCMC) methods for randomly sampling from posterior distributions. DRAM is a modified version of the standard Metropolis–Hastings (MH) algorithm [73] with a combination of adaptive Metropolis samplers [74, 75] and delayed rejection [76, 77, 78] and performs in two steps: (i) the *Delayed Rejection (DR)* step allows for the proposal function to be updated after a rejection, which allows easier computation in terms of CPU time; and (ii) the *Adaptive Metropolis (AM)* algorithm [75] allows for the online tuning of the proposal distribution based on the previous sample path of the MCMC chain. In this study, a DRAM code is created using the MCMC toolbox [38]. Model parameters and their correlations with each other are explored by employing the DRAM algorithm. The toolbox provide statistics that are provided in Table 2.2.

Table 2.2: DRAM Statistics.

	Description
mean	the mean from the chain
std	the standard deviation from the chain
MC_err	the Monte Carlo error of the estimates
tau	the integrated auto-correlation time that is time required for the new state not to have a ‘memory’ associated behavioral problem from the previous state
geweke	a simple test for a null hypothesis that the chain has converged (See [79] for Geweke’s MCMC convergence diagnostic)

2.7 Metrics

Differences between the observations $\mathbf{v} = \{v_i\}_{i=1}^n$ and the predictions $\mathbf{y} = \{y_i\}_{i=1}^n$ are quantified in terms of following metrics:

- The coefficient of determination,

$$R^2 = 1.0 - \frac{SS_{q,res}}{SS_{q,tot}}. \quad (2.6)$$

Algorithm 1 The Delayed Rejection Adaptive Metropolis [37, 38].

- 1: **procedure** THE DELAYED REJECTION ADAPTIVE METROPOLIS ALGORITHM
 - 2: Determine the design parameters n_s, σ_s^2 and number of iterations M
 - 3: Determine the initial parameters: $\theta_{opt} = \operatorname{argmin}_{\theta \in \Theta} \sum_i^n [v_i - f(q_i)]^2$
 - 4: Estimate the initial sum of squares: $SS_{q^0} = \sum_i^n [v_i - f_i(q^0)]^2$
 - 5: Estimate the initial variance: $s_0^2 = \frac{SS_{q^0}}{(n-p)}$
 - 6: Construct the covariance matrix: $V = s_0^2 [\chi^T(q^0)\chi(q^0)]^{-1}$, and $R = \operatorname{chol}(V)$.
 - 7: for $k = 1, \dots, M$:
 - 8: Sample $z_k \sim \mathcal{N}(0, I_p)$
 - 9: Construct the candidate $q^* = q^{k-1} + R'z_k$
 - 10: Sample $u_\alpha \sim \mathcal{U}(0, 1)$
 - 11: Compute $SS_{q^*} = \sum_i^n [v_i - f_i(q^*)]^2$
 - 12: Estimate $\alpha(q^*|q^{k-1}) = \min\left(1, e^{-[SS_{q^*} - SS_{q^{k-1}}]/(2s_k^2)}\right)$
 - 13: **if** $u_\alpha < \alpha$ **then**
 - 14: $q^k = q^*$ and $SS_{q^k} = SS_{q^*}$
 - 15: **else**
 - 16: Apply DR algorithm (see Algorithm 2)
 - 17: Update $s_k^2 \sim \Gamma^{-1}(a_{val}, b_{val})$ with $\alpha_{val} = 0.5(n_s + n)$ and $b_{val} = 0.5(n_s\sigma_s^2 + SS_{q^k})$
 - 18: **if** $u_\alpha < \alpha$ **then**
 - 19: Update $V_k = s_p \operatorname{cov}(q^0, q^1, \dots, q^k)$
 - 20: **else**
 - 21: $V_k = V_{k-1}$
 - 22: Update $R_k = \operatorname{chol}(V_k)$
-

Algorithm 2 The Delayed Rejection [37, 38]

- 1: **procedure** THE DELAYED REJECTION ALGORITHM
 - 2: Set design parameter: $\gamma_2 = \frac{1}{5}$
 - 3: Sample $z_k \sim \mathcal{N}(0, I_p)$
 - 4: Sample the second-stage candidate $q^{*2} = q^{k-1} + \gamma_2 R_k z_k$
 - 5: Sample $u_\alpha \sim \mathcal{U}(0, 1)$
 - 6: Compute $SS_{q^{*2}} = \sum_i^n [v_i - f_i(q^{*2})]^2$
 - 7: Compute: $J(q^a|q^b) = \frac{1}{\sqrt{(2\pi)^p |V|}} \exp\left(-\frac{1}{2} [(q^a - q^b)V^{-1}(q^a - q^b)^T]\right)$
 - 8: Estimate $\alpha(q^{*2}|q^{k-1}, q^*) = \min\left(1, \frac{\pi(q^{*2}|v)J(q^*|q^{*2})(1-\alpha(q^*|q^{*2}))}{\pi(q^{k-1}|v)J(q^*|q^{k-1})(1-\alpha(q^*|q^{k-1}))}\right)$
 - 9: **if** $u_\alpha < \alpha$ **then**
 - 10: $q^k = q^{*2}$ and $SS_{q^k} = SS_{q^{*2}}$
 - 11: **else**
 - 12: $q^k = q^{k-1}$ and $SS_{q^k} = SS_{q^{k-1}}$
-

- The Euclidean distance,

$$d(\mathbf{y}, \mathbf{v}) = \sqrt{\sum_{i=1}^n (y_i - v_i)^2}. \quad (2.7)$$

- The Manhattan distance,

$$d_M(\mathbf{y}, \mathbf{v}) = \sum_{i=1}^n |y_i - v_i|. \quad (2.8)$$

- The root-mean-square error,

$$RMSE = \frac{d(\mathbf{y}, \mathbf{v})}{\sqrt{n}}. \quad (2.9)$$

- The root-mean-square of relative errors,

$$rRMSE = \frac{d(1, \mathbf{y}/\mathbf{v})}{\sqrt{n}}. \quad (2.10)$$

where

SS_q = the sum of square,

\mathbf{v} = $\{v_i\}_{i=1}^n$ the observations (e.g., either experimental or synthetic data)

\mathbf{y} = $\{y_i\}_{i=1}^n$, the predictions, and

n = the number of samples.

Kernel–Density Estimation

Rosenblatt [80] developed the kernel–density estimation (KDE) concept originally, given in the following relation. The kernel density estimation is a method to estimate the probability density function (PDF) of a random variable in a non-parametric way [81]. Gaussian kernels $\mathcal{N}(\mu, \sigma^2)$ are used as the kernel density function in this study.

$$\hat{f}_h(x) = \frac{1}{nh} \sum_{i=1}^n K\left(\frac{x - x_i}{h}\right), \quad (2.11)$$

where:

$K(\cdot)$ = the kernel function (i.e., $\int K(t)dt = 1$), and

h = the bandwidth parameter.

Kolmogorov–Smirnov Test

The Kolmogorov–Smirnov (KS) test tries to determine if two data sets differ significantly. The test has the advantage of making no assumption about the distribution of data. It is a non-parametric hypothesis test which measures the probability that a chosen univariate data set is drawn from the same parent population as a continuous model (*the one-sample KS test*) or a second data set (*the two-sample KS test*). The latter is the primary interest in this study. Kolmogorov [82] and Smirnov [83, 84] proved that is the basis for an efficient goodness-of-fit

test when continuous data are involved. The test starts with the definition of the cumulative (or empirical) distribution function (CDF), \hat{F}_n for n real numbers x . The KS statistics are basically measures of the supremum distance between the CDFs. The KS *statistic* D in a two-sample test is

$$D_{n_1, n_2} = \sup_x \left| \hat{F}_{1, n_1}(x) - \hat{F}_{2, n_2}(x) \right|, \quad (2.12)$$

where:

\sup_x = the supremum of the set of distances, and
 \hat{F}_{i, n_i} = the empirical distribution functions of the i -th sample.

The KS test provides a test of a *null hypothesis* against the alternative hypothesis for two independent samples—given the sequences $\mathbf{x}_1 = \{x_i\}_{i=1}^{n_1}$ and $\mathbf{x}_2 = \{x_i\}_{i=1}^{n_2}$ —with their respective distribution function $F_i(x)$ and the sample CDF $\hat{F}_{1, n_i}(x)$ for $i = 1, 2$. The null hypothesis is a type of hypothesis used in statistics to propose that there is no statistical significance in the given samples (i.e., large KS statistic, small p -value).

Algorithm 3 Two-Sample Kolmogorov–Smirnov Test [39]

- 1: **procedure** TWO-SAMPLE KOLMOGOROV–SMIRNOV TEST
 - 2: Test the null hypothesis $H_0 : F_1(x) = F_2(x)$ against the alternative hypotheses
 - 3: **if** $H_1 : F_1(x) \neq F_2(x)$ **then**
 - 4: Determine the largest absolute deviation between the two sample CDFs
 - 5: D_{n_1, n_2}
 - 6: **else if** $H_2 : F_1(x) > F_2(x)$ **then**
 - 7: Determine the largest positive deviation between the two sample CDF functions
 - 8: $D_{n_1, n_2}^+ = \max \left\{ \hat{F}_{1, n_1}(x) - \hat{F}_{1, n_2}(x), 0 \right\}$
 - 9: **else if** $H_3 : F_1(x) < F_2(x)$ **then**
 - 10: Determine the largest positive deviation between the two sample CDF functions
 - 11: $D_{n_1, n_2}^- = \max \left\{ \hat{F}_{1, n_2}(x) - \hat{F}_{1, n_1}(x), 0 \right\}$
-

2.8 Chapter Summary

This chapter provides the basics of the verification, validation, and uncertainty quantification that are used for development of the newly-developed framework and integration of the new modeling options in the code.

CHAPTER

3

FUEL MODELING CAPABILITY, CTFFUEL

CTF, a modernized version of Coolant Boiling in Rod Arrays–Two Fluid (COBRA-TF), is jointly developed by the Reactor Dynamics and Fuel Modeling Group at North Carolina State University and the DOE—funded CASL at Oak Ridge National Laboratory [42, 85]. CTF is incorporated as the thermal hydraulics subchannel code in the CASL’s VERA-CS [86]. The code is capable of modeling the physical phenomena that occur within a LWR pressure vessel during nominal operating conditions and reactor transients. The code has a simplified fuel rod model to compute changes in the fuel temperature during a transient for feedback calculations, which was originally developed for the VIPRE-01 code [87] based on work in the GAPCON [88, 89] and FRAP series [90, 91, 92] of fuel performance codes, but with simplified mechanics and fill gas pressure models.

Prior to this work, CTF’s fuel rod model could only be run as part of the combined fluid and solid solution. In this study, a new fuel performance modeling capability is constructed to simulate steady state and transient thermal-mechanical response of LWR fuel rods using CTF’s simplified fuel rod model with specification of fuel rod boundary conditions [93, 94, 95]. The capability is called *CTFFuel* that interfaces CTF’s fuel performance modeling capabilities and includes its own input deck to be used independently. All of the CTF fuel rod modeling capabilities are made available to the user for modeling both steady state and transient conditions through this capability.

This chapter provides an overview of this fuel modeling capability CTFFuel. A brief description of methodology to construct the code in Section 3.1. The code’s structure with integration of model models to the code is outlined in Section 3.2. This chapter is summarized in Section 3.3.

3.1 CTFFuel

A new standalone fuel modeling capability, *CTFFuel* is constructed to simulate the steady state and transient thermal response of LWR fuel rod based on CTF’s simplified fuel rod model with specification of fuel rod boundary conditions [94, 95]. It interfaces CTF’s fuel modeling capabilities and this capability provides several benefits, including (i) flexibility to the users in terms of defining similar physics and/or parameters for a better code comparison between fuel performance codes of interest; (ii) verification of the numerical scheme of CTF’s conduction solution; and (iii) isolation of sensitivity/uncertainty analysis of CTF’s fuel performance capabilities by eliminating possible uncertainties that might propagate from thermal-hydraulic calculations in CTF. CTF’s fuel rod model could only be run as part of the combined fluid and solid solution. Figure 3.1 shows a schematic illustration of how CTFFuel interfaces CTF’s fuel rod model. The codes have consistent mathematical models, numerical scheme, and material properties. Therefore, the model development is only performed in CTF, and CTFFuel calls the necessary subroutines for the fuel rod model.

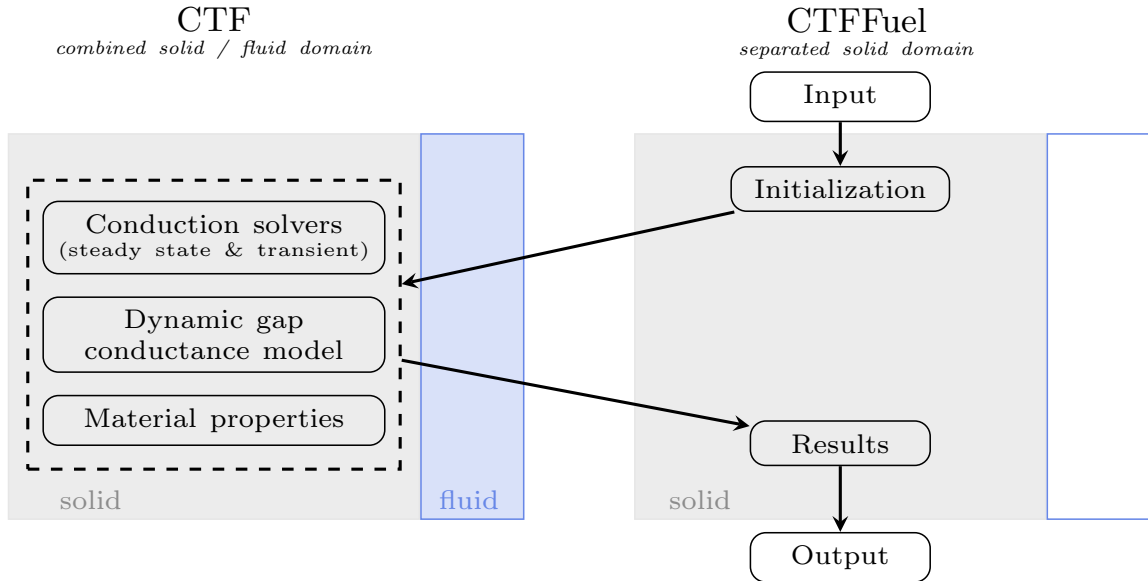


Figure 3.1: Schematic illustration of how CTFFuel interfaces CTF’s fuel rod model. Shaded areas represent solid and fluid domains with corresponding calculations. The dashed rectangle represents shared subroutines between the codes.

CTFFuel executes with an independent input as a standalone capability. The code input is keyword based, which allows many input parameters to be omitted and defaulted to reasonable defaults. The aim is to perform single pin simulations comparable to other fuel performance codes. Therefore, the nuclear fuel rod geometry is the primary interest of the code. Then the

code calls the necessary subroutines for the heat transfer solution from CTF and computes results. At the end, results are outputted to an independent output in HDF5 data format, unlike typical CTF outputs. A list of the input/output parameters and more information can be found in CTFFuel User’s Manual [94].

To ensure that consistent predictions from CTFFuel to CTF predictions in development of CTFFuel, defect tests were performed at both steady state and transient conditions in Toptan et al. [93, 95]. The defect tests are simple tests to examine specific sections of the code or whole code functions as expected and are free of coding mistakes. These tests were added to code’s test matrix to protect code’s capabilities based on coding guidelines established by CASL [96]. CTF has extensive unit testing for its features; CTFFuel inherits all SQA of CTF that tests aspects of the solid conduction solution (e.g., material properties, closure relations for gap conductance etc.). Toptan et al. confirmed with the defect tests that CTFFuel was constructed properly and numerical solution is consistent with CTF. The predictions from two codes agreed well on the fuel rod behavior at steady state and transient. The agreement was quantified in terms of temperature differences between the codes, which was found to be less than 0.3K. Later, Toptan et al. [97] demonstrated the code’s transient capabilities were demonstrated for reactivity insertion accident transient against FRAPTRAN [45, 9].

3.1.1 CTF’s Conduction Model

The conduction equation is expressed as a summation of the net rate of heat conducted and the rate of energy generated internally that is equal to the net rate of energy stored for each differential volume.

$$\rho C_P \frac{\partial T}{\partial t} = \nabla \cdot (\lambda \nabla T) + \dot{q}, \quad (3.1)$$

where

- $T = T(\vec{r}, t)$, the temperature as a function of the position vector \vec{r} , and time t ,
- λ = the thermal conductivity,
- \dot{q} = the internal heat generation rate,
- ρ = the density, and
- C_P = the specific heat capacity.

The CTF’s conduction model specifies conductor geometry with associated material properties and solves the conduction equation. Two types of conductors exist in the code: (i) a *heated conductor* for nuclear fuel rods, and geometries for solid heater tube, tube, and wall are supported. The nuclear fuel rod defaults to uranium dioxide fuel enclosed by Zircaloy cladding. The code contains built-in property tables for the default nuclear fuel rod, in addition to the material property correlations; and (ii) an *unheated conductor* for structural heat transfer surfaces.

The code solves a finite difference form of the conduction equation in Eq. 3.1 based on the *thermal resistance analogy*. The finite difference nodes of the conduction equation are modeled as control volumes connected by thermal resistances that allow to average the thermal conductivity at cell edges. Note that the control volumes are equally spaced in the fuel region and there is no control volume at centerline where the centerline temperature is interpolated.

A schematic of the CTF's radial meshing is shown in Figure 3.2 for the nuclear fuel rod. The radial conduction equation for a control volume is derived for i -th node with following relation.

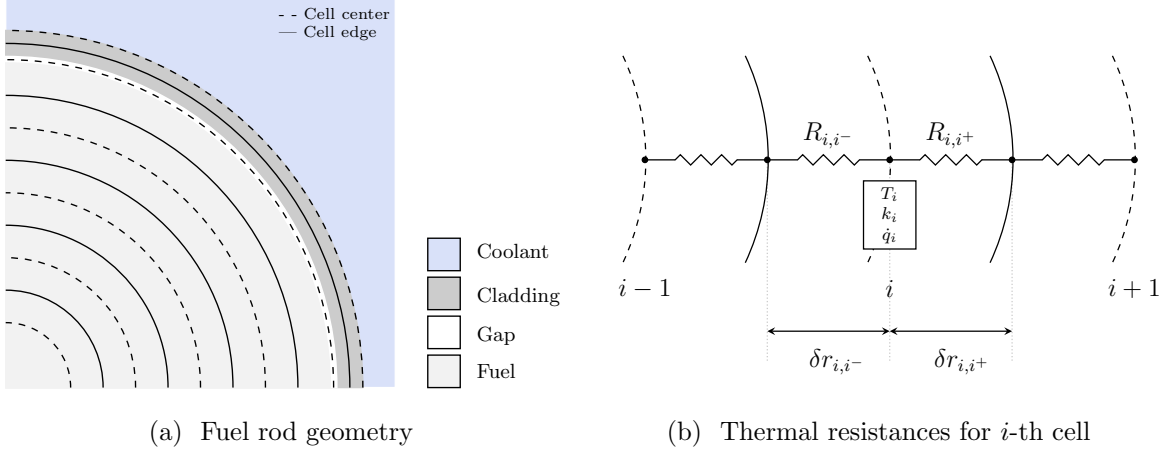


Figure 3.2: Schematic of CTF's radial meshing (not to scale).

$$(mC_P)_i \frac{\partial T_i}{\partial t} = -q_{i,i^-} - q_{i,i^+} + \dot{q}_i V_i, \quad (3.2)$$

where

- m = the mass associated with the node i (= the cold density $\rho \times$ the node volume V_i),
- T = the temperature for the node i ,
- \dot{q}_i = the volumetric heat generation rate for the node i ,
- $q_{i,i^*} = -\frac{1}{R_{i,i^*} + R_{i^*,i}} (T_{i^*} - T_i)$, the radial heat flow from the node i to the boundary i^* , and
- R_{i,i^*} = the thermal resistance between the node i to the boundary i^* .

Heat transfer through a node is computed from the conductivity of the material and temperature gradient across the node. The thermal resistances are computed for each node as a function of geometry and thermal conductivity that is updated at each time step based on previous step temperatures. The thermal resistance from the node i to boundary i^* is expressed in Eq. 3.3a for a cylinder. The thermal conductivity is calculated from Eq. 3.3b that approximates to the harmonic mean of the thermal conductivities of the node and the boundary.

$$R_{i,i^*} = \frac{\ln \left(\frac{r_i + \delta_{i,i^*}}{r_i} \right)}{2\pi \lambda_{i,i^*} \delta r_{i,i^*}}, \quad (3.3a)$$

$$\lambda_{i,i^*} = \lambda_{i^*,i} = \frac{2\pi \lambda_i \lambda_{i^*} \delta x}{\lambda_{i^*} \ln \left(\frac{r_i + \delta r_{i,i^*}}{r_i} \right) + \lambda_i \ln \left(\frac{r_{i^*}}{r_i + \delta r_{i,i^*}} \right)}. \quad (3.3b)$$

The radial conduction equation in Eq. 3.2 with differentiated temporal derivative at the

new time level becomes

$$\frac{(mC_P)_i}{\Delta t}(T_i - T_i^n) = \frac{(T_{i-1} - T_i)}{R_{i,i-}^n + R_{i-,i}^n} + \frac{(T_{i+1} - T_i)}{R_{i,i+}^n + R_{i+,i}^n} + \dot{q}_i V_i, \quad (3.4)$$

where

Δt = the time increment, and
 n = the superscript denotes the old time level.

This equation is solved by Gaussian elimination for all nodes at a given axial level with an implicit formulation in the radial direction. To solve the conduction problem in three dimensions, axial and azimuthal conduction terms are added on the right hand side of Eq. 3.4 as source terms analogous to the radial conduction terms:

$$\begin{aligned} \frac{(mC_P)_i}{\Delta t}(T_i - T_i^n) = & \frac{(T_{i-1} - T_i)}{R_{i,i-}^n + R_{i-,i}^n} + \frac{(T_{i+1} - T_i)}{R_{i,i+}^n + R_{i+,i}^n} \\ & + \frac{(T_{j-1} - T_i)}{R_{i,j-}^n + R_{j-,i}^n} + \frac{(T_{j+1} - T_i)}{R_{i,j+}^n + R_{j+,i}^n} \\ & + \frac{(T_{k-1} - T_i)}{R_{i,k-}^n + R_{k-,i}^n} + \frac{(T_{k+1} - T_i)}{R_{i,k+}^n + R_{k+,i}^n} + \dot{q}_i V_i. \end{aligned} \quad (3.5)$$

where

j, k = the subscripts denote respectively axial and azimuthal nodes, and
 $-, +$ = the superscripts denote the nearest cell edges at the node i in negative and positive direction, respectively.

The heat transfer surface is coupled to the fluid coolant at each surface heat transfer node where a heat transfer coefficient and a fluid sink temperature are specified for each phase of the fluid. The fraction of rod surface in contact with a given phase is taken into consideration during calculation of the heat transfer coefficient. Then, the rod heat flux q'' is expressed with the following relation. The last term on right hand side of Eq. 3.6 is added as a stability term in the code to handle oscillations that can occur during boiling/two-phase heat transfer that are strongly dependent on the wall temperature [98].

$$q'' = h_l(T_w - T_l^n) + h_v(T_w - T_v^n) + \frac{dh_l}{dT}(T_w - T_w^n)(T_w^n - T_l^n), \quad (3.6)$$

where

h = the heat transfer coefficient, and
 l, v, w = the subscripts denote the liquid, vapor, and wall, respectively.

3.1.2 CTF's Dynamic Gap Conductance Model

The code allows two options for specification of gap conductance; user-defined gap conductance and dynamic calculation of the gap conductance. The dynamic gap conductance model can be summarized into two categories; thermal and mechanical aspects of the gap [99].

Thermal aspects

The gap conductance is calculated, considering three separate heat paths in parallel across the gap, as a summation of (i) conduction through the actual solid constriction; composed of both purely metallic and surface oxide contributions; (ii) conduction (and sometimes convection) through the interfacial gas; and (iii) by direct radiation across the interspace [100]. The convective heat transfer in the gap is ignored due to a thin gap approximation.

Mechanical Aspects

The changes in the gap thickness are due to fuel and cladding differential thermal and irradiation-driven expansion and contraction. The fuel rod deformation model is used to predict changes in the gap width caused by elastic thermal stresses while the cladding deformation model is considered under both mechanical and thermal stresses. If the gap is open, elastic deformation is due to the difference between the internal gas pressure and system pressure. If the gap is closed, elastic displacement of the cladding in addition to the fuel thermal expansion is calculated with neglected plastic deformation. Note that change in rod dimensions is only reflected on the gap thickness in order to calculate gap conductance. Thermo-mechanical responses are only computed once the dynamic gap conductance model is enabled by the user.

The total radial movement at fuel pellet surface is determined from the summation of expansions at all fuel nodes as in Eq. 3.7a and analogously, axial expansion of the fuel stack is computed from Eq. 3.7b.

$$(\Delta r_{th})_f = \sum_i^{N_r} \varepsilon_r(T_i)_j \delta r_i, \quad (3.7a)$$

$$(\Delta l_{th})_f = \sum_j^{N_z} \varepsilon_z(\bar{T}_j) \delta x_j, \quad (3.7b)$$

where

- $\varepsilon_r(T_i)_j$ = the radial thermal strain at j -th axial node and i -th radial node,
- $\varepsilon_z(\bar{T}_j)$ = the axial thermal strain at j -th axial node,
- \bar{T}_j = the average cladding temperature at j -th axial node,
- δr_i = the radial thickness of i -th radial node,
- δx_j = the height of j -th axial node,
- N_r = the number of radial nodes in the fuel, and
- N_z = the number of axial nodes.

The radial and axial expansion of the cladding is determined from Eq. 3.8a and Eq. 3.8b, respectively. Only two nodes are defined for the cladding.

$$(\Delta r_{th})_c = \varepsilon_r(\bar{T}_j)\bar{r}_c, \quad (3.8a)$$

$$(\Delta l_{th})_c = \sum_j^{N_z} \varepsilon_z(\bar{T}_j)\delta x_j, \quad (3.8b)$$

where

$\varepsilon_r(\bar{T}_j)$ = the radial thermal strain at j -th axial node,
 $\varepsilon_z(\bar{T}_j)$ = the axial thermal strain at j -th axial node, and
 \bar{r}_c = the the cladding mean radius.

The cladding is assumed to be a thin shell cylinder and loaded by internal and external pressures. Therefore, radial and axial deformation of the cladding due to hoop and axial stresses—defined in Eq. 3.9a and Eq. 3.9b, respectively—are caused by the pressure difference.

$$\sigma_\theta = \frac{r_{ci}P_i - r_{co}P_o}{r_{co} - r_{ci}}, \quad (3.9a)$$

$$\sigma_z = \frac{r_{ci}^2P_i - r_{co}^2P_o}{r_{co}^2 - r_{ci}^2}, \quad (3.9b)$$

where

r_{ci} = the cladding inside radius,
 r_{co} = the cladding outside radius,
 P_o = the system pressure, and
 P_i = the internal fill gas pressure that is calculated for open and closed gap Eq. 3.11 and Eq. 3.15, respectively.

From the Hook's Law, the hoop and axial strains are determined from Eq. 3.10a and Eq. 3.10b, respectively.

$$\varepsilon_\theta = \frac{\Delta r}{\bar{r}} = \frac{1}{E} (\sigma_\theta - \nu\sigma_z), \quad (3.10a)$$

$$\varepsilon_z = \frac{\Delta l}{l} = \frac{1}{E} (\sigma_z - \nu\sigma_\theta), \quad (3.10b)$$

where

E = the Young's (or elasticity) modulus,
 ν = the Poisson's ratio (e.g., $\nu = E/2G - 1$ with the shear modulus G).

A statistical lumped pressure model is considered with a constant fission gas inventory and uniform pressure throughout the fuel pin. When the gap is open, the internal fill gas pressure is basically determined using the ideal gas law from Eq. 3.11.

$$P_G = \frac{MR}{\frac{V_p}{T_p} + \sum_j^{N_z} \pi \delta x_j \left(\frac{(r_{ci}^2 - r_{fo}^2)}{T_g} + \frac{r_v^2}{T_v} + \frac{(r_{fo}^2 - r_f^2)}{T_f} \right)}, \quad (3.11)$$

where

- M = the gas moles in fuel rod,
- R = the universal gas constant,
- V_P = the gap plenum volume,
- r_f = the fuel outside radius that includes thermal expansion,
- r_{fo} = the fuel outside radius that includes thermal and relocation,
- r_v = the radius of central hole,
- T_F = the average fuel pellet temperature.
- T_G = the gap temperature,
- T_P = the gap plenum temperature that is defined as the outlet fluid temperature plus $10K$,
- and
- T_V = the central void temperature.

The gap thickness is calculated mechanistically for the open gap and closed gap from Eq. 3.12 and Eq. 3.13, respectively. When there is a contact between fuel pellet and cladding, the minimum gap thickness is set to a surface roughness value that maintains a minimum gas layer. The criterion for the pellet-clad contact is either the gap thickness to be less than a constant times the summation of the fuel and clad inner surface roughnesses or non-zero contact pressure.

$$t_g = t_g^{cold} - (\Delta r_{th})_f + (\Delta r_{el})_c + (\Delta r_{th})_c, \quad (3.12)$$

$$\begin{aligned} (\Delta r_{th})_f &= (\Delta r_{th})_c + C_R(\xi_f + \xi_c) - t_g^{cold}, \\ (\Delta r_{th})'_f &= (\Delta r_{th})_f - (\Delta r_{th})_c + C_R(\xi_f + \xi_c) - t_g^{cold}, \\ (\Delta r_{el})_c &= (\Delta r_{th})'_f, \end{aligned} \quad (3.13)$$

where

- $(\Delta r_{th})_f$ = the fuel radial deformation,
- $(\Delta r_{th})'_f$ = the applied fuel displacement on cladding,
- $(\Delta r_{el})_c$ = the cladding radial elastic deformation,
- $(\Delta r_{th})_c$ = the cladding radial thermal deformation,
- t_g^{cold} = the cold gap thickness,
- C_R = the empirical coefficient, and
- ξ = the surface roughness.

The fuel radial deformation accounts for effects of thermal expansion, swelling, irradiation induced densification, and relocation. These models were initially integrated to the code [95, 101] considering rigid pellet fuel deformation of Fuel Rod and Cladding Analysis Subcode (FRACAS) model [102] in the code. Detailed information regarding the models can be found in Appendix A. The radial deformation of the pellet with a free-ring expansion model is determined from Eq. A.1. Note that the effect of relocation is added to thermal response, but no hard contact is allowed until the other fuel expansion components recover half of the original relocated pellet radius [44].

$$(\Delta r_{th})_f = \sum_{i=1}^{N_r} \delta r_i \left(\alpha_{T_i} + \varepsilon_f^s + \varepsilon_f^d + \varepsilon_f^r \right), \quad (3.14)$$

where

- α_{T_i} = the thermal expansion coefficient of the i -th radial temperature,
- T_i = the average temperature of i -th radial ring,
- ε_f^s = the swelling strain (positive),
- ε_f^d = the densification strain (negative), and
- ε_f^r = the relocation strain (positive).

Note that change in rod dimensions is only reflected on the gap thickness in order to calculate gap conductance. Then, the pressure at the fuel and cladding interface generated by the applied displacement is computed as

$$P_{int} = \frac{Et_c(r_{co}^2 - r_{ci}^2)(\Delta r_{th})'_f}{\bar{r}_c [r_{ci}(r_{co}^2 - r_{ci}^2) - r_{ci}^2 t_c \nu]} + P_o \frac{r_{co}(r_{co}^2 - r_{ci}^2) - r_{co}^2 t_c \nu}{r_{ci}(r_{co}^2 - r_{ci}^2) - r_{ci}^2 t_c \nu}, \quad (3.15)$$

where

- t_c = the cladding thickness.

3.2 Code Structure

This section provides brief information on the CTF's standalone fuel solver, CTFFuel. The simulation results from CTFFuel are in HDF5 data format. Therefore, post-processing of data is slightly different than typical CTF outputs. Details are provided in CTFFuel User's Manual [94]. CTFFuel is executed with an independent input as a stand-alone capability. To illustrate some of geometry parameters, a nodalization scheme of fuel rod is provided in Figure 3.3. The input is constructed based on several blocks which are:

- [CONTROL] to define system and boundary conditions,
- [GEOM] to define rod dimensions and initial gap condition,
- Time-dependent state parameters,
 - [HTCV] to define vapor heat transfer coefficient as a boundary condition,
 - [HTCL] to define liquid heat transfer coefficient as a boundary condition,
 - [TV] to define vapor temperature as a boundary condition,
 - [TL] to define liquid temperature as a boundary condition,
 - [TW] to define a fixed wall temperature,
 - [PRESSURE] to define the mesh-dependent pressure vector in the channel, and
 - [RODQ] to define axial power distribution
- Other state parameters.
 - [RADP] to define radial power distribution,

- [EXPOSURE] to define mesh-dependent fuel burnup, and
- [GAD] to define mesh-dependent gadolinia content.

CTFFuel outputs two sets of data; [CORE] data block with axial/radial scalar mesh information and [STATE] data blocks with simulation results (for example, pin temperature 'pin_temp') at defined state(s). [STATE_0000] is referred to the steady-state solution (i.e., simulation at time= 0.0). The STATE numbers increase based on the predefined time-steps in the input deck.

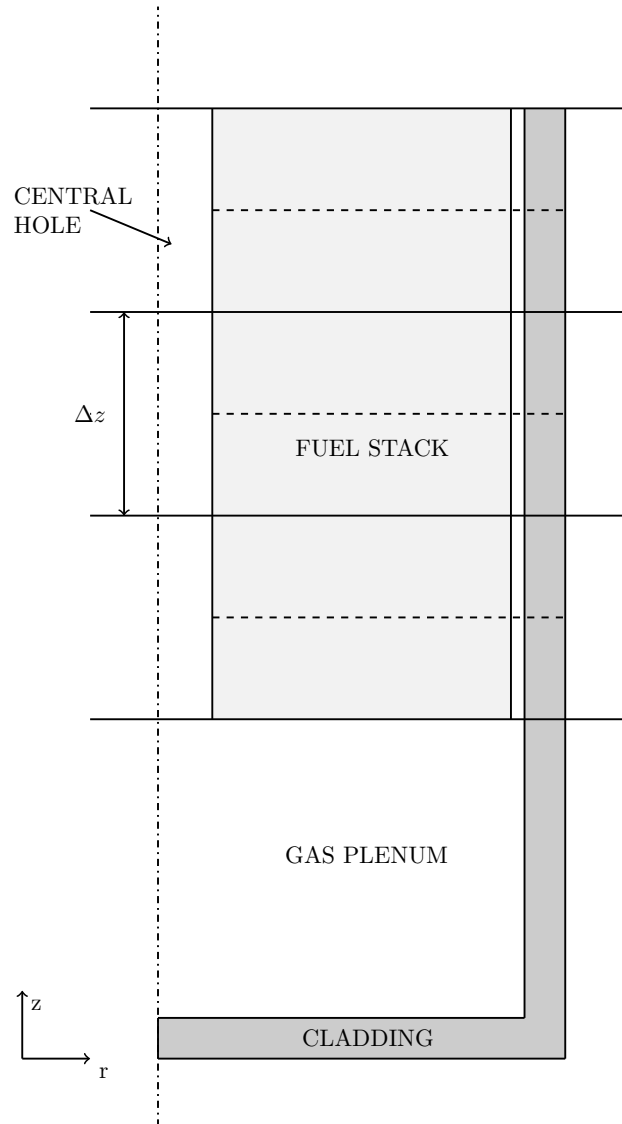


Figure 3.3: CTFFuel's single pin nodalization.

3.3 Chapter Summary

This study focused on isolating the CTFs fuel performance capabilities to be used as a standalone capability. This new capability, CTFFuel, was successfully constructed to interface CTFs fuel performance modeling capabilities. New modeling options were added to investigate the fuel thermal conductivity degradation of LWR oxide fuels and fuel radial deformation accounts for effects of thermal expansion, swelling, irradiation induced densification, and relocation. The models were implemented according to the CASL coding guidelines [96] and were initially tested [103, 104]. Work performed in this study improved the thermal modeling capabilities of both CTF and CTFFuel. Other material property correlations such fuel, cladding emissivities were also updated. These models are available in the source code, and protected through unit tests. Efforts are being continue to assess through verification problems and code comparisons with FRAPCON-4.0 and FRAPTRAN by Toptan et al. [105, 106], and with Bison by CASL team at Oak Ridge National Laboratory (ORNL). Some of the initial assessment studies on CTFFuel are provided in the next chapters. In the future, material property correlations (e.g., the thermal conductivity model) can be included using auxiliary files as user-defined functions calibrated for a specific material/data set, including proprietary information. The code should be modified so that users can define their functions using auxiliary files. This is similar to what is done with user-defined functions in computational fluid dynamic codes. This approach will reduce the labor-intensive work to add material property correlations to the code and will provide flexibility to users in terms of defining their models.

CHAPTER

4

FUEL THERMAL CONDUCTIVITY DEGRADATION

This study introduces additional modeling options that account for burnup dependency of the fuel thermal conductivity. A preliminary work on the implementation of a burnup-dependent thermal conductivity model was conducted [107]. The initial implementation was tested in a code-to-code benchmark. Though this study clearly demonstrated the motivation for improvement of the thermal conductivity models, the methods used for code comparison are not clearly delineated. This study improved CTF's temperature predictions by adding new fuel thermal conductivity models that account for the irradiation effects at the macroscopic scale with a reduced number of parameters (e.g., burnup and content of the additives such as plutonium and gadolinium). Previous versions of CTF incorporated a temperature-dependent fuel thermal conductivity model, but in reality, fuel thermal conductivity is affected by fission product buildup and radiation damage. This results in a degradation of fuel thermal conductivity and a corresponding increase in fuel temperature due to the impaired heat transfer in the fuel. Accounting for the irradiation effects on the fuel thermal conductivity is particularly important for correct prediction of the fuel temperature profile. This is required to calculate correct thermal feedback effects (e.g., prediction of the Doppler effect). The new models that account for the effects of thermal conductivity degradation of LWR oxide fuels were implemented in the code according to the CASL coding guidelines [96] and were initially tested [103, 104].

This chapter provides an overview of CTFFuel with a case study on the thermal conductivity degradation of LWR fuel rods. The overall thermal conductivity model in the code is described in Section 4.1. A solution verification test to ensure proper second-order convergence of the numerical scheme and a code verification test to ensure proper convergence of the numerical solution to the exact solution are described in Section 4.2. The code results are compared to a

reference fuel performance code, and the differences are examined to understand and quantify the code’s algorithm verification and epistemic uncertainties in Section 4.3. Concluding remarks are provided in Section 4.4.

4.1 Background

Thermal conductivity is defined as the rate at which heat passes through a material, and Fourier’s law directly relates the heat flux and the thermal conductivity. In a nuclear reactor, irradiation and high operating temperatures can change the material composition and microstructure of the fuel, which complicates the thermal conductivity modeling. Many parameters determine thermal conductivity of irradiated fuel: porosity, fission gas bubbles, distribution of the additives at the mesoscale, and soluble and insoluble fission products in the lattice, stoichiometry, fission density at the microscale. However, this causes difficulty in modeling each effect separately. The fuel thermal conductivity is described at the macroscopic scale by globally defined parameters like irradiation temperature, additive content, and burnup to describe the state of the fuel with sufficient precision [108]. In this manner, a general expression for the thermal conductivity can be expressed as a summation of the phonon–phonon interaction (significant up to 1,600 K), k_{phonon} , and high temperature contribution due to the electron vacancy pair mobility, $k_{electronic}$. The thermal conductivity is defined for unirradiated material at 95% theoretical density (TD) as

$$\lambda_{95} = \lambda_{phonon} + \lambda_{electronic},$$

$$\lambda_{95} = \frac{1}{A + BT} + \frac{C}{T^n} \exp\left(\frac{D}{T}\right), \quad (4.1)$$

where n is the exponent, and constants A through D are coefficients that are varied to account for the irradiation effects [108, 109]. The thermal conductivity correlation for the nuclear fuel rod is often given at a specified TD (often 95%). To obtain representative thermal conductivity of a material, the correlation is multiplied by a correction factor recommended by Lucuta [110]. There are a large number of publications on modeling the fuel thermal conductivity. Extensive literature is available for more information on the thermal conductivity degradation of LWR fuels [108, 109, 111].

CTF is modified to read the burnup and additive content(s) in the fuel as input parameters to the new models. Though it is not possible for the code to account for these changes dynamically, it is important that they can be accounted for manually when they can be estimated. For example, in coupled simulations, they can be passed through an application programming interface. The default UO₂ thermal conductivity is computed in CTF from the MATPRO-9 correlation [112], which is only temperature-dependent. The implemented burnup-dependent models are;

1. a modified version [113] of the Nuclear Fuel Industries (NFI) model [114],
2. the Halden model [113], and

3. the Duriez/modified NFI model [113] that is a combination of the Duriez correlation [115] and the modified NFI model.

These new correlations are used because they account for the effects of irradiation and presence of additives (e.g., Gd, Pu), and enable comparison of code predictions to other nuclear fuel performance codes such as FRAPCON [44] and Bison [43]. Note that the k_{phonon} term in the Halden model is multiplied by 0.92 to account for the reduction of fresh fuel conductivity due to the presence of plutonium, Pu , to obtain the MOX fuel thermal conductivity. Implementation of the new models is described in the CTF's Theory Manual [42]. Instructions on how to use the models are provided in the code manuals [116, 94].

The temperature-dependent MATPRO-9 model is given by the following relation. The model is valid in $500 \leq T \leq 3000K$.

$$\lambda = C \left\{ \max \left(0.0194, \frac{40.4}{(190.85 + T)} + 1.216 \times 10^{-4} e^{(1.867 \times 10^{-3}(T-273.15))} \right) \right\}, \quad (4.2)$$

where

$$C = 100 \left(\frac{1.0 - \beta(1 - TD)}{1.0 - 0.05\beta} \right), \text{ and}$$

$$\beta = 2.58 - 5.8 \times 10^{-4}(T - 273.15).$$

The burnup-dependent fuel thermal conductivity is generalized as the following relation. The Lucuta's [110] recommendation for spherical-shaped pores is utilized to correct the thermal conductivity for the material of interest. The model is valid in the following ranges: $0 \leq Bu \leq 62$ MWd/kgU; $300 \leq T \leq 3000K$; $0.92 \leq TD \leq 0.97$; and $0 \leq gad \leq 10\text{wt.}\%$. The model coefficients are provided in Table Table 4.1 for each modeling option.

$$\lambda = 1.0789 \lambda_{95} \left(\frac{TD}{1.0 + 0.5(1 - TD)} \right), \quad (4.3)$$

$$\lambda_{95} = \frac{1}{A + a \cdot gad + BT + f(Bu) + g(Bu)h(T)} + \frac{E}{T^m} \exp \left(-\frac{F}{T^n} \right).$$

Figure 4.1 compares fuel thermal conductivity model options in the code at 95% TD. The irradiated fuel thermal conductivity is compared against the unirradiated fuel thermal conductivity to emphasize the fuel thermal conductivity degradation. The default model does not account for the burnup dependence of the thermal conductivity, while thermal degradation of the conductivity is observed significantly at low temperatures and high burnups when the burnup-dependent models are enabled. For example, roughly 40% reduction in the fuel thermal conductivity is observed at 300K at 60 MWd/kgU as compared to the fresh fuel.

Table 4.1: The empirical coefficients for the generalized burnup-dependent model.

	modified NFI	Duriez/mod.NFI	Halden
$f(Bu)$	$0.00187Bu$		$0.004Bu^*$
$g(Bu)$	$0.038Bu^{0.28}(1.0 - 0.9 \exp(-0.04Bu))$		$2.475 \times 10^{-4}(1.0 - 0.00333Bu^*)$
$h(T)$	$\frac{1}{1+396 \exp(-\frac{6380}{T})}$		$\min(1650, (T - 273.15))$
a	1.1599		
$A(x)$	0.0452	$2.85x+0.035$	$0.1148+1.1599x$
$B(x)$	2.46×10^{-4}	$(2.86-7.15x) \times 10^{-4}$	0
E	3.5×10^9	1.5×10^9	0.0132
F	16,361	13,520	-0.00188
m	2		0
n	1		-1

Bu , the burnup (MWd/kgU)

Bu^* , the burnup (MWd/kgUO₂)

T , the temperature (K)

gad , the weight fraction gadolinia (not expected in MOX)

$x = 2.0 - O/M$, the deviation from stoichiometry

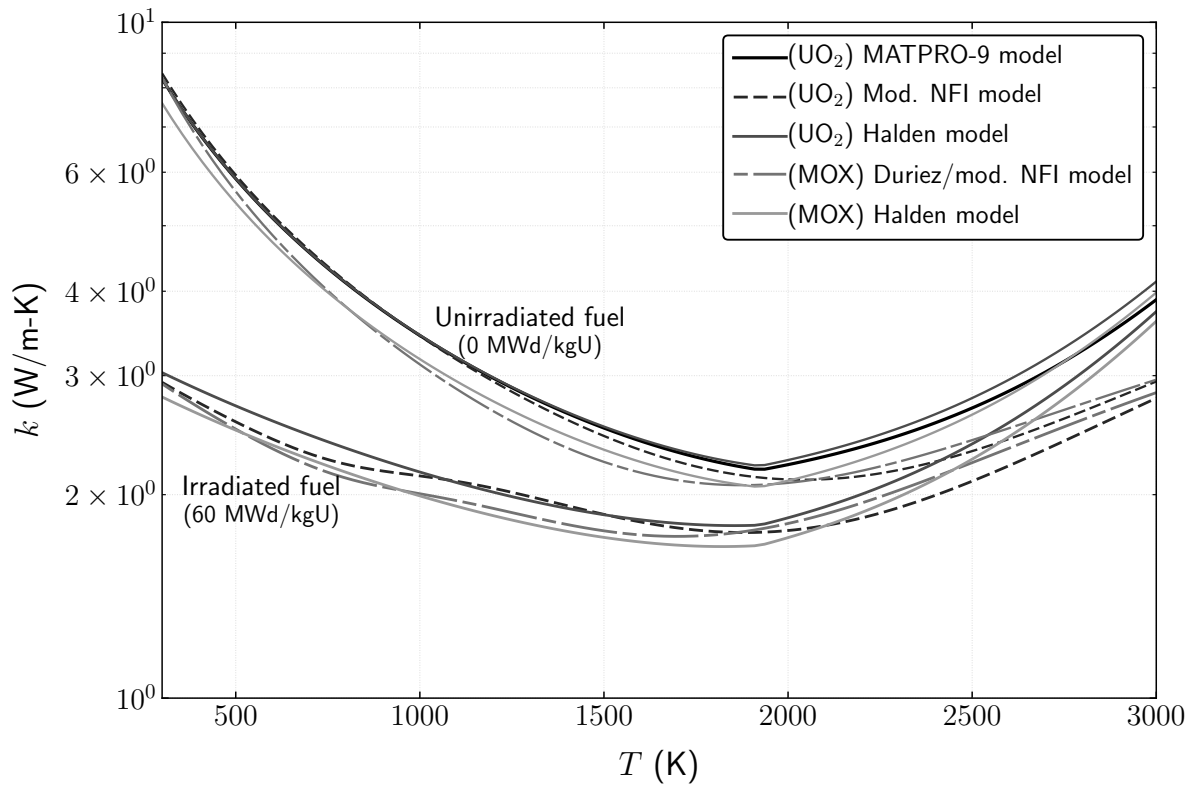


Figure 4.1: Comparison of thermal conductivity of 95% TD fuel with different correlations

4.2 Order-of-accuracy tests

This section outlines order-of-accuracy tests that are designed to assess the steady state conduction solution of CTFFuel. The exact solution to the mathematical model is given first for the nuclear fuel rod geometry. Then, results and discussions are provided for the tests.

4.2.1 Exact Solution to the Mathematical Model

For a common representation of a nuclear fuel rod, the fuel is surrounded by cladding, the fuel is perfectly located at the center, and the zone between the fuel and cladding is filled with inert gas, as illustrated in Figure 3.2. The steady state, radial conduction is

$$\frac{1}{r} \frac{d}{dr} \left(kr \frac{dT}{dr} \right) + \dot{q} = 0. \quad (4.4)$$

The material is assumed to be isotropic, and its properties are kept constant in this analysis. The fuel is subjected to uniform internal energy generation. Then, Eq. 4.4 is solved for the boundary conditions of $T(r = r_f) = T_f$ and $T(r \rightarrow 0) \Rightarrow$ finite (i.e., the finiteness requirement). The solution for the temperature profile in the fuel is obtained as:

$$T(r) = T_f + \frac{q'}{4\pi k_f} \left(1 - \frac{r^2}{r_f^2} \right), \quad (4.5)$$

where

$T_{ci} = T(r = 0)$, the centerline temperature, and
 T_f = the fuel surface temperature.

The volumetric heat generation rate, \dot{q} , is converted to the linear heat rate, q' , using the relation $\dot{q} (\pi r_f^2) = q'$, since the linear heat rate is used as an input for both codes.

Similarly, the homogeneous (i.e., no internal heat generation in Eq. 4.4) differential equation of the steady state conduction equation is solved in the gap and cladding. Temperature jumps over the gap and cladding are obtained using the identity of continuous heat flux at the interfaces. Then, the temperature jumps across the gap and cladding, respectively, are:

$$T_f - T_{ci} = \frac{q'}{2\pi r_f h_{gap}}, \quad (4.6a)$$

$$T_{ci} - T_{co} = \frac{q'}{2\pi k_c} \ln \left(\frac{r_{co}}{r_{ci}} \right), \quad (4.6b)$$

where

T_{ci} = the cladding inside temperature,
 T_{co} = the cladding outside temperature, and
 k_c = the cladding thermal conductivity.

4.2.2 Results & Discussion

A steady state solution verification test is designed to ensure that the addition of the burnup-dependent thermal conductivity model does not disturb the CTF's second order convergence. The verification model is designed as a radial conduction problem of a single nuclear fuel rod. The rod's dimensions are selected to represent a pressurized water reactor. The difference in the temperature at a specified node between successive iterations is quantified using a Euclidean norm

$$l_2 = \sqrt{(T_i^{\text{refined}} - T_i^{\text{coarse}})^2}. \quad (4.7)$$

Additionally, a true code verification problem is designed to assess whether the error in the discrete solution relative to the exact solution of the mathematical model reduces as the mesh is refined. A test case is designed with constant fuel thermal conductivity. The exact solution to the mathematical model is given in the previous section. The difference in the temperature at the specified node between refined and the exact solution is quantified using a Euclidean norm

$$l_2 = \sqrt{(T_i^{\text{refined}} - T_i^{\text{exact}})^2}. \quad (4.8)$$

The results of the steady state solution are summarized for the fuel thermal conductivity options in Figure 4.2 for unirradiated and irradiated fuels. The latter provides insight on how the introduction of burnup and additives impacts the convergence. The results are similarly summarized for the constant thermal conductivity in Figure 4.3. The order of accuracy is estimated by calculating the line of best fit in the form $l_2 = C\Delta r^p$, and the observed order of accuracy p is shown on the plot.

It is important to note that the observed order of accuracy, p , is often limited to be $p \approx p_F$, where p_F is the formal order of accuracy of the discretization scheme, which is 2.0 for this study. Figure 4.2 shows that the second order convergence of CTF for the steady state conduction solution is retained with the enabled burnup-dependent thermal conductivity option. Additionally, the introduction of the new input parameters do not change the code's formal order of accuracy, which is a good indication that it is relatively free of coding mistakes and is placed correctly within the rest of the code.

The order-of-accuracy tests verified that the numerical scheme for CTF's steady state solid conduction solution was coded correctly, and its results matched the exact solution as shown in Figure 4.3.

4.3 Code Comparison

NRC's steady state fuel performance code, FRAPCON-4.0 [44] was selected as the reference code. The CTFFuel temperature predictions were compared against the reference code that employs a similar finite difference method. The code-to-code benchmark is a common approach to testing the correctness of the code, yet agreement between the two codes does not imply that either code is correct. However, it is useful to improve one code's credibility against

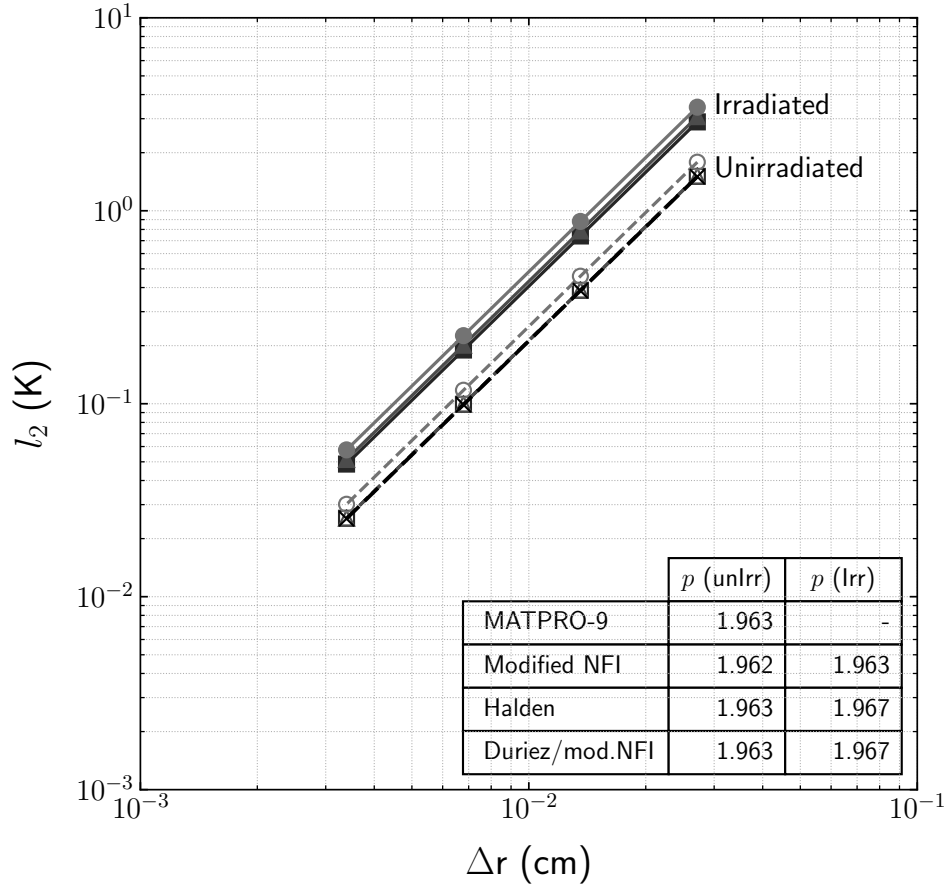


Figure 4.2: Solution verification with the thermal conductivity model

the reference code. The comparison enhances understanding of the differences between the two codes when the similar mathematical models under controlled conditions are used. See Trucano et al. [65] for more detailed discussion on code comparison principles.

The code comparison was automated using a script that read the required input parameters from FRAPCON output files and creates CTFFuel input files. The test suite was carefully designed to perform a controlled comparison, which is illustrated in Figure 4.4. The procedure can be outlined as follows:

- The rod dimensions and boundary conditions were specified based on the reference code.
- The thermal conductivity models were chosen identical in both codes: the modified version of the NFI model for UO_2 fuels and $\text{UO}_2+\text{Gd}_2\text{O}_3$ fuels; the Duriez/modified NFI model for MOX fuels. The default model in CTF, the MATPRO-9 model, was used to demonstrate significance of the burnup dependency in the fuel thermal conductivity.
- To eliminate possible uncertainties in the gap calculations of CTFFuel in the code comparison, the gap conductance was set constant from the reference code at each time step to ensure that the exact same fuel surface temperature in both codes. By this way,

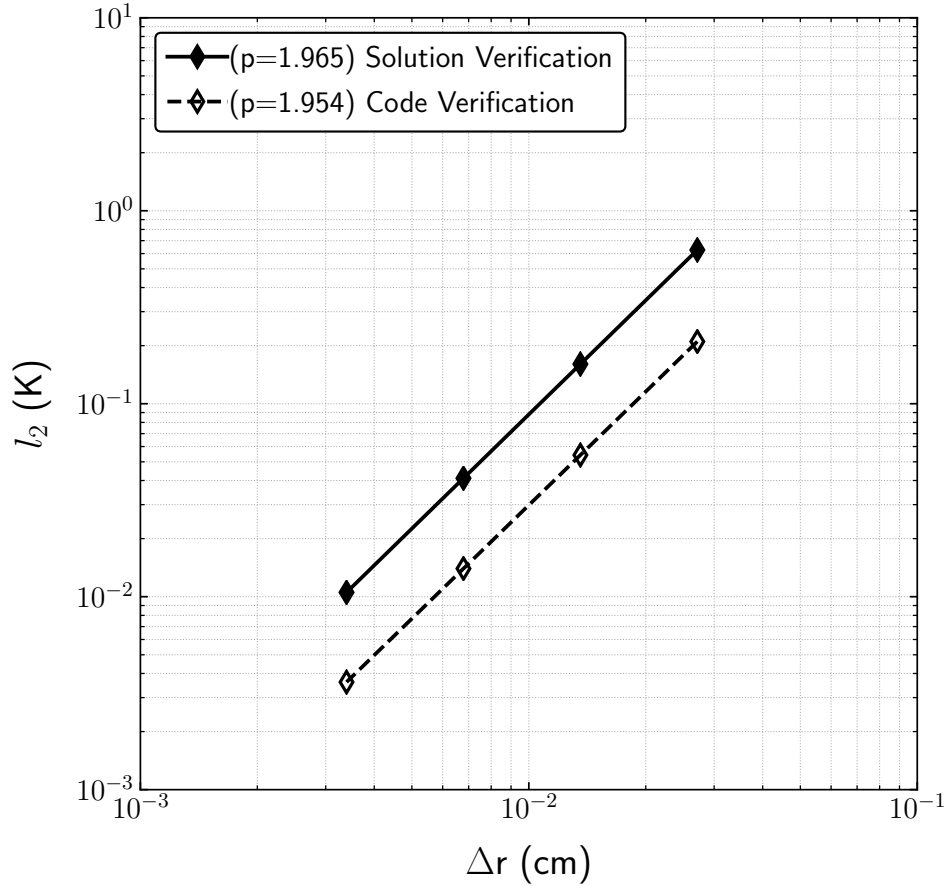


Figure 4.3: Solution and code verification with the constant thermal conductivity

the thermal conductivity degradation in the fuel can be investigated clearly. Note that thermo-mechanical responses were not computed since the dynamic gap conductance model was not used in this analysis.

- Then the reference code passed the input parameters that were not computed dynamically in CTFFuel such as the radial/axial power distribution, burnup, etc.

The quantity of interest was the centerline temperature because it is an integral result to investigate the improvement in this study. Instrumented Fuel Assembly (IFA) test cases of the Organisation for Economic Co-operation and Development (OECD) Halden Reactor Project were selected in the code comparison from the FRAPCON Integral Assessment [3]. These test cases were chosen to investigate the impact of using the burnup-dependent thermal conductivity option in realistic examples. The selected test cases are summarized in Table 4.2.

Table 4.2: Description of the steady state fuel rod test cases, generated based on FRAPCON-4.0 [3]

Source	IFA	Rod Bu (MWd/kgU)	Gd (%)
UO ₂ fuels			
[117]	432	1	45.0
	432	3	45.0
[118]	515.10	B1	80.0
[119]	558	6	41.0
[120]	562	18	76.0
[121]	597	8	71.0
[122, 123]	677.1	2	32.0
[124]	681	1	33.0
	681	5	32.0
UO ₂ +Gd ₂ O ₃ fuels			
[118]	515.10	A2	80.0
	515.10	B2	80.0
[125]	636	2	25.0
	636	4	25.0
[124]	681	2	23.0
	681	3	12.0
	681	4	22.0
	681	6	13.0
MOX fuels			
[126]	597-4-5-6-7	10	35.7
	597-4-5-6-7	11	36.8
[127, 128]	606 Phase2		49.0
[129, 130]	610	2	56.0
	610	4	57.0
[131]	629-1	1	33.0
	629-1	2	40.0
[132]	629.3	5	72.0
	629.3	6	68.0
[133]	633-1	6	32.0
[134]	648.1	1	62.0
	648.1	2	62.0
[135]	651-1	1	22.4
	651-1	3	21.7
	651-1	6	20.3

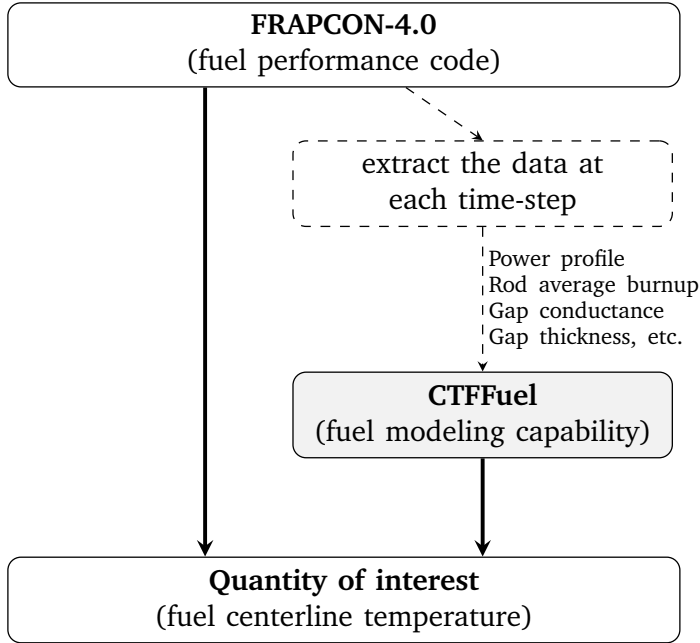


Figure 4.4: Design of the code comparison. Manually and dynamically calculated parameters are represented, respectively, by dashed and solid lines.

4.3.1 Results & Discussion

The assessment of temperature predictions through the reactor’s life in the benchmark of thermal conductivity degradation was performed for all fuel types. The CTFFuel predictions are compared with FRAPCON’s predictions of fuel centerline temperature in Figure 4.5 using the old model and the burnup-dependent thermal conductivity model. The temperature predictions are summarized in terms of the root-mean-square error (RMSE) to quantify the total distance between the codes:

$$RMSE = \sqrt{\frac{1}{n} \sum_{i=1}^n \left(T_{cl,i}^{\text{FRAPCON}} - T_{cl,i}^{\text{CTFFuel}} \right)^2}. \quad (4.9)$$

The associated RMSE value is computed including all data points from IFA test cases for each fuel type and tabulated in Table 4.3. Use of the old model leads to around 160 K difference in the fuel centerline temperature predictions once the same boundary conditions are provided at every time step. Once the burnup-dependent thermal conductivity model is enabled, CTFFuel temperature predictions agree within approximately 10 K. The code uses uniform spatial discretization while FRAPCON employs non-uniform spatial discretization—placing more nodes near the pellet surface—to account for rim effects, which leads to mesh-related uncertainty since number of rings in the fuel are kept constant in this comparison. Still, this temperature difference is in acceptable range.

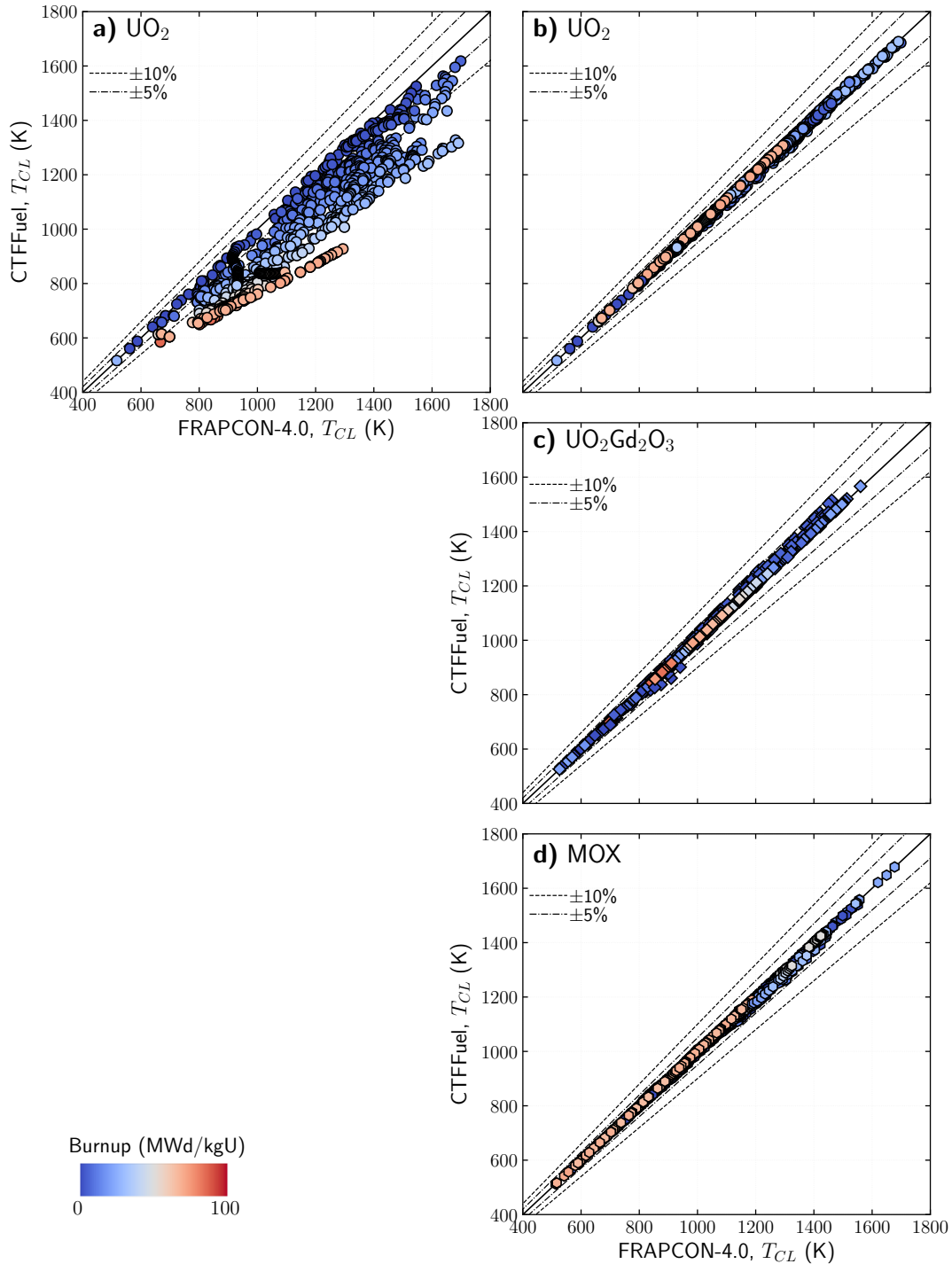


Figure 4.5: CTFFuel vs. FRAPCON-4.0 fuel centerline temperature predictions. CTFFuel uses the old thermal conductivity model (left column) and the new burnup-dependent thermal conductivity model (right column). Note that FRAPCON-4.0 uses the burnup-dependent thermal conductivity model (modified version of the the NFI model for UO_2 and $UO_2+Gd_2O_3$ fuels; the Duriez/modified NFI for MOX fuels).

Table 4.3: Overall code comparison results in terms of RMSE

	UO ₂	UO ₂ +Gd ₂ O ₃	MOX
Old model	163.2 K	–	–
New model	8.7 K	13.0 K	7.1 K

4.4 Chapter Summary

A case study on the thermal conductivity degradation of LWR fuel rods was demonstrated. New modeling options were added to investigate the fuel thermal conductivity degradation. Work performed in this study improved the thermal conductivity modeling capabilities of the code and provided a pedigree for the model, which is an important improvement over the previous state. The analyses ensured that the fuel thermal conductivity function gives the correct output for a given input and that the fuel thermal conductivity model was implemented as expected. Code and solution verification study was performed to demonstrate that the observed convergence of the discretization error by comparing to the mathematically derived convergence and comparing the results from successive refinements of the solution domain, respectively. The numerical method was verified through mesh refinement of a single rod model using the fuel solver, CTFFuel. The order-of-accuracy tests verified that the numerical scheme for CTF's steady state solid conduction solution is coded correctly, and CTF outputs results that match the exact solution. After the software quality was assessed, verification and code comparison activities indicated that the code solves the intended equations. The thermal conductivity feature is integrated to the most recent version of the code, documented, and protected in the code through unit and regression tests.

CHAPTER

5

SENSITIVITY ANALYSIS AND UNCERTAINTY QUANTIFICATION

This chapter summarizes sensitivity and uncertainty quantification analyses that are performed to understand possible sources of uncertainties that might require further exploration to improve. In Section 5.1, SA is performed to understand how simulation results depend on selected input parameters, assumptions, or mathematical models in the analysis, which informs the user about the most important factors in uncertain results. In Section 5.2, UQ is performed to quantify how accurately a mathematical model describes the physical problems in both computational and real world applications. The fuel temperature is the system response quantity (SRQ) in this study. Concluding remarks are provided at the end of this chapter.

5.1 Sensitivity Analysis

In Section 5.1.1, the fuel temperature is examined in terms of sensitivities on gap conductance, power, and fuel thermal conductivity. In Section 5.1.2, the fuel temperature is examined in terms of sensitivities on the radial power distribution, and fuel thermal conductivity modeling options.

5.1.1 Fuel Temperature Predictions

The input parameters are selected considering the constructed formula to obtain a fuel temperature profile, and they are gap conductance (`hgap`), linear heat rate (`qprime`), wall tempera-

ture (**twall**), rod average burnup (**burn**), and Gadolinium concentration (**gad**). Three different methods are studied using CTFFuel to examine the effects of the selected input parameters for each SRQ:

1. the fuel centerline temperature, T_{cl}
2. the volume-averaged fuel temperature,

$$\bar{T} = \frac{\int_0^{R_f} T(r)rdr}{\int_0^{R_f} rdr} \quad (5.1)$$

3. Nuclear Energy Agency (NEA) temperature [136, 137],

$$T_{NEA} = 0.3 \cdot T_{cl} + 0.7 \cdot T_{surf} \quad (5.2)$$

The last two are often used in the calculation of the Doppler temperature. Since it is confirmed that the look-up tables agree well with CTFFuel’s predictions, these results are also true for the tabulated factors. The results are summarized in terms of maximum temperature deviation from the nominal value.

Parametric study 5% and 10% perturbations are applied around the nominal states in the centered parameter study. Each input parameter is evaluated independently. As expected, the temperature is very sensitive to the linear heat rate; deviation from the nominal value of the effective Doppler temperature is around 20 K for a 5% perturbation and 40 K for a 10% perturbation of the linear heat rate.

Morris screening Reasonable bounds are used for the uniform distribution as tabulated in Table 5.1. The interactions of input parameters can be examined in this study. Figure 5.1 shows the sensitivity results in terms of means and standard deviations. Maximum uncertainty is observed in the gap conductance, as expected, due to the specified largest uncertainty band.

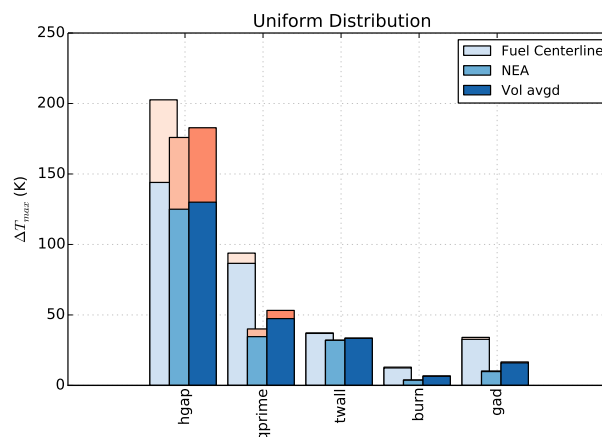


Figure 5.1: Morris results of mean (blue) and standard deviation (orange)

Random sampling The same bounds of the uniform distribution as in Table 5.1 are used. Figure 5.2 shows the correlation coefficients from the random sampling study. Note that the correlation coefficients vary in $[-1,1]$. Larger values of the coefficients indicated strong correlation, while 0 refers to no correlation between input parameter to the response parameter. The power, burnup, and Gd content are proportionally correlated to the temperatures, while the gap conductance is inversely proportional. Since the responses are meaningful as expected, it appears that the code is functioning as intended.

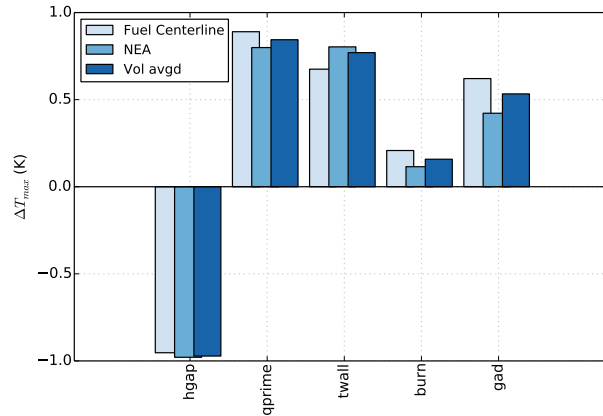


Figure 5.2: Correlation coefficients from the random sampling study

Table 5.1: Selected uncertainty bounds for the uniform distribution

Description		Lower Bounds	Upper Bounds
hgap	gap conductance	0.50	1.50
qprime	linear heat rate	0.95	1.05
twall	wall temperature	0.95	1.05
burn	rod average burnup	0.95	1.05
gad	gadolinia concentration	0.90	1.10

5.1.2 Radial Power Distribution and Fuel Thermal Conductivity

In this study, the radial power distribution is altered as well as the thermal conductivity options (see Table 5.2). The radial power profile is constructed in the form of

$$p(r) = ar^n + b. \quad (5.3)$$

for the specified a and n , b is calculated numerically to meet the normalization criterion. For the repeatability of this study, this process is automated through scripts.

Table 5.2: Thermal conductivity options

	Constant	MATPRO	Modified NFI model			
	k_{fuel}	model	a	b	c	d
Burnup (MWd/kgU)	-	-	0.0	60.0	60.0	0.0
Gd Content (-)	-	-	0.0	0.0	0.1	0.1

Figure 5.3 shows changes in the fuel centerline temperature for chosen radial power profiles as compared to the nominal power shape. It is easily observed that radial power shape and effects of thermal conductivity degradation are notable on the centerline temperature. Therefore, any simplified assumptions on this behavior would significantly deteriorate feedback calculations in multi-physics applications.

5.2 Uncertainty Quantification

A statistical black box uncertainty propagation method is used with a sample size of 59, which is the required number of code runs for the upper 95% percentile [138]. The margin of the licensing criteria is of primary interest for regulatory purposes. Therefore, the one-sided tolerance limit can be applied for a 95th percentile with 59 calculations [139]. The automated method includes three steps:

1. Nominal values are calculated at each time step from the reference code. Then, the specified uncertainties are propagated through CTFFuel inputs. The uniform (\mathcal{U}) and normal (\mathcal{N}) distributions are applied in this study. Bounds of the burnup are assumed to be similar to the uncertainty in power.
2. An input deck is created for each of the sampled inputs at each time step, the decks are run, and the quantities of interest are extracted from the output decks. The quantities of interest are the fuel centerline temperature (T_{CL}), fuel surface temperature (T_{FS}), and Doppler temperature ($T_{Doppler}$) for this study.
3. The simulated results are compared to the reference predictions in terms of absolute error difference and RMSE. The absolute error, $|T_{CL}|$, is used to quantify distance between the

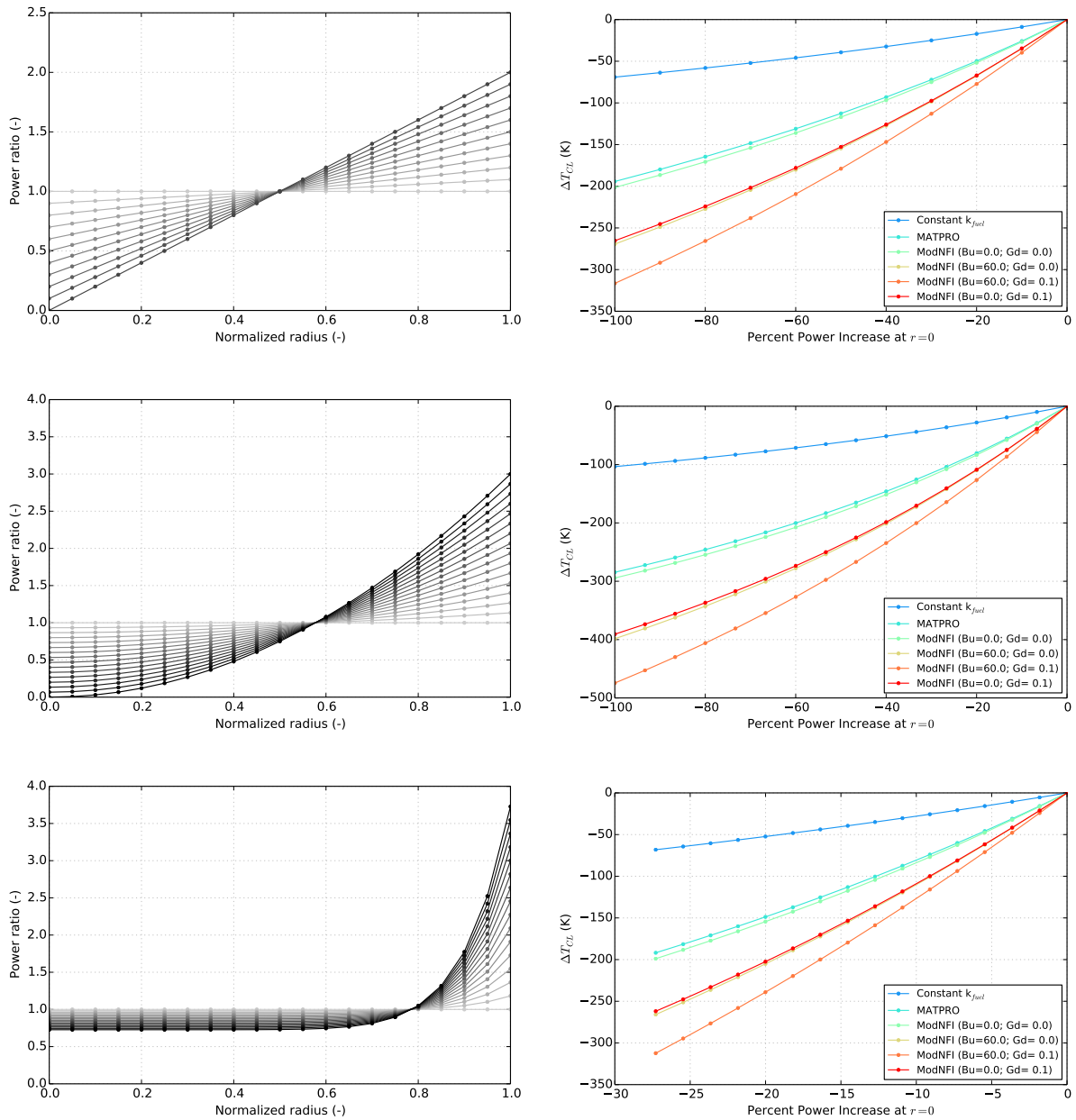


Figure 5.3: Difference in the centerline temperature for a given radial power shape and uniform power profile vs. percent power change at the centerline $r = 0$.

quantified CTFFuel and reference code for a single prediction at a given time step

$$|T_{CL}| = \left| T_{CL}^{ref} - \bar{T}_{CL}^{code} \right|, \quad (5.4)$$

and RMSE, $\|T_{CL}\|$, is used to present overall response of the predictions over all time steps.

$$\|T_{CL}\| = \sqrt{\frac{1}{N} \sum_{i=1}^N \left(T_{CL,i}^{ref} - \bar{T}_{CL}^{code} \right)^2}, \quad (5.5)$$

where

- \bar{T}_{CL}^{code} = the mean centerline temperature,
- T_{CL}^{ref} = the centerline temperature from the reference code, and
- N = the number of time-steps for the selected rod.

In this section, an uncertainty propagation study is performed by statistically sampling uncertain inputs, running codes, and obtaining a quantity of interest to estimate the associated tolerance limit. A black box uncertainty propagation method is defined for uncertainty propagation in Section 2.5 to estimate the uncertainty in quantity of interest(s) through CTFFuel in a coupled calculation with a reference fuel performance code. The NRC steady state fuel performance code, FRAPCON-4.0 is selected as a reference code for this study [44]. The quantity of interest for this study is the fuel centerline temperature. For this reason, test cases are selected from Halden Instrumented Fuel Assembly (IFA) test cases in the FRAPCON Integral Assessment to be representative of realistic problems [3]. Halden IFA test case IFA681 [140] is selected as the data set for the centerline temperatures, as it contains data for both UO_2 and $\text{UO}_2\text{Gd}_2\text{O}_3$ fuels. A sample size of 59 was used for one-sided 95th percentile based on Wilks' formula [138]. The NRC's safety limit for the peak fuel centerline temperature, 3077 K, is studied to demonstrate that the safety limit is not exceeded by 95% in the uncertainty quantification.

The following sections describe the procedure for the uncertainty propagation, and the results and discussions are summarized.

5.2.1 Procedure

The uncertainty propagation process is automated using a script that reads the required input parameters from the reference code's output files. The uncertainties are propagated for the input parameters which are passed from the reference code through CTFFuel. The rod dimensions, boundary conditions and the spatial discretization are specified based on the reference code. The gap conductance of CTFFuel is set to a constant value at each time step from the reference code. Then, the reference code passes the input parameters which are not computed dynamically in CTFFuel, such as the power distribution and burnup. A list of selected input uncertainties is provided in Table 5.3. Later, the propagated uncertainties are processed in CTFFuel. The quantity of interest is the centerline temperature for this study. At the end, the quantified centerline temperature is calculated and summarized in terms of prediction metrics (see Section 2.5).

Table 5.3: Selected input uncertainties [4, 5].

Parameter	Nominal	Lower bound	Upper bound	Distribution Type
System pressure	1.000	0.990	1.010	\mathcal{N}
Power	1.000	0.950	1.050	\mathcal{N}
Cladding thickness	1.000	0.963	1.037	\mathcal{N}
Gap thickness	1.000	0.772	1.256	\mathcal{N}
Fuel pellet radius	1.000	0.998	1.002	\mathcal{N}
Central hole radius	1.000	0.998	1.002	\mathcal{N}
Wall temperature	1.000	± 1.5 K		\mathcal{U}
Burnup	1.000	0.950	1.050	\mathcal{N}
Gd content	1.000	0.995	1.005	\mathcal{U}
Fuel density	1.000	0.984	1.016	\mathcal{N}
Gap conductance	1.000	0.500	1.500	\mathcal{N}

5.2.2 Results & Discussion

The uncertainty quantification is performed considering steady state CTFFuel simulations at each time-step, and the input uncertainties are propagated through CTFFuel around the calculated nominal values from the reference code, FRAPCON-4.0 at each time-step. Each case models a single rod with the same spatial discretization as in the reference code. The same fuel thermal conductivity model option is used for both fuel types in both codes, which is a modified version of the Nuclear Fuel Industries (NFI) model [114, 141].

For the selected IFA681 data set with UO_2 and $\text{UO}_2 + \text{Gd}_2\text{O}_3$ fuels, the prediction metrics for the centerline temperature are shown in Figure 5.5, and the results are summarized in Figure 5.4 for each rod. Rod X of IFA681 is labeled as IFA681rX in the plots, and four rods are examined in this analysis. The plots in Figure 5.4 include the quantified mean, predicted (nominal), and measured centerline temperatures. Grey shaded areas on the plots represent two standard deviations around the quantified mean temperatures, while dashed lines signify the 95% percentile that is calculated based on Wilks' formula. Since the 95% percentile is approximately equal to two standard deviations for a normal distribution, the two results agree well on the plot. Nonetheless, the relatively small sample size in the present analysis could lead to large statistical error in the standard deviation, therefore it is only a measure of data spread.

Figure 5.5 shows CTFFuel's mean and nominal prediction metrics for the centerline temperature. The prediction metrics are summarized in terms of the RMSE, $\|T_{CL}\|$ for each rod in Figure 5.5a. The quantified results are slightly larger as compared to the nominal values; however, the differences are negligible as relative to the mean centerline temperature for each rod. Additionally, CTFFuel's nominal predictions accurately align with the reference code's predictions as compared to the quantified results. The quantified results are more conservative, as is expected regarding definitions of tolerance limits for regulatory purposes in Figure 5.5b.

Uncertainty quantification was performed considering steady state CTFFuel simulations at each time step, and the input uncertainties are propagated through CTFFuel around the calculated nominal values from FRAPCON-4.0. Wilks' formula was a better representation in

this study as standard deviation is more sensitive to the sample size. A larger sample size will reduce statistical errors but will increase computational time. The one-sided tolerance limit was sufficient for this analysis since the quantity of interest was the fuel centerline temperature, which must be below the fuel melting temperature for regulatory purposes. The NRC's safety limit for the peak fuel centerline temperature is 3077 K, which is not exceeded by the 95% percentile in the uncertainty quantification step. It is important to note that validation metrics were not provided for Halden IFA test cases in this paper because CTFFuel predictions are meant only to match FRAPCON.

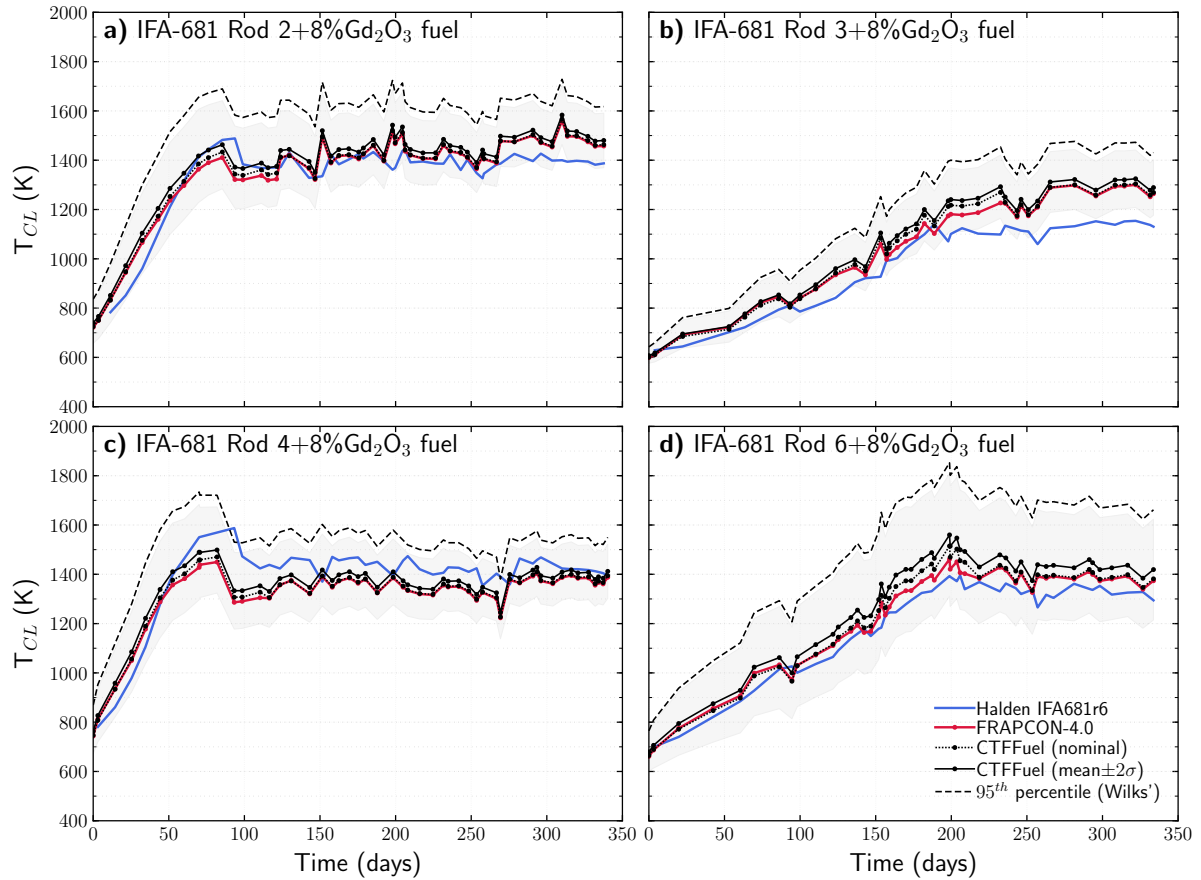


Figure 5.4: Centerline temperature predictions and measurements for IFA681 rods. Grey shaded areas on the plots represent two standard deviations around the quantified mean temperatures, while dashed lines signify the 95% percentile that is calculated based on Wilks' formula.

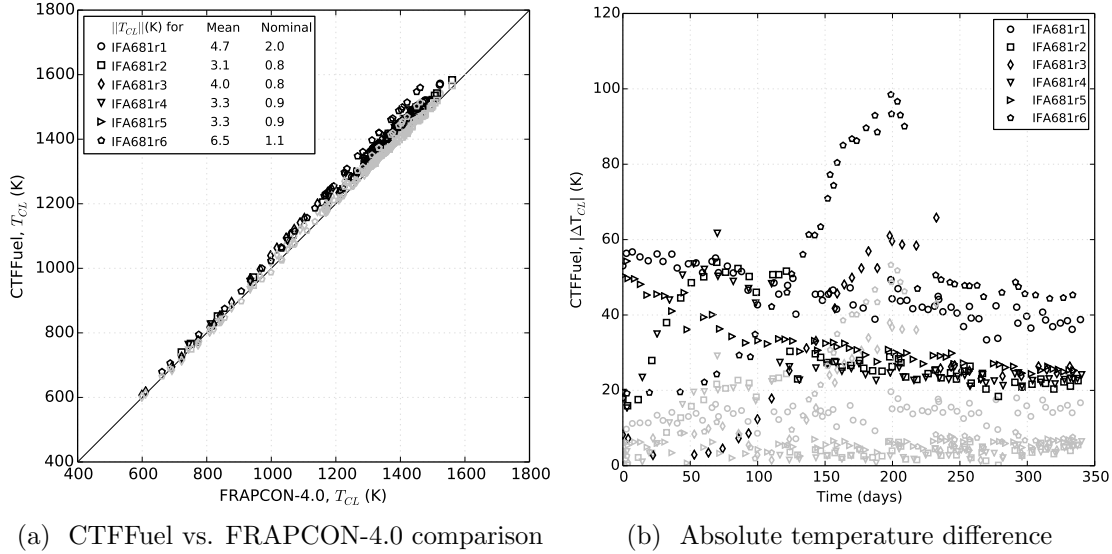


Figure 5.5: Prediction results with mean and nominal predictions.

5.3 Chapter Summary

A sensitivity study is performed on the Doppler temperature for the selected input parameters; gap conductance, power, wall temperature, fuel burnup and Gadolinium content. It is important to note that the sensitivity study is limited by the code’s capabilities and focus of the study. The results showed that the code’s responses are meaningful, therefore, it appears that the code functions as intended. From the Morris screening study, the Doppler temperature is most sensitive to the gap conductance for the given uncertainty bounds.

The uncertainty quantification was performed considering steady state CTFFuel simulations at each time step, and the input uncertainties are propagated through CTFFuel around the calculated nominal values from FRAPCON-4.0. A sample size of 59 was used for a one-sided 95% percentile based on Wilks formula. Wilks formula was a better representation in this study since standard deviation is more sensitive to the sample size. A larger sample size will reduce statistical errors but will increase computational time. The one-sided tolerance limit was sufficient for this analysis since the quantity of interest was the fuel centerline temperature, which must be below fuel melting temperature for regulatory purposes. The NRCs safety limit for the peak fuel centerline temperature is 3077 K, which is not exceeded by the 95% percentile in the uncertainty quantification step.

CHAPTER

6

FILL GAS THERMAL CONDUCTIVITY

Pressure dependence on thermal conductivity is neglected in today's nuclear fuel performance codes that assumes gas behaves a dilute gas; however, the pressure will be more pronounced at temperatures lower than ten times the critical temperature of each pure gas. The validity of this assumption for nuclear fuel performance is examined. Theory related to dilute and dense gas properties are provided in addition to its validation against to literature data up to 30 MPa for selected inert gases. Underlying assumptions are clearly described for each model and their possible impacts on gap conductance calculations are discussed.

This study attempts to examine the validity of the dilute gas assumption for gas thermal conductivity in nuclear fuel rod gap calculations. Theories related to dilute and dense gas properties are described and validated with literature data from Section 6.1 to Section 6.3. A case study is performed to examine the integral effect on fuel centerline temperature in Section 6.4. Concluding remarks and discussion of future work are provided at the end of this chapter.

6.1 Single-Component Gas Thermal Conductivity

The gap between fuel and cladding is initially pressurized to prevent unstable thermal behavior and to maintain cladding integrity. Helium is often chosen as the initial fill gas in nuclear fuel rods to improve the heat transfer through the gap between the fuel and cladding. In light water reactors, this initial pressure ranges from 0.3 to 3.45 MPa [24], and tends to increase throughout the life of the reactor due to expansion/contraction of the fuel and cladding, fission gas release, and et cetera. In some cases, the rod internal pressure approaches the external pressure (e.g., burst failure of the cladding during reactivity insertion accident transients [36]) or exceeds it (e.g., lift-off phenomena at the end of reactor's life [142, 143, 144, 129, 130]).

At the present time, nuclear performance codes/capabilities (e.g., Bison [48], FRAPCON [44], FRAPTRAN [45], CTFFuel [145]) use thermal conductivity correlations from the Handbook of Material Properties [49] for inert gases of interest. The correlations are only temperature-dependent and calibrated to experimental data at pressures below 0.1 MPa [50, 51]. However, the thermal conductivity of all gases increases with pressure, though the extent of this dependence varies depending upon the pressure. Three distinct pressure regions exist:

1. a very low pressure (below 0.1 kPa) region where the thermal conductivity is almost proportional to pressure, *the Knudsen domain*,
2. a low pressure (below 1.0 MPa) region where the pressure dependence is generally neglected in literature due to its less than one percent contribution to the thermal conductivity per bar [146, 147], and
3. a high pressure (above 1.0 MPa) region where increasing pressure increases the thermal conductivity.

Thus, it can be simply stated that the thermal conductivities of low pressure gases increase with temperature, and increase with pressure at high pressures [148]. Therefore, the use of these models in nuclear applications, particularly in gap conductance calculations is questionable. Analysts often compensate for the inaccuracy of these models by applying large uncertainties, for example in the Consortium for Advanced Simulation of Light Water Reactors (CASL) applications, fifty percent uncertainty is employed [149]. Better understood physics will reduce this uncertainty and yield more accurate estimation of fuel temperatures.

Tournier and El-Genk [150, 6] semi-empirically expressed the thermal conductivities of dense inert gases as

$$\lambda(T, P) = \lambda^0(T) + \lambda_c^* \Psi_k \left(\frac{\rho}{\rho_c} \right), \quad (6.1)$$

where

- $\lambda^0 = (15R_g/4M) \mu^0(T)$, thermal conductivity of pure dilute gases based on the kinetic theory (Figure 6.1),
- $\mu^0 = A_\mu (T - T_\mu)^n$, dynamic viscosity of pure dilute gases (Figure 6.1),
- M = molecular weight,
- $\lambda_c^* = 0.201 \times 10^{-4} T_c^{0.277} M^{-0.465} (0.291 \times V^*)^{-0.415}$, pseudo-critical thermal conductivity,
- $V^* = (R_g T_c / P_c)$, characteristic molar volume,
- $\Psi_k = 0.645 \rho_r + 0.331 \rho_r^2 + 0.0368 \rho_r^3 - 0.0128 \rho_r^4$, excess thermal conductivity, and
- $\rho_r = (\rho / \rho_c)$, reduced density.

Figure 6.1 shows the dynamic viscosity and thermal conductivity of the dilute gases for inert gases of interest. MATPRO-11 correlations for thermal conductivity based on [50] are added to the plot for comparison, which underestimate for helium and overestimate for krypton. Note that thermal conductivity of neon is not provided in [49]. As expected, the largest discrepancy is observed at higher temperatures. For example, 5.8% underestimation for helium, 12.3% overestimation for krypton, and 8.2% overestimation for xenon at $T = 1000$ K. Meanwhile, disagreement is negligibly small for argon.

The accuracy of the correlation given in Eq. 6.1 is examined in Figure 6.2 with the literature data up to 30 MPa. The data are from Kestin et al. [14], Michels et al. [15], Rosenbaum

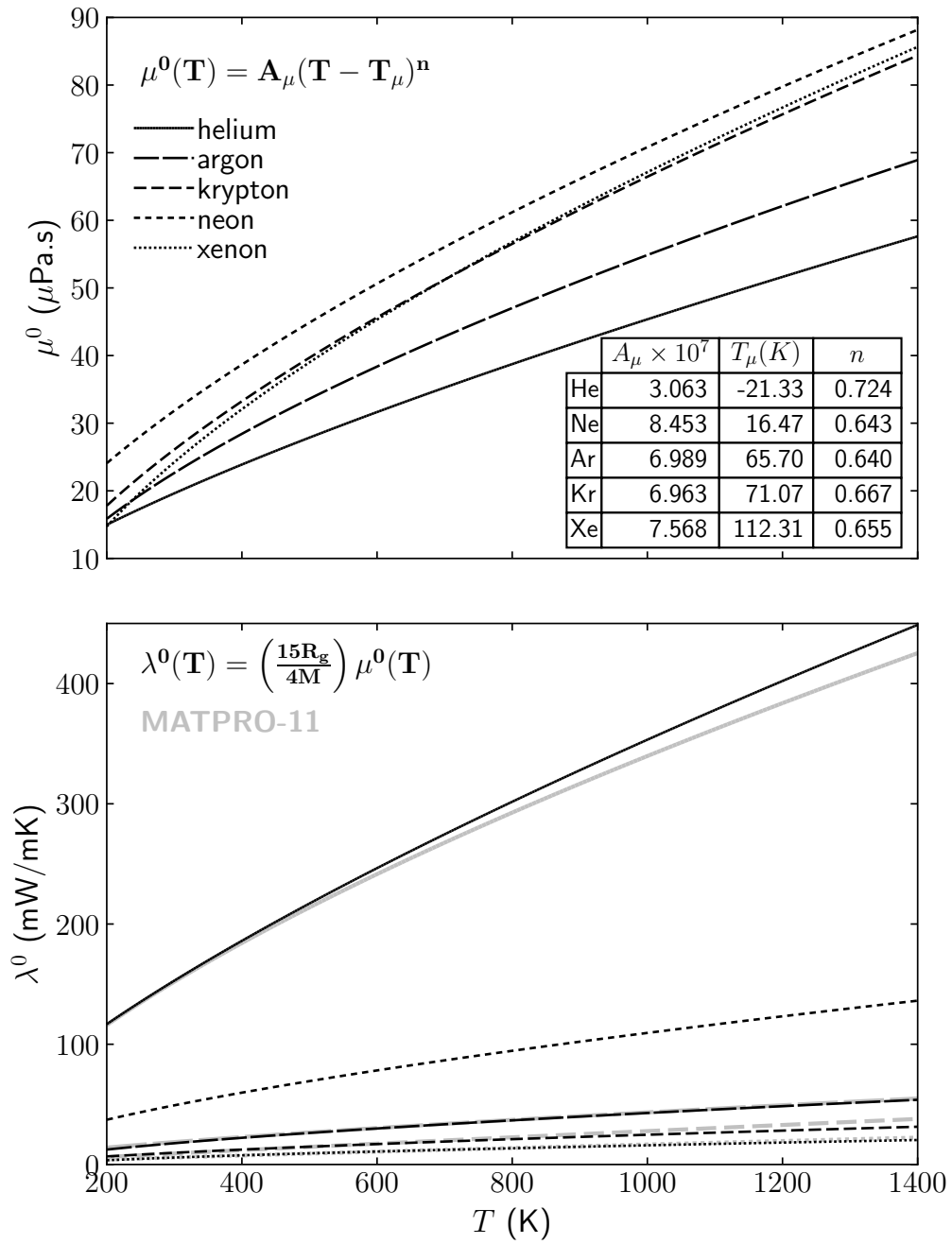


Figure 6.1: The dynamic viscosity (upper plot) and thermal conductivity (lower plot) of the dilute inert gases based on the closure relations given by Tournier and El-Genk [6].

Table 6.1: The parameters from Tournier and El-Genk [6] for selected rare gases. The critical parameters are denoted by the subscript c .

	He	Ne	Ar	Kr	Xe
M (g/mol)	4.003	20.18	39.948	83.798	131.293
P_c (MPa)	0.2275	2.678	4.863	5.51	5.84
ρ_c (kg/m ³)	69.64	481.9	535.6	908.4	1110.0
T_c (K)	5.2	44.4	150.69	209.4	289.7
T_μ (K)	-21.33	16.47	65.70	71.07	112.31
$A_\mu \times 10^7$	3.063	8.453	6.989	6.963	7.568
n	0.724	0.643	0.640	0.667	0.655

et al. [16], Johnston and Grilly [151], Kannuluik and Carman [152], Nain [153], Saxena and Saxena [154], Freud and Rothberg [155], and Sengers [17]. Differences between the predictions and the data are quantified in terms of following validation metrics that are summarized on the plot. The agreement is within a deviation of 2.8% over 356 experimental data points.

The theory of corresponding states was originally developed by van der Waals [156] and reduced-state plots are based on this theory. In this study, the reduced-state plot of thermal conductivity for the selected inert gases is obtained following the approach developed by Owens and Thodos [157]. Reduced thermal conductivities are calculated using Eq. 6.1 and plotted against the reduced temperatures on a log–log plot in Figure 6.3. Extreme bounds for the gas temperature are presented on the plot for a nuclear fuel rod. Overall, the pressure dependence is more substantial at lower gas temperatures, particularly temperatures lower than ten times the critical temperature of each pure gas (i.e., $T_r \leq 10$). Clearly, both He and Ne are less influenced by the pressure within the given temperature range as compared to Xe, Ar, and Kr.

6.2 Multi-Component Gas Thermal Conductivity

The mixture thermal conductivity of a gas mixture is often not a linear function of mole fraction due to differences in polarity, molecular weights or sizes of the constituents [148, 158, 159]. The thermal conductivity for a mixture of non-reacting, monatomic gases may be obtained to any degree of approximation. Kennard [18] indicated that a simple quadratic expression is sufficient to estimate viscosity and thermal conductivity of binary gas mixtures for practical purposes; however, more detailed work is necessary to understand multi-component mixing mechanism. The formulations in the literature are often the result of rigorous kinetic theory developments [160, 161, 162]. Wassilijewa [163] proposed that the binary mixture of thermal conductivity is analogous to the binary mixture viscosity form suggested by Sutherland [164] based on kinetic theory. Later, Lindsay and Bromley [165] generalized the equation, λ'_m for multi-component mixtures—similar to the work of Buddenberg and Wilke [166] for the gas viscosity—as Eq. 6.2.

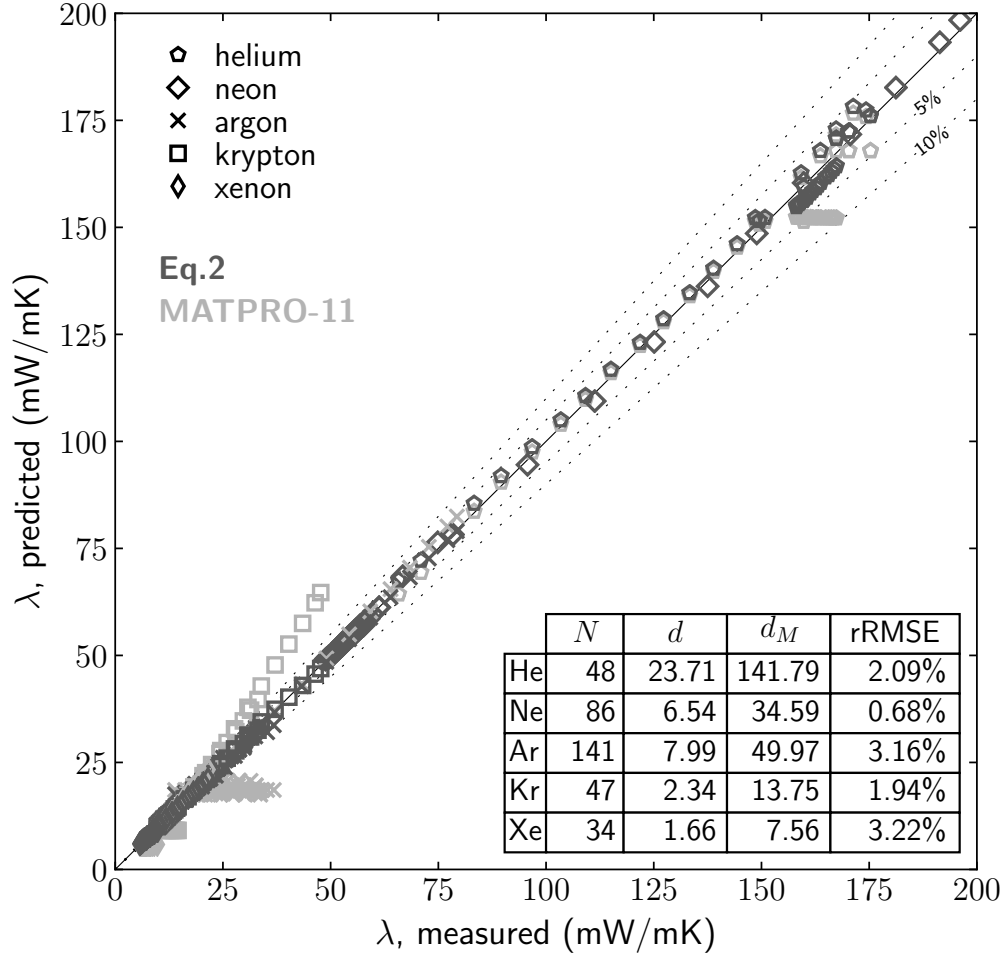


Figure 6.2: Comparison of predicted and measured thermal conductivity using the literature data up to 30 MPa. Tabulated validation metrics belong to the predictions with $\lambda(T, P)$ given in Eq. 6.1. Note that MATPRO-11 correlations with the assumption of $\lambda(T, P) \approx \lambda^0(T)$ are only added for visual comparison.

$$\lambda'_m = \sum_{i=1}^n \frac{x_i \lambda_i}{\sum_{j=1}^n \Psi_{ij} x_j} = \sum_{i=1}^n \frac{\lambda_i}{1 + \sum_{j=1, j \neq i}^n \Psi_{ij} \frac{x_j}{x_i}}, \quad (6.2)$$

where

- n = number of constituents in the gas mixture,
- λ = monatomic (or translational) thermal conductivity of the constituent,
- x = mole fraction of constituent, and
- Ψ_{ij} = empirical expression that is a function of thermal conductivities, Sutherland constants, temperature, and molecular weights of the constituents.

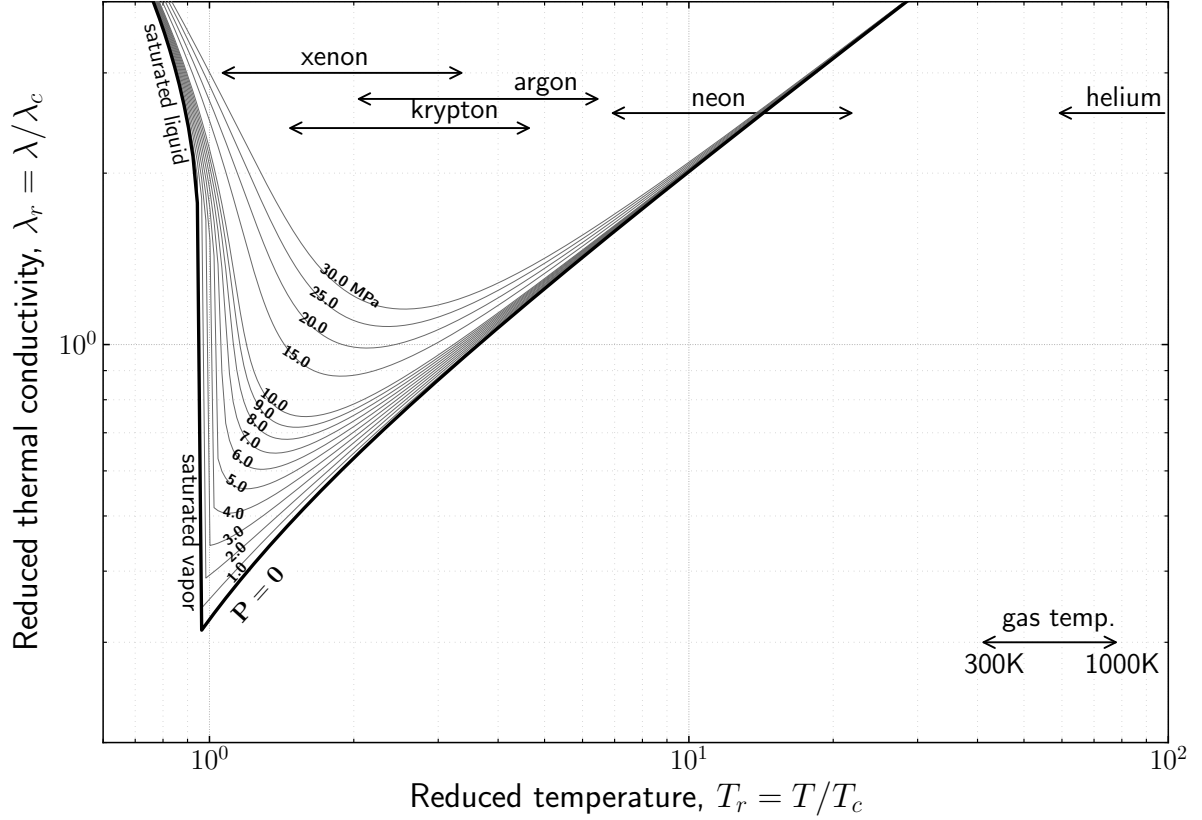


Figure 6.3: Reduced-state plot of thermal conductivity for the selected inert gases according to the critical parameters from Tournier and El-Genk [6].

An alternative expression for Ψ_{ij} was suggested by Lindsay and Bromley [165] in terms of the thermal conductivities, the molecular weights, and inter-molecular potentials as

$$\Psi_{ij} = \Phi_{ij} \left\{ 1 + \left(\frac{M_i - M_j}{M_i + M_j} \right)^2 \left(\frac{15}{4A_{ij}^*} - 1 \right) \times \left[1 + \left(\frac{12B_{ij}^* + 5}{30 - 8A_{ij}^*} \right) \frac{M_j}{M_i - M_j} \right] \right\}, \quad (6.3)$$

where

M = molecular weight of the constituent,

Φ_{ij} = the empirical expression that is proportional to the ratio of translational to fictitious conductivity characterizing the interaction between unlike molecules [167], and

A_{ij}^*, B_{ij}^* = the inter-molecular potential functions.

Hirschfelder indicated that A_{ij}^* and B_{ij}^* are nearly unity (e.g., $A_{ij}^* = 1.099$ and $B_{ij}^* = 1.093$ for Ne-H₂ gas pair) [160]. Brokaw [168, 167] simplified the expression with realistic values of the potential functions (i.e., $A_{ij}^* = B_{ij}^* \cong 1.10$) that resulted in the relation given in Eq. 6.4a.

If the rigid sphere formulas that relate viscosity and thermal conductivity are used, relation given in Eq. 6.4b is obtained. The term in the numerator, $(\lambda_i/\lambda_j)^{1/2} (M_i/M_j)^{1/4}$ is replaced by $(\mu_i/\mu_j)^{1/2} (M_j/M_i)^{1/4}$ for the gas mixture viscosity. Mason and Saxena [169] modified Eq. 6.4b multiplying by 1.065.

$$\Psi_{ij} = \Phi_{ij} \left[1 + 2.41 \frac{\left(1 - \frac{M_i}{M_j}\right) \left(0.142 - \frac{M_i}{M_j}\right)}{\left(1 + \frac{M_i}{M_j}\right)^2} \right], \quad (6.4a)$$

$$\Phi_{ij} = \frac{\left[1 + \left(\frac{\lambda_i}{\lambda_j}\right)^{1/2} \left(\frac{M_i}{M_j}\right)^{1/4} \right]^2}{2\sqrt{2} \left(1 + \frac{M_i}{M_j}\right)^{1/2}}. \quad (6.4b)$$

In nuclear applications, the fill gas is composed of mostly monatomic gases, therefore, contribution of the diffusional transport of internal energy is neglected on the gas mixture thermal conductivity. However, for the use of polyatomic gases, the thermal conductivity of a mixture is approximated as a superposition of the collisional transport of translational kinetic energy, λ'_m and the diffusional transport of internal energy, λ''_m . The former completely accounts for the mixture thermal conductivity of monatomic inert gases [167], given in Eq. 6.2. For the latter, Hirschfelder [170] analogously derived an expression λ''_m by replacing Ψ_{ij} in the denominator with Φ_{ij} in Eq. 6.2. Another important consideration is to correct the monatomic thermal conductivity with the Eucken factor [171] that is $\lambda_i = \lambda_i/E_i$. Hirschfelder [172] suggested an improved value of the Eucken factor as $E = 0.115 + 0.354\gamma/(\gamma - 1)$ in terms of the ratio of specific heat at constant pressure to that at constant volume, $\gamma = C_p/C_v$. The specific heat capacities are practically independent of temperature for the monatomic gases; however, for all gases—except the monatomic gases—increase with temperature [7], which leads to discrepancy from the theory. This requires special treatment for the mixture thermal conductivity of polyatomic gases in today's nuclear fuel performance codes. Additional difficulty might arise from mixture of monatomic and polyatomic constituents. There are data available in the literature [160, 173, 174, 175, 176, 177]; however, this is beyond the scope of this work.

Thermal conductivities of gas mixtures at high pressures (above 1 MPa) and temperatures are treated differently [178, 179, 180, 181]. The mixture model given in Eq. 6.2 is employed for the gases at either low/moderate pressures (below 1 MPa). Since simple gases are considered in nuclear applications, use of this model should result in an acceptable level of accuracy. The model is validated using both low and high-pressure literature data in Figure 6.4 for binary and ternary mixtures of inert gases. The low-pressure data are from Srivastava and Barua [182], Wachsmuth [183], Ubisch [184], Saxena [185], Muckenfuss and Curtiss [186], Mason and Saxena [169, 187], Hirschfelder et al. [160], Gandhi and Saxena [51], Dael [188], Burnett [189], and Barua [173]. The high-pressure data are from Peterson et al. [175], and Clifford et al. [190]. The error is minimized by multiplying Φ_{ij} in Eq. 6.4b by the Mason and Saxena modification for the high-pressure comparison; however, this is not the same for the low-pressure comparison. Once the combined data are compared over 543 data points at both low and high pressure, the relative agreement of 6.08% for Eq. 6.4b, and 6.69% for Eq. 6.4b that is multiplied by 1.065 according to the Mason and Saxena modification. For the rest of this manuscript, the former

form is used.

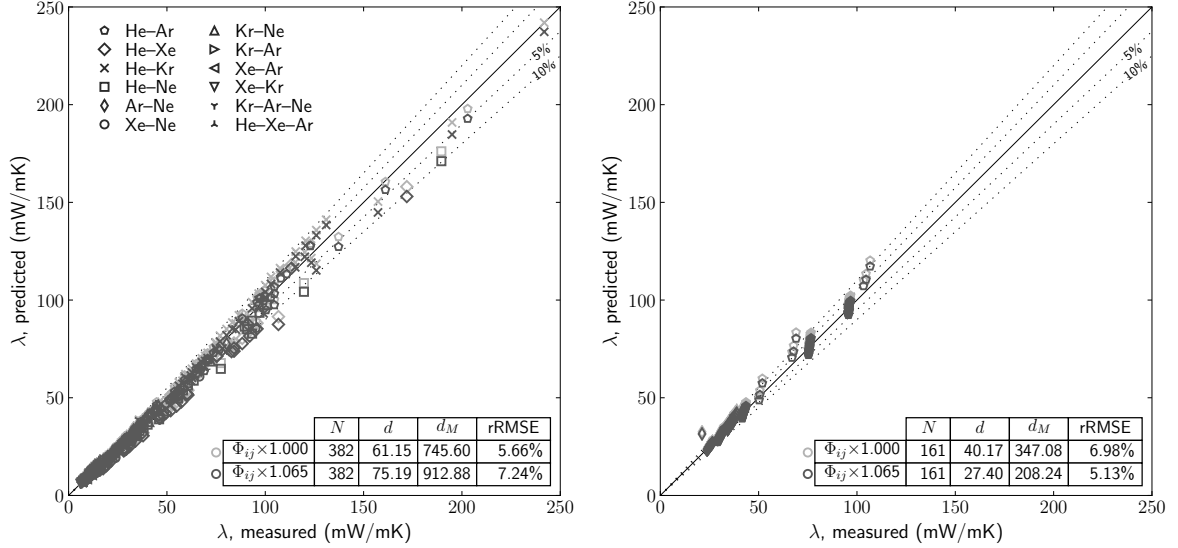


Figure 6.4: Comparison of predicted and measured gas thermal conductivity using the literature data up to 30 MPa. The thermal conductivities of binary and ternary gas mixtures are calculated according to Eq. 6.1. Consistent legend is used in both figures (left plot: the low-pressure; right plot: the high-pressure).

6.3 Gas Density

The behavior of a fluid deviates from the ideal gas law as its density increases. Many corrections are introduced in the literature to account for this deviation, which lead to the virial expansion form of the ideal gas law in terms of the macroscopic thermodynamic properties and particle interactions [191, 192]. The virial equation of state is expressed as

$$\frac{P}{R_g T} = \hat{\rho} + B_2(T)\hat{\rho}^2 + B_3(T)\hat{\rho}^3, \quad (6.5)$$

where

- Z = compressibility factor,
- $\hat{\rho}$ = $1/V$, molar density,
- V = volume, and
- $B_i(T)$ = i -th virial coefficient that is only function of temperature.

The first term corresponds to a case with no interactions, the second $B_2(T)\hat{\rho}$ to two interacting particles, and so on. For larger volumes (or $\hat{\rho} \rightarrow 0$), this equation approaches ideal gas behavior, which is consistent with the virial equation of state. If the gas temperature and

pressure are known, the density of the gas is computed by solving the cubic equation given in Eq. 6.5, and the density is obtained by employing a root-finding algorithm. Since it is a cubic equation, there may be three possible solutions:

1. single real root (vapor and liquid phases in equilibrium when $T = T_{sat}$ and $P = P_{sat}$),
2. three real roots (the highest value for gas phase; the lowest value for liquid phase; no physical meaning for the intermediate solution), or
3. one real and two complex roots (the real value assigned for the gas phase).

Briefly, the highest real value is assigned for the gas molar density. Using the virial coefficients in Figure 6.5, the density predictions are validated with the literature data [14, 15, 16, 17] up to 30 MPa. The predictions agree with the measured data with a maximum error of 0.66% over 213 measured data points in Figure 6.6.

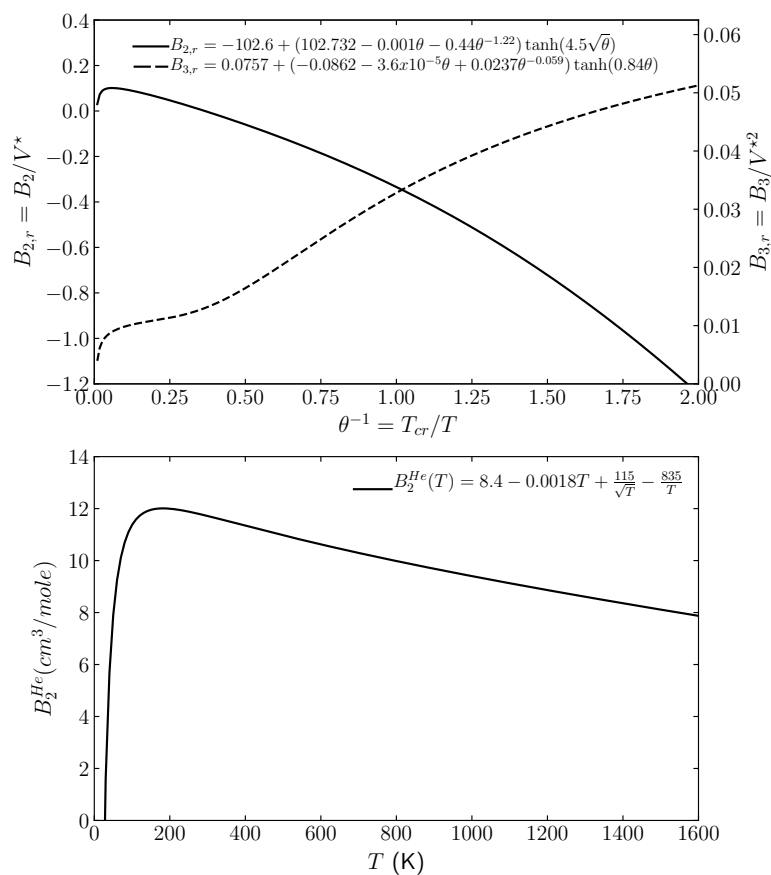


Figure 6.5: The reduced second and third virial coefficients, $B_{2,r}$ and $B_{3,r}$ vs. the reduced temperature, θ for Xe, Kr, Ar and Ne (upper plot). The second virial coefficient for He as a function of temperature (lower plot), where its third virial coefficient is neglected due to its dilute gas behavior. The closure relations are calibrated based on the literature data by Tournier and El-Genk [6].

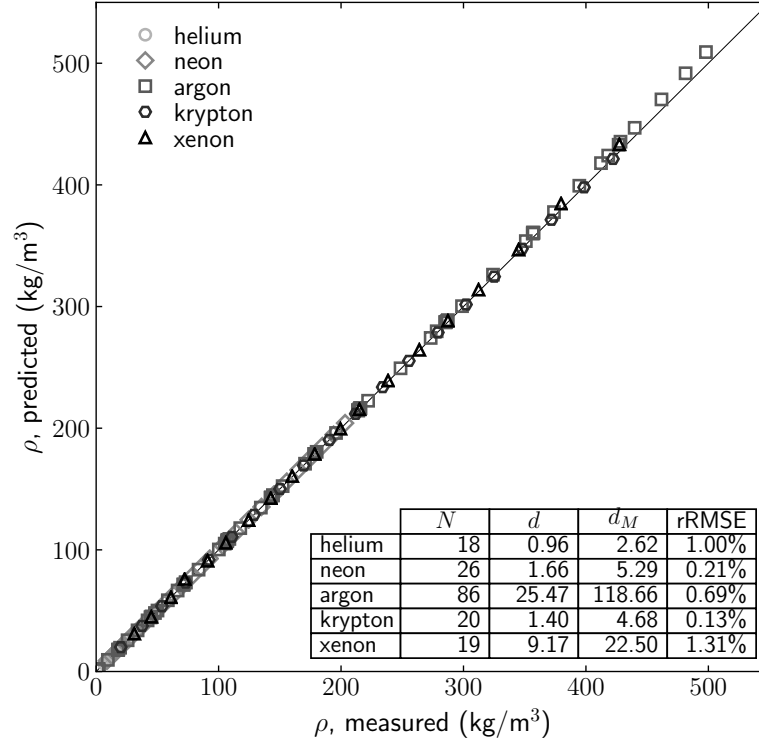


Figure 6.6: Comparison of predicted and measured density using the literature high-pressure data up to 30 MPa. The data are from Kestin et al. [14], Michels [15], Rosenbaum [16], and Sengers[17].

6.4 Case Study

Conductance across the gap is calculated considering three separate heat paths in parallel, which are summed: conductance through the interfacial gas, h_g , conductance through solid contact, h_c , and conductance due to direct thermal radiation, h_r . The gas thermal conductivity is taken into account in the fill gas conductance that is calculated as the ratio of the thermal conductivity to the effective gap thickness. In this study, the validity of the dilute gas assumption is examined by calculating the fill gas thermal conductivity in two different ways:

1. $\lambda_g(T)$ correlations from MATPRO-11 [49] that are widely used in nuclear fuel performance codes, and
2. $\lambda_g(T, P)$ using Eq. 6.1 from Tournier and El-Genk [6].

Thus, the corresponding gap conductance, h_{gap} is calculated as

$$\begin{aligned}
h_{gap} &= \xi h_g + (1.0 - f_g) h_{gap} \\
&= \xi \left(\frac{\lambda_g(T)}{d^*} \right) + (1.0 - f_g) h_{gap},
\end{aligned} \tag{6.6}$$

where

$$\begin{aligned}
f_g &= (h_g/h_{gap}), \text{ the fraction of the gap conductance due to the fill gas conductance,} \\
\xi &= \begin{cases} 1.0, & \text{traditional approach} \\ \frac{\lambda_g(T,P)}{\lambda_g(T)}, & \text{new approach} \end{cases}, \\
\lambda_g &= \text{the gas thermal conductivity, and} \\
d^* &= \text{the effective gap thickness.}
\end{aligned}$$

The initial fill gas is assumed to be either He or Ar and gradually altered with burnup by the addition of (lower-conductivity) gaseous fission products such as Xe and Kr. Figure 6.7 shows the thermal conductivity comparison for He–Kr–Xe and Ar–Kr–Xe ternary mixtures at varied gas temperatures and rod internal pressures for an arbitrary gap inventory. Clearly, the pressure dependence on the thermal conductivity is more substantial at lower temperatures, as illustrated previously in Figure 6.3. Since He has high thermal conductivity, the contribution from the fission gas products is less significant once the gap is mostly occupied by He. However, the pressure effects are more pronounced once its thermal conductivity approaches the thermal conductivity of heavier inert gases in the gap (such as Kr and Xe). This is more significant for the Ar-filled case, since its thermal conductivity is of a similar order to that of either Xe or Kr.

The aim is to investigate the impact of eliminating the dilute gas assumption on the temperature predictions of nuclear fuel. Two steady state Halden IFA (Instrumented Fuel Assembly) test cases are chosen from FRAPCON-4.0’s integral assessment test matrix [44, 3]: IFA432 Rod 1 and IFA681 Rod 6. The former is initially filled with He, and the latter with a binary mixture of He and Ar. Note that rods are not in contact at the beginning of life, and the gap shrinks as the fuel burns out. Therefore, changes at the beginning of life will propagate through the reactor’s end of life and will impact the overall performance of the fuel rod. In this manner, the overall change in gas thermal conductivity is computed using a script given the rod internal pressure history for each rod. This is basically the same with changes in the cold gap thickness (Eq. 6.6). Without doing code changes, FRAPCON-4.0 simulations are repeated with altered cold gap thicknesses to see their significance for the fuel centerline temperature.

The Halden IFA432 Rod 1 is initially filled with helium and pressurized to 0.2 MPa. The UO₂ fuel is separated by a 114 μm as-fabricated radial gap [117]. An average 3.05% increase in gas thermal conductivity is computed. The gap thickness is reduced by the same amount and results are summarized in Table 6.2. The maximum temperature difference is found to be around 50 K (Figure 6.8).

The Halden IFA681 Rod 6 is initially filled with a binary mixture of helium and argon (i.e., 50% He and 50% Ar). The rod is initially pressurized to around 2.2 MPa. The UO₂+8% Gd₂O₃ fuel is separated by an 85 μm radial gap [124]. Note that the gas composition does not vary for this case. An average 4.20% increase in gas thermal conductivity is computed. The gap thickness is reduced by the same amount; results are summarized in Table 6.2. The maximum temperature difference is around 20 K (Figure 6.9).

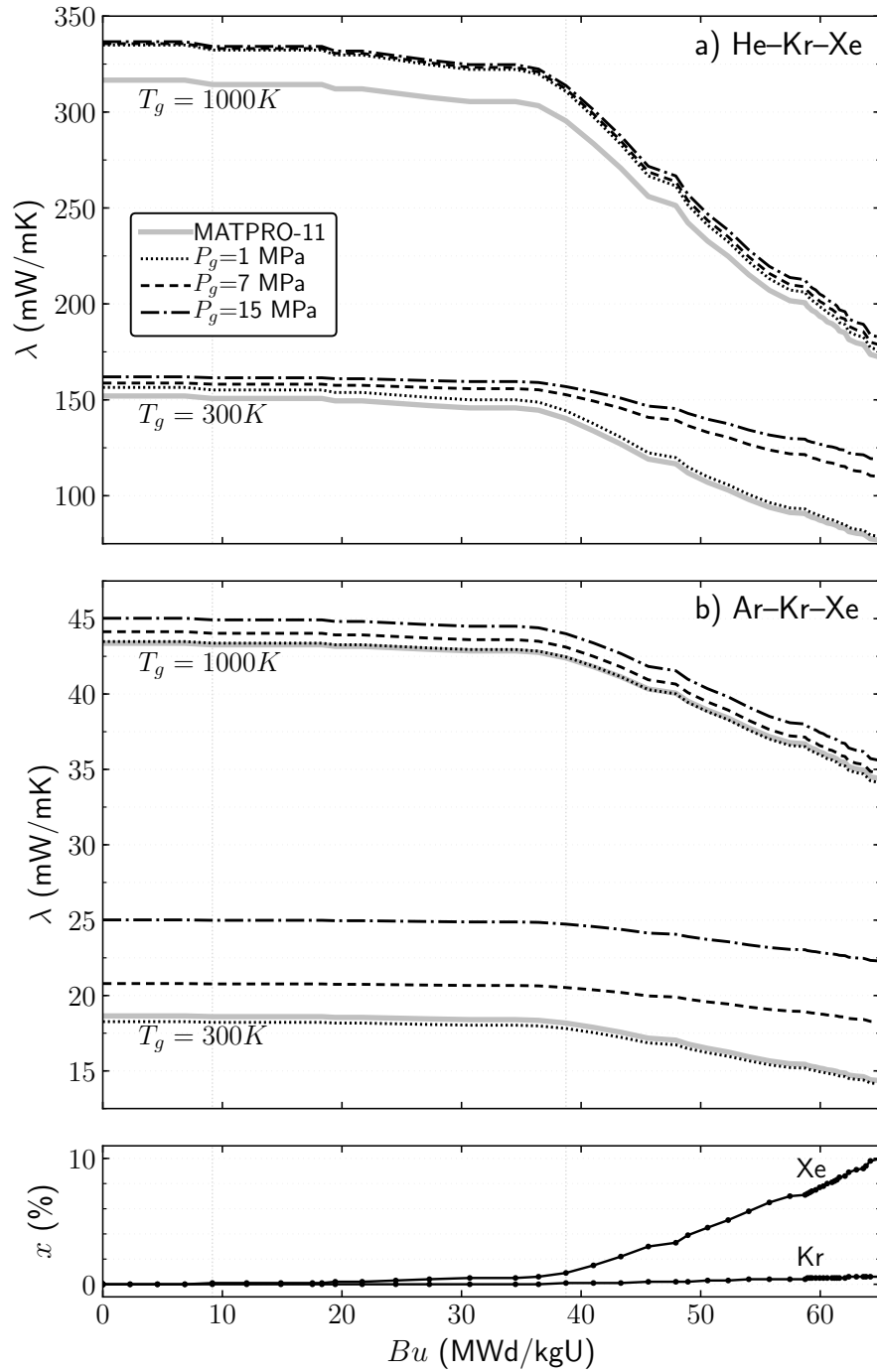


Figure 6.7: Thermal conductivities of (a) He-Kr-Xe and (b) Ar-Kr-Xe ternary mixtures at varied gas temperatures and rod internal pressures.

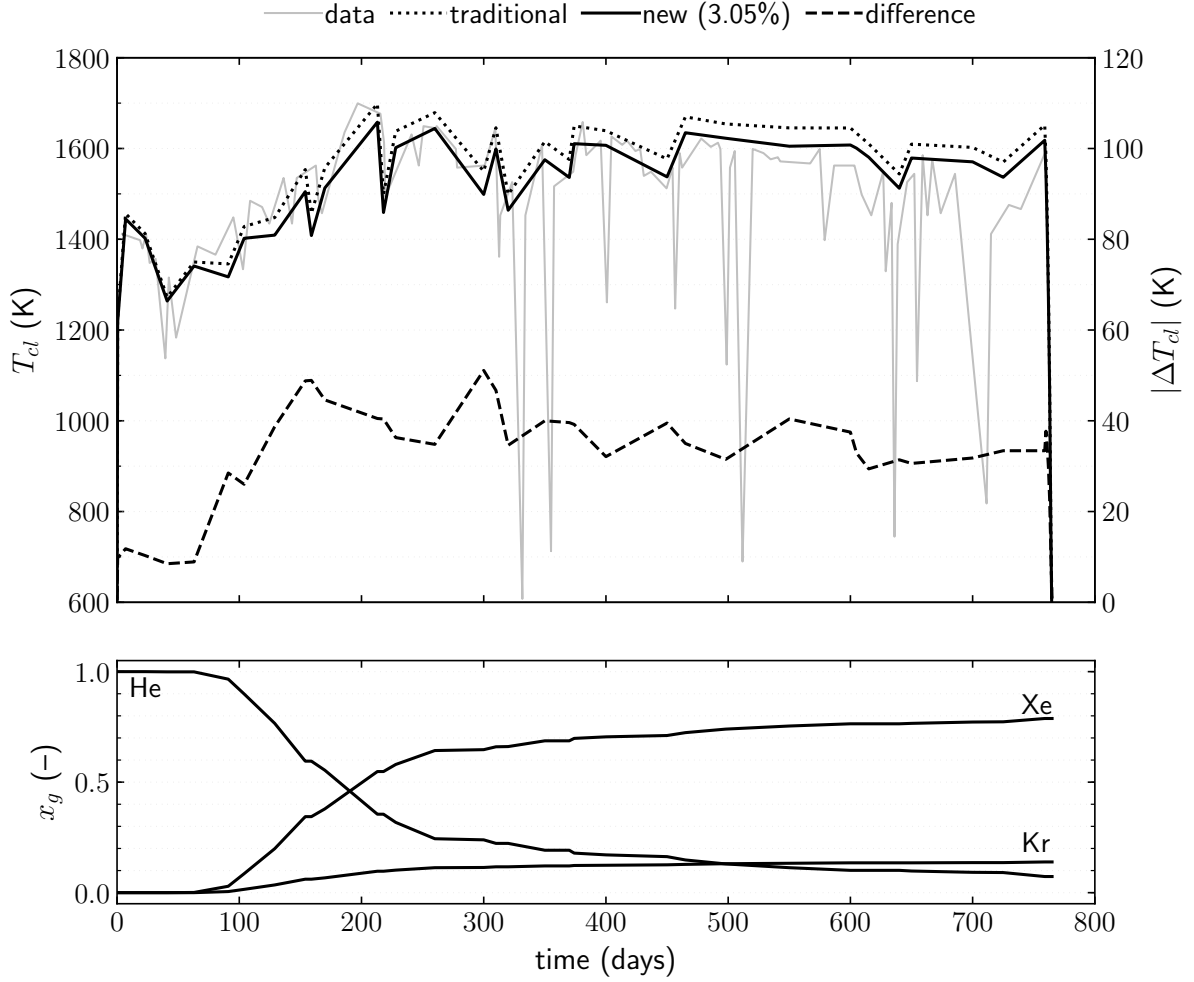


Figure 6.8: (a) Measured and predicted centerline temperature for IFA432 Rod 1 with UO_2 fuel at lower thermocouple position (burnup=45 MWd/kgU, cold radial gap= $114\mu\text{m}$, rod internal pressure= 0.2 to 4.2 MPa, open gap), and (b) gas composition with respect to time.

Table 6.2: Fuel centerline predictions between the traditional and new approaches are summarized in terms of the metrics for the selected IFA rods.

	$ \Delta\xi $ (%)	ΔT_{cl}^{max} (K)	d (K)	d_M (K)	RMSE (K)	rRMSE (%)
IFA432 Rod 1	3.05	51.1	214.3	1280.2	32.3	2.09
IFA681 Rod 6	4.20	19.3	109.0	734.6	15.7	1.22

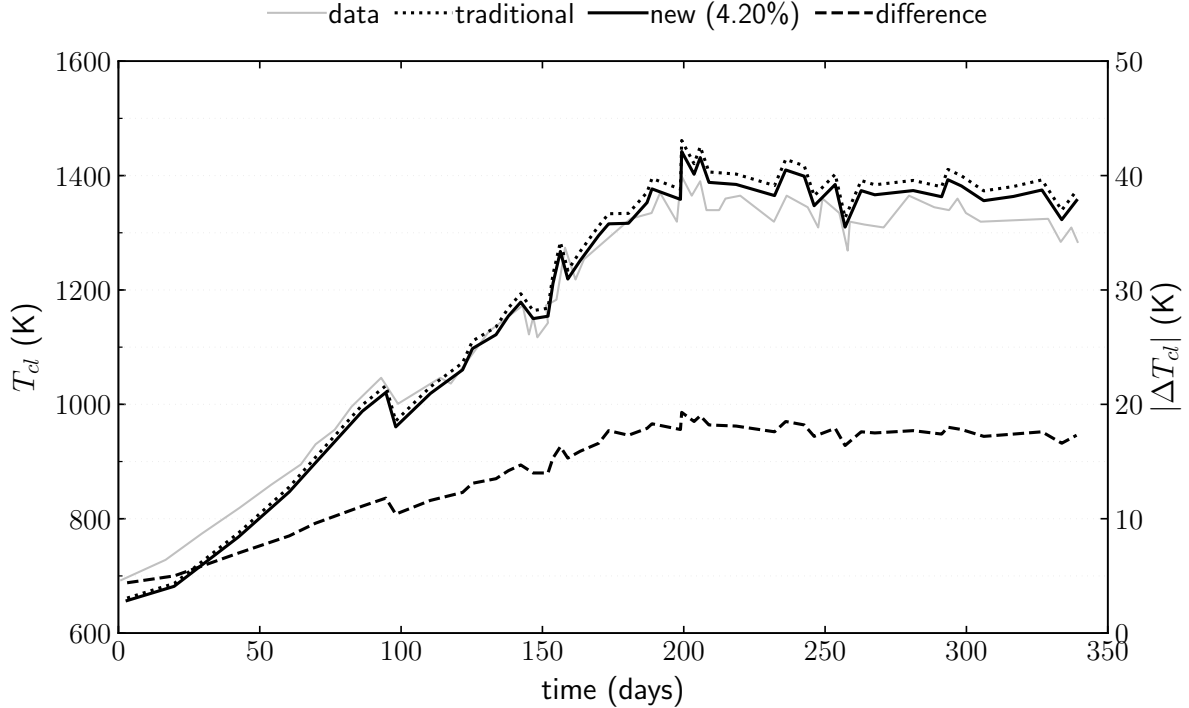


Figure 6.9: Measured and predicted centerline temperature for IFA681 Rod 6 $\text{UO}_2+8\% \text{Gd}_2\text{O}_3$ fuel. (burnup=13 MWd/kgU, cold radial gap= $85\mu\text{m}$, rod internal pressure= 2.2 to 4.3 MPa, open gap). The gas mixture is composed of 50% He and 50% Ar.

A better agreement is observed with the new model for the selected cases; however, this cannot be generalized for all cases because it depends on several factors (e.g., the gas temperature and gas pressures, gap configuration, and power). For example, the error in IFA 432 Rod 1 has larger error than in IFA 681 Rod 6, which is a relatively higher power case with a larger gap thickness. Additionally, one is doped with gadolinia, so the thermal characteristics will differentiate between the two.

6.5 Chapter Summary

Pressure dependence on thermal conductivity is neglected in today's nuclear fuel performance codes that assume gas behaves as a dilute gas; however, the pressure effect will be more pronounced for reactor operating conditions. Error due to this assumption will be more pronounced in nuclear applications for cases when the rod internal pressure approaches/exceeds the external pressure or in open gap configurations due to relocated fuel at higher pressures. A robust application of the theory will minimize uncertainties for gap conductance calculations and enable accurate prediction of fuel temperatures. Future work should include integration of this model in a nuclear fuel performance code and test it during anticipated transients.

CHAPTER

7

GAP CONDUCTANCE THEORY

Accurate estimation of gap conductance is important in nuclear fuel performance because heat transfer across the gap heavily impacts fuel temperatures and the thermo-mechanical performance of nuclear fuel rods. In a standard nuclear fuel rod, a fuel pellet is enclosed by a cladding. The pellet and cladding are separated by a thin gap that is initially filled with inert monatomic gas and pressurized to prevent unstable thermal behavior and to maintain cladding integrity. The initial fill gas is assumed to be either helium or argon and is gradually altered with burnup by the addition of gaseous fission products. The initial rod internal pressure ranges from 0.3 to 3.45 MPa for light water reactors and increases throughout the reactor's life. For example, the rod internal pressure is initially 1.5–2 MPa for pressurized water reactor (PWR) and 0.2–0.8 MPa for boiling water reactor (BWR) [24].

The gap behavior is a complicated problem due to the inclusion of many physical phenomena such as evolution of the gap due to expansion/contraction of the fuel and cladding, changing gap inventory due to fission gas release, single- and multi-component gas properties, and heat transfer characteristics in the gap. The literature categorizes the gap behavior into two categories: (i) the mechanical aspects of the gap (e.g., changes in the gap thickness, the rod internal pressure, the gas inventory); and (ii) the thermal aspects of the gap (e.g., the heat transfer calculations across the gap). The latter is the interest of this study. In this chapter, theoretical considerations and underlying assumptions are provided for the gap conductance modeling. The gap conductance is calculated considering three summed heat paths in parallel [23] as

$$h_{gap} = h_g + h_s + h_r, \quad (7.1)$$

where

h_g = fill gas conductance (Section 7.1),
 h_s = solid contact conductance (Section 7.2), and
 h_r = direct thermal radiation (Section 7.3).

Each heat transfer mechanism is described in details in the following sections, including both traditional modeling approaches and improved theory. The concluding remarks and future work are provided at the end.

7.1 Fill Gas Conductance

Heat transfer kinetics between gas molecules are divided into four regimes: continuum, slip, transition, and free-molecular. The regimes are identified based on the Knudsen number (Kn), which is defined as the ratio between the molecular mean free path l and the distance between the two bounding surfaces d . Figure 7.1 shows three different geometries with the identical gap thickness for ‘plane’, ‘cylinder’, and ‘sphere’. The heat transfer regimes is detailed as the below.

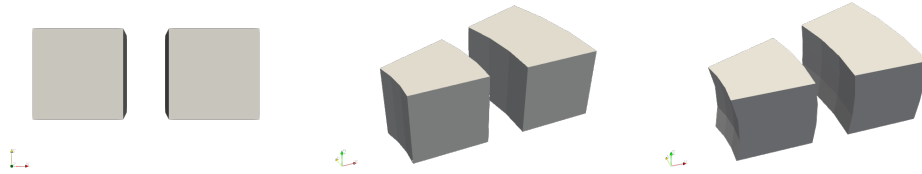


Figure 7.1: Two block geometry (left to right; plane, cylinder, and sphere). The gap distance is referred to the distance between two solid blocks.

Continuum flow

In the continuum flow, the ‘ideal’ fill gas conductance is derived from Fourier’s law using thermal resistances, for the radii $r_1 < r_2$ in the curvilinear coordinates, as

$$h_g = \begin{cases} \frac{\lambda_g}{d}, & \text{plane} \\ \frac{\lambda_g}{r_1 \ln\left(\frac{r_2}{r_1}\right)}, & \text{cylinder} \\ \frac{\lambda_g}{r_1^2 \left(\frac{1}{r_1} - \frac{1}{r_2}\right)}, & \text{sphere} \end{cases}, \quad (7.2)$$

where

λ_g = thermal conductivity of the fill gas, and
 d = gap distance.

Figure 7.2 shows the fill gas conductance in the continuum flow with respect to the pressure for the single-and the multi-component gases. The gas compositions are arbitrarily chosen with the gaseous fission products such as xenon and krypton. Clearly, the pressure dependence on the formulation is only due to the fill gas thermal conductivity, as mentioned previously (Figure 6.3).

Slip flow

In the *slip flow*, there exists a discontinuity in temperature at the wall, which is known as the temperature jump condition. The fill gas conductance is calculated for the radii $r_1 < r_2$ in the curvilinear coordinates as Eq. 7.3. The use of this model is reasonable when g/d is rather small. Traditionally in nuclear fuel performance codes, the slip regime is postulated for the fill gas conductance calculations. The idea is to serve a numerical stability criterion with the non-zero temperature jump distance as the gap distance approaches to zero for smooth fuel and clad surfaces.

$$h_g = \begin{cases} \frac{\lambda_g}{d+g_1+g_2}, & \text{plane} \\ \frac{\lambda_g}{r_1 \left(\ln\left(\frac{r_2}{r_1}\right) + \frac{g_1}{r_1} + \frac{g_2}{r_2} \right)}, & \text{cylinder} \\ \frac{\lambda_g}{r_1^2 \left(\left[\frac{1}{r_1} - \frac{1}{r_2} \right] + \frac{g_1}{r_1^2} + \frac{g_2}{r_2^2} \right)}, & \text{sphere} \end{cases}, \quad (7.3)$$

where

g = temperature jump distance.

Figure 7.3 shows the fill gas conductance in the slip flow with respect to the pressure for the single-and the multi-component gases. The temperature jump distance is more pronounced at low pressures, particularly for the helium that has the largest temperature jump distance. Apparently, continuum assumption for the fill gas conductance will provide a better representation of the fill gas conductance.

Free-molecular flow

In the *free-molecular flow* ($Kn \gg 1$), inter-molecular collisions are negligible and the heat transfer rate is determined by Kennard [18] as

$$h_g = h_{FM} = \frac{1}{2}(T_1 - T_2)(1 + \gamma) \frac{c_V P}{(2\pi RT)^{1/2}} \Lambda_{12}, \quad (7.4a)$$

$$\Lambda_{12} = \begin{cases} \frac{\alpha_1 \alpha_2}{\alpha_1 + \alpha_2 - \alpha_1 \alpha_2}, & \text{plane} \\ \frac{\alpha_1 \alpha_2}{\alpha_2 + \alpha_1(1 - \alpha_2) \left(\frac{r_1}{r_2} \right)}, & \text{cylinder} \\ \frac{\alpha_1 \alpha_2}{\alpha_2 + \alpha_1(1 - \alpha_2) \left(\frac{r_1}{r_2} \right)^2}, & \text{sphere} \end{cases}, \quad (7.4b)$$

and the relation is simplified by replacing $R = R_g/M$, and $c_V = (\nu R_g)/2$ to:

$$h_g = h_{FM} = \frac{(1 + \gamma)\nu}{4\sqrt{2\pi}}(T_1 - T_2)P\sqrt{\frac{R_g M}{T}}\Lambda_{12}, \quad (7.5)$$

where

- P = pressure,
- T = temperature,
- M = molecular weight,
- R_g = the gas constant (8.314 J/mol-K),
- α = thermal accommodation coefficient,
- $\gamma = (c_P/c_V)$, ratio of specific heats, and
- ν = degrees of freedom (Table 7.1).

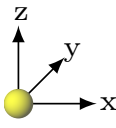
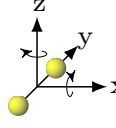
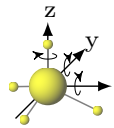
Here, Λ_{12} reduces to $\alpha/(2 - \alpha)$ between two parallel plates, and $\alpha/(1 + (1 - \alpha)r_1/r_2)$ for the curvilinear surfaces with the radii $r_1 < r_2$ for similar surfaces (i.e., $\alpha_1 = \alpha_2 = \alpha$).

Kennard indicated that the free-molecular expression is independent of the distance between the bounding surfaces. Later, inserting the expression of temperature jump distance into Eq. 7.5 yields

$$h_{FM} = \frac{\lambda_g}{g_1 + g_2}(T_1 - T_2), \quad (7.6)$$

while Garnier & Begej [25] approximated the expression to $h_{FM} = \lambda_g/(g_1 + g_2)$. Figure 7.4 shows the fill gas conductance in the free-molecular flow with respect to the pressure for the single-and the multi-component gases.

Table 7.1: Molal specific heat capacities and degrees of freedom for a number of gases at near room temperature [7]. The specific heat at constant pressure is related by $c_P = c_V + R_g$.

	monatomic	diatomic	polyatomic
	He, Ar, ...	N ₂ , H ₂ , ...	H ₂ O, ...
ν	3	5	6
c_V/R_g	$\frac{3}{2}$	$\frac{5}{2}$	$\frac{6}{2}$
$\gamma = c_P/c_V$	$\frac{5}{3}$	$\frac{7}{5}$	$\frac{4}{3}$
			

Transition flow

In the *transition flow* between slip and free-molecular flow, there is no standard method of analysis. A postulated method by Garnier & Begej [25] is to weight the gap conductance between the surrounding flows with the probability that a molecule could reach the opposite wall without intervening collisions, $e^{-1/Kn}$.

7.1.1 Temperature Jump Distance

The difference between the wall temperature and gas temperature at the wall is known as *temperature jump condition*, as illustrated in Figure 7.5. Poisson proposed that the discontinuity in temperature as

$$T_k - T_w = g \left(\frac{\partial T}{\partial n} \right), \quad (7.7)$$

where

T_w = wall temperature, and

T_k = temperature continued without change right up to the wall itself.

Kennard calculated the proportionality constant g by equating the excess energy carried by the incident stream to the total heat conducted across a parallel plane out in the gas. Kennard's expression for the temperature jump distance is

$$g = \left(\frac{2 - \alpha}{\alpha} \right) \sqrt{2\pi RT} \frac{\lambda}{(1 + \gamma)c_v P}. \quad (7.8)$$

Eq. 7.8 is generalized to the curvilinear coordinates for polyatomic gases as

$$g = \frac{\sqrt{8\pi}}{(1 + \gamma)\nu} \frac{\lambda}{P\Lambda_{12}} \sqrt{\frac{T}{R_g M}}, \quad (7.9)$$

by replacing $R = R_g/M$, and $c_v = (\nu R_g)/2$. The main reason behind the generalization of the expression is its incorrect use in the nuclear fuel performance codes for the diatomic/polyatomic gases as of the monatomic gases. The specific heat capacities are practically independent of temperature for the monatomic gases; therefore, calculations are simplified to neglect the dependence of specific heat on temperature. However, the specific heat capacities increase with temperature for all other gases [7].

$$\begin{aligned} \frac{\sqrt{8\pi/R_g}}{(1 + \gamma)\nu} &\approx 0.2173 \quad \text{for the monatomic gases,} \\ &\approx 0.1149 \quad \text{for the diatomic gases, and} \\ &\approx 0.1242 \quad \text{for the polyatomic gases.} \end{aligned} \quad (7.10)$$

at the room temperature. Note that 0.2173 in Eq. 7.9 for the monatomic gases is consistent with existing models in the literature [193, 194, 88, 195, 19].

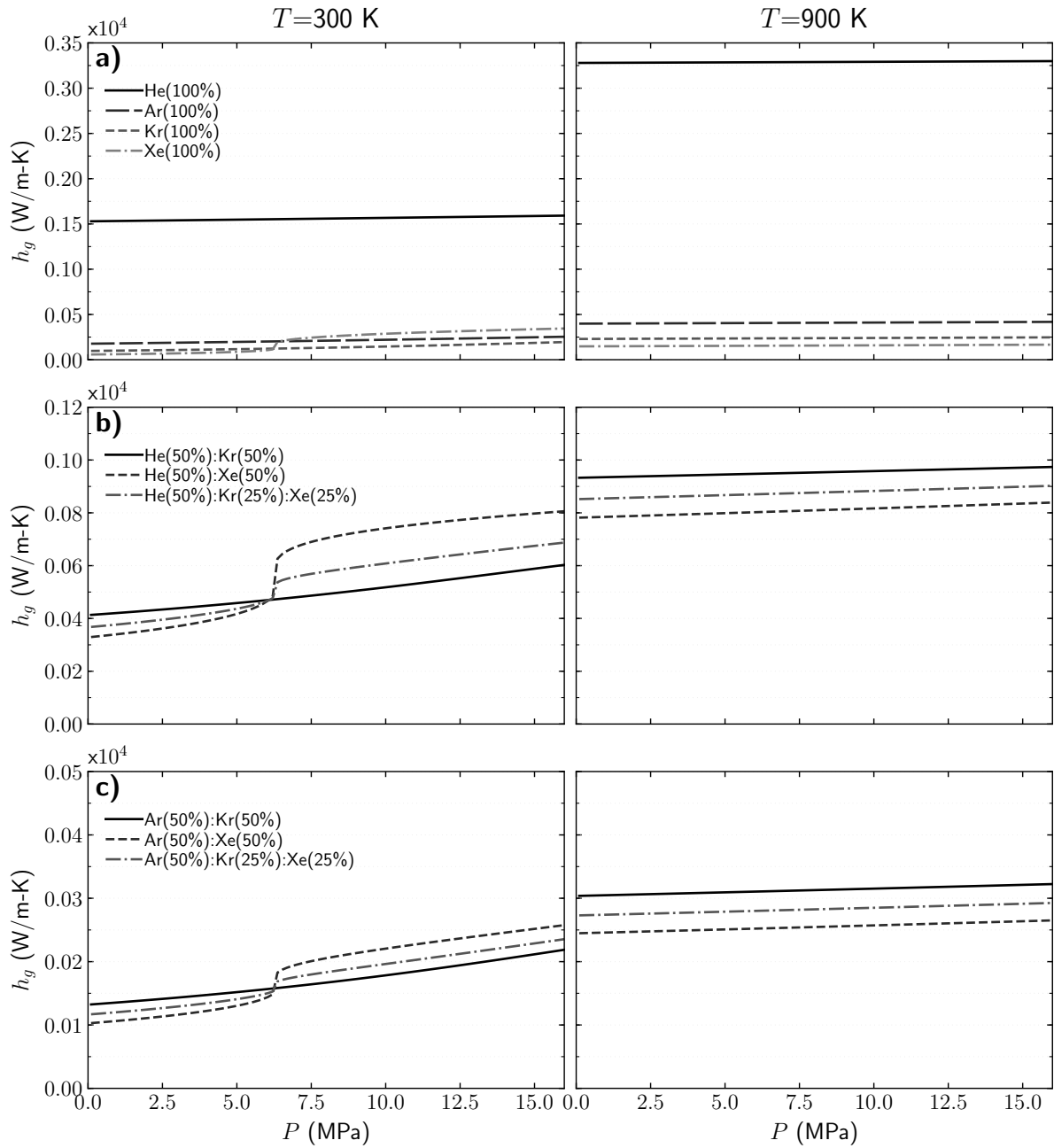


Figure 7.2: The fill gas conductance in the continuum flow with respect to the pressure for (a) the single-component gases, (b) the gas mixtures of helium with the gaseous fission products, and (c) the gas mixtures of argon with the gaseous fission products. The gas compositions are arbitrarily chosen. The fill gas temperature is set to 300 K (left column) and 900 K (right column). The plane geometry is chosen and $(g_1 + g_2) \approx 2g$. The gap distance is set to $100\ \mu\text{m}$, while $r_1 = 0.005\text{m}$.

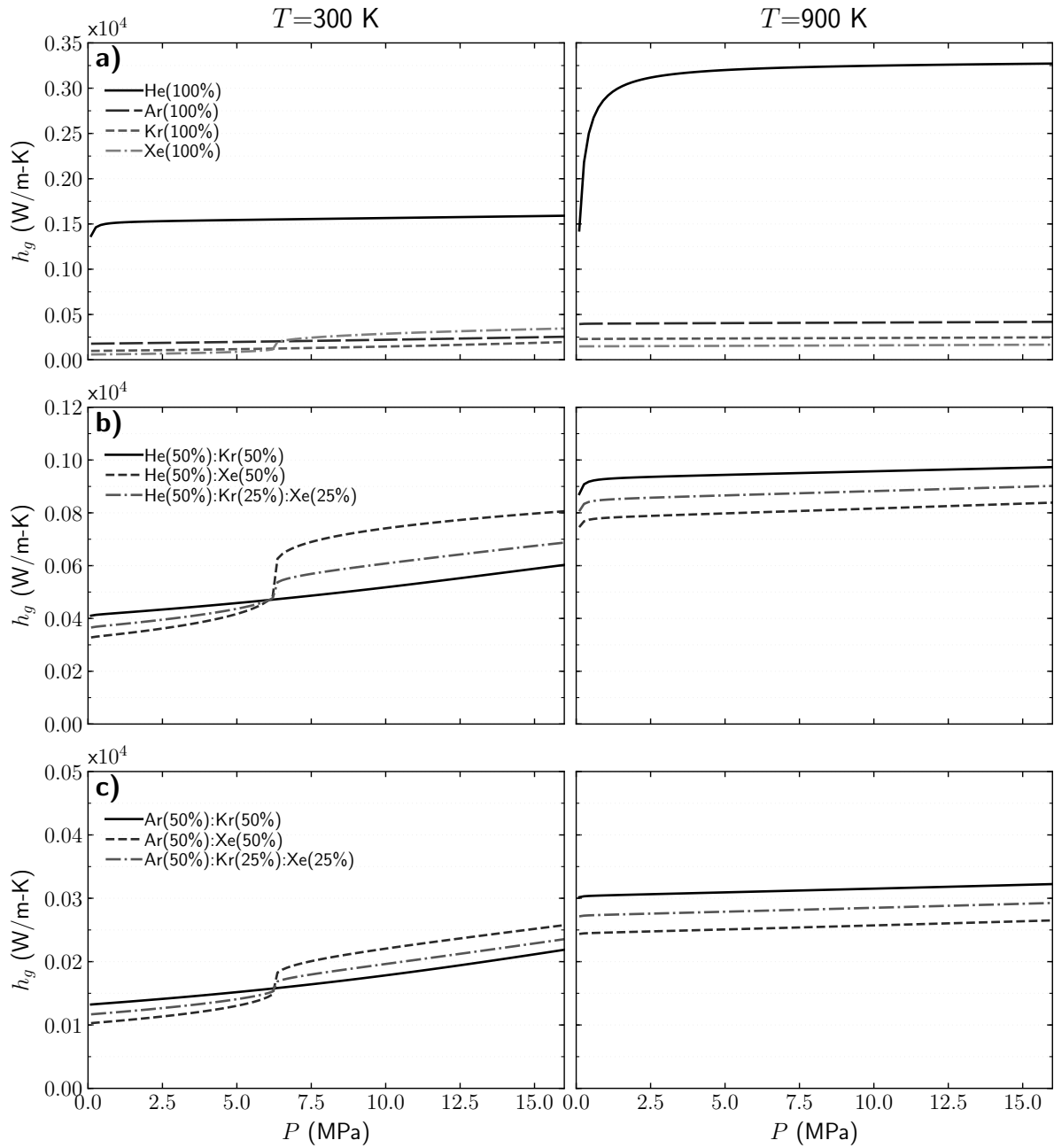


Figure 7.3: The fill gas conductance in the continuum flow with respect to the pressure for (a) the single-component gases, (b) the gas mixtures of helium with the gaseous fission products, and (c) the gas mixtures of argon with the gaseous fission products. The gas compositions are arbitrarily chosen. The fill gas temperature is set to 300 K (left column) and 900 K (right column). The plane geometry is chosen and $(g_1 + g_2) \approx 2g$. The gap distance is set to $100\ \mu\text{m}$, while $r_1 = 0.005\text{m}$.

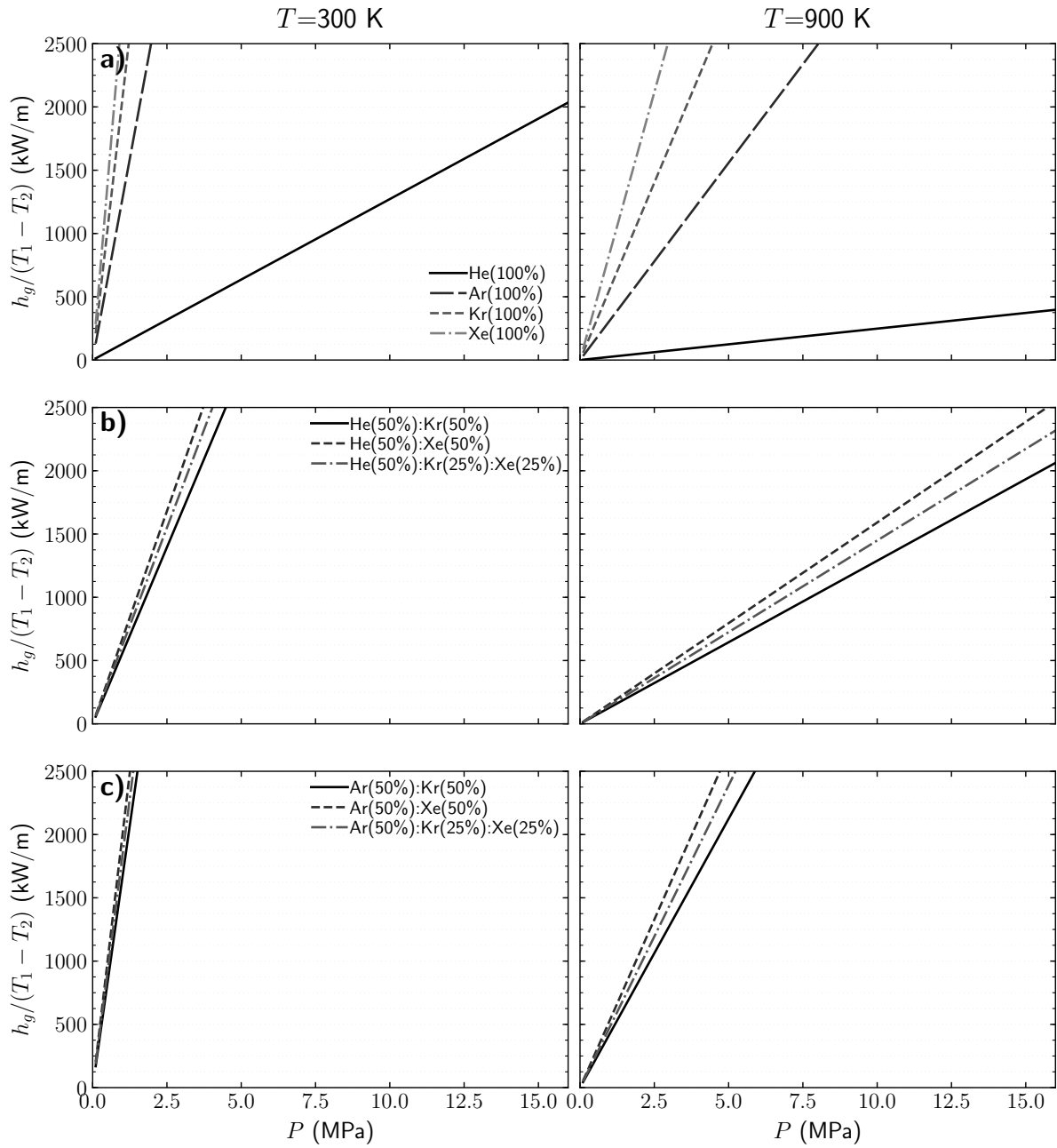


Figure 7.4: The fill gas conductance in the free-molecular flow with respect to the pressure for (a) the single-component gases, (b) the gas mixtures of helium with the gaseous fission products, and (c) the gas mixtures of argon with the gaseous fission products. The gas compositions are arbitrarily chosen. The fill gas temperature is set to 300 K (left column) and 900 K (right column). The plane geometry is chosen and $(g_1 + g_2) \approx 2g$. The gap distance is set to $100 \mu\text{m}$, while $r_1 = 0.005\text{m}$.

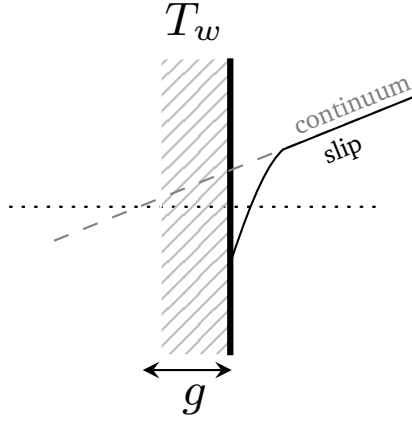


Figure 7.5: Schematic illustration of the temperature jump distance [18].

The temperature jump distances are compared at various temperatures and pressures for the monatomic inert gases in Figure 7.6 and their mixtures in Figure 7.7. Temperature jump distance changes abruptly for each inert gas less than 1 MPa, and order of the magnitudes are quite different since $g \propto 1/\sqrt{M}$. As the temperature increases, the jump distance increases as expected.

The temperature jump distance for a mixture is simply calculated by inserting the mixture properties into Eq. 7.9, which yields

$$g_m = \frac{\sqrt{8\pi}}{(1 + \gamma_m)\nu_m} \frac{\lambda_m}{P\Lambda_{12,mix}} \sqrt{\frac{T}{R_g M_m}}, \quad (7.11)$$

where $\Lambda_{12,mix}$ is calculated by replacing $\alpha = \alpha_m$ in Eq. 7.4b. The specific heats of a mixture can be calculated using classical thermodynamics [196, 197]. It is noticed that the literature models generally incorporated \sqrt{M} proportionally in the Kennard's expression (Eq. 7.8) because of accounting R as R_g . However, this is inconsistent with the theory and introduces significant error in gap conductance calculations once multi-component gases are involved. For this reason, the models [193, 194, 88, 195, 19] for g_m often differentiate from the single-component gases due to inclusion of the mixture molecular weight in the expression.

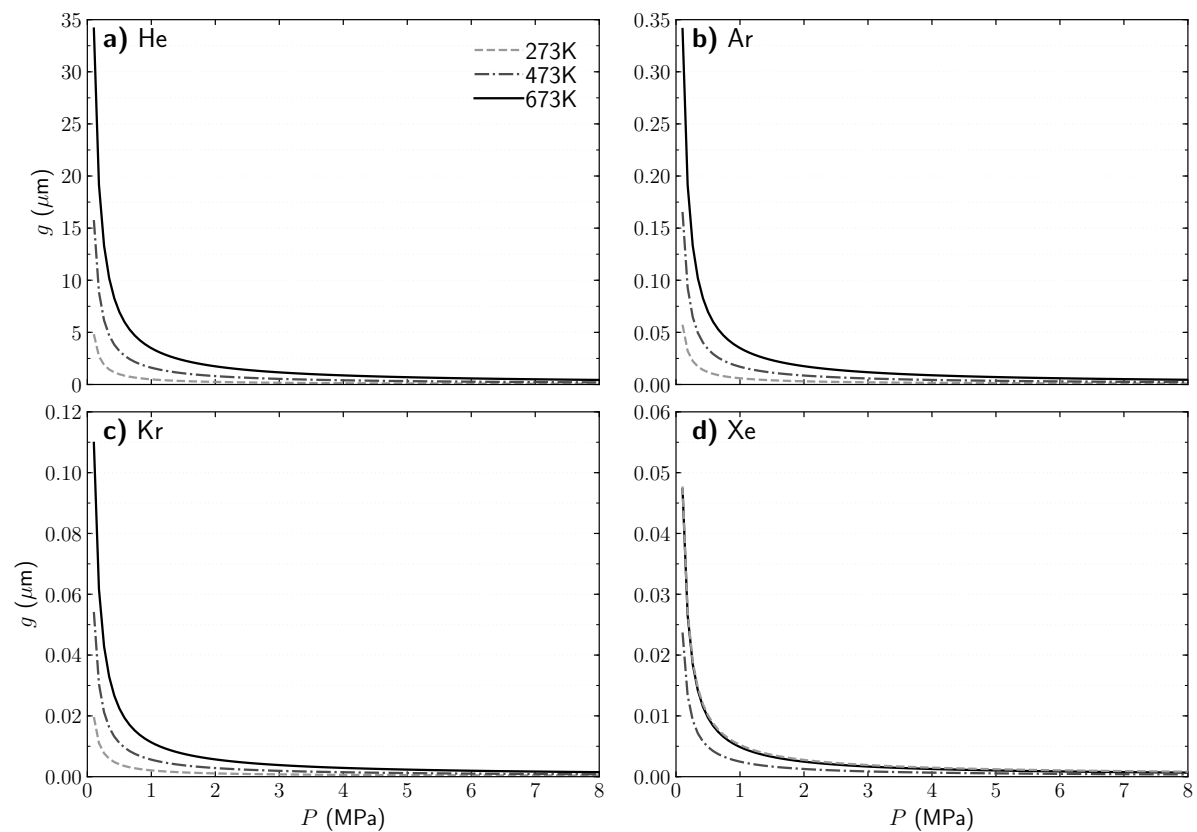


Figure 7.6: Temperature jump distance comparison at various gas pressures and temperatures for: (a) helium, (b) argon, (c) krypton, and (d) xenon.

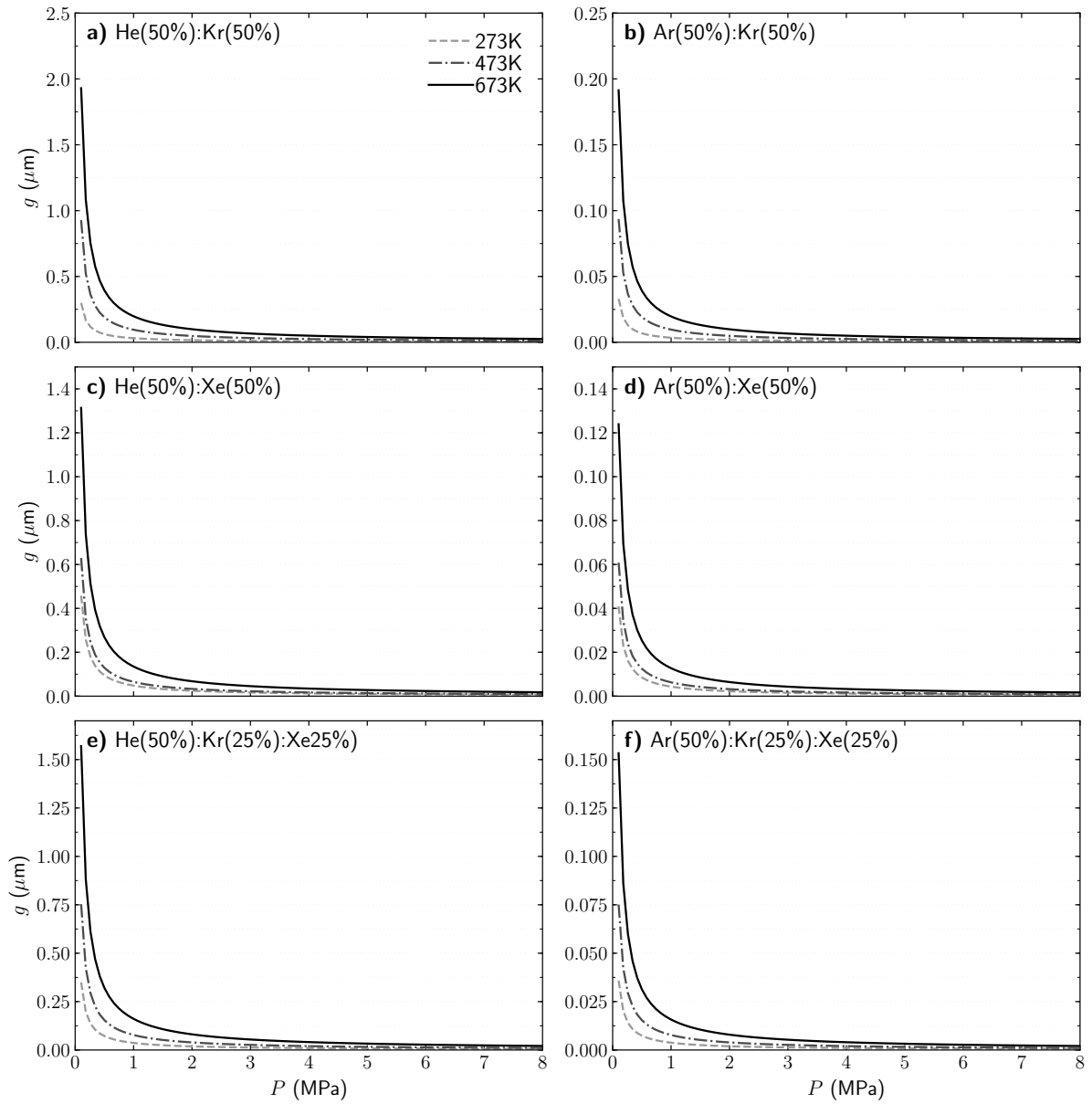


Figure 7.7: Temperature jump distance comparison at various gas pressures and temperatures for the gas mixtures of helium (left column) and argon (right column) with the gaseous fission products. The gas compositions are arbitrarily chosen.

7.1.2 Thermal Accommodation Coefficient

The accommodation coefficient is a measure of the interaction at a gas–solid interface and indicates the degree to which molecules are accommodated to the surface. Smoluchowski [198] performed experiments to study this effect in 1898. Later, Knudsen [199] introduced the accommodation coefficient, a as

$$E_i - E_r = a(E_i - E_w), \quad (7.12)$$

and preferred to attach a temperature to each of these streams of molecules as

$$T_i - T_r = \alpha(T_i - T_w), \quad (7.13)$$

where

- α = thermal accommodation coefficient,
- E_r = energy reflected at the reflection temperature T_r ,
- E_i = energy brought up by the incident stream at the incident temperature T_i , and
- E_w = energy carried away by the gas molecules that are assumed to leave as a Maxwellian stream at the wall temperature T_w .

Baule [200] proposed a closed-form expression for α considering interactions between two hard spheres. The first is an incident gas atom and the other is an initially stationary solid atom. Under these assumptions, the accommodation coefficient is $\alpha = 2\mu/(1 + \mu)^2$. There exist many models available in the literature; however, Goodman and Wachman's [201] formula is widely used. The formulation is altered as

$$\alpha(T) = 1 - \left(1 - \alpha_\infty \tanh \left[\frac{\sqrt{M_i T}}{\alpha_\infty} \theta_1 \right] \right) \exp \left(-\frac{\theta_2}{T} \right), \quad (7.14)$$

where

- M_i = molecular weight of the incident gas,
- M_s = molecular weight of the stationary solid,
- $\alpha_\infty = 2.4\mu/(1 + \mu)^2$, and
- $\mu = (M_i/M_s)$, ratio of the molecular weights.

In this study, Eq. 7.14 is calibrated to the literature data for interactions between selected monatomic inert gases and typical engineering surfaces. Model predictions are plotted with the data in Figure 7.8. The calibrated model parameters are shown on the plot in addition to the traditional approach used in nuclear fuel performance codes. The traditional approach is to estimate the thermal accommodation coefficient of a gas by interpolating based on its molecular weight between the thermal accommodation values of helium and xenon [19].

Mikami et al. [202] expressed the thermal accommodation coefficient of a gas mixture from the energy balance as

$$\alpha_m = \frac{\sum_{i=1}^n \frac{x_i \alpha_i}{\sqrt{M_i}}}{\sum_{i=1}^n \frac{x_i}{\sqrt{M_i}}}. \quad (7.15)$$

where the summation is over each individual component of the mixture.

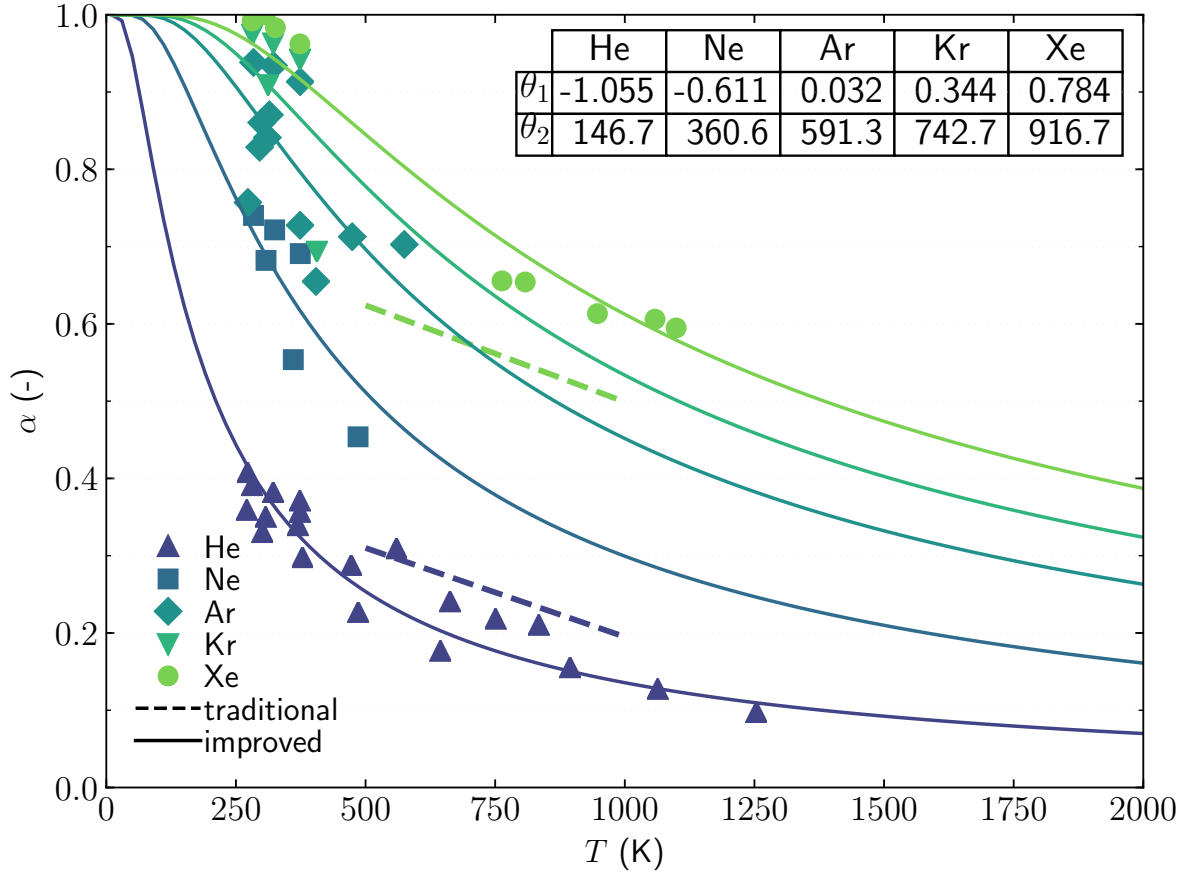


Figure 7.8: The thermal accommodation coefficient of the selected inert gases using the improved model (Eq. 7.14) and the traditional approach by Lanning and Hahn [19] for He and Xe for 500–1000 K according to Ullman data [20]. Note that the mass of the solid is set to a very large value (i.e., $M_s = 1 \times 10^5$ g/mol) in the calibration. Experimental data are extracted from Song and Yovanovich [21].

7.2 Solid Contact Conductance

When there is partial or complete contact between the fuel and cladding, an additional heat transfer term is necessary. The resistance at the interface is called constriction (or contact) resistance, R_c and is defined as

$$R_c = \frac{\Delta T_c}{(q/A_a)} = \frac{1}{h_c A_a}, \quad (7.16)$$

where

q = heat flow rate,
 ΔT_c = temperature drop to overcome the thermal resistance at the contact, and
 A_a = apparent area.

Originally, Kottler [203] used the classical electrical analogy to solve the constriction resistance in an electrical conductor exhibiting a discontinuous reduction in cross-section. Maxwell [204] indicated that the temperature difference plays the same role in the flow of heat as the electrical potential does in the theory of electric current; therefore, thermal resistances may be expressed mathematically in the same manner as electric resistances except that electrical resistivity is equivalent to the reciprocal thermal conductivity. Holm [205] extended the work of Kottler and solved the thermal constriction resistance for an isothermal circular contact area with a radius r_a on a flat surface of a semi-infinite body as

$$R_c = \left(\frac{1}{4r_a\lambda} \right), \quad (7.17)$$

and the total constriction resistance of two similar semi-infinite bodies as

$$R_c = \left(\frac{1}{2r_a\lambda} \right). \quad (7.18)$$

Clark and Powell [206] derived the total constriction resistance of two dissimilar semi-infinite bodies over the circular area as

$$R_c = \left(\frac{1}{4r_a\lambda_1} + \frac{1}{4r_a\lambda_2} \right) = \frac{1}{2a\Lambda}, \quad (7.19)$$

where

$$\Lambda = \left(\frac{2\lambda_1\lambda_2}{\lambda_1+\lambda_2} \right), \text{ harmonic mean of thermal conductivities of the surrounding solids.}$$

If the idealized contact geometry is assumed, the total parallel resistance of n_c solid contacts in a particular region can be approximated [207] as

$$R_c = \left(\frac{1}{2r_a\Lambda n_c} \right). \quad (7.20)$$

With the approximated constriction resistance on the contact spot, the contact conductance can be estimated once the apparent area is known.

Archard expressed the contact area when the deformation is truly elastic as $A_a \propto KW^{2/3}$, where K is a constant depending upon the local radius of curvature and elastic constants of the materials. Analogously, Archard correlated the contact area as $A_a \propto W/p_m$ where p_m is the flow pressure or hardness of the softer material when the asperities are permanently deformed *plastically* [208, 209]. The relationship between the apparent area and the contact area can be generalized to the form of

$$\frac{A_a}{A} \propto \left(\frac{W}{H} \right)^n, \quad (7.21)$$

where

W = load on the contact interface,
 H = Meyer's hardness of the softer material, and
 n = index of departure from elastic deformation (e.g., $n=0$ for elastic, $n=1$ for plastic).

As indicated by Bowden and Tabor [210], a plastic deformation mechanism is postulated since the real area of contact is nearly proportional to the load for all types and shapes of practical surface irregularities. This is the reason why early thermal contact models [211, 212, 213, 214, 215] in the literature assumed this model function form. Thus, inserting the total contact area (i.e., $A_a = \pi r_a^2 n_c$) in Eq. 7.16 yields

$$h_c = \frac{2r_a \Lambda n_c}{A_a} = C \frac{\Lambda}{r_a} \left(\frac{W}{H} \right). \quad (7.22)$$

Determination of contact shapes, deformation of surface irregularities, or number of contact spots is neither known nor accurately measurable in nuclear reactor conditions. Due to the difficulty of determining these quantities, they have attracted the attention of many researchers in the past [216, 217, 218, 100, 219, 220, 221, 222, 223, 224]. Some researchers attempted to develop approximate analytical models for idealized contact shapes [211, 225, 214, 226, 227, 207, 228, 229, 215, 230, 231, 232, 233, 234, 235, 236]. However, it is still difficult to accurately describe the surface characteristics of operating nuclear fuel rods or to model these characteristics in nuclear fuel performance codes. For this reason, approximated gap closure relations [237, 238, 52] are used in nuclear fuel performance modeling. The Ross-Stoute model [52] is one common solid contact model where r_a is introduced into the correlation as a function of the surface roughness ξ . Their justification for the replacement is that the contact area is nearly constant at moderate and high pressures [239, 240, 241], and it is therefore reasonable to correlate $r_a \propto \sqrt[4]{\xi_1^2 + \xi_2^2}$ according to data from Ascoli and Germagrolì [241]. Then, they calibrated the model on heat transfer measurements between the common reactor materials (uranium dioxide and Zircaloy-2). More discussion is provided in the following chapter that is related to the contact conductance modeling in nuclear applications.

7.3 Thermal Radiation

The heat transfer due to thermal radiation is calculated using the expression of Bird et al. [242]—which assumes two infinite parallel gray surfaces, where radiation leaving the first body and is directly intercepted by the second body—as

$$h_r = \frac{\sigma_{SB}(T_1^2 + T_2^2)(T_1 + T_2)}{\frac{1}{\varepsilon_1} + \left(\frac{r_1}{r_2}\right)^b \left(\frac{1}{\varepsilon_2} - 1\right)}, \quad (7.23)$$

where

- σ_{SB} = Stefan–Boltzmann constant (5.67×10^{-8} W/m²K⁴),
- ε = emissivity, and
- b = exponent to represent the ratio of areas (0.0 for planar, 1.0 for cylindrical, 2.0 for spherical).

7.4 Chapter Summary

An overview of the theoretical considerations and the underlying assumptions of gap conductance modelling is provided in addition to the traditional modeling approaches in nuclear fuel performance codes. First, the models are generalized to curvilinear coordinates for diatomic/polyatomic gases due to their previous incorrect use in nuclear fuel performance codes. Second, the expressions for temperature jump distance and thermal accommodation coefficients are made consistent with kinetic theory for both single- and multi-component gases. It is noticed that the literature models for the temperature jump distance generally incorporate square-root of the molecular weight proportionally in the Kennard's expression; however, this is inconsistent with the theory and introduces significant error in gap conductance calculations once multi-component gases are involved. Furthermore, the thermal accommodation coefficient is updated with the Goodman and Wachman formulation and a generalized model is calibrated with the literature data for interactions between monatomic inert gases and typical engineering surfaces. This allows a better representation of real world data. Lastly, the fill gas thermal conductivity is updated to include its dependence on rod internal pressure, which is ignored in the nuclear fuel performance codes. However, the pressure dependence is important when the initial fill gas is not helium or replaced by lower conductivity gaseous fission products during the reactor's operation.

Hitherto, this chapter focused on the gap conductance theory. In the next chapter, a conventional gap conductance model is optimized for uranium dioxide-Zircaloy interfaces to be used for practical purposes in nuclear fuel performance codes. Additionally, an uncertainty quantification study is performed to estimate parameter uncertainty of the optimized model.

CHAPTER

8

OPTIMIZED GAP CONDUCTANCE MODEL FOR UO_2 -ZIRCALOY INTERFACES

The gap conductance is calculated considering three summed heat paths [23]: fill gas conductance, direct thermal radiation, and solid contact conductance. The first two can be estimated theoretically; however, the thermal contact model requires knowledge about the contact shape, deformation mechanism of surface irregularities, and number of contact spots. These quantities are neither known nor measurable in an operating nuclear reactor. Due to this difficulty, the importance of the contact model has attracted the attention of many researchers [216, 217, 218, 100, 219, 220, 221, 222, 223, 224]. Some researchers have developed approximate analytical models for idealized contact shapes [211, 225, 213, 214, 226, 227, 207, 228, 229, 215, 243, 230, 231, 232, 233, 234, 235, 236]; however, difficulty arises from describing the surface characteristics of operating nuclear fuel. For this reason, approximate gap closure relations [237, 238, 52] are used in nuclear fuel performance codes.

The model conventionally used to calculate heat transfer across the fuel-to-cladding gap in light water nuclear reactors is a modified version of the Ross-Stoute model [52]. The model was modified to include gap distance in the formulation, which introduced additional uncertainty because the model parameters were not adjusted after the modification. In this study, this conventional model is optimized for uranium dioxide-Zircaloy interfaces using experimental data at high pressure for single- and multi-component gases. Then, model uncertainties are estimated by performing uncertainty quantification. Note that the gap conductance model has aleatory uncertainty due to unknowable geometry and epistemic uncertainty due to uncertain model parameters. Analysts often apply large uncertainties to compensate for these large inaccuracies,

for example one study applied a fifty percent uncertainty in the gap conductance [149].

In this chapter, the model conventionally used in nuclear fuel performance codes to conduct heat across the fuel-cladding gap is optimized for uranium dioxide–Zircaloy interfaces [244]. The conventional model is provided in Section 8.1. Methods to estimate parameter uncertainty of the model are described in Section 8.2. Optimization results and discussion are given in Section 8.3 with quantified uncertainties. The concluding remarks and future work are provided at the end.

8.1 Modeling

The Ross-Stoute model [52] is a commonly used gap conductance model for two solids in contact (Eq. 8.1); however, its use in fuel performance codes deviates from the original form. In most applications, gap distance d between two solid bodies is added to the formulation (Eq. 8.2).

$$h_{gap} = \frac{\lambda_g}{1.2(\xi_1 + \xi_2) + (g_1 + g_2)} + \frac{10.0\Lambda}{\sqrt[4]{0.5(\xi_1^2 + \xi_2^2)}} \left(\frac{W}{H} \right), \quad (8.1)$$

$$h_{gap} = \frac{\lambda_g}{d + 1.2(\xi_1 + \xi_2) + (g_1 + g_2)} + \frac{10.0\Lambda}{\sqrt[4]{0.5(\xi_1^2 + \xi_2^2)}} \left(\frac{W}{H} \right), \quad (8.2)$$

where

λ_g = gas thermal conductivity (W/m-K),

d = gap distance (m),

ξ = surface roughness (m) that is defined as a one-dimensional parameter to represent the mean deviation of surface irregularities,

g = temperature jump distance (m),

$\Lambda = \left(\frac{2\lambda_1\lambda_2}{\lambda_1 + \lambda_2} \right)$, harmonic mean of thermal conductivities of the surrounding solids (W/m-K),

W = load on the contact interface (N/m²), and

H = Meyer's hardness of the softer material (N/m²).

Eq. 8.2 uses the actual gap distance, which introduces additional uncertainties, since the parameters in the original model are not adjusted to account for this change. To understand the sources of uncertainty, the model form is parameterized for optimization as

$$h_{gap} = \frac{\lambda_g}{d + \theta_1(\xi_1 + \xi_2) + (g_1 + g_2)} + \frac{\theta_2\Lambda}{\sqrt{\xi_1^2 + \xi_2^2}} \left(\frac{W}{H} \right), \quad (8.3)$$

with the model parameters, $\theta = \{\theta_1, \theta_2\}$ to be estimated. The two terms on right side of the equation are the fill gas conductance and the thermal contact conductance under a static load, respectively. The latter is divided by $\sqrt{\xi_1^2 + \xi_2^2}$ instead of $\sqrt[4]{\xi_1^2 + \xi_2^2}$ in order to have a unitless model parameter, θ_2 . Note that the radiation term is not included due to its negligible contribution in the temperature range of interest.

Considering one-dimensional heat transfer across the gap, it is possible that θ_1 can be estimated analytically from

$$d + \theta_1(\xi_1 + \xi_2) = \frac{1}{(x_2 - x_2^0)} \int_{x_2^0}^{x_2} [f_1(\mathbf{x}) - f_2(\mathbf{x})] dx_2, \quad (8.4)$$

with the computed area between the surface profiles, $f_i(\mathbf{x})$ for $i = 1, 2$ (Figure 8.1).

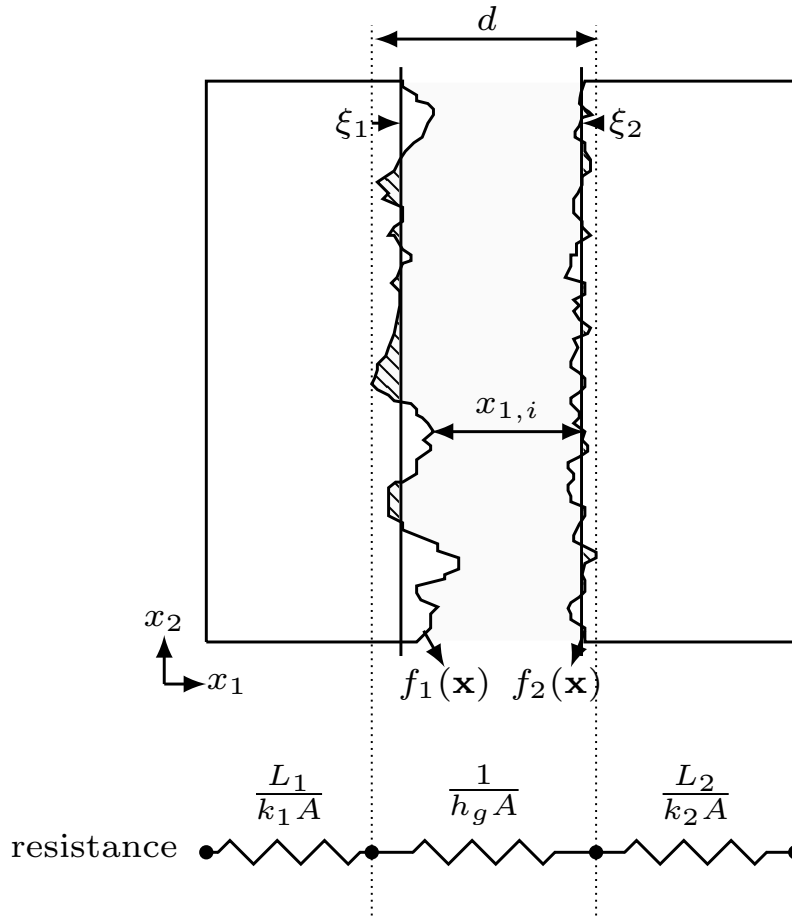


Figure 8.1: Schematic illustration of gap between two solid bodies along with equivalent circuit for the system (not to scale).

Physical interpretation of the model parameters can be listed under two gap configurations:

- *open gap* ($\theta_1 \neq 0; \theta_2 = 0$), θ_1 becomes -1 from the analytical expression because the integral reduces to $(d - (\xi_1 + \xi_2))(x_2 - x_2^0)$ on the right side of Eq. 8.3. Note that the

integral in Eq. 8.4 reduces to $d(x_2 - x_2^0)$ in case of the open gap with smooth surfaces (i.e., $\xi_i = 0$ for $i = 1, 2$). Additionally, note that the description of the gap distance will define the sign of the model parameter θ_1 .

- *closed gap* ($\theta_1 \neq 0; \theta_2 \neq 0$), θ_1 provides information regarding the fill gas conductance in the vicinity of surface irregularities and indirect information about the contacts, while θ_2 indicates contact areas at the interface.

8.2 Methods

A schematic representation of the optimization process and the uncertainty propagation employed is illustrated in Figure 8.2. The experimental data are used in calibration of the computational model and uncertainty bounds from the optimization are propagated through a statistical black box uncertainty propagation method to estimate the computational model uncertainty. The experimental data are described in Section 8.2.1. Calibration and uncertainty quantification methods are outlined in Section 8.2.2 and Section 8.2.3, respectively.

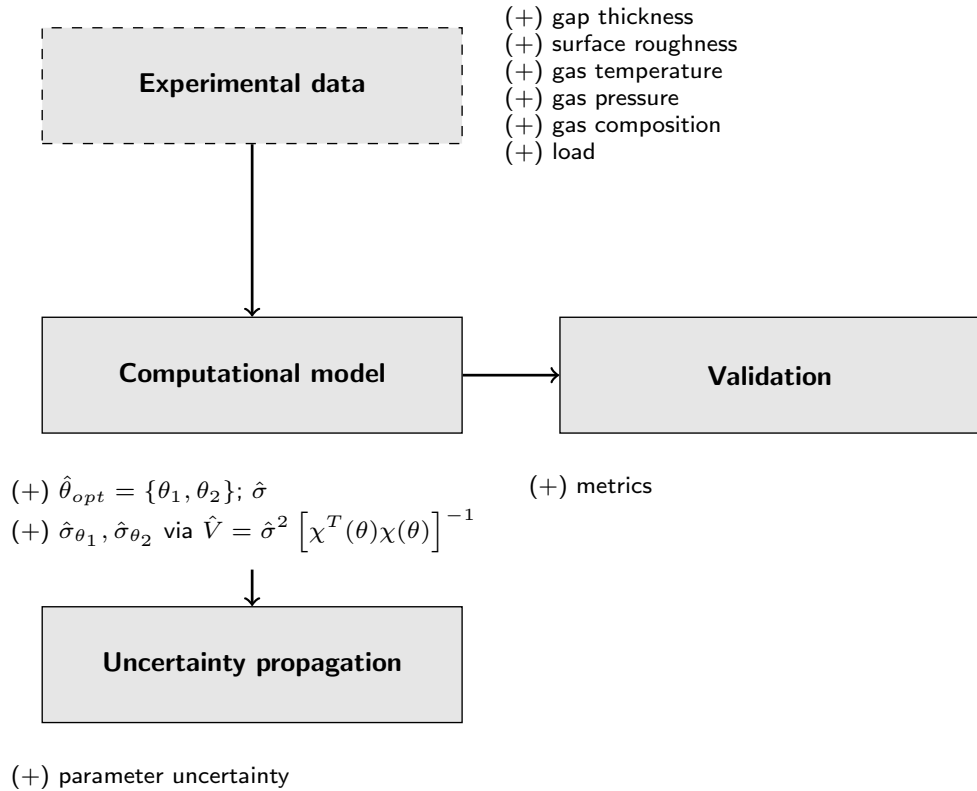


Figure 8.2: Schematic illustration of analysis including model optimization and uncertainty quantification to estimate uncertainty of the computational model.

8.2.1 Experimental Data

Garnier and Begej performed ex-reactor experiments in 1979–80 at Pacific Northwest National Laboratory to determine contact conductance between depleted uranium dioxide and Zircaloy-4 interfaces at low [25] and at high pressure [22]. The latter is chosen for calibration, since the pressure range is more representative of nuclear fuel. A transient measurement technique was employed in which a signal detector was used to measure the thermal energy transmitted through a sample pair due to a heat pulse. The sample pair were either in contact or physically separated. In the data, the solids are in contact for a non-zero load, in which the gap thickness does not necessarily need to be zero. The experiments were performed between two parallel circular plates with varying local distances between the sample pairs and varying surface characteristics. Fill gas between the sample pair was composed of He and Ar, or of He–Ar and He–Xe gas pairs at temperatures ranging from 283 to 673 K. An optical height gauge was used in the experiments to determine the average mean-plane of separation between the pairs. The average gap thickness is calculated as the arithmetic mean of the local distances at the measurement points. The gap thickness was 5.9 μm . The load applied was varied from 0 to 1300 N/m² (i.e., light contact) in their experiments.

8.2.2 Calibration

The frequentest approach is utilized for the calibration of the gap conductance model. Array elements of the sensitivity matrix, $\hat{\chi}_{ij}(= \partial f_i(\hat{\theta})/\partial \theta_j)$ of the model function are computed numerically as

$$\begin{aligned} \frac{\partial f(\hat{\theta})}{\partial \theta_1} &= -\frac{\lambda_g(\xi_1 + \xi_2)}{\left[d + \hat{\theta}_1(\xi_1 + \xi_2) + (g_1 + g_2)\right]^2}, \\ \frac{\partial f(\hat{\theta})}{\partial \theta_2} &= \frac{\Lambda}{\sqrt{\xi_1^2 + \xi_2^2}} \left(\frac{W}{H}\right). \end{aligned} \quad (8.5)$$

In the calibration, properties/models are dependent on gas conditions (i.e., temperature, pressure, gas composition etc.); therefore, they are fixed for clear examination of the model function forms. Details regarding the models can be found in the first part of this paper [23]. The following are taken into consideration:

- (i) measured fuel/clad thermal conductivities [22];
- (ii) gas thermal conductivity as a function of temperature and pressure $\lambda_g(T, P)$;
- (iii) temperature jump distance for plane geometry for similar surfaces ($\alpha_1 = \alpha_2 = \alpha$);

$$g = 0.2173 \left(\frac{2 - \alpha}{\alpha}\right) \frac{\lambda}{P} \sqrt{\frac{T}{M}}, \quad (8.6)$$

- (iv) approximating $(g_1 + g_2) \approx 2g$; and

- (v) Meyer’s hardness of the cladding, H (in N/m^2) as a function of temperature, T (in K) that is calibrated based on experimental data [245]:

$$H = 3.337 \times 10^9 \exp(-2.795 \times 10^{-5}T). \quad (8.7)$$

In Figure 7.6, temperature jump distances are compared at various temperatures and pressures, where order of magnitudes in the temperature jump distance deviate significantly for the selected inert gases.

8.2.3 Uncertainty Quantification

Garnier and Begej [22] calculated uncertainty in the gap conductance by perturbing data uncertainties on measurable state variables in the model according to Kline and McClintock [246]. In this study, only parameter uncertainty is considered and uncertainty in the state variables is neglected. Dakota [70] is used to perform a statistical black box uncertainty propagation with 1,000 samples. The model parameters are randomly sampled as marginal normal distributions (determined from the calibration in Section 8.2.2), where the correlation between parameters is not treated. Uncertainties in the model parameters and the observational error, $\varepsilon_i \sim \mathcal{N}(0, \hat{\sigma})$ are propagated in the computational model as

$$y_i = f(x_i, \hat{\theta}) + \varepsilon_i, \quad (8.8)$$

where $f(x_i, \hat{\theta})$ is the computational model (Eq. 8.3) in this study. Estimated parameter uncertainty of the calibrated model is provided on the plots.

8.3 Results & Discussion

This section includes predictions from the aforementioned models against the experimental data for non-contact in Section 8.3.1 and contact in Section 8.3.2. Differences between the predictions and the observations are quantified in terms of the validation metrics (Section 2.7).

8.3.1 No Contact Results & Discussion

In Figure 8.3, model predictions are compared against the experimental data for helium. The validation metrics are provided in Table 8.1. The agreement is found to be within an average deviation of 61.6% using the calibrated model, 41.2% using the analytically derived expression (i.e., $\theta = \{-1, 0\}$ in Eq. 8.3), 234.8% using the original Ross-Stoute model, and 45.2% using the modified Ross-Stoute model. Estimated parameter uncertainty, $\hat{\sigma}_M$ of the calibrated model is about 66.8% for no contact between the solids.

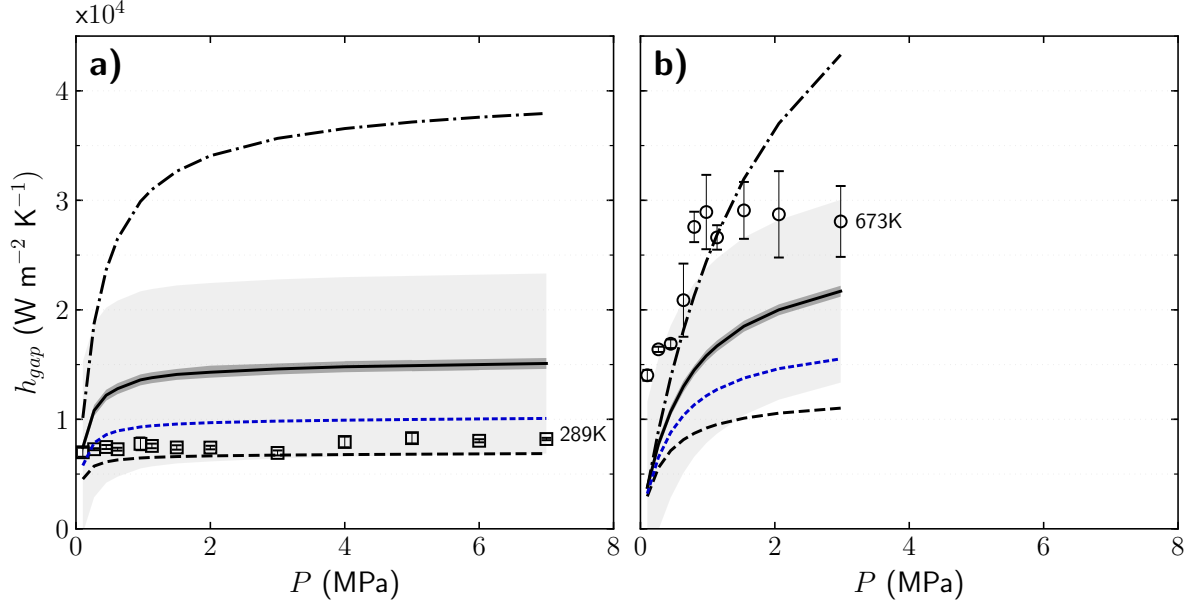


Figure 8.3: Model fit for helium at (a) 289 K, and (b) 673 K using the calibrated model (—) with $\hat{\theta} = \{-2.406 \pm 0.496, 0\}$ and $\hat{\sigma} = 8069.009 \text{ W/m}^2\text{-K}$, the Ross-Stoute model (---), the modified Ross-Stoute model (---), and analytically derived expression (.....) with $\theta = \{-1, 0\}$. The grey areas in the plot correspond to $\pm\hat{\sigma}_M$ around the mean (—) and 95% confidence interval (—). The data are from Garnier and Begej [22].

Table 8.1: Non-contact results for the gap conductance, h_{gap} for helium in Figure 8.3.

	$\{\theta_1, \theta_2\}$	d (W/m ² -K)	d_M (W/m ² -K)	RMSE (W/m ² -K)	rRMSE (%)
		<i>the original Ross-Stoute model (Eq. 8.1)</i>			
He	—	8.91	35.40	1.858	234.8
		<i>the modified Ross-Stoute model (Eq. 8.2)</i>			
He	—	5.04	16.98	1.050	45.2
		<i>the calibrated model (Eq. 8.3)</i>			
He	$\{-2.406, 0\}$	3.78	16.65	0.789	61.6
He	$\{-1.000, 0\}$	4.20	15.10	0.876	41.2

8.3.2 Contact Results & Discussion

To understand sources of uncertainties in the model parameters, analysis is started from the calibration of single-component gases, and enhanced to include multi-component gases. Results and discussions are provided for the single-component gases in Section 8.3.2 and the multi-component gas mixture in Section 8.3.2. Later, a generalized model is calibrated combining all of the data in Section 8.3.2.

Single-component gases

In Figure 8.4 and Figure 8.5, model predictions are compared against to the experimental data for helium and argon, respectively. Calibrations are performed separately for each gas. The validation metrics are provided in Table 8.2. The best agreement is found to be within an average deviation of 27.3% for He, and 5.9% for Ar using the calibrated model. Estimated parameter uncertainty, $\hat{\sigma}_M$ of the calibrated model is about 27.1% for He, and 18.5% for Ar. The original Ross-Stoute model more accurately fits the data than the modified Ross-Stoute model. The differences between the predictions and the data are relatively large for helium, which is likely because the assumptions in Eq. 8.3 do not sufficiently describe the appropriate heat transfer regime [23].

Multi-component gas mixture

In Figure 8.6, model predictions and the experimental data are compared for a binary mixture of helium and argon. The calibration is performed for this data set. The best agreement is found to be 3.3% with the data using the calibrated model, while the agreement is 9.7% for the original Ross-Stoute model, and 36.7% for the modified Ross-Stoute model. Estimated parameter uncertainty, $\hat{\sigma}_M$ of the calibrated model is about 5.9%. Note that the slope at lower pressures agrees well with the data set, which indicates that the temperature jump distance is calculated correctly in addition to the mixture properties. Also, the results indicate that the heat transfer regime is appropriately represented with the conventional model.

Combined data

It is noticed that $2g \gg d$ for helium (Figure 7.6) in the data set, which is not physical and introduces additional uncertainties in the calibration. For this reason, the temperature jump distance is eliminated from the model (i.e., continuum assumption) by setting $g = 0$ in Eq. 8.3. The calibration is performed with the all data included for similar temperature ranges of interest at the pressure that is limited to be ≥ 0.3 MPa. Note that the initial rod internal pressure ranges from 0.3 to 3.45 MPa in light water reactors [24].

In Figure 8.7, gap conductance difference between the experimental data and predictions from the aforementioned models are plotted for He, Ar, and He–Ar gas pair. The best agreement is found to be within an average deviation of 17.7% for He, 3.3% for Ar, and 7.3% for

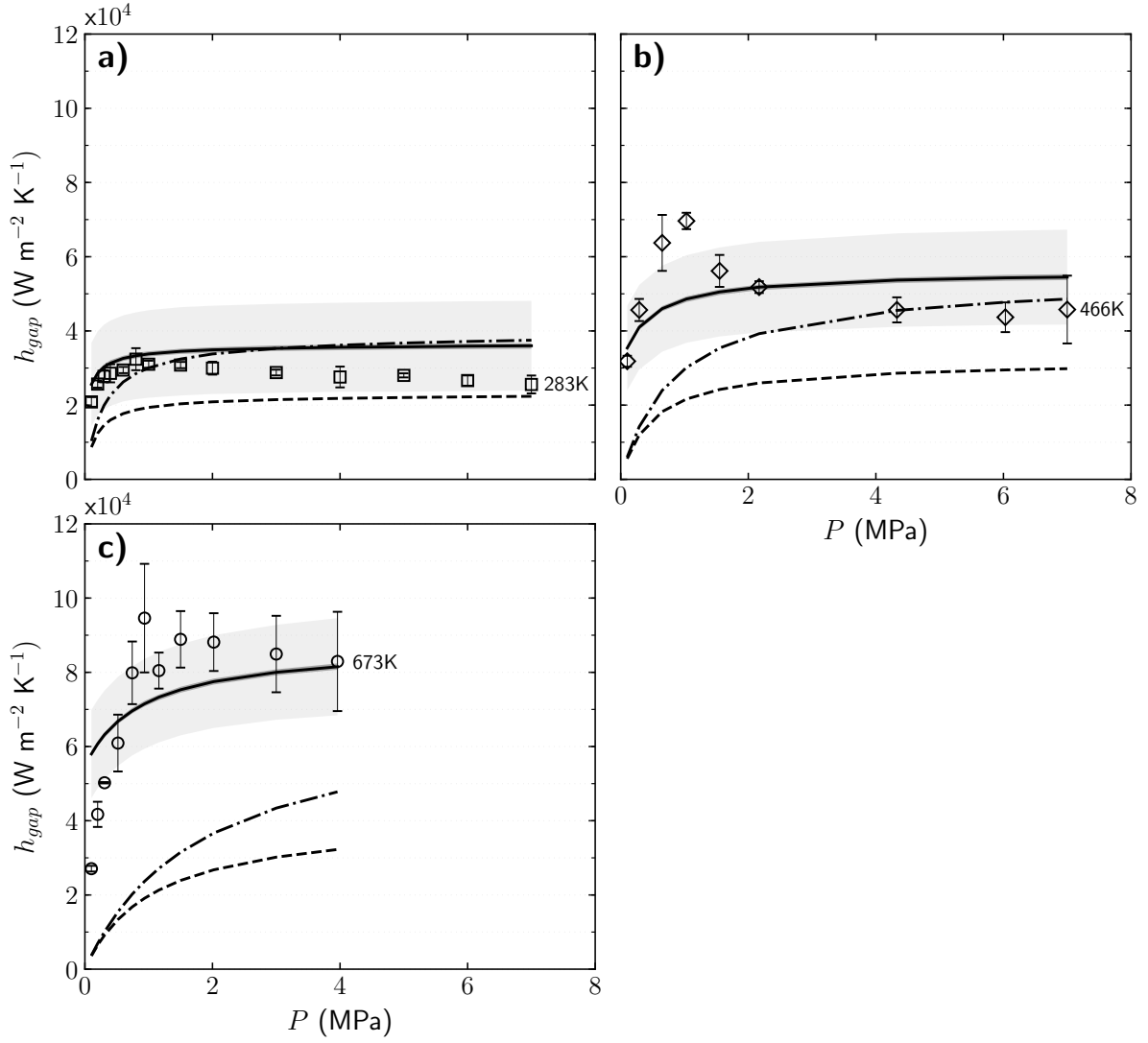


Figure 8.4: Model fit for helium at (a) 283 K, (b) 466 K, and (c) 673 K using the calibrated model (—) with $\hat{\theta} = \{1.807 \pm 0.566, 168.754 \pm 13.552\}$ and $\hat{\sigma} = 11208.501 \text{ W/m}^2\text{-K}$, the Ross-Stoute model (---), and the modified Ross-Stoute model (- - -). The grey areas in the plot correspond to $\pm \hat{\sigma}_M$ around the mean (—) and 95% confidence interval (—). The data are from Garnier and Begej [22].

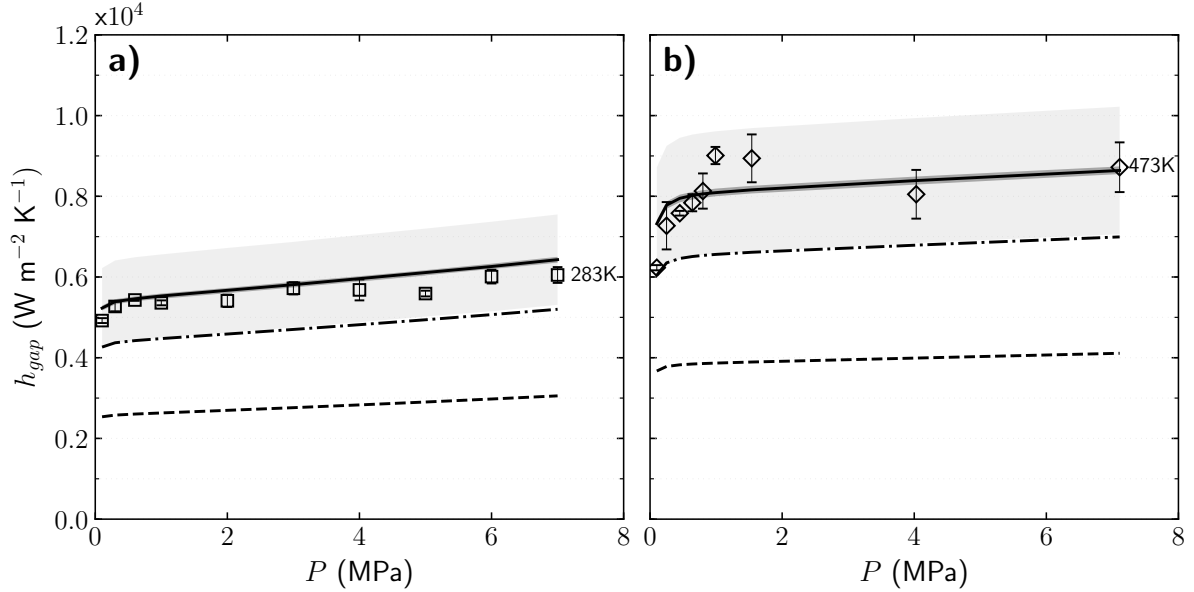


Figure 8.5: Model fit for argon at (a) 283 K, and (b) 473 K using the calibrated model (—) with $\hat{\theta} = \{0.140 \pm 0.121, -0.277 \pm 5.468\}$ and $\hat{\sigma} = 463.261 \text{ W/m}^2\text{-K}$, the Ross-Stoute model (---), and the modified Ross-Stoute model (- - -). The grey areas in the plot correspond to $\pm \hat{\sigma}_M$ around the mean (■) and 95% confidence interval (—). The data are from Garnier and Begej [22].

their binary mixture using the calibrated model. Though the largest error is observed for He, its contribution to the gas mixture is negligible. At the end, the overall agreement including the all data is found to be 11.8% for the calibrated model, 21.0% for the Ross-Stoute model, and 40.9% for the modified Ross-Stoute model. Estimated parameter uncertainty, $\hat{\sigma}_M$ of the calibrated model including the combined data is about 38.5%. Furthermore, a *cross-validation* study is performed to assess how results of the calibrated model will generalize to an independent data set, He(89.4%):Xe(10.6%) gas pair. The agreement is found to be: 27.9% for the calibrated model from the combined data; 37.2% for the original Ross-Stoute model; and 36.2% for the modified Ross-Stoute model. The results indicate that additional data are required to explore the gap conductance model for gas mixtures of helium and/or argon with gaseous fission products such as xenon and krypton at high pressures and temperatures.

When the model is calibrated to each gas separately, estimated parameter uncertainty of the model is about 27.1% for He, 18.5% for Ar, and 5.9% for He-Ar gas pair for the solids in contact. When all data are combined, the parameter uncertainty is estimated about 38.5%. This is slightly larger because it is difficult to generalize a model due to:

1. inaccurate estimation of contact characteristics (e.g., number of solid contacts, deformation mechanism of surface irregularities, contact shapes) that differentiate for each experimental setup and various conditions,
2. non-physical ratio of temperature jump distance to the gap distance, g/d ,

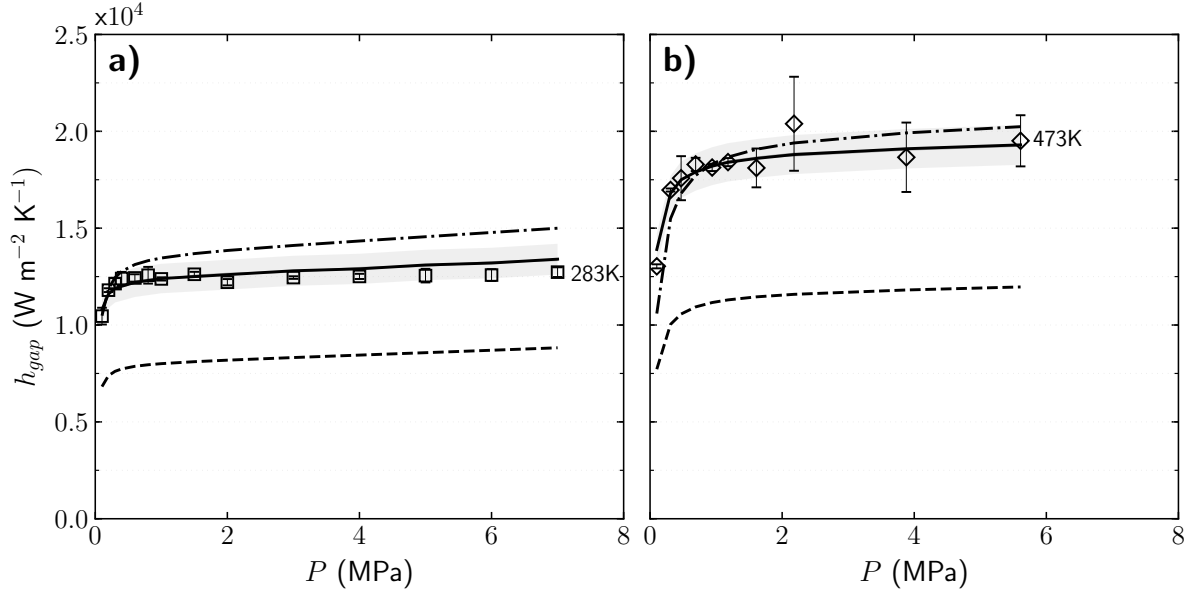


Figure 8.6: Model fit for He(51.79%):Ar(48.21%) gas pair at (a) 283 K and (b) 473 K using the calibrated model (—) with $\hat{\theta} = \{0.914 \pm 0.082, 29.377 \pm 3.361\}$ and $\hat{\sigma} = 521.531 W/m^2-K$, the Ross-Stoute model (---), and the modified Ross-Stoute model (-.-). The grey areas in the plot correspond to $\pm \hat{\sigma}_M$ around the mean (■) and 95% confidence interval (■). The data are from Garnier and Begej [22].

3. insufficient description of the appropriate heat transfer regime with the assumed model form of the computation model, and
4. inclusion of pressure-effect in the fill thermal conductivity because the thermal conductivity of inert gases besides helium are dependent on the pressure while helium is independent, which will introduce complications in the model calibration.

8.4 Chapter Summary

The conventional form of the gap conductance model in nuclear fuel performance is optimized for uranium dioxide-Zircaloy interfaces using the available literature data at high pressure for the single- and multi-component gases of helium and argon. Validation results indicated that the optimized model results in reduction of fuel temperatures due to the enhanced heat transfer across the gap [247].

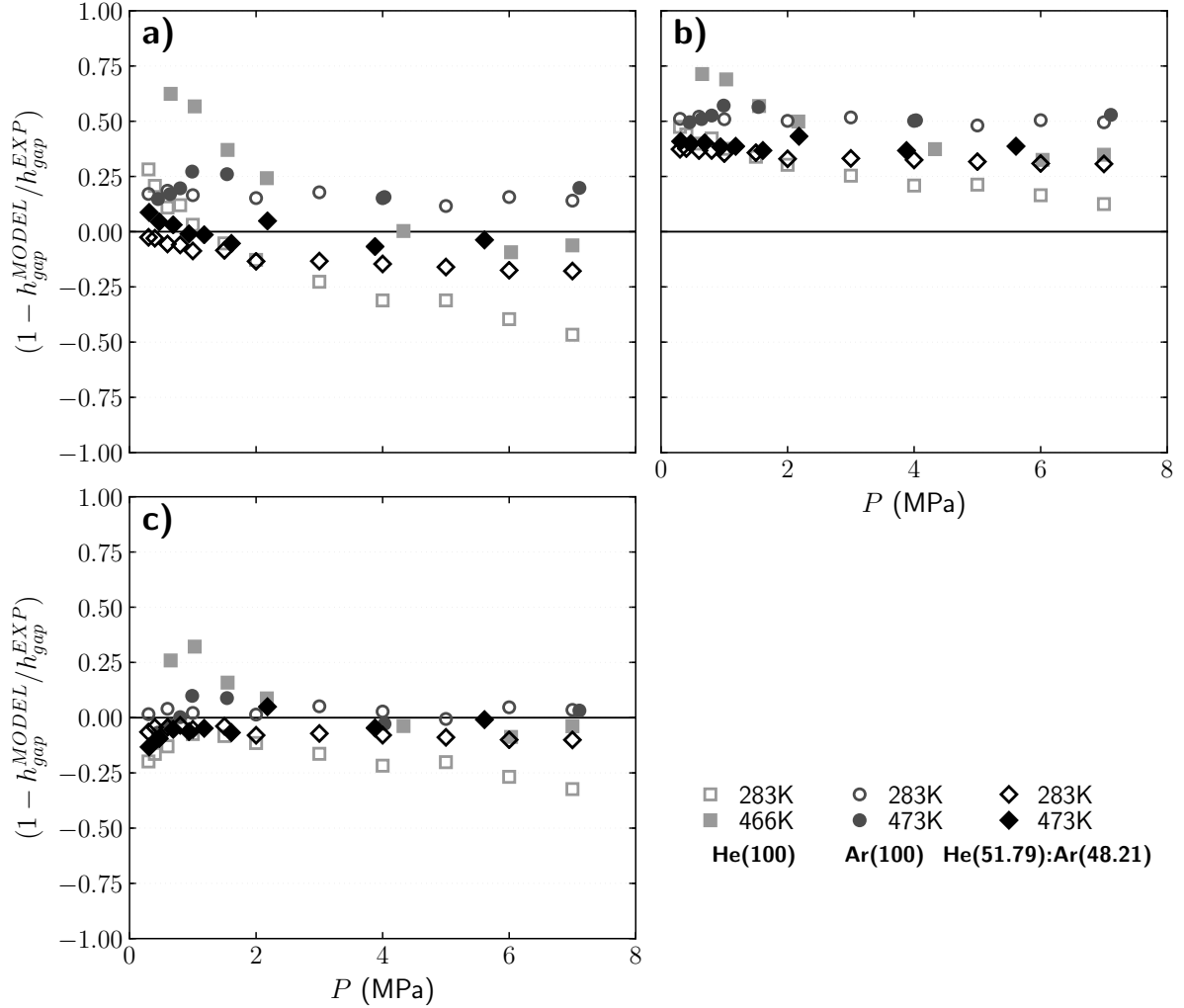


Figure 8.7: Relative gap conductance difference for helium, argon, and a binary mixture of helium and argon at 283–473 K between the experimental data and predictions from (a) the Ross-Stoute model, (b) the modified Ross-Stoute model, and (c) the calibrated model with $\hat{\theta} = \{0.605 \pm 0.096, 14.522 \pm 7.896\}$ and $\hat{\sigma} = 4754.568 \text{ W/m}^2\text{-K}$. The data are from Garnier and Begej [22].

Table 8.2: Validation results for the gap conductance, h_{gap} for the single-component gases, multi-component gases, and combined data.

	$\{\theta_1, \theta_2\}$	d (W/m ² -K)	d_M (W/m ² -K)	RMSE (W/m ² -K)	rRMSE (%)
<i>the original Ross-Stoute model (Eq. 8.1)</i>					
He [†]	—	17.88	78.37	3.066	50.3
Ar [‡]	—	0.55	2.15	0.126	17.1
He-Ar [‡]	—	0.63	2.56	0.128	9.7
combined*	—	6.63	23.60	0.887	20.8
<i>the modified Ross-Stoute model (Eq. 8.2)</i>					
He	—	20.63	96.96	3.538	57.9
Ar	—	1.53	6.48	0.351	50.7
He-Ar	—	2.75	12.98	0.562	36.7
combined	—	9.41	48.02	1.257	42.8
<i>the calibrated model (Eq. 8.3) with $g = 0$</i>					
He	{1.807, 168.754}	6.34	28.48	1.087	27.3
Ar	{0.140, -0.277}	0.19	0.57	0.044	5.9
He-Ar	{0.914, 29.377}	0.24	0.92	0.050	3.3
combined	{0.605, 14.522}	3.49	13.93	0.467	11.6

[†] He(100%) in Figure 8.4

[‡] Ar(100%) in Figure 8.5

[‡] He(51.79%):Ar(48.12%) in Figure 8.6

* the combined data in Figure 8.7

CHAPTER

9

THERMAL BEHAVIOR ASSESSMENT IN BISON

This study demonstrates fuel temperature predictions with the improved gap heat transfer modeling for nuclear applications, particularly fuel centerline temperature and Doppler temperature, using the DOE funded nuclear fuel performance code Bison [43]. The code is a finite-element based nuclear fuel performance code and is the state-of-art fuel performance code for modeling nuclear thermo-mechanical behavior. The code is applicable to a variety of fuel types and has been developed by INL and solves the fully-coupled equations of thermo-mechanics and species diffusion in multi dimensions. The code works on the Multiphysics Object Oriented Simulation Environment (MOOSE) framework which is a high-performance, open-source finite element toolkit developed at INL. Background on the gap conductance modeling in the code is provided in Section 9.1 and validated against the experimental data by performing a series of validation tests to ensure that the code is capable of accurately modeling real world problems. To address this, two types of tests are performed: (i) separate effects validation in Section 9.2; and (ii) integral effects assessment in Section 9.3. The concluding remarks and future work are provided at the end of this chapter.

9.1 Gap Conductance Modeling in Bison

The mechanical contact model in Bison is based on the methodology of Heinsteins and Laursen [248], which utilizes node to face constraints to prevent nodes on one surface from penetrating the face of another surface [8]. The evolution of the gap is determined using a geometric search algorithm and total conductance across the gap is computed as three summed

heat paths: fill gas conductance, direct thermal radiation, and solid contact conductance. For the sake of completeness, basics of the gap conductance modeling are provided here. Bison models the gap conductance using a modified version of the Ross–Stoute model [52] with an unknown origin for the fill gas conductance and the thermal contact conductance (Eq. 9.1); and the conductance due to the thermal radiation from Bird et al. [242] with a unity ratio of the areas.

$$h_{gap} = \frac{\lambda_g}{d + 1.5(\xi_1 + \xi_2) + (g_1 + g_2)} + \frac{10\Lambda}{\sqrt{0.8(\xi_1 + \xi_2)}} \left(\frac{W}{H} \right), \quad (9.1)$$

where

λ_g = gas thermal conductivity (W/m-K),

d = gap distance (m),

ξ = surface roughness (m) that is defined as a one-dimensional parameter to represent the mean deviation of surface irregularities,

g = temperature jump distance (m),

$\Lambda = \left(\frac{2\lambda_1\lambda_2}{\lambda_1 + \lambda_2} \right)$, harmonic mean of thermal conductivities of the surrounding solids (W/m-K),

W = load on the contact interface (N/m²), and

H = Meyer’s hardness of the softer material (N/m²).

The original Ross-Stoute model [52] is given by Eq. 8.1. The model conventionally used in nuclear fuel performance codes to conduct heat across the gap is a modified version of the Ross–Stoute model. The model was modified to include gap distance d in the formulation (Eq. 8.1), which introduced additional uncertainty because the model parameters were not adjusted after the modification [244]. Note that this relation is for the contact-conductance calculations; however, it is also used for the non-contact conditions. More discussion can be found in Chapter 8. In this study, the following model (Eq. 9.2) is tested against the original model in Bison to examine its impacts on fuel temperature predictions.

$$h_{gap} = \frac{\lambda_g}{d + 0.605(\xi_1 + \xi_2)} + \frac{14.522\Lambda}{\sqrt{\xi_1^2 + \xi_2^2}} \left(\frac{W}{H} \right). \quad (9.2)$$

Figure 9.1 shows a comparison of predictions from the aforementioned models against the experimental data. The original model in Bison (Eq. 9.1) appears to inadequately fit the experimental data. Similar behavior is observed when the modified version of Ross-Stoute model is used in Chapter 8. This model underestimates the gap conductance significantly, which will result in an overestimation of fuel temperatures. The Ross-Stoute model (Eq. 8.1) fits the data better than the modified version except in the case where helium is selected as the fill gas. In fact, the temperature jump distance is significantly larger than the gap distance ($2g \gg d$) for helium in addition to the fact that the model does not sufficiently describe the appropriate heat transfer regime [23, 244]. The best agreement is found with Eq. 9.2 which appears to be sufficiently describing the heat transfer regime (i.e., continuum) for the nuclear applications considering representative initial rod internal pressures for LWRs; 0.3 to 3.45 MPa [24].

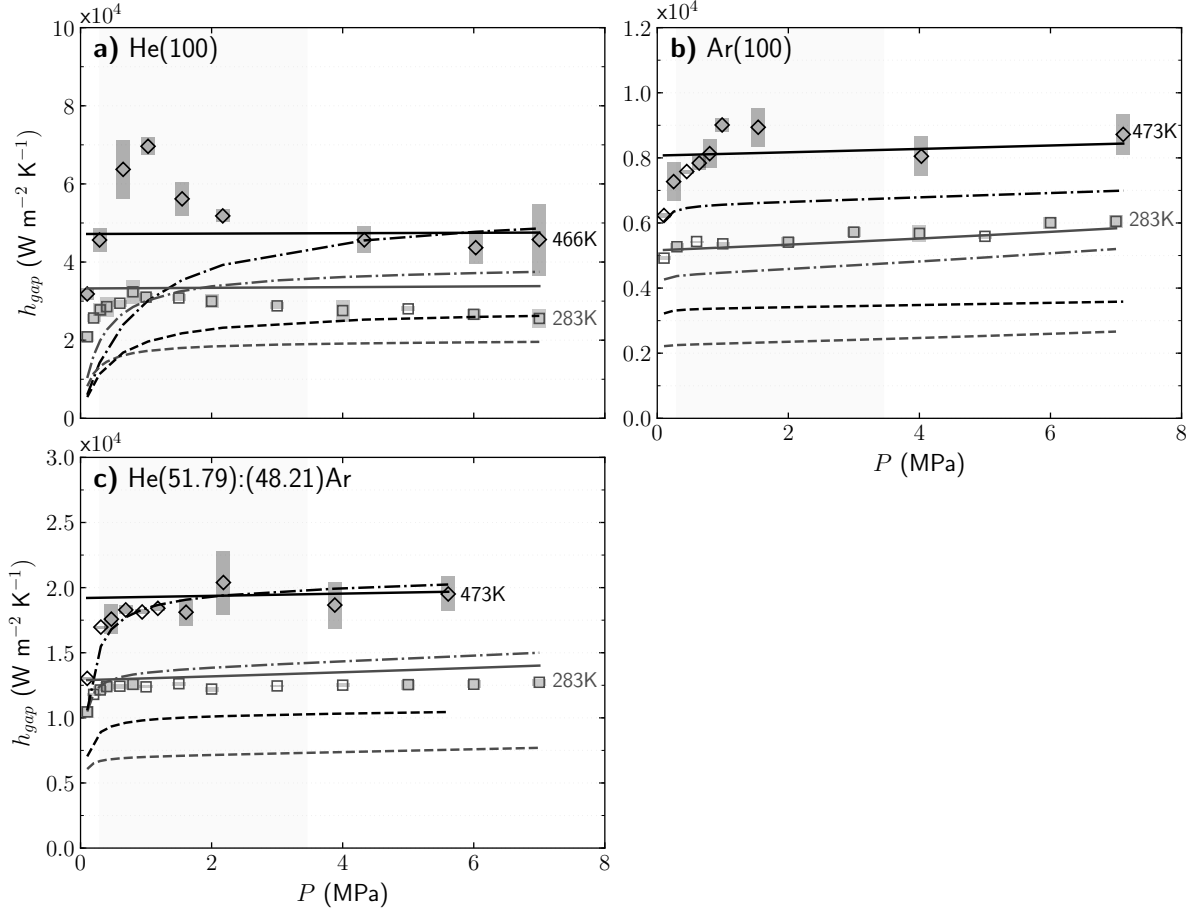


Figure 9.1: Gap conductance comparison at various temperatures and pressures for (a) helium only, (b) argon only, and (c) a binary mixture of helium and argon using the newly implemented model, Eq. 9.2 (—), the original Ross-Stoute model, Eq. 8.1 (— · —), and Bison's default model, Eq. 9.1 (---). Temperature jump distance, accommodation coefficient, and the gas thermal conductivity are calculated based on the expressions given in [23]. The shaded areas (—) represent the initial rod internal pressure ranges from 0.3 to 3.45 MPa in LWRs [24]. The experimental data are from Garnier & Begej [22] and represented with $\pm 1\sigma$ data uncertainty (■). The applied load is $1300 N/m^2$. The gap thickness is $5.9 \mu m$.

9.2 Separate Effects Validation

Garnier and Begej performed ex-reactor experiments in 1979–80 at the Pacific Northwest National Laboratory to determine contact conductance between depleted uranium dioxide and Zircaloy-4 interfaces at low [25] and high pressure [22] using two measurement techniques: (i) the modified pulse design (MPD), a transient measurement technique in which a signal detector was used to measure the thermal energy transmitted through a sample pair due to a heat pulse; and (ii) the modified longitudinal design (MLD), a steady state measurement technique. Experiments were performed between two parallel plates with varying local distances between the sample pairs and surface characteristics. An optical height gauge was used in the experiments to determine the average mean-plane of separation between the pairs. Measurements were performed at 19 coordinates including the center point. The average gap thickness was calculated as the arithmetic mean of the local distances at the measurement points (Figure 9.2).

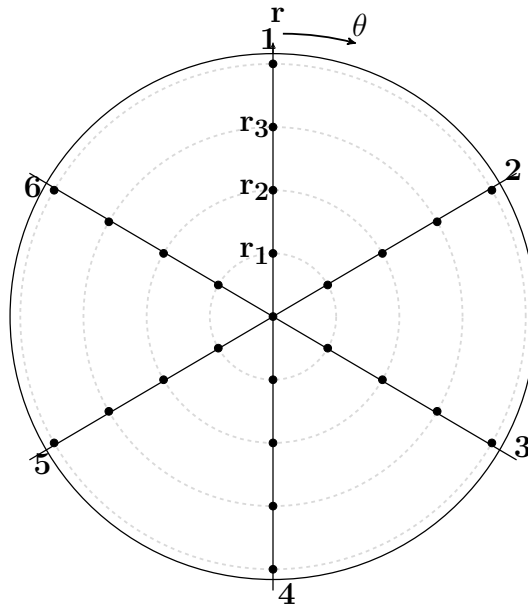


Figure 9.2: Configuration of the measurement points, regenerated from Garnier and Begej [25]. Upper plate and bottom plate faces only at those 19 points. Therefore, the data are measured at 19 points including the center point.

9.2.1 Bison Model Description

Geometry and Mesh Figure 9.2 shows a schematic illustration of the problem setup in Bison. For simplicity, the circular plate geometry in the experiments was simplified into columnar geometry considering one-dimensional heat transfer within the gap between the plates. The

geometry was meshed using two-dimensional, axisymmetric quadratic elements.

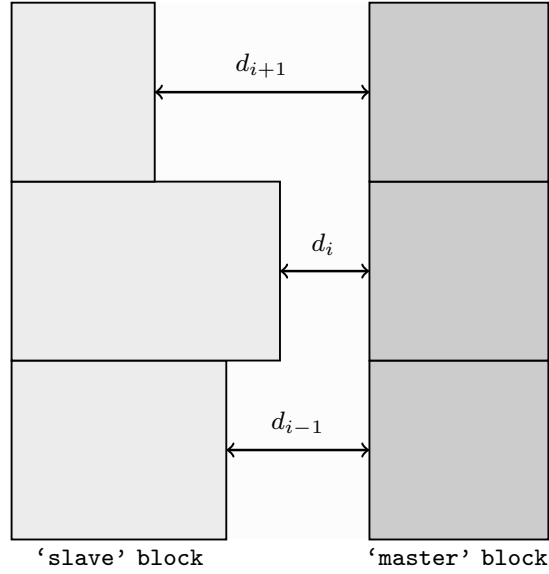


Figure 9.3: Schematic illustration of the geometry constructed for Bison simulations (not to scale). d_i denotes the i -th local gap distance between the sample plates, and is varied for $i = 1, 19$ including all measurement points.

Material and Behavioral Models The following material and behavioral models were used for the sample pairs: (i) the material properties were calculated through a pre-processing script from the measured properties in the experiments; and (ii) solid mechanics were not utilized.

Boundary and Operating Conditions This benchmark only included the MLD benchmark that had temperature difference information to estimate correct boundary conditions in Bison simulations. The boundary conditions were calculated from the experiments using reported gas temperature and temperature jump across the gap.

$$T_{gap} = \frac{1}{2} (T_{gapLeft} + T_{gapRight}), \quad (9.3a)$$

$$\Delta T_{gap} = (T_{gapLeft} - T_{gapRight}). \quad (9.3b)$$

where

- T_{gap} = gas temperature,
- ΔT_{gap} = temperature difference across the gap,
- $T_{gapLeft}$ = temperature at far left boundary, and
- $T_{gapRight}$ = temperature at far right boundary.

Note that the boundary conditions at the far left and the far right were estimated by adding $\pm\Delta T = (qL/kA)$ to the surrounding temperatures since the planar thermal resistance is given by $R = (L/kA)$.

Automation Figure 9.4 shows the automated process to create the geometry and the mesh from experimental conditions (e.g., measurement points for the surface configuration, gas composition, etc.) to generate the Bison inputs. The simulations are run in Bison. Later, Bison predictions are compared against the experimental data for the gap conductance.

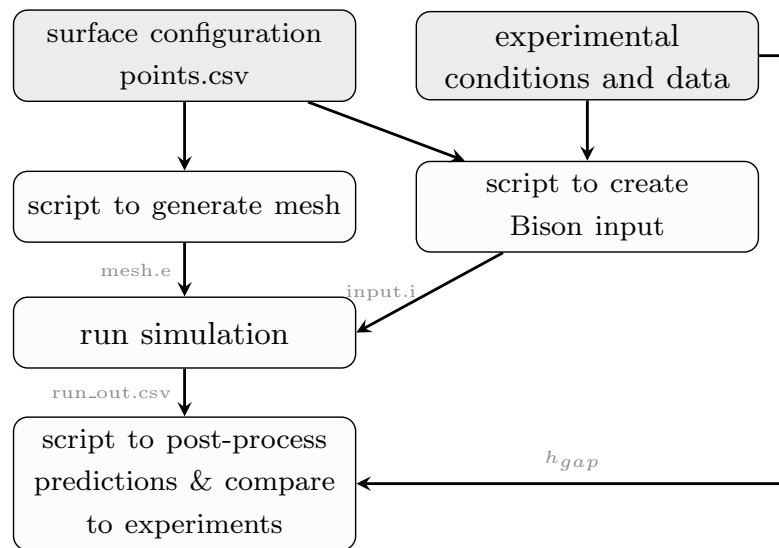


Figure 9.4: Schematic of the automated benchmark. Darker gray boxes represent the gold files for each surface configuration that includes local gap distances, and the experimental conditions/data.

9.2.2 Results & Discussion

Figure 9.5 shows a comparison of the predictions from Bison and hand calculations against the MLD experimental data [25] for the open gap configuration. Note that Toptan et al. [244] calibrated Eq. 9.2 with the MPD experimental data by Garnier and Begej [22]. Therefore, this benchmark can be considered as a cross-validation study to assess how results of the calibrated model will generalize to an independent data set, the MLD data. Additionally, the gap conductance can be estimated through hand calculations and its benchmark is incorporated as defect testing to ensure that the code capabilities are consistent with the expected physical values without any computing errors. Note that the hand calculations are only provided for Eq. 9.2 as no temperature jump calculations are included. The validation metrics are summarized on the

plot given in Figure 9.5. Bison predictions and the experimental data are in agreement within 28.0% relative error for the open gap configuration.

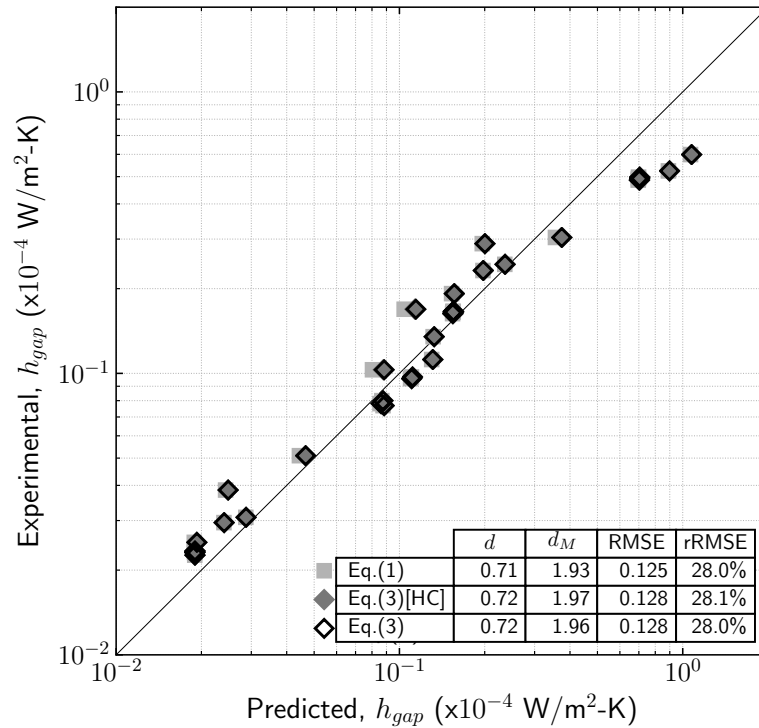


Figure 9.5: Gap conductance comparison of the Bison predictions against the experimental data. Open gap configuration. Hand calculations (HC) are presented for Eq. 9.2 to confirm that the computational model setup is done correctly set in the code. The fill gas thermal conductivity is computed from the models as in the code.

9.3 Integral Effects Assessment

Bison predictions are compared for the selected test cases which are tabulated in Table 9.1 from Bison’s assessment test matrix [249]. These cases are specifically chosen from Williamson et al. [8] to demonstrate the impact of the proposed gap conductance model on Bison predictions. Figure 9.6 shows the power histories for the selected Halden IFA cases to be used in Bison integral effects validation. In Table 9.1, the four cases are listed for the through-life temperature data for IFA-515.10 and IFA-562 rods [118, 250]. The four cases are composed of annular uranium dioxide fuel pellets that are enclosed in Zircaloy cladding.

Table 9.1: Overview of the fuel centerline temperature experimental data for Bison integral effects validation, from Williamson et al. [8].

Source	Experiment	Rod	Final burnup
Tverberg and Amaya [118]	IFA-515.10	A1	86.6 MWd/kgU
Lösönen [250]	IFA-562.2	15	56.7 MWd/kgU
		16	56.2 MWd/kgU
		17	56.2 MWd/kgU

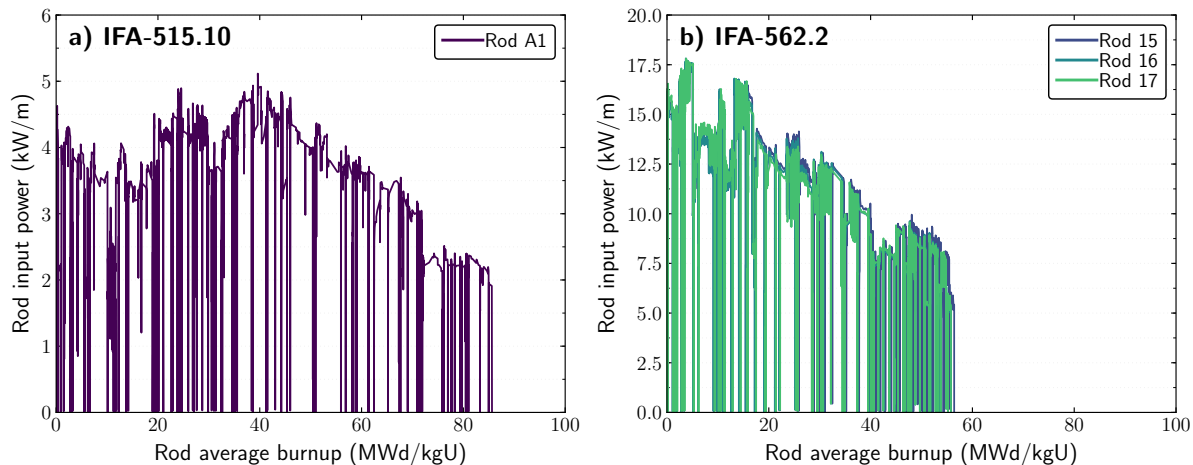


Figure 9.6: The average linear heat rate histories for (a) the Halden IFA-515.10 irradiation and (b) the Halden IFA-562 irradiation.

9.3.1 Results & Discussion

The SRQs are the fuel centerline temperature and Doppler temperatures. The Doppler temperature is calculated from the predictions in two different ways:

1. a volume-averaged fuel temperature T_D is

$$T_D = \frac{\int_{R_0}^{R_f} T_f(r) r dr}{\int_{R_0}^{R_f} r dr}, \quad (9.4)$$

where

- $T_f(r)$ = the temperature profile within the fuel,
- R_0 = the fuel inner radius, and
- R_f = the fuel surface radius.

2. An ‘NEA’ approximation [136] is used to capture most of the U^{238} absorption self-shielding which occurs at a temperature closer to the pellet surface than the centerline temperature

is:

$$T_D^{NEA} = 0.7T_{fs} + 0.3T_{cl}, \quad (9.5)$$

where

T_{fs} = the fuel surface temperature,
 T_{cl} = the fuel centerline temperature.

Fuel Centerline Temperature

Figure 9.7 shows the differences between fuel centerline temperature predictions in Bison using the original model and the proposed model. The temperature difference is calculated as

$$\Delta T = T_{cl} - T_{cl}^*, \quad (9.6)$$

where

T_{cl} = the centerline temperature with Bison's original model (Eq. 9.1), and
 T_{cl}^* = the centerline temperature with the proposed model (Eq. 9.2).

Figure 9.8 shows a comparison of Bison's fuel centerline predictions for the burnup range of [0, 30 MWd/kgU]. These results are tabulated in Table 9.2. With use of the proposed model, the fuel temperature predictions are underestimated in comparison to the original model predictions, where the optimized models tend to result in higher gap conductance values. The underestimation is approximately 5.0%. For the Halden IFA-515.10 Rod A1, the temperature difference is 14.0 K and the maximum temperature difference is 21.5 K. For the Halden IFA-562.2 irradiation, the temperature difference is around 50 K and the maximum temperature difference is around 75 K. Note that the former case is a lower power rod as compared to the latter, as shown in Figure 9.6.

Figure 9.9 shows the KS test results for Bison's fuel centerline temperature predictions. Note that the value of the KS test statistics will not be affected by scale changes such as using a log scale as the test is robust and takes into account only the relative distribution of the data. The KS statistics are tabulated in Table 9.2 for the selected tests. The results indicate that the null hypothesis cannot be rejected (i.e., the distributions of the two samples are identical) for the IFA-515.10 Rod A1 with small KS statistic, D is small and there is a high p -value. This is reasonable because the temperature difference is negligible for this case.

Doppler Temperature, T_D

Figure 9.10 shows the differences between Doppler temperature predictions in Bison using the original model and the proposed model. The Doppler temperature is calculated according to the volume averaged fuel temperature (Eq. 9.4). The temperature difference is calculated as

$$\Delta T = T_D - T_D^*, \quad (9.7)$$

where

T_D = the centerline temperature with Bison's original model (Eq. 9.1), and
 T_D^* = the centerline temperature with the proposed model (Eq. 9.2).

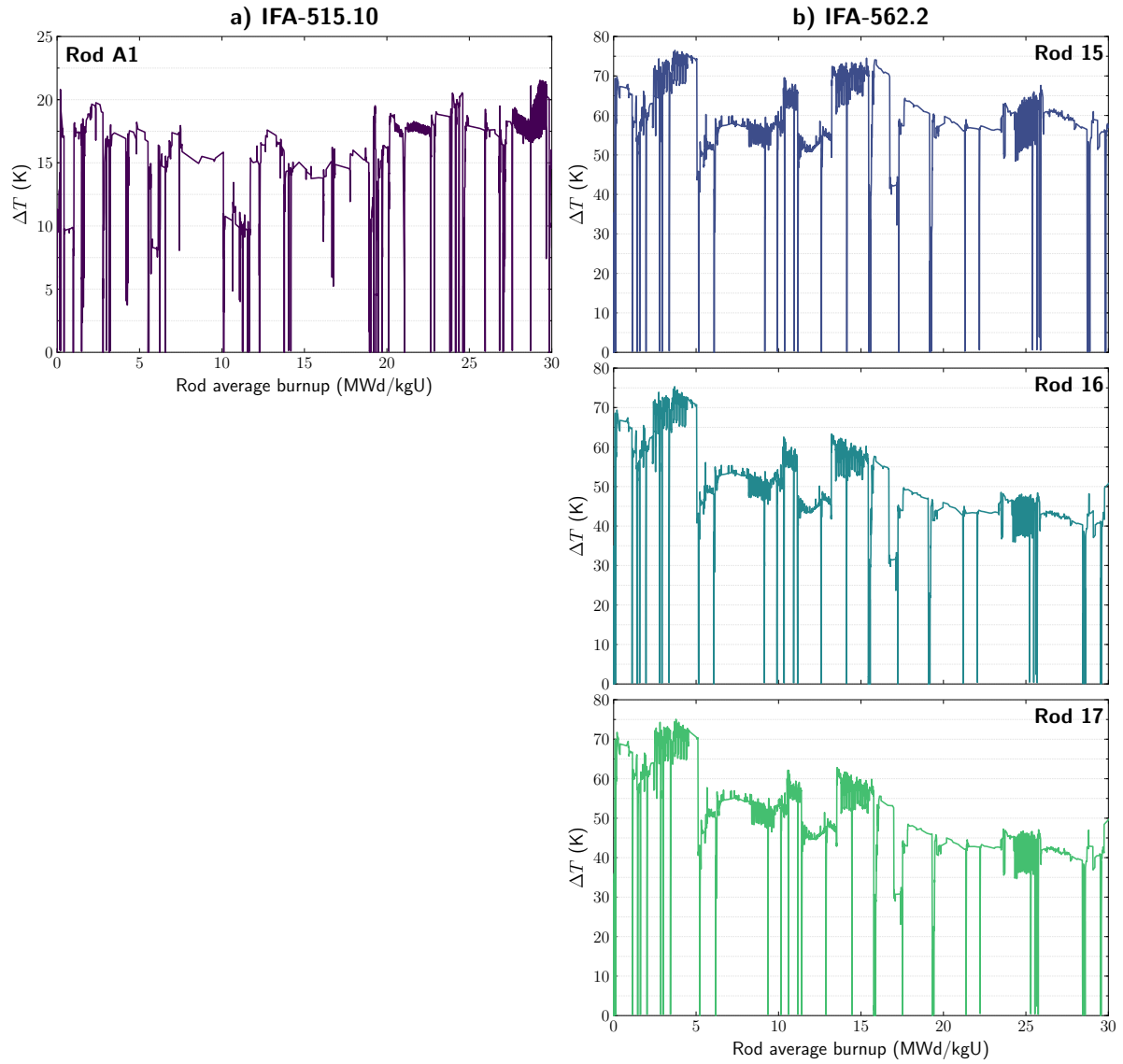


Figure 9.7: Fuel centerline temperature differences using Bison's original model and the proposed model with respect to the rod average burnup for (a) the Halden IFA-515.10 irradiation and (b) the Halden IFA-562 irradiation.

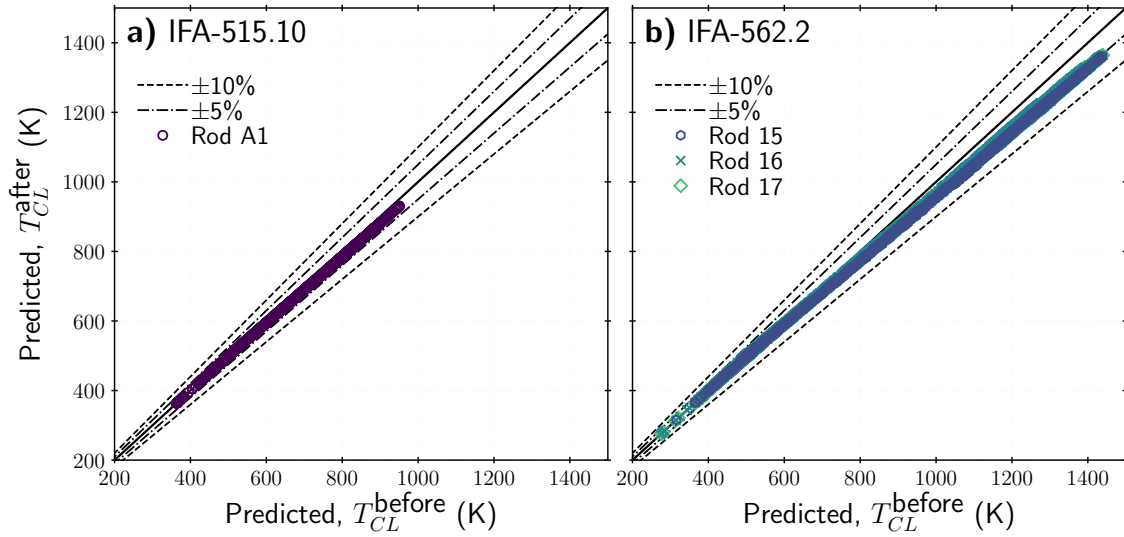


Figure 9.8: Comparison of the fuel centerline temperature predictions using Bison’s original model and the proposed model for the burnup range of $[0, 30 \text{ MWd/kgU}]$.

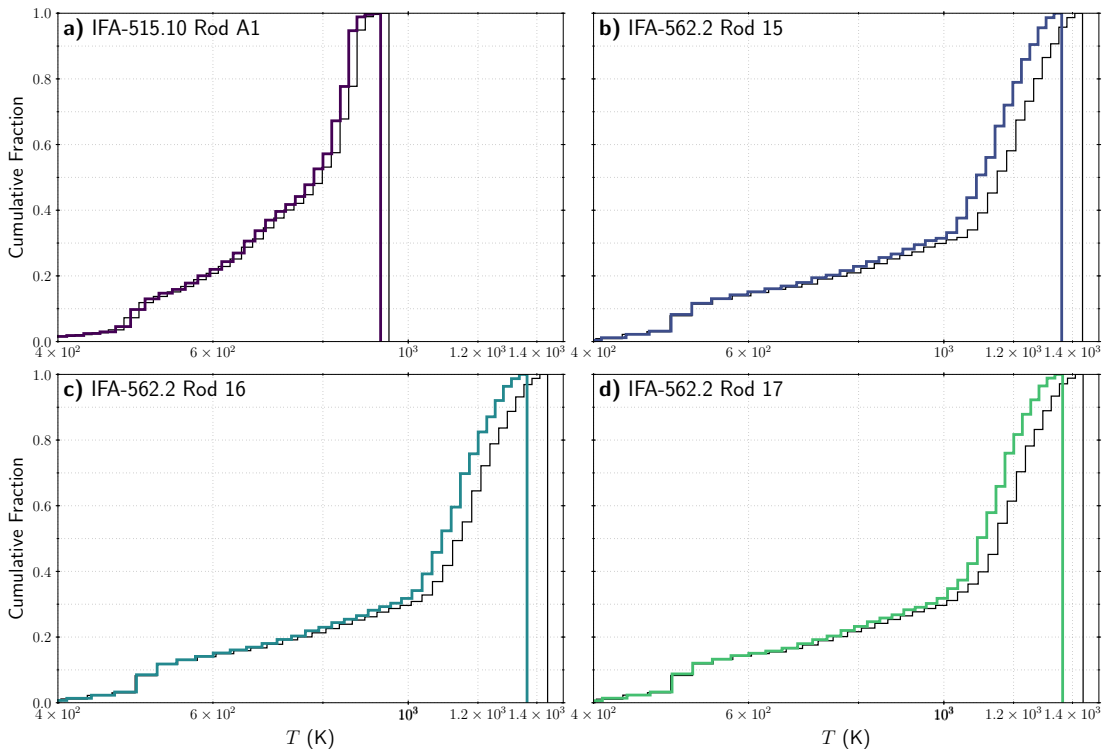


Figure 9.9: KS-test comparison cumulative fraction plot of the fuel centerline temperature predictions using Bison’s original model and the proposed model for the burnup range of $[0, 30 \text{ MWd/kgU}]$.

Table 9.2: Results for the fuel centerline temperatures for the rod average burnup of [0, 30 MWd/kgU].

Experiment	Rod No.	RMSE (K)	max(ΔT) (K)	D (-)	p (-)
IFA-515.10	A1	14.0	21.5	0.0184	0.4814
IFA-562.2	15	52.2	76.5	0.0576	0.0000
	16	45.4	75.3	0.0531	0.0000
	17	45.7	75.1	0.0528	0.0000

Figure 9.11 shows a comparison of Bison’s Doppler temperature predictions for the burnup range of [0, 30 MWd/kgU]. The results are tabulated in Table 9.2. With use of the proposed model, the fuel temperature predictions are underestimated in comparison to the original model predictions, where the optimized models tend to result in higher gap conductance values. The underestimation is approximately 5.0%. For the Halden IFA-515.10 Rod A1, the temperature difference is 13.6 K and the maximum temperature difference is 21.1 K. For the Halden IFA-562.2 irradiation, the temperature difference is around 45 K and the maximum temperature difference is around 65 K. Note that the former case is a lower power rod as compared to the latter, as shown in Figure 9.6.

Figure 9.12 shows the KS test results for Bison’s fuel centerline temperature predictions. Note that the value of the KS test statistics will not be affected by scale changes like using a log scale as the test is robust and takes into account only the relative distribution of the data. The KS statistics are tabulated in Table 9.3 for the selected tests. The results indicate that the null hypothesis cannot be rejected (i.e., the distributions of the two samples are identical) for the IFA-515.10 Rod A1 with small KS statistic, D is small and high p -value. This is reasonable because the temperature difference is negligible for this case.

Table 9.3: Results for the volume averaged fuel temperatures for the rod average burnup of [0, 30 MWd/kgU].

Experiment	Rod No.	RMSE (K)	max(ΔT) (K)	D (-)	p (-)
IFA-515.10	A1	13.6	21.1	0.0194	0.4157
IFA-562.2	15	47.8	67.6	0.0598	0.0000
	16	41.3	64.4	0.0546	0.0000
	17	41.5	64.2	0.0543	0.0000

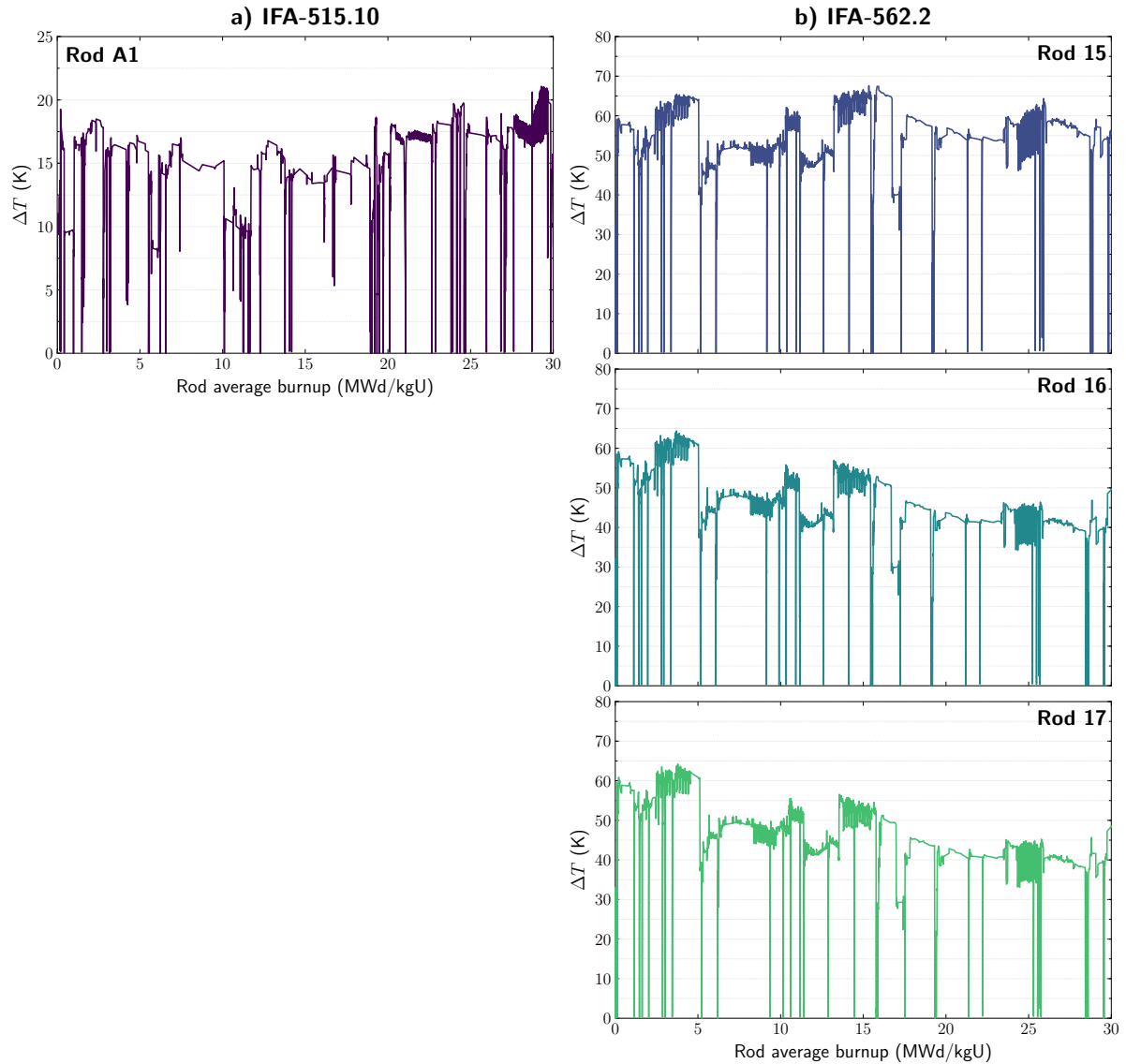


Figure 9.10: Volume averaged fuel temperature differences using Bison's original model and the proposed model with respect to the rod average burnup for (a) the Halden IFA-515.10 irradiation and (b) the Halden IFA-562 irradiation.

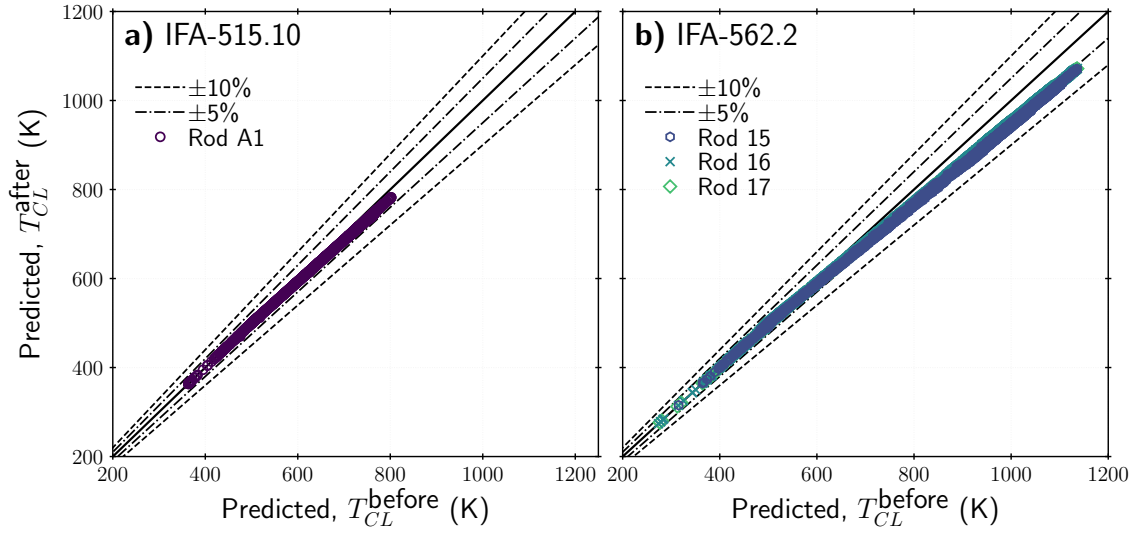


Figure 9.11: Comparison of the volume averaged fuel temperature predictions using Bison's original model and the proposed model for the burnup range of $[0, 30 \text{ MWd/kgU}]$.

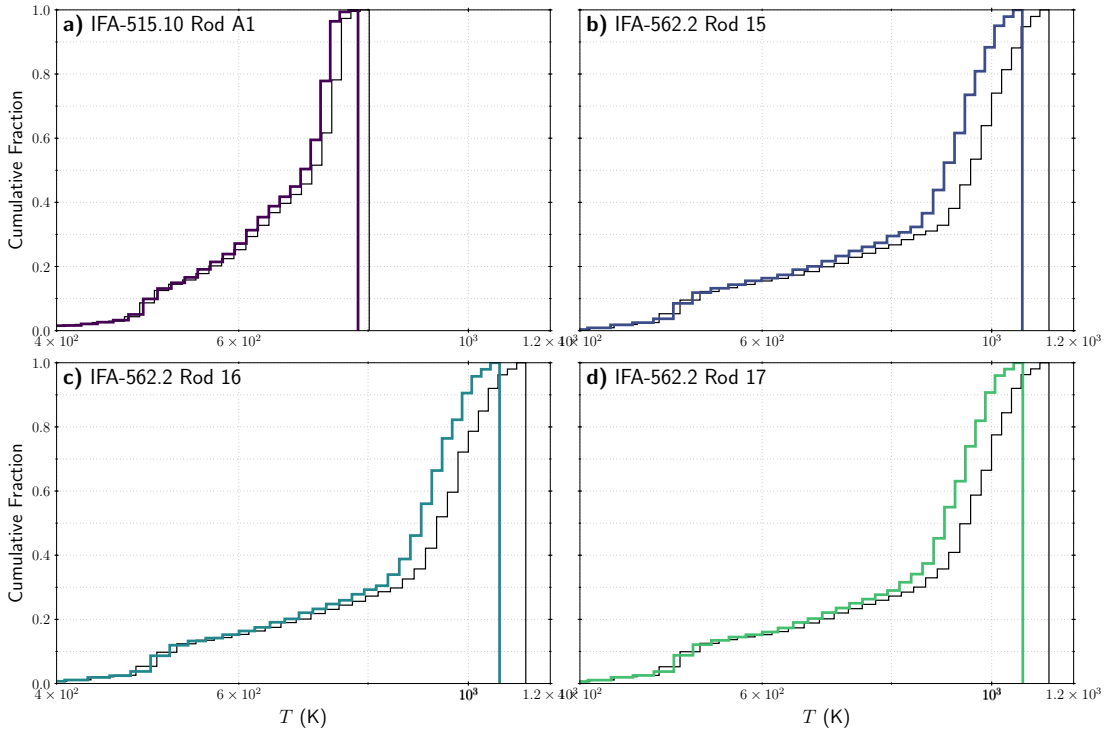


Figure 9.12: KS-test comparison cumulative fraction plot of the volume averaged fuel temperature predictions using Bison's original model and the proposed model for the burnup range of $[0, 30 \text{ MWd/kgU}]$.

Doppler Temperature, T_D^{NEA}

Figure 9.14 shows the differences between Doppler temperature predictions in Bison using the original model and the proposed model. The Doppler temperature is calculated according to the volume averaged fuel temperature (Eq. 9.5). The temperature difference is calculated as

$$\Delta T = T_D^{NEA} - T_D^{NEA,*}, \quad (9.8)$$

where

T_D = the centerline temperature with Bison’s original model (Eq. 9.1), and
 T_D^* = the centerline temperature with the proposed model (Eq. 9.2).

Figure 9.14 shows a comparison of Bison’s Doppler temperature predictions for the burnup range of [0, 30 MWd/kgU]. The results are tabulated in Table 9.2. With use of the proposed model, the fuel temperature predictions are underestimated against the original model predictions, where the optimized models tend to result in higher gap conductance values. The underestimation is slightly less than 10.0%. The reason is that the proposed model results in higher gap conductance values. For the Halden IFA-515.10 Rod A1, the temperature difference is 13.0 K and the maximum temperature difference is 20.1 K. For the Halden IFA-562.2 irradiation, the temperature difference is around 40 K and the maximum temperature difference is around 60 K. Note that the former is a lower power case rod as compared to the latter, as shown in Figure 9.6.

Figure 9.15 shows the KS test results for Bison’s fuel centerline temperature predictions. Note that the value of the KS test statistics will not be affected by scale changes like using log scale since the test is robust and takes into account only relative distribution of the data. The KS statistics are tabulated in Table 9.4 for the selected tests. The results indicate that the null hypothesis cannot be rejected (i.e., the distributions of the two samples are identical) for the IFA-515.10 Rod A1 with small KS statistic, D is small and high p -value. This is reasonable because the temperature difference is negligible for this case.

Table 9.4: Results for the volume-averaged fuel temperatures for the rod average burnup of [0, 30 MWd/kgU].

Experiment	Rod No.	RMSE (K)	max(ΔT) (K)	D (-)	p (-)
IFA-515.10	A1	13.0	20.1	0.0199	0.3848
IFA-562.2	15	43.8	61.3	0.0608	0.0000
	16	37.8	57.1	0.0548	0.0000
	17	37.9	56.9	0.0546	0.0000

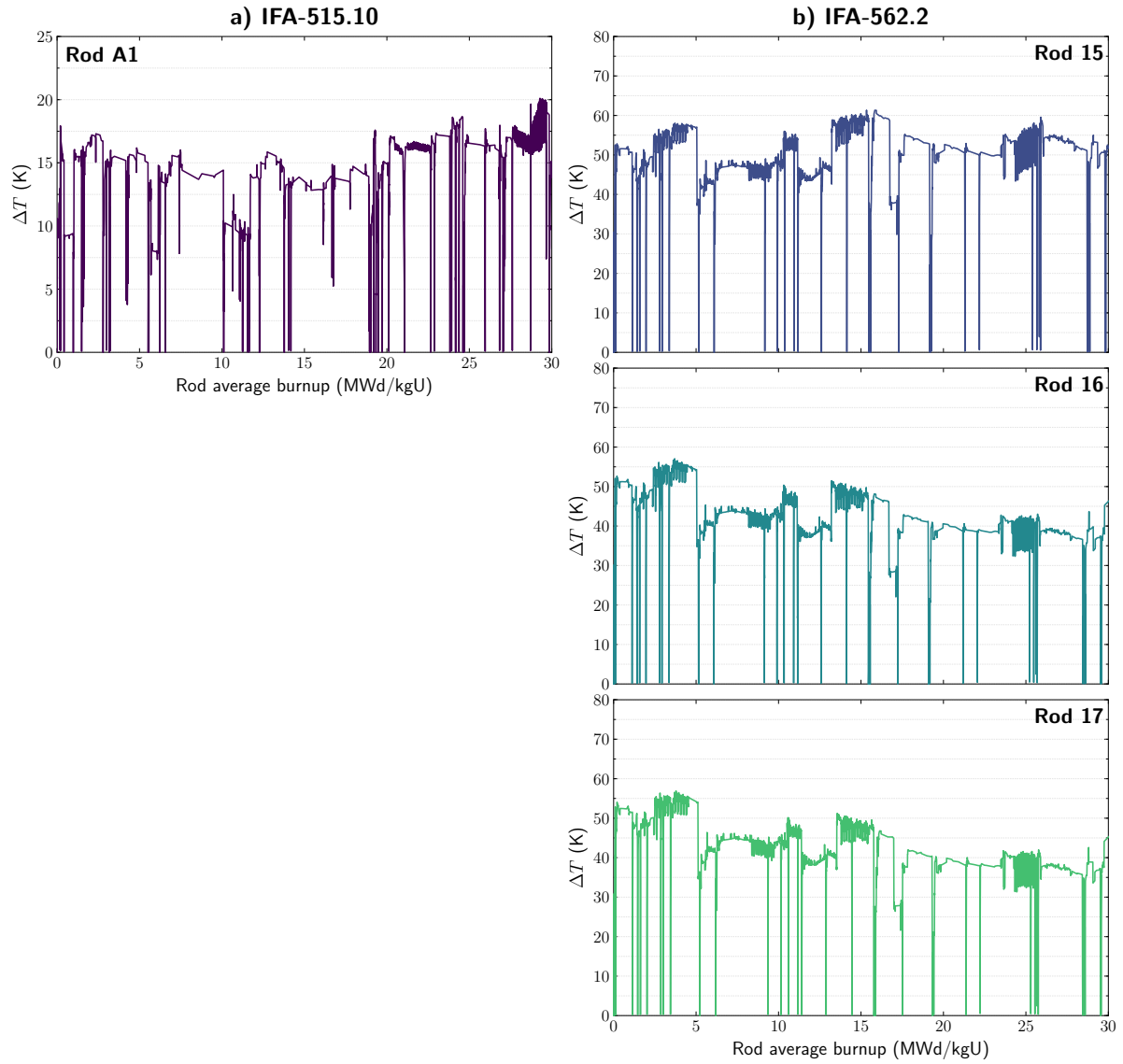


Figure 9.13: NEA temperature differences using Bison's original model and the proposed model with respect to the rod average burnup for (a) the Halden IFA-515.10 irradiation and (b) the Halden IFA-562 irradiation.

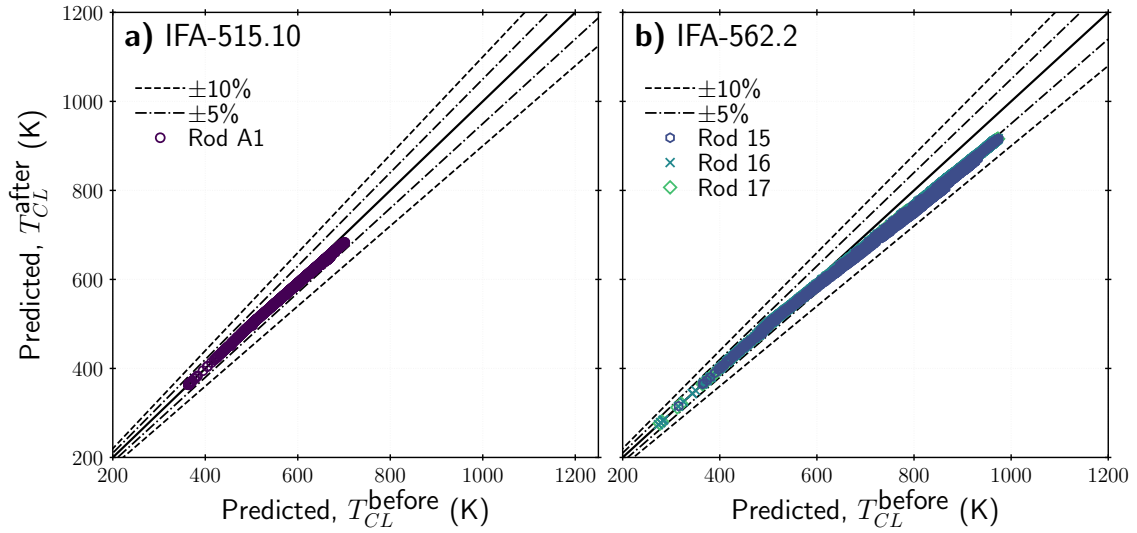


Figure 9.14: Comparison of the NEA temperature predictions using Bison’s original model and the proposed model for the burnup range of $[0, 30 \text{ MWd/kgU}]$.

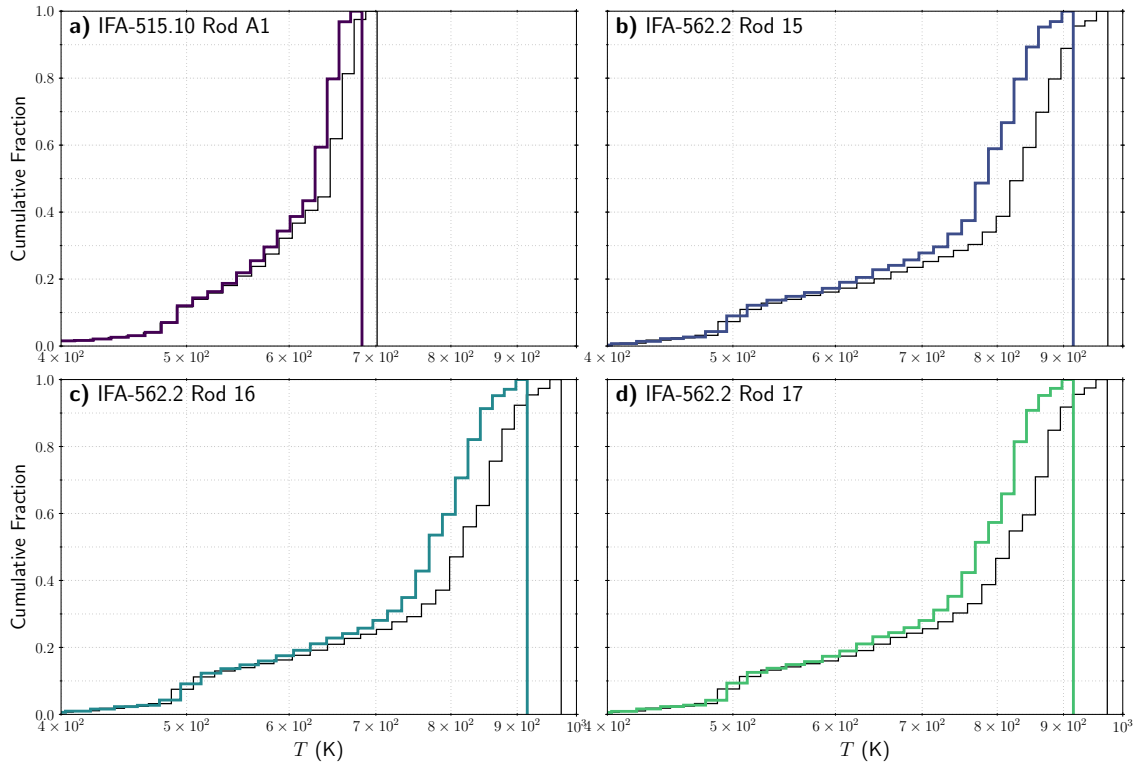


Figure 9.15: KS-test comparison cumulative fraction plot of the NEA temperature predictions using Bison’s original model and the proposed model for the burnup range of $[0, 30 \text{ MWd/kgU}]$.

9.4 Chapter Summary

The test series are performed to assess the codes capability to accurately model real world problems. Garnier and Begej's gap conductance data are used as separate effects validation, though the results do not give a clear indication that the new model is more accurate. This can be attributed to the negligible contribution of the roughness once the gap thickness is large enough for the open gap configuration. In addition, hand calculations confirmed that the model is implemented in the code as intended. The Halden IFA-515.10 and IFA-562.2 through-life rods are used as the integral effects tests from Bison's test matrix [249]. Prior to this work, Williamson et al. [8] indicated that Bison's fuel temperature predictions are strongly influenced by the gap heat transfer between fuel and cladding. In their integral effects validation, an approximately 10% overestimation is presented in the fuel centerline temperature predictions using Bison's original model against the measurements. This work serves as a promising enhancement on the heat transfer across the fuel-to-cladding gap with the proposed modeling. The model results in a reduction of fuel temperatures due to the enhanced gap heat transfer. Preliminary results presented around a five percent reduction of the fuel centerline temperatures against Bison's previous predictions, and similarly for Doppler temperatures. In the future, the results will be compared against experimental data which are currently confidential to the Bison team of INL.

CHAPTER

10

CONCLUDING REMARKS

The primary contributions in this dissertation are detailed as follows.

In Chapter 3, CTFFuel, was successfully constructed to interface CTF's fuel performance modeling capabilities for the simulation of the steady state and transient thermal response of an LWR fuel rod. New modeling options were added to investigate radial fuel deformation to account for the effects of thermal expansion, swelling, irradiation-induced densification, and relocation. Work performed in this study improved the thermal modeling capabilities of both CTF and CTFFuel. The models were integrated in the code according to the CASL coding guidelines.

In Chapter 4, new modeling options were added to investigate the fuel's thermal conductivity degradation of LWR oxide fuels. Work performed in this study improved the thermal conductivity modeling capabilities of the code and provided a pedigree for the model. The analyses ensured that the fuel thermal conductivity function gives the correct output for a given input and that the fuel thermal conductivity model was implemented as expected. After the software quality was assessed, verification and code comparison activities indicated that the code solves the intended equations. The thermal conductivity feature is integrated into the most recent version of the code, and is documented and protected in the code through unit and regression tests.

In Chapter 5, a sensitivity study was performed on the fuel temperature predictions for the selected input parameters of the gap heat transfer coefficient, power, wall temperature, fuel burnup, and gadolinia concentration. The fuel temperature predictions were found to be the most sensitive to the gap heat transfer coefficient. Additionally, a sensitivity study was performed on the radial power distribution and fuel thermal conductivity. The radial power shape and effects of thermal conductivity degradation were notable on the fuel temperatures. Therefore, any simplified assumptions on this behavior would significantly deteriorate feedback

calculations in multi-physics applications. Lastly, an uncertainty quantification was performed. A sample size of 59 was used for one-sided 95% percentile based on Wilks formula. The one-sided tolerance limit was sufficient for this analysis since the quantity of interest was fuel centerline temperature, which is supposed remain below fuel melting temperature for regulatory purposes. The NRCs safety limit for the peak fuel centerline temperature is 3077 K, and the 95% percentile range calculated from the uncertainty quantification step does not exceed this value. Overall, this study provided a baseline for VERA-CS calculations to improve coupling between CTFFuel and MPACT in VERA-CS, and motivated the necessity of better understanding the physics to reduce these large uncertainties in the gap conductance calculations for more accurate estimation of fuel temperatures.

In Chapter 6, the fill gas thermal conductivity model was updated to include its dependence on rod internal pressure, which is typically ignored in the nuclear fuel performance codes. However, the pressure dependence is important when the initial fill gas is not helium or replaced by lower conductivity gaseous fission products during the reactor's operation [251]. Error due to this assumption will be more pronounced in nuclear applications for cases when the rod internal pressure approaches or exceeds the external pressure or in open gap configurations due to relocated fuel at higher pressures. A robust application of the theory will minimize uncertainties for gap conductance calculations and enable accurate prediction of fuel temperatures. This study confirmed that the pressure dependence is important when the initial fill gas is not helium or replaced by lower conductivity gaseous fission products (e.g., xenon, krypton) during the reactors operation.

In Chapter 7, an overview of the theoretical considerations and the underlying assumptions of gap conductance modeling were provided in addition to the traditional modeling approaches in nuclear fuel performance codes. Deficiencies of traditional approaches were discussed. The models were generalized to curvilinear coordinates and for diatomic/polyatomic gases due to their incorrect use in the nuclear fuel performance codes. The expressions (e.g., thermal accommodation coefficient, temperature jump distance) were made consistent with kinetic theory to be more representative of real world data. The fill gas thermal conductivity was updated to include its dependence on rod internal pressure, which is presently ignored in the nuclear fuel performance codes.

In Chapter 8, the conventional gap conductance model in nuclear applications was optimized for uranium dioxide-Zircaloy interfaces using available experimental data at high pressure for single- and multi-component gases. The model conventionally used in nuclear fuel performance codes to conduct heat across the fuel-cladding gap is a modified version of the Ross-Stoute model. The model was modified in nuclear applications to include gap distance in the formulation, which introduced additional uncertainty as the model parameters were not adjusted after the modification. In this study, this conventional model was optimized and overall uncertainty in the gap conductance was quantified by performing uncertainty propagation. The validation results confirmed that the proposed model results in a larger gap conductance with significantly reduced error.

In Chapter 9, the proposed model serves for a promising enhancement in the heat transfer prediction across the fuel-to-cladding gap. To demonstrate predictions with the improved gap heat transfer modeling in nuclear applications, a finite-element based nuclear fuel performance code, Bison is utilized. The simulation results indicated that the proposed model resulted in

significant reduction of fuel temperatures due to the higher gap conductance estimates with the proposed model. The model resulted in reduction of fuel temperatures due to the higher gap conductance estimates with the new model. Preliminary results presented around a five percent reduction of the fuel centerline temperatures against Bison's previous predictions, and similarly for the Doppler temperatures.

The following studies are also performed in addition to the aforementioned improvements and developments.

- A code comparison was performed between CTFFuel and FRAPTRAN to benchmark transient calculations during a reactivity initiated accident (RIA) transient. This comparison is automated to reduce possible human errors in the process. These test cases are added to CTFFuels test matrix (Appendix B).
- A rigorous model was constructed to correct fuel temperature profiles through the flux depression factors to account for the self-shielding effect on radial power distribution (Appendix C).
- CTF's frictional pressure drop calculations are enhanced with the integration of the friction factor models (Appendix D).

References

- [1] Ben H. Thacker, Scott W. Doebling, Francois M. Hemez, Mark C. Anderson, J Pépin, and E. Artés Rodríguez. Concepts of model verification and validation. 2004.
- [2] W. L. Oberkampf and C. J Roy. *Verification and Validation in Scientific Computing*. Cambridge University Press, Cambridge, UK, first edition, November 2010.
- [3] K. J Geelhood and W. G. Luscher. Frapcon-4.0: Integral assessment. Technical Report PNNL-19418, Vol.2 Rev.2, Pacific Northwest National Laboratory, September 2015.
- [4] J Hou et al. Benchmark for Uncertainty Analysis in Modeling (UAM) for Design, Operation and Safety Analysis of LWRs, Volume II: Specification and Support Data for Core Cases. Technical report, OECD/NEA, 2017.
- [5] V. A. Mousseau et al. Demonstration of Integrated DA/UQ for VERA-CS on a Core Physics Progression Problem. *CASL*, (CASL-I-2014-0158-000), 2014.
- [6] J-M P Tournier and M S El-Genk. Properties of Noble Gases and Binary Mixtures for Closed Brayton Cycle Applications. *Energy Conversion and Management*, 49(3):469–492, 2008. doi: 10.1016/j.enconman.2007.06.050.
- [7] F. W. Sears and G. L. Salinger. *Thermodynamics, Kinetic Theory, and Statistical Thermodynamics*. Reading, Mass. : Addison–Wesley Pub. Co., 3rd edition, 1975.
- [8] R. L. Williamson, K. A. Gamble, D. M. Pereza, S. R. Novascone, G. Pastorea, R. J Gardner, J D. Hales, W. Liu, and A. Mai. Validating the BISON fuel performance code to integral LWR experiments. *Nuclear Engineering and Design*, 301:232–244, 2016. doi: 10.1016/j.nucengdes.2016.02.020.
- [9] K. J Geelhood and W. G. Luscher. FRAPTRAN-1.5: Integral Assessment. Technical Report NUREG/CR-7023; PNNL-19400; Vol.2 Rev.1, Pacific Northwest National Laboratory, Richland, WA 99352, May 2014.
- [10] D. R. Olander and A. T. Motta. *Light Water Reactor Materials*, volume I: Fundamentals. American Nuclear Society, 2017.
- [11] J Y. R. Rashid, S. K. Yagnik, and R. O. Montgomery. Light water reactor fuel performance modeling and multi-dimensional simulation. *J Metals*, 63:81–88, 2011. doi: 10.1007/s11837-011-0144-9.
- [12] Donald R. Olander. *Fundamental Aspects of Nuclear Reactor Fuel Elements*. National Technical Information Center, April 1976. doi: 10.2172/7343826.
- [13] S. Schlesinger et al. Terminology for model credibility. simulation. 32:103–104, 1979. doi= 10.1177/003754977903200304.

- [14] J Kestin, R Paul, A A Clifford, and W A Wakeham. Absolute determination of the thermal conductivity of the noble gases at room temperature up to 35 MPa. *J Physica*, 100A(2):349–369, 1980. doi: 10.1016/0378-4371(80)90125-9.
- [15] A Michels, J V Sengers, and L J M Klundert. The thermal conductivity of argon at elevated densities. *J Physica*, 29(2):149–160, 1963. doi: 10.1016/S0031-8914(63)80201-3.
- [16] B M Rosenbaum, S Oshen, and G Thodos. Thermal conductivity of argon in the dense gaseous and liquid regions. *J Chemical Physics*, 44:2831–38, 1966. doi: 10.1063/1.1727141.
- [17] J V Sengers, W T Bolk, and C J Stigter. The thermal conductivity of neon between 25°C and 75°C at pressures up to 2600 atmospheres. *J Physica*, 30(5):1018–1026, 1964. doi: 10.1016/0031-8914(64)90233-2.
- [18] E. H. Kennard. *Kinetic Theory of Gases, with an Introduction to Statistical Mechanics*. McGraw-Hill Book Company, inc., New York, London, 1938.
- [19] D. D. Lanning and C. R. Hann. Review of Methods Applicable to the Calculation of Gap Conductance in Zircaloy-Clad UO₂ Fuel Rods. Technical Report BNWL-1894, Pacific Northwest Laboratory, Richland, Washington, April 1975.
- [20] A. Ullman, R. Acharya, and D. R. Olander. Thermal accommodation coefficients of inert gases on stainless steel and UO₂. *J Nuclear Materials*, 51:277, 06 1974. doi: 10.1016/0022-3115(74)90016-6.
- [21] S Song and M M Yovanovich. Correlation of thermal accommodation coefficient for engineering surfaces. Pittsburgh, PA, August 1987. National Heat Transfer Conference.
- [22] J E. Garnier and S. Begej. Ex-reactor determination of thermal gap conductance between uranium dioxide and Zircaloy-4 interfaces. stage II: High gas pressure. Technical Report NUREG/CR-0330; PNL-3232; Vol. 2, Pacific Northwest Laboratory, May 1980. doi: 10.2172/1076471.
- [23] A Toptan, D J Kropaczek, and M N Avramova. Gap conductance modeling I: Theoretical considerations on the model for single- and multi-component gases. *J Nuclear Eng Design*, 2019. (under review).
- [24] D D Baron and L Hallstadius. 2.19 - Fuel Performance of Light Water Reactors (Uranium Oxide and MOX). *Comprehensive Nuclear Materials*, 2:481–514, 2012. doi: 10.1016/B978-0-08-056033-5.00040-9.
- [25] J E. Garnier and S. Begej. Ex-reactor determination of thermal gap and contact conductance between uranium dioxide and Zircaloy-4 interfaces. stage I: low gas pressure. Technical Report NUREG/CR-0330; PNL-2696; TRN: 79-016918, Pacific Northwest Laboratory, April 1979. doi: 10.2172/6268967.
- [26] W.G. Luscher, K.J Geelhood, and I.E. Porter. Material property correlations: Comparisons between frapcon-4.0, fraptran-2.0, and matpro. Technical Report PNNL-19417 Rev. 2, Pacific Northwest National Laboratory, September 2015.

- [27] P. J. Baldock, W. E. Spindler, and T. W. Baker. The x-ray thermal expansion of near-stoichiometric UO_2 . *J Nuclear Materials*, 18(3):305–313, 1966. doi: 10.1016/0022-3115(66)90171-1.
- [28] M. D. Burdick and H. S. Parker. Effect of particle size on bulk density and strength properties of uranium dioxide specimens. *J American Ceramic Society*, 39(5):181–187, 1956. doi: 10.1111/j.1151-2916.1956.tb15641.x.
- [29] F. Grønvold. High-temperature x-ray study of uranium oxides in the UO_2 - U_3O_8 region. *J Inorganic and Nuclear Chemistry*, 1(6):357–370, 1955. doi: 10.1016/0022-1902(55)80046-2.
- [30] J. A. Christensen. Thermal expansion and change in volume of uranium dioxide on melting. *J American Ceramic Society*, 46(12):607–608, 1963. doi: 10.1111/j.1151-2916.1963.tb14628.x.
- [31] C. P. Kempter and R. O. Elliott. Thermal expansion of $\langle \text{UN} \rangle$, $\langle \text{UO}_2 \rangle$, $\langle \text{UO}_2 \cdot \text{ThO}_2 \rangle$ and $\langle \text{ThO}_2 \rangle$. *J Chemical Physics*, 30(6):1524–1526, 1958. doi: 10.1063/1.1730230.
- [32] D. G. Martin. The thermal expansion of solid UO_2 and (U,Pu) mixed oxides a review and recommendations. *J Nuclear Materials*, 152(2–3):94–101, 1988. doi: 10.1016/0022-3115(88)90315-7.
- [33] A. C. Momin, E. B. Mirza, and M. D. Mathews. High temperature x-ray diffractometric studies on the lattice thermal expansion behaviour of UO_2 , ThO_2 and $(\text{U}_{0.2}\text{Th}_{0.8})\text{O}_2$ doped with fission product oxides. *J Nuclear Materials*, 185(3):308–310, 1991. doi: 10.1016/0022-3115(91)90521-8.
- [34] M. Tokar and A. W. Nutt. Thermal expansion of puo_2 from 25 to 1420°C . *Transaction of the American Nuclear Society*, 10:210–211, 1972.
- [35] N. H. Brett and L. E. Russell. The thermal expansion of puo_2 and some other actinide oxides between room temperature and 1000°C . *Proceedings of the Second International Conference on Plutonium Metallurgy*, pages 397–410, April 1960.
- [36] T. Fuketa. 2.22 - Transient Response of LWR Fuels (RIA). *Comprehensive Nuclear Materials*, 2:579–593, 2012. doi: 10.1016/B978-0-08-056033-5.00044-6.
- [37] H. Haario, M. Laine, A. Mira, and E. Saksman. DRAM: Efficient adaptive MCMC. *Statistics and Computing*, 16(4):339–354, 2006. doi: 10.1007/s11222-006-9438-0.
- [38] Marko Laine. MCMC toolbox for Matlab, March 2017.
- [39] OriginLab Corporation. Nag library function document, nag_2_sample_ks_test (g08cdc).
- [40] B. Kochunas, B. Collins, S. Stimpson, R. K. Salko, et al. VERA core simulator methodology for pressurized water reactor cycle depletion. *J Nuclear Engineering and Design*, 185(1):217–231, 2017. 10.13182/NSE16-39.
- [41] Mpack theory manual. Technical Report CASL-U-2016-1107-000, June 2016.

- [42] R. K. Salko, M. Avramova, et al. CTF Theory Manual. Technical Report CASL-U-2017-1263-000, CASL/NCSU, 2017.
- [43] J D. Hales et al. *BISON Theory Manual The Equations Behind Nuclear Fuel Analysis*. Idaho National Laboratory, Idaho Falls, Idaho, October 2014.
- [44] K. J Geelhood, W. G. Luscher, P. A. Raynaud, and I. E. Porter. FRAPCON-4.0: A computer code for the calculation of steady-state, thermal-mechanical behavior of oxide fuel rods for high burnup. Technical Report PNNL-19418, Vol.1 Rev.2, Pacific Northwest National Laboratory, September 2015.
- [45] K. J Geelhood, W. G. Luscher, and J M. Cuta. FRAPTRAN-1.5: A Computer Code for the Transient Analysis of Oxide Fuel Rods. Technical Report NUREG/CR-7023; PNNL-19400; Vol. 1. Rev. 1, Pacific Northwest National Laboratory, Richland, WA 99352, 2014.
- [46] K. Lassman, A. Schubert, P. Van Uffelen, C. Hyorbi, and J van de Laar. TRANSURANUS Handbook. Technical report, Institute for Transuranium Elements, 1975-2011.
- [47] Y. Rashid, R. Dunham, and R. Montgomery. Fuel Analysis and Licensing Code: FALCON MOD01, Volume 1: Theoretical and Numerical Bases. Technical Report EPRI 1011307, Electric Power Research Institute, December 2004.
- [48] J D. Hales, R. L. Williamson, S. R. Novascone, G. Pastore, B. W. Spencer, D. S. Stafford, K. A. Gamble, D. M. Perez, R. J Gardner, W. Liu, J Galloway, C. Matthews, C. Unal, and N. Carlson. BISON Theory Manual - The Equations Behind Nuclear Fuel Analysis. Technical Report INL/EXT-13-29930 Rev. 3, Idaho National Laboratory, September 2016.
- [49] D.L. Hagrman, G.A. REymann, and R.E. Manson. Matpro-version 11 (revision 1): A handbook of materials properties for use in the analysis of light water reactor fuel rod behavior. USNRC Report NUREG/CR-0497, TREE-1290, Idaho National Engineering Laboratories, February 1980.
- [50] Fuel Densification. Technical Report Point Beach Nuclear Plant, Unit 2, Docket 50301-78, Wisconsin Electric Power Company, December 1972.
- [51] J M. Gandhi and S. C. Saxena. Correlated thermal conductivity data of rare gases and their binary mixts. at ordinary pressures. *J Chemical & Engineering Data*, 13(3):357–361, 07 1968. doi: 10.1021/je60038a016.
- [52] A. M. Ross and R. L. Stoute. Heat Transfer Coefficient Between UO₂ and Zircaloy-2. Technical Report CRFD-1075; AECL-1552, Atomic Energy of Canada, Chalk River, Ontario, June 1962.
- [53] W. L. Oberkampf and C. J Roy. *Verification and Validation in Scientific Computing*. Cambridge University Press, Cambridge, UK, first edition, November 2010.
- [54] W. L. Oberkampf, M. Pilch, and T. G. Trucano. Predictive Capability Maturity Model for Computational Modeling and Simulation. Technical Report SAND2007-5948, Sandia National Laboratories, October 2007.

- [55] T. G. Trucano, L. P. Swiler, T. Igusa, W. L. Oberkampf, and M. Pilch. Calibration, Validation, and Sensitivity Analysis: What’s What. *Reliability Engineering and System Safety*, 91:1131–1357, 2006. doi: 10.1016/j.ress.2005.11.031.
- [56] Roger W. Logan and Cynthia K. Nitta. Verification & validation: Process and levels leading to qualitative or quantitative validation statements. *SAE Transactions*, 113:804–816, 2004.
- [57] W. L. Oberkampf, T. G. Trucano, and C. Hirsch. Verification, validation, and predictive capability in computational engineering and physics. *ASME Applied Mechanics Reviews*, 57(5):345–384, 2004. doi: 10.1115/1.1767847.
- [58] P. J. Roache. Code verification by the method of manufactured solutions. *ASME J Fluids Engineering*, 124(1):4–10, 2001. doi: 10.1115/1.1436090.
- [59] P. J. Roache. *Verification and Validation in Computational Science and Engineering*. Hermosa Publishers, 1998.
- [60] S. Eddins. Taking control of your code: Essential software development tools for engineers. Atlanta, GA, 2006. International Conference on Image Processing.
- [61] B. Kleb and W. A. Wood. Computational simulations and the scientific method. *J Aerospace Computing, Information, and Communication*, 3(6):244–250, 2006. doi: 10.2514/1.12949.
- [62] R. S. Pressman. *Software Engineering: A Practitioner’s Approach*. McGraw-Hill, Boston, MA, 2005.
- [63] P. F. Duvall, S. M. Matyas, and A. Glover. *Continuous Integration: Improving Software Quality and Reducing Risk*. Addison-Wesley Professional, first edition, 2007.
- [64] P. M. Knupp and C. C. Ober. A code-verification evidence-generation process model and checklist. Technical Report SAND20084832, Sandia National Laboratories, 2008.
- [65] T. G. Trucano, M. Pilch, and W. L. Oberkampf. On the role of code comparison in verification and validation. Sandia Report SAND2003-2752, Sandia National Laboratories, August 2003.
- [66] W. L. Oberkampf, M. Pilch, and T. G. Trucano. Predictive Capability Maturity Model for Computational Modeling and Simulation. Technical Report SAND2007-5948, Sandia National Laboratories, October 2007.
- [67] T. G. Trucano, L. P. Swiler, T. Igusa, W. L. Oberkampf, and M. Pilch. Calibration, Validation, and Sensitivity Analysis: What’s What. *Reliability Engineering and System Safety*, 91(10–11):1331–1357, 2006. doi: 10.1016/j.ress.2005.11.031.
- [68] Armen Der Kiureghian and Ove Ditlevsen. Aleatory or epistemic? does it matter? *J Structural Safety*, 31:105–112, 2009. doi: 10.1016/j.strusafe.2008.06.020.

- [69] M C Kennedy and Anthony O'Hagan. Bayesian calibration of computer models. *J Royal Statistical Society B*, 63(3):425–464, 2001. doi: 10.1111/1467-9868.00294.
- [70] B. M. Adams, L. E. Bauman, W. J Bohnhoff, K. R. Dalbey, M. S. Ebeida, J. P. Eddy, M. S. Eldred, P. D. Hough, K. T. Hu, J. D. Jakeman, J. A. Stephens, L. P. Swiler, D. M. Vigil, and T. M. Wildey. Dakota, A Multilevel Parallel Object–Oriented Framework for Design Optimization, Parameter Estimation, Uncertainty Quantification, and Sensitivity Analysis: Version 6.0 Users Manual. Sandia Technical Report SAND2014-4633, Sandia National Laboratories, November 2015.
- [71] J A Nelder and R Mead. A simplex method for function minimization. *The Computer Journal*, 7(4):308–313, 1965. doi: 10.1093/comjnl/7.4.308.
- [72] K A Maupin, L P Swiler, and N W Porter. Validation metrics for deterministic and probabilistic data. *J Verif Valid Uncert*, 3(3), January 2019. doi: 10.1115/1.4042443.
- [73] L. Tierney. Markov Chains for Exploring Posterior Distributions. *The Annals of Statistics*, 22(4):1701–1762, 1994. doi: 10.1214/aos/1176325750.
- [74] H. Haario, E. Saksman, and J Tamminen. Adaptive Proposal Distribution for Random Walk Metropolis Algorithm. *Computational Statistics*, 14(3):375–395, 1994. doi: 10.1007/s001800050022.
- [75] H. Haario, E. Saksman, and J Tamminen. An Adaptive Metropolis Algorithm. *Bernoulli*, 7(2):223–242, 2001. doi: 10.2307/3318737.
- [76] L. Tierney and A. Mira. Some Adaptive Monte Carlo Methods for Bayesian Inference. *Statistics in Medicine*, 18(17–18):2507–2515, 1999. doi: 10.1002/(SICI)1097-0258(19990915/30)18:17/18;2507::AID-SIM272;3.0.CO;2-J.
- [77] P. J. Green and A. Mira. Delayed Rejection in Reversible Jump Metropolis-Hastings. *Biometrika*, 88(4):1035–1053, 2001. doi: 10.1093/biomet/88.4.1035.
- [78] A. Mira. Ordering and Improving the Performance of Monte Carlo Markov Chains. *Statistical Science*, 16(4):340–350, 2002. doi: 10.1214/ss/1015346319.
- [79] S. P. Brooks and G. O. Roberts. Assessing Convergence of Markov Chain Monte Carlo Algorithms. *Statistics and Computing*, 8(4):319–335, 1998. doi: 10.1023/A:1008820505350.
- [80] M. Rosenblatt. Remarks on Some Nonparametric Estimates of a Density Function. *Ann. Math. Statist.*, 27(3):832–837, 2004. doi: 10.1214/aoms/1177728190.
- [81] T. Ledl. Kernel Density Estimation: Theory and Application in Discriminant Analysis. *Austrian Journal of Statistics*, 33(3):267–279, 2004. doi: 10.17713/ajs.v33i3.441.
- [82] A. N. Kolmogorov. Sulla Determinazione Empirica di una Legge di Distribuzione. *Giornale dell'Istituto Italiano degli Attuari*, 4:83–91, 1933.

- [83] N. V. Smirnov. On the Estimation of the Discrepancy Between Empirical Curves of Distribution for Two Independent Samples. *Bulletin Mathematique de l'Universite de Moscou*, 2, 1939.
- [84] N. V. Smirnov. Table for Estimating the Goodness of Fit of Empirical Distributions. *Ann. Math. Statist.*, 19(2):279–281, 1948. doi: 10.1214/aoms/1177730256.
- [85] The Consortium for Advanced Simulation of Light Water Reactors.
- [86] J. A. Turner, K. Clarno, M. Sieger, R. Bartlett, B. Collins, R. P. Pawlowski, R. C. Schmidt, and R. Summers. The Virtual Environment for Reactor Applications (VERA). *J Computational Physics*, 326:544–568, 2016. doi: 10.1016/j.jcp.2016.09.003.
- [87] C. W. Stewart, J M. Cuta, A. S. Koontz, J M. Kelly, K. L. Basehore, T. L. George, and D. S. Rowe. VIPRE-01 A Thermal-Hydraulics Analysis Code for Reactor Cores: Volume 1, Mathematical Modeling. [PWR; BWR]. Technical Report EPRI-NP-2511-CCM-Vol.1; ON: DE83013094, Battelle Pacific Northwest Labs., Richland, WA (USA), 1983.
- [88] C. E. Beyer, C. R. Hann, D. D. Lanning, F. E. Panisko, and L. J Parchen. GAPCON-Thermal 2: A Computer Program for Calculating the Thermal Behavior of an Oxide Fuel Rod. Technical Report BNWL-1898, Pacific Northwest Laboratories, Richland, WA 99352, November 1975.
- [89] D. D. Lanning, C. L. Mohr, F. E. Panisko, and K. B. Stewart. GAPCON-Thermal-3: Code Description. Technical Report PNL-2434; NRC-1, 3, Pacific Northwest Laboratories, January 1978.
- [90] J Dearien et al. FRAP-S3: A Computer Code for the Steady- State Analysis of Oxide Fuel Rods- Report I, Analytical Models and Input Manual. Technical Report TFBP-TR-164, Idaho National Engineering Laboratory, Idaho Falls, Idaho, October 1977.
- [91] L. J Siefken, M. P. Bohn, S. O. Peck, and J A. Dearien. FRAP-T5: A Computer Code for Transient Analysis of Oxide Fuel Rods. Technical Report NUREG/CR-0840; TREE-1281, Idaho National Engineering Laboratory, 1979.
- [92] G. A. Berna et al. FRAPCON-1: A Computer Code for the Steady-State Analysis of Oxide Fuel Rods. Technical Report CDAP-TR-032-R1, Idaho National Engineering Laboratory, Idaho Falls, Idaho, 1978.
- [93] A. Toptan, R. K. Salko, M. N. Avramova, D. J Kropaczek, and K. Clarno. Assessment Of The Newly Developed Fuel Solver Code, CTFFuel. In *Multi-Physics Multi-Scale Simulations with Uncertainty*, number BEPU2018-255 in The Best Estimate Plus Uncertainty International Conference, Lucca, Italy, 2018.
- [94] A. Toptan, R. K. Salko, and M. N. Avramova. CTFFuel User's Manual. Technical report, CASL/NCSU, 2017.
- [95] A. Toptan, R. K. Salko, and M. N. Avramova. Development and assessment of ctffuel. Milestone Report CASL-U-2017-1418-000, CASL, September 2017.

- [96] M. Sieger. CASL-QA-030 CASL Software Quality Assurance Requirements. Technical Report CASL-U-2015-0010-000, Consortium for Advanced Simulation of Light Water Reactors, 2015.
- [97] A. Toptan, R. K. Salko, M. N. Avramova, K. Clarno, and D. J Kropaczek. Continuing Efforts for CTFFuel’s SQA & Its Comparison to FRAPTRAN for RIA Transient. Milestone Report CASL-U-2018-1549-000, CASL, Oak Ridge, TN, March 2018.
- [98] M. J Thurgood et al. COBRA/TRAC - A Thermal-Hydraulics Code for Transient Analysis of Nuclear Reactor Vessels and Primary Coolant Systems. Equations and Constitutive Models NUREG/CR-3046, PNL-4385, Vol. 1, R4, Pacific Northwest Laboratory, Richland, WA 99352, 1982.
- [99] A. Toptan, R. K. Salko, and M. N. Avramova. Review of CTF’s Fuel Rod Modeling Using FRAPCON-4.0’s Centerline Temperature Predictions. In *Transactions of the American Nuclear Society*, volume 116, 2017.
- [100] H. Y. Wong. A Survey of the Thermal Conductance of Metallic Contacts. Technical Report C.P. No. 973, Ministry of Technology, 1968.
- [101] A Toptan, R K Salko, M N Avramova, K Clarno, and D J Kropaczek. A new fuel modeling capability, CTFFuel, with a case study on the fuel thermal conductivity degradation. *Nuclear Eng Design*, 341:248–258, 2018. doi: 10.1016/j.nucengdes.2018.11.010.
- [102] M. P. Bohn. FRACAS: A Subcode for the Analysis of Fuel Pellet–Cladding Mechanical Interaction. Technical Report TREE-NUREG-1028, EG&E Idaho, Inc., Idaho National Engineering Laboratory, Idaho Falls, ID, 1977.
- [103] A. Toptan and M. N. Avramova. Advances in Fuel Rod Modeling in Subchannel Thermal–hydraulic Codes. In *Transactions of the American Nuclear Society*, volume 115, 2016.
- [104] A. Toptan, R. K. Salko, and M. N. Avramova. Fuel rod modeling in ctf: Incorporation of burnup dependent fuel thermal conductivity models and review of ctf’s dynamic gap conductance model. Milestone Report CASL-U-2016-1181-000, CASL, Oak Ridge, TN, 2016.
- [105] A. Toptan, R. K. Salko, M. N. Avramova, D. J Kropaczek, and K. Clarno. Development and Assessment of CTFFuel. Technical Report CASL-U-2017-1418-000, CASL, 2017.
- [106] A. Toptan, R. K. Salko, M. N. Avramova, K. Clarno, and D. J Kropaczek. Continuing Efforts for CTFFuel’s SQA & Its Comparison to FRAPTRAN for RIA Transient. Technical Report CASL-U-2018-1549-000, CASL, March 2018.
- [107] M. O. Yilmaz, M. N. Avramova, and J G. M. Andersen. Development, verification, and validation of a fuel thermal conductivity degradation model in ctf. *Annals of Nuclear Energy*, 97:246–261, November 2016. doi: 10.1016/j.anucene.2016.07.020.
- [108] Rudy J M. Konings, T. R. Allen, R. E. Stoller, and S. Yamanaka, editors. *Comprehensive Nuclear Materials*, volume 2. Elsevier Ltd., Amsterdam, Netherlands, 2012.

- [109] Donald R. Olander. *Fundamental Aspects of Nuclear Reactor Fuel Elements*. Technical Information Center, Office of Public Affairs, Energy Research and Development Administration, April 1976.
- [110] P. G. Lucuta, HJ Matzke, and I. J Hastings. A Pragmatic Approach to Modelling Thermal Conductivity of Irradiated UO₂ Fuel: Review and Recommendations. *J Nuclear Materials*, 232:166–180, 1996. doi: 10.1016/S0022-3115(96)00404-7.
- [111] D. R. Olander and A. T. Motta. *Light Water Reactor Materials*, volume I: Fundamentals. American Nuclear Society, 2017.
- [112] P. E. MacDonald et al. Matpro - version 9: A handbook of materials properties for use in the analysis of light water reactor fuel rod behavior. Technical Report TREE-NUREG-1005, Idaho National Engineering Laboratories, 1976.
- [113] D. D. Lanning, C. E. Beyer, and K. J Geelhood. Frapcon-3 updates, including mixed-oxide fuel properties. Technical Report PNNL-11513, Pacific Northwest National Laboratory, Richland, WA, 2005.
- [114] K. Ohira and N. Itagaki. Thermal conductivity measurements of high burnup uo₂ pellet and a benchmark calculation of fuel center temperature. pages 541–549, Portland, Oregon, March 2-6 1997. ANS Topical Meeting on Light Water Reactor Fuel Performance.
- [115] C. Duriez, J-P. Alessandri, T. Gervais, and Y. Philipponneau. Thermal Conductivity of Hypostoichiometric Low Pu Content (U,Pu)O_{2-x} Mixed Oxide. *J Nuclear Materials*, 277:143–158, 2000. doi: 10.1016/S0022-3115(99)00205-6.
- [116] M. N. Avramova et al. Ctf user’s manual. Technical Report CASL-U-2017-1262-000, CASL/NCSU, 2017.
- [117] D.D. Lanning. Irradiation history and final post-irradiation data for ifa-432. Technical Report PNL-5977, Pacific Northwest Laboratory, Richland, Washington, 1986.
- [118] T. Tverberg and M. Amaya. Study of Thermal Behaviour of UO₂ and (U,Gd)O₂ to High Burnup (IFA-515). Technical Report HWR-671, OECD Halden Reactor Project, Halden, Norway, 2001.
- [119] Turnbull and White 2002. The thermal performance of the gas flow rigs: A review of experiments and their analyses. Technical Report HWR-715, OECD Halden Reactor Project, Halden, Norway, 2002.
- [120] W. Wiesnack. Experimental techniques and results related to high burn-up investigations at the oecd halden reactor project. Number IAEA-TECDOC-697, page 118, Pembroke, Ontario, Canada, April 28-May 1 1992. In Proceedings of a Technical Committee Meeting.
- [121] I. Matsson and J.A. Turnbull. The integral fuel rod behaviour test ifa-597.3: Analysis of the measurements. Technical Report HWR-543, OECD Halden Reactor Project, Halden, Norway, 1998.

- [122] B. Thérache. Thermal performance, densification, swelling, fission gas release, pcmi, uO_2 , doped uO_2 . Technical Report HWR-819, OECD Halden Reactor Project, Halden, Norway, 2005.
- [123] R. Jösef. The high initial rating test ifa-677.1: Final report on in-pile results. Technical Report HWR-872, OECD Halden Reactor Project, Halden, Norway, 2008.
- [124] L. Klecha. Comparative Integral Irradiation Test on Gadolina Fuel (IFA-681). Technical Report HWR-872, OECD Halden Reactor Project, Halden, Norway, 2006.
- [125] T. Tverberg, B. Volkov, and J-C. Kim. Final report on the uO_2 - Gd_2O_3 fuel performance test in ifa-636. Technical Report HWR-817, OECD Halden Reactor Project, Halden, Norway, 2005.
- [126] H. Koike. The MOX Fuel Behaviour Test IFA-597.4/.5/.6/.7; Summary of In-Pile Fuel Temperature and Gas Release Data. Technical Report HWR-729, OECD Halden Reactor Project, Halden, Norway, 2004.
- [127] L. Mertens, M. Lippens, and J Alvis. The figaro programme: The behaviour of irradiated mox fuel tested in the ifa-606 experiment, description of results and comparison with comethe calculation. Technical Report HPR 349/30, OECD Halden Reactor Project, Halden, Norway, 1998.
- [128] L. Mertens and M. Lippens. Study of fission gas release on high burnup mox fuel. In *ENS Topfuel 2001 Conference*, Stockholm, Sweden, May 28-30 2001.
- [129] S. Beguin. The lift-off experiment with mox fuel rod in ifa-610.2 initial results. Technical Report HWR-603, OECD Halden Reactor Project, Halden, Norway, 1999.
- [130] H. Fujii and J Claudel. The lift-off experiments, ifa-610.3 (uO_2), and ifa-610.4 (mox) evaluation of in-pile measurement data. Technical Report HWR-650, OECD Halden Reactor Project, Halden, Norway, 2001.
- [131] R.J White. The re-irradiation of mimas mox fuel in ifa-629.1. Technical Report HWR-586, OECD Halden Reactor Project, Halden, Norway, 1999.
- [132] B. Petiprez. Ramp tests with two high burnup mox fuel rods in ifa-629.3. Technical Report HWR-714, OECD Halden Reactor Project, Halden, Norway, 2002.
- [133] J Wright. The SBR MOX and UO_2 Comparison Test in Gas Flow Rig IFA-633: Results after Seven Cycles of Irradiation. Technical Report HWR-764, OECD Halden Reactor Project, Halden, Norway, 2004.
- [134] J Claudel and F. Huet. Results from the burnup accumulation test with high exposure (63mwd.kg hm) model fuel (ifa-648). Technical Report HWR-651, OECD Halden Reactor Project, Halden, Norway, 2001.
- [135] P. Blair and J Wright. The IFM/MOX Comparative Test, IFA-651.1: Results after Four Cycles of Irradiation. Technical Report HWR-763, OECD Halden Reactor Project, Halden, Norway, 2004.

- [136] T. Kozłowski and T. J. Downar. PWR MOX/UO₂ core transient benchmark. Technical Report NEA/NSC/DOC(2006)20, Nuclear Energy Agency, January 2007.
- [137] T. Kozłowski and T. J. Downar. PWR MOX/UO₂ Core Transient Benchmark. Final Report NEA/NSC/DOC(2006)20, NEA, January 2007.
- [138] S. S. Wilks. Determination of Sample Sizes for Setting Tolerance Limits. *Ann. Math. Stat.*, 12:91–96, 1941. doi: 10.1214/aoms/1177731788.
- [139] Best Estimate Safety Analysis For Nuclear Power Plants: Uncertainty Evaluation. Technical Report Safety Reports Series No. 52, INTERNATIONAL ATOMIC ENERGY AGENCY, Vienna, Austria, 2008.
- [140] L. Klecha. Comparative Integral Irradiation Test on Gadolinia Fuel (IFA-681). Technical Report HWR-832, OECD Halden Reactor Project, Halden, Norway, 2006.
- [141] D. D. Lanning, C. E. Beyer, and K. J. Geelhood. *FRAPCON-3 Updates, Including Mixed-Oxide Fuel Properties*. Richland, WA 99352, May 2005.
- [142] M. Grounes and H. Tomani. Tying up fuel rod overpressure problems with ROPE I and II. *J Nuclear Eng International*, 37(451):30–32, 1992.
- [143] M. Grounes, C. Gräslund, G. Lysell, and H. Tomani. Fuel R&D at Studsvik III. Studies of special phenomena in fuel behaviour: lift-off and defect fuel degradation. *J Nuclear Eng and Design*, 168(1–3):167–176, 1997. doi: 10.1016/S0029-5493(96)01369-6.
- [144] M. Grounes, H. Tomani, A. Lassing, and M. Carlsson. Fuel R&D at Studsvik I. Introduction and experimental facilities. *J Nuclear Eng and Design*, 168(1–3):129–149, 1997. doi: 10.1016/S0029-5493(96)01367-2.
- [145] A. Toptan, R. K. Salko, M. N. Avramova, K. Clarno, and D. J. Kropaczek. A new fuel modeling capability, CTFFuel, with a case study on the fuel thermal conductivity degradation. *Nuclear Eng Design*, 341:248–258, 2018. doi: 10.1016/j.nucengdes.2018.11.010.
- [146] W. G. Kannuiliuk and H. B. Donald. The Pressure Dependence of the Thermal Conductivity of Polyatomic Gases at 0°C. *Aust J Scientific Research*, 3(3):417–427, 1950. doi: 10.1071/CH9500417.
- [147] R. G. Vines and L. A. Bennett. The Thermal Conductivity of Organic Vapors. The Relationship between Thermal Conductivity and Viscosity, and the Significance of the Eucken Factor. *J Chemical Physics*, 22(3):360, 1954. doi: 10.1063/1.1740075.
- [148] B. E. Poling, J. M. Prausnitz, and J. P. O’Connell. *The Properties of Gases and Liquids*. McGraw–Hill, 5 edition, 2000.
- [149] V. A. Mousseau et al. Demonstration of Integrated DA/UQ for VERA-CS on a Core Physics Progression Problem. Technical Report CASL-I-2014-0158-000, CASL, 2014.
- [150] J.-M. P. Tournier and M. S. El-Genk. Properties of Helium, Nitrogen, and HeN₂ Binary Gas Mixtures. *Thermophysics and Heat Transfer*, 22(3):442–456, 2007. doi: 10.2514/1.36283.

- [151] H L Johnston and E R Grilly. The thermal conductivities of eight common gases between 80° and 380°K. *J Chemical Physics*, 14:233–238, 1946. doi: 10.1063/1.1724125.
- [152] W G Kannuluik and E H Carman. The thermal conductivity of rare gases. *Proceedings of the Physical Society. Section B*, 65(9):701–709, 1952. doi: 10.1088/0370-1301/65/9/307.
- [153] VPS Nain, R A Aziz, P C Jain, and S C Saxena. Interatomic potentials and transport properties for neon, argon, and krypton. *J Chemical Physics*, 65:3242–3249, 1976. doi: 10.1063/1.433497.
- [154] V. K. Saxena and S. C. Saxena. Thermal conductivity of krypton and xenon in the temperature range 350–1500°K. *J Chemical Physics*, 51(8):3361–3368, 1969. doi: 10.1063/1.1672520.
- [155] P J Freud and G M Rothberg. Method for measuring pressure dependence of thermal conductivity of gases. *The Review of Scientific Instruments*, 38(2):238–242, 1967. doi: 10.1063/1.1771364.
- [156] J D van der Waals. *Beiblätter Ann Physik*, 5:250, 1881.
- [157] E J Owens and G Thodos. Thermal-conductivity-reduced-state Correlation for the Inert Gases. *J AIChE*, 3(4):454–461, 1957. doi: 10.1002/aic.690030407.
- [158] P Gray, S Holland, and A O S Maczek. Thermal Conductivities of Binary Mixtures of Organic Vapours and Inert Diluents. *Trans Faraday Society*, 66:107, 1970. doi: 10.1039/TF9706600107.
- [159] D Misić and G Thodos. The Thermal Conductivity of Hydrocarbon Gases at Normal Pressures. *J AIChE*, 7(2):264, 1961. doi: 10.1002/aic.690070219.
- [160] J O Hirschfelder, C F Curtiss, and R B Bird. *Molecular Theory of Gases and Liquids*. John Wiley and Sons, Inc., New York, 1954.
- [161] D Enskog. *Kinetische Theorie der Vorgänge in Mässig Verdünnten Gasen, Inaugural Dissertation*. Teildruck Diss. Universität Uppsala, 1917.
- [162] C F Curtiss and J O Hirschfelder. Transport Properties of Multicomponent Gas Mixtures. *J Chemical Physics*, 17:550–555, 1949. doi: 10.1063/1.1747319.
- [163] A. Wassilijewa. Wärmeleitung in Gasgemischen. *Physikalische Zeitschrift*, 5(22):737–742, 1904.
- [164] W Sutherland. XXXVII. The Viscosity of Mixed Gases. *The London, Edinburgh, and Dublin Philosophical Magazine and Journal of Science*, 40:421–431, 1895. doi: 10.1080/14786449508620789.
- [165] A. L. Lindsay and L. A. Bromley. Thermal Conductivity of Gas Mixtures. *Industrial and Engineering Chemistry*, 42(8):1508–1511, 1950. doi: 10.1021/ie50488a017.

- [166] J W Buddenberg and C R Wilke. Calculation of gas mixture viscosities. *Industrial & Engineering Chemistry*, 41(7):1345–1347, 1949. doi: 10.1021/ie50475a011.
- [167] R. S. Brokaw. Energy Transport in High Temperature and Reacting Gases. 1959.
- [168] R. S. Brokaw. Approximate Formulas for the Viscosity and Thermal Conductivity of Gas Mixtures. *J Chemical Physics*, 29(2):391–397, 1958. doi: 10.1063/1.1744491.
- [169] E. A. Mason and S. C. Saxena. Approximate formula for the thermal conductivity of gas mixtures. *Physics of Fluids*, 1(5):361–369, 1958. doi: 10.1063/1.1724352.
- [170] J. O. Hirschfelder. Proceedings of the joint conference on thermodynamic and transport properties of fluids. London, July 1958. Institution of Mechanical Engineers.
- [171] A Eucken. Über das wärmeleitvermögen, die spezifische wärme und die innere reibung der gase. *Physikalische Zeitschrift*, 14:324–332, 1913.
- [172] J O Hirschfelder. Heat conductivity in polyatomic or electronically excited gases. II. *J Chemical Physics*, 26:282–285, 1957. doi: 10.1063/1.1743285.
- [173] A K Barua. Thermal conductivity and Eucken type correction for binary mixtures of N₂ with some rare gases. *J Physica*, 25:1275–1286, 1959. doi: 10.1016/0031-8914(59)90049-7.
- [174] T L Ibbs and A A Hirst. The Thermal Conductivity of Gas Mixtures. *Proceedings of the Royal Society of London. Series A, Containing Papers of a Mathematical and Physical Character*, 123(791):134–142, 1929. doi: 10.1098/rspa.1929.0060.
- [175] J N Peterson, T F Hahn, and E W Comings. Thermal conductivity of mixtures of argon-helium, argon-nitrogen, and argon-neon. *J AIChE*, 17(2):289–291, 1971. doi: 10.1002/aic.690170211.
- [176] B. N. Srivastava and A. K. Barua. Thermal conductivity and eucken correction for diatomic gases and binary gas mixtures. *J Chemical Physics*, 30(5):1200–1205, 1959. doi: 10.1063/1.1730155.
- [177] B. N. Srivastava and A. K. Barua. Thermal conductivity of binary mixtures of diatomic and monatomic gases. *J Chemical Physics*, 32(2):427–435, 1960. doi: 10.1063/1.1730711.
- [178] M Yorizane, S Yoshimura, H Masuoka, and H Yoshida. Thermal Conductivities of Binary Gas Mixtures at High Pressures: Nitrogen-Oxygen, Nitrogen-Argon, Carbon dioxide-Argon, and Carbon dioxide-Methane. *J Ind Eng Chem Fundamen*, 22(4):458–463, 1983. doi: 10.1021/i100012a018.
- [179] L I Stiel and G Thodos. The Thermal Conductivity of Nonpolar Substances in the Dense Gaseous and Liquid Regions. *J AIChE*, 10(1):26–30, 1964. doi: 10.1002/aic.690100114.
- [180] T H Chung, L L Lee, and K E Starling. Applications of Kinetic Gas Theories and Multi-parameter Correlation for Prediction of Dilute Gas Viscosity and Thermal Conductivity. *J Ind Eng Chem Fundamen*, 23(1):8–13, 1984. doi: 10.1021/i100013a002.

- [181] T H Chung, M Ajlan, L L Lee, and K E Starling. Generalized Multiparameter Correlation for Nonpolar and Polar Fluid Transport Properties. *J Ind Eng Chem Res*, 27(4):671–679, 1988. doi: 10.1021/ie00076a024.
- [182] B. N. Srivastava and A. K. Barua. Formulas for thermal conductivity of ternary gas mixtures. *J Chemical Physics*, 27(2):583–584, 1957. doi: 10.1063/1.1743774.
- [183] J Wachsmuth. *Physik*, 235, 1908.
- [184] H von Ubisch. *Arkiv Fysik*, 16, 1959.
- [185] S. C. Saxena. Thermal conductivity of He–A–Xe ternary mixture. *J Chemical Physics*, 25:360–361, 1956. doi: 10.1063/1.1742891.
- [186] C Muckenfuss and C F Curtiss. Thermal conductivity of multicomponent gas mixtures. *J Chemical Physics*, 29(6):1273–1277, 1958. doi: 10.1063/1.1744709.
- [187] E. A. Mason and S. C. Saxena. Thermal conductivity of multicomponent gas mixtures. ii. *J Chemical Physics*, 31(2):511–514, 1959. doi: 10.1063/1.1730386.
- [188] W Van Dael and H Cauwenbergh. Measurements of the thermal conductivity of gases: I. experimental method. data for pure gases. *Physica*, 40:165–172, 1968. doi: 10.1016/0031-8914(68)90014-1.
- [189] D Burnett. Viscosity and thermal conductivity of gas mixtures. accuracy of some empirical formulas. *J Chemical Physics*, 42(7):2533–2540, 1965. doi: 10.1063/1.1696328.
- [190] A A Clifford, R Fleeter, J Kestin, and W A Wakeham. Thermal conductivity of some mixtures of monatomic gases at room temperature and at pressures up to 15 MPa. *J Physica*, 98(3):467–490, 1979. doi: 10.1016/0378-4371(79)90148-1.
- [191] H K Onnes. Expression of the Equation of State of Gases and Liquids by Means of Series. in *Koninklijke Nederlandse Akademie van Wetenschappen Proceedings Series B Physical Sciences*, 4:125–147, 1901.
- [192] E A Mason and T H Spurling. *The Virial Equation of State*. Toronto, Pergamon Press, 1969.
- [193] W. R. Lloyd et al. Heat Transfer in Multi-Component Monatomic Gases in the Low, Intermediate, and High Pressure Regime. In *Nuclear Thermionics Conference*, 1978.
- [194] S.K. Loyalka. Temperature Jump in a Gas Mixture. *Physics Fluids*, 17(5):897–899, 1974. doi: 10.1063/1.1694828.
- [195] R O A Hall and D G Martin. The evaluation of temperature jump distances and thermal accommodation coefficients from measurements of the thermal conductivity of UO₂ packed sphere beds. 101(3):249–258, 1987. doi: 10.1016/0029-5493(87)90053-7.
- [196] S M S Wahid and C V Madhusudana. Gap conductance in contact heat transfer. *Int J Heat and Mass Transfer*, 43(24):4483–4487, 2000. doi: 10.1016/S0017-9310(00)00071-5.

- [197] T D Eastop and A McConkey. *Applied Thermodynamics for Engineering Technologists*. Pearson Education Ltd, Longman, New York, 5 edition, 1970.
- [198] R M Smoluchowski. Ueber wärmeleitung in verdünnten gasen. *Annalen der Physik*, 300(1):101–130, 1898. doi: 10.1002/andp.18983000110.
- [199] M. Knudsen. Die molekulare Wärmeleitung der Gase und der Akkommodationskoeffizient. *Annalen Der Physik*, 34(4):593–656, 1911. doi: 10.1002/andp.19113390402.
- [200] B Baule. Theoretische behandlung der erscheinungen in verdünnten gasen. *Annalen der Physik*, 349(9):145–176, 1914. doi: 10.1002/andp.19143490908.
- [201] F O Goodman and H Y Wachman. Formula for Thermal Accommodation Coefficients. *J Chemical Physics*, 46(6):2376–2386, 1967. doi: 10.1063/1.1841046.
- [202] H Mikami, Y Endo, and Y Takashima. Heat transfer from a sphere to rarefied gas mixtures. *Int J Heat and Mass Transfer*, 9(12):1435–1448, 1966. doi: 10.1016/0017-9310(66)90139-6.
- [203] F. Kottler. Elektrostatik der Leiter. *Theorien der Elektrizität Elektrostatik*, 12:472–473, 1927. doi: 10.1007/978-3-642-99428-9_4.
- [204] J. C. Maxwell. *A Treatise on Electricity and Magnetism*, volume I of *Clarendon Press Series*. Oxford University Press, London, 1873.
- [205] R. Holm. *Electrical Contacts Handbook*. Springer Verlag, Berlin, 1958.
- [206] W. T. Clark and R. W. Powell. Measurement of Thermal Conduction by the Thermal Comparator. *J Scientific Instruments*, 39(11):545–551, 1962. doi: 10.1088/0950-7671/39/11/303.
- [207] A. M. Clausing and B. T. Chao. Thermal Contact Resistance in A Vacuum Environment. *J Heat Transfer*, 87(2):243–250, May 1965. doi: 10.1115/1.3689082.
- [208] J F. Archard. Elastic Deformation and the Contact of Surfaces. *Nature*, 172:918 – 919, 11 1953. doi: 10.1038/172918a0.
- [209] J F. Archard. Elastic Deformation and the Laws of Friction. *Proceedings of the Royal Society of London, Series A, Mathematical and Physical Sciences*, 243(1233):190–205, 12 1957. doi: 10.1098/rspa.1957.0214.
- [210] F. P. Bowden and D. Tabor. *The Friction and Lubrication of Solids*. Oxford University Press, New York, 1950.
- [211] T. N. Cetinkale and M. Fishenden. Thermal Conductance of Metal Surfaces in Contact. In *General Discussion on Heat Transfer*, pages 271–275. Conf. of Inst. of Mech. Eng. and ASME, September 1951.
- [212] F. Boeschoten and E. Van der Held. The Thermal Conductance of Contacts Between Aluminum and Other Metals. *Physica*, 23:37–44, 1957. doi: 10.1016/S0031-8914(57)90236-7.

- [213] H. Fenech and W. M. Rohsenow. Thermal Conductance of Metal Surfaces in Contact. USAEC Report NYO-2136, Massachusetts Inst. of Tech., Cambridge. Heat Transfer Lab., 1959.
- [214] L. C. Laming. Thermal Conductance of Machined Metal Contacts. volume I, pages 65–76. ASME International Heat Transfer Conference, 1961.
- [215] M. G. Cooper, B. B. Mikic, and M. M. Yovanovich. Thermal Contact Conductance. *Int. J Heat and Mass Transfer*, 12:279–300, 3 1969. doi: 10.1016/0017-9310(69)90011-8.
- [216] R. C. Gex. Thermal Resistance of Metal-to-Metal Contacts: An Annotated Bibliography. Technical report, Armed Services Technical Information Agency, Arlington Hall Station, Arlington 12, Virginia, 1961.
- [217] C. M. Vidoni. Thermal Resistance of Contacting Surfaces: Heat Transfer Bibliography. Technical Report UCRL-14264, NSA-19-040744, W-7405-ENG-48, Lawrence Radiation Lab., Univ. of California, Livermore, United States, 1965.
- [218] H. Atkins. Bibliography on Thermal Metallic Contact Conductance. NASA Technical Memorandum NASA TM X-53227, NASA, George C. Marshall Space Flight Center, Huntsville, Alabama, April 1965.
- [219] C. J Moore, H. Atkins, and H. A. Blum. Subject Classification Bibliography for Thermal Contact Resistance Studies. Technical Report 68-WA/HT-18, ASME, United Engineering Center, New York, N.Y. 10017, 1969.
- [220] C K Hsieh and F E Davis. Bibliography on Thermal Contact Conductance. Technical Report AFML-TR-6924, Thermophysical Properties Research Center, Purdue University, March 1969.
- [221] L. S. Fletcher. Recent Developments in Contact Conductance Heat Transfer. *J Heat Transfer*, 110(4b):1059–1070, 1988. doi: 10.1115/1.3250610.
- [222] M. A. Lambert and L. S. Fletcher. Review of Models for Thermal Contact Conductance of Metals. *J Thermophysics and Heat Transfer*, 11(2):129–140, 1997. doi: 10.2514/2.6221.
- [223] S Song, M Yovanovich, and K Nho. Thermal gap conductance - effects of gas pressure and mechanical load. *Thermophysics and Heat Transfer*, 6(1):62–68, 1992. doi: 10.2514/3.319.
- [224] M. M. Yovanovich. Four Decades of Research on Thermal Contact, Gap, and Joint Resistance in Microelectronics. *IEEE Transactions on Components and Packaging Technologies*, 28(2):182–206, 2005. doi: 10.1109/TCAPT.2005.848483.
- [225] F. Tachibana. Thermal Resistance of Metallic Contact Parts. *J J S. M. E.*, 155(397), 1954.
- [226] J. S. Moon and R. N. Keeler. A Theoretical Consideration of Directional Effects in Heat Flow at the Interface of Dissimilar Metals. *Int. J Heat Mass Transfer*, 5:967–971, 1962. doi: 10.1016/0017-9310(62)90076-5.

- [227] J. H. Heasley. Transient Heat Flow Between Contacting Solids. *Int. J Heat Mass Transfer*, 8:147–154, 1965. doi: 10.1016/0017-9310(65)90104-3.
- [228] H. Fenech and W. M. Rohsenow. Prediction of thermal conductance of metallic surfaces in contact. *J Heat Transfer*, 85:15–24, 1963. doi: 10.1115/1.3686003.
- [229] B. B. Mikic and W. M. Rohsenow. Thermal Contact Resistance. Technical Report 4542-41, Department of Mechanical Engineering, Engineering Projects Laboratory, MIT, Cambridge, Massachusetts, September 1966.
- [230] B. B. Mikic. Thermal contact conductance; theoretical considerations. *International Journal of Heat and Mass Transfer*, 17(2):205–214, 1974. doi: 10.1016/0017-9310(74)90082-9.
- [231] J Dundurs and C. Panek. Heat conduction between bodies with wavy surfaces. *Int. J Heat Mass Transfer*, 19(7):731–736, 1976. doi: 10.1016/0017-9310(76)90125-3.
- [232] T. N. Veziroğlu, H. Yüncü, and S. Kakaç. Analysis of Thermal Conductance of Contacts with Interstitial Plates. *Int. J Heat Mass Transfer*, 19:959–966, 1976. doi: 10.1016/0017-9310(76)90176-9.
- [233] T. N. Veziroğlu, A. Williams, S. Kakaç, and P. Nayak. Prediction and Measurement of the Thermal conductance of Laminated Stacks. *Int. J Heat Mass Transfer*, 22:447–459, 1979. doi: 10.1016/0017-9310(79)90011-5.
- [234] H. Fenech. Thermal Conductance at Solid Interfaces: an application of the Fenech-Rohsenow model. *J Heat Mass Transfer*, 29(8):1103–1108, 1986. doi: 10.1016/0017-9310(86)90141-9.
- [235] C. V. Madhusudana and L. S. Fletcher. Contact Heat Transfer – The last decade. *AIAA Journal*, 24(3):510–523, 1986. doi: 10.2514/3.9298.
- [236] L. S. Fletcher and D. G. Blanchard. Thermal Conductance of Multilayered Metallic Sheets. *J Thermophysics and Heat Transfer*, 7(1):120–126, 1993. doi: 10.2514/3.11578.
- [237] R W Cross and L S Fletcher. Thermal contact conductance of uranium dioxide-zircaloy interfaces. Huntsville, AL, January 1978. AIAA 16th Aerospace Sciences Meeting. doi: 10.2514/6.1978-85.
- [238] G Jacobs and N Todreas. Thermal Contact Conductance in Reactor Fuel Elements. *Nuclear Science and Engineering*, 50(3):283–290, 1973. doi: 10.13182/NSE73-A28981.
- [239] D. Tabor. *The Hardness of Metals*. Monographs on the Physics and Chemistry of Materials. Oxford : Clarendon Press, London, 1951.
- [240] E. P. Diban, N. M. Kondac, and I. V. Shvets. Contact Heat Transfer Between Machine Components. Technical Report IGRL-T/W.12, UKAEA, 1956.
- [241] A. Ascoli and E. Germagnoli. Misure della resistenza termica di contatto tra superfici piane di uranio e alluminio. *J Energia Nucleare*, 3(1):23–31, 1956.

- [242] R. B. Bird, W. E. Stewart, and E. N. Lightfoot. *Transport Phenomena*. John Wiley & Sons, Inc., New York, 1960.
- [243] L. S. Fletcher. *Heat Transfer Between Surfaces in Contact: An Analytical and Experimental Study of Thermal Contact Resistance of Metallic Interfaces*. PhD thesis, Mechanical Engineering Department, Arizona State University, Tempe, Arizona, July 1968.
- [244] A Toptan, D J Kropaczek, and M N Avramova. Gap conductance modeling II: Optimized model for UO₂-Zircaloy interfaces. *J Nuclear Eng Design*, 2019. (under review).
- [245] I. D. Peggs and D. P. Godin. The Yield Strength-Hot Hardness Relationship of Zircaloy-4. *J Nuclear Materials*, 57:246–248, 1975. doi: 10.1016/0022-3115(75)90266-4.
- [246] S J Kline and F A McClintock. Describing uncertainties in single-sample experiments. *Mech. Eng.*, 75:3–8, 1953.
- [247] A. Toptan, D. J Kropaczek, and M. N. Avramova. Gap conductance: Theory and applications in bison. Milestone Report CASL-U-2018-1664-000, CASL, 2018.
- [248] M. W. Heinsteins and T. A. Laursen. An Algorithm for the Matrix-Free Solution of Quasistatic Frictional Contact Problems. *Int. J Numerical Methods in Engineering*, 44(9):1205–1226, March 1999. doi: 10.1002/(SICI)1097-0207(19990330)44:9<1205::AID-NME550>3.0.CO;2-0.
- [249] Bison Team. Assessment of BISON: A Nuclear Fuel Performance Analysis Code. Technical Report INL/MIS-13-30314 Rev. 4, Idaho National Laboratory, Idaho Falls, Idaho, September 2017.
- [250] P. Lösönen. Early-in-life Irradiation of IFA-562.2 (The Ultra High Burn-up Experiment). Technical Report HWR-247, OECD Halden Reactor Project, Halden, Norway, 1989.
- [251] A Toptan, D J Kropaczek, and M N Avramova. On the validity of dilute gas assumption for gap conductance calculations in nuclear fuel performance codes. 2019.
- [252] J Papin, B. Cazalis, J.M. Frizonnet, E. Fédérici, and F. Lemoine. Synthesis of cabri-ria tests interpretation. In *The Eurosafe Forum*, Paris, France, November 25 and 26 2003.
- [253] V. Georgenthum. Influence of test conditions on the PCMI behaviour during RIA based on CIP0-1, VA-1 and VA-3 tests. In *Fuel Safety Research Meeting*, Tokai Mura, Japan, May 20 and 21 2009.
- [254] F. Jeury, C. Hee, J.C. Giacalone, and B. Siri. Quick Look report of the CIP0-1 test, CABRI/WL 2003/41. In *Institut de Radioprotection et de Sûreté Nucléaire (IRSN)*, Fontenay-aux-Roses, France, 2003.
- [255] F. Jeury, C. Hee, J.C. Giacalone, and J Guillot. Analysis report of the CABRI CIP0-1 test, CABRI/WL 2004/55. In *Institut de Radioprotection et de Sûreté Nucléaire (IRSN)*, Fontenay-aux-Roses, France, 2004.

- [256] T. Fuketa, H. Sasajima, Y. Tsuchiuchi, Y. Mori, T. Nakamura, and K. Ishijima. NSRR/RIA Experiments with High Burnup PWR Fuels. In *ANS Topical Meeting on LWR Fuel Performance*, Portland, OR, March 26 1997.
- [257] A. Toptan, R.K. Salko, and M. Avramova. Improvement of CTF’s wall drag capabilities. Transactions of the American Nuclear Society, 2016.
- [258] G. B. Wallis. *One-Dimensional Two-Phase Flow*. McGraw-Hill, first edition, August 1969.
- [259] S. P. Sutera and R. Skalak. The history of Poiseuille’s Law. *Annual Review of Fluid Mechanics*, 25:1–20, 1993. doi: 10.1146/annurev.fl.25.010193.000245.
- [260] E. C. Koo. *Mechanisms of Isothermal and Non-Isothermal Flow of Fluids in Pipes*. PhD thesis, Massachusetts Institute of Technology. Dept. of Chemical Engineering, 1932.
- [261] C. F. Colebrook. Turbulent flow in pipes with particular reference to the transition region between smooth and rough pipes. *J Institution of Civil Engineering*, 133(4):133–156, 1939. doi: 10.1680/ijoti.1939.13150.
- [262] L. F. Moody and N. J Princeton. Friction factors for pipe flow. In *ASME Transactions*, volume 6, pages 671–684, 1944.
- [263] Dejan Brkić. Review of explicit approximations to the colebrook relation for flow friction. *J Petroleum Science and Engineering*, 77(1):34–48, 2011. doi: 10.1016/j.petrol.2011.02.006.
- [264] Xiande Fang, Yu Xu, and Zhanru Zhou. New correlations of single-phase friction factor for turbulent pipe flow and evaluation of existing single-phase friction factor correlations. *Nuclear Engineering and Design*, 241(3):897–902, 2011. doi: 10.1016/j.nucengdes.2010.12.019.
- [265] Gürol Yıldırım. Computer-based analysis of explicit approximations to the implicit colebrook–white equation in turbulent flow friction factor calculation. *Advances in Engineering Software*, 40(11):1183–1190, 2009. doi: 10.1016/j.advengsoft.2009.04.004.
- [266] D. J Zigrang and N. D. Sylvester. Explicit approximations to the solution of colebrook’s friction factor equation. *AIChE Journal*, 28(3):514–515, 1982. doi: 10.1002/aic.690280323.
- [267] S. W. Churchill. Friction factor equation spans all fluid-flow regimes. *Chemical Engineering*, 7:94–95, November 1977.
- [268] Office of Nuclear Regulatory Research, US NRC, Washington, DC 20555-0001. *TRACE V5.0 Theory Manual: Field Equations, Solution Methods and Physical Models*.
- [269] Nuclear Systems Analysis Operations. *RELAP5/MOD3.3 Code Manual Volume I: Code Structure, System Models, and Solution Methods*, October 2010.

- [270] Neil E. Todreas and Mujid S. Kazimi. *Nuclear Systems II: Elements of Thermal Hydraulic Design*. Taylor & Francis, London, 2001.
- [271] G. Gaspari, A. Hassid, and G. Vanoli. Some consideration on critical heat flux in rod clusters in annular dispersed vertical upward two-phase flow. In *Proceeding of the 4th International Heat Transfer Conference*, Paris, France, 1970.
- [272] G. Gaspari, A. Hassid, and F. Lucchini. A rod-centered subchannel analysis with turbulent (enthalpy) mixing for critical heat flux prediction in rod clusters cooled by boiling water. In *5th International Heat Transfer Conference*, Tokyo, Japan, 1974.
- [273] A. Toptan, N. W. Porter, R. K. Salko, and M. N. Avramova. Implementation and Assessment of Wall Friction Models for LWR Core Analysis. *Annals of Nuclear Energy*, 115:565–572, May 2018. doi: 10.1016/j.anucene.2018.02.022.

Appendices

APPENDIX

A

FUEL RADIAL DEFORMATION MODELS

The fuel radial deformation accounts for effects of thermal expansion, swelling, irradiation induced densification, and relocation. These models were initially implemented in [95] considering rigid pellet fuel deformation of FRACAS model [102] in the code. The radial deformation of the pellet with a free-ring expansion model is determined from Eq. A.1. Note that the effect of relocation is added to thermal response, but no hard contact is allowed until the other fuel expansion components recover half of the original relocated pellet radius [44].

$$(\Delta r_{th})_{fuel} = \sum_{i=1}^{N_r} \delta r_i \left(\alpha_{T_i} + \varepsilon_f^s + \varepsilon_f^d + \varepsilon_f^r \right), \quad (\text{A.1})$$

where

- α_{T_i} = the thermal expansion coefficient of the i -th radial temperature (Section A.1),
- T_i = the average temperature of i -th radial ring,
- ε_f^s = the swelling strain (Section A.2),
- ε_f^d = the densification strain (Section A.3), and
- ε_f^r = the relocation strain (Section A.4).

A.1 Fuel Thermal Expansion

Linear strain caused by thermal expansion (equal to zero at 300K) is given by

$$\left(\frac{\Delta L}{L}\right) = K_1 T - K_2 + K_3 \exp\left(-\frac{E_D}{k_B T}\right) \quad (\text{A.2})$$

where

- E_D = energy of formation of a defect,
- k_B = the Boltzmann's constant (1.38×10^{-23} J/K),
- R_{molten} = fraction of the molten fuel (solid 0.0; molten 1.0), and
- T = temperature.

Empirical coefficients for the models for UO_2 and PuO_2 fuels in Table A.1. For UO_2 - Gd_2O_3 fuels, the fuel thermal expansion is weighted between UO_2 and PuO_2 fuels based on the gadolinia concentrations. Models fit to the experimental data are shown in Figure A.1.

Table A.1: Fuel thermal expansion models

		MATPRO	FRAPCON	
	unit	UO_2	UO_2	PuO_2
K_1	1/K	1.0×10^{-5}	9.80×10^{-6}	9.0×10^{-6}
K_2	-	3.0×10^{-3}	2.61×10^{-3}	2.7×10^{-3}
K_3	-	4.0×10^{-2}	3.16×10^{-1}	7.0×10^{-2}
E_D	J	6.9×10^{-20}	1.32×10^{-19}	7.0×10^{-20}

During melting, an expansion equal to a linear strain of 0.043 occurs. Eq. A.3a is used for the fuel is partially molten and Eq. A.3b for the entirely molten fuel.

$$\left(\frac{\Delta L}{L}\right) = \left(\frac{\Delta L}{L}\right)_{T_m} + 0.043 \cdot R_{molten} \quad (\text{A.3a})$$

$$\left(\frac{\Delta L}{L}\right) = \left(\frac{\Delta L}{L}\right)_{T_m} + 0.043 + 3.5 \times 10^{-5} [T - (T_m + \Delta T_m)] \quad (\text{A.3b})$$

where

$(\Delta L/L)_{T_m}$ = the thermal expansion of solid fuel at fuel melting temperature T_m .

The melting temperature is calculated based on the plutonium/gadolinia contents as:

- for $X_{Pu} = 0$

$$T_m = 3113.15 - 5.0 \times 10^{-4} Bu \quad (\text{A.4})$$

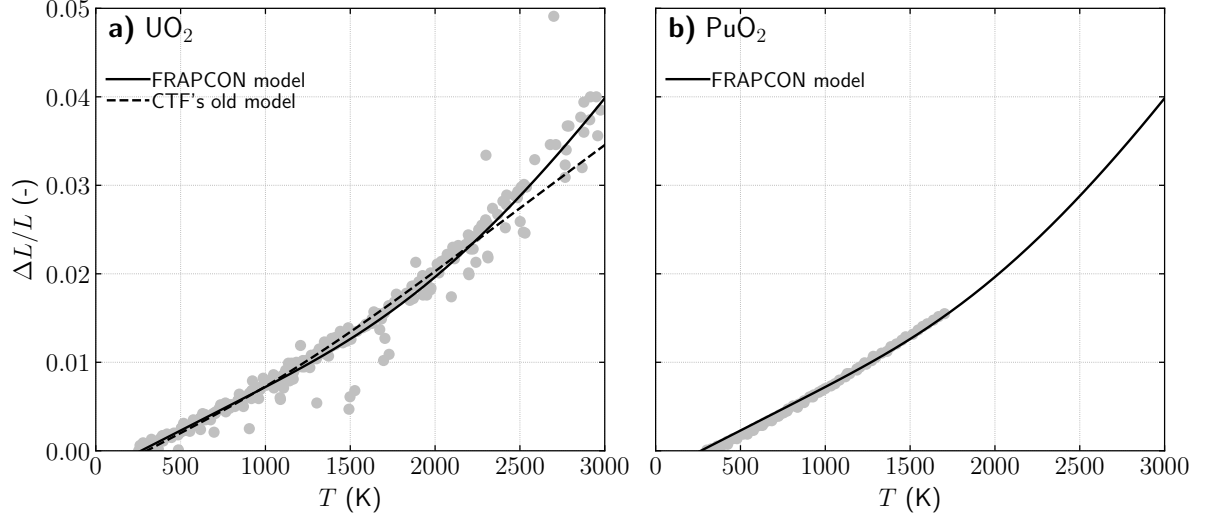


Figure A.1: Model comparison to experimental data for fuel thermal expansion model with respect to temperature for (a) UO_2 fuel and (b) PuO_2 fuel. The data are extracted from Material Property Correlations [26] that include the experimental data for UO_2 fuel [27, 28, 29, 30, 31, 32, 33] and PuO_2 fuel [34, 35].

- for $X_{Pu} \neq 0$

$$T_m = T_{sldus} + 273.15 - 5.0 \times 10^{-4} Bu \quad (\text{A.5a})$$

$$\Delta T_m = T_{liq dus} - T_{sldus} - 5.0 \times 10^{-4} Bu \quad (\text{A.5b})$$

- for Gd-doped urania:

$$T_m = 3115 - 4.8 X_{Gd_2O_3} \quad (\text{A.6})$$

where the solidus and liquidus boundaries for the melting temperature of UO_2 and MOX are calculated as follows:

$$T_{sldus} = 2840 - 5.41395 X_{Pu} + 7.46839 \times 10^{-3} X_{Pu}^2 \quad (\text{A.7a})$$

$$T_{liq dus} = 2840 - 3.21860 X_{Pu} + 1.448518 \times 10^{-2} X_{Pu}^2 \quad (\text{A.7b})$$

where

- Bu = fuel burnup (MWd/MTU),
- $X_{Gd_2O_3}$ = concentration of gadolinia (wt.%),
- X_{Pu} = content of plutonium (wt.%),
- T_{sldus} = solidus temperature ($^{\circ}C$),
- $T_{liq dus}$ = liquidus temperature ($^{\circ}C$),
- T_m = fuel melting temperature (K), and
- ΔT_m = temperature range between the solidus and liquidus (K).

A.2 Fuel Swelling

The fuel swelling is calculated from the increased volume that fission products must occupy. It is a positive volume change resulting from different solubilities, chemical states, lattice parameters, numbers of atoms, and chemical valancies of the atoms resulting from the nuclear fission process. It is assumed that swelling deformation is isotropic. One-third of the volume is assumed increase in each direction.

Fractional volume change due to the solid fission products is given by:

- MATPRO-11 model,

$$\left(\frac{\Delta V}{V}\right)_s = 2.5 \times 10^{-23} Bu^* \quad (\text{A.8})$$

- FRAPCON-4.0 model,

$$\left(\frac{\Delta V}{V}\right)_s = \begin{cases} 2.315 \times 10^{-23} Bu^*, & Bu < 80 \text{ MWd/kgU} \\ 3.211 \times 10^{-23} Bu^*, & Bu > 80 \text{ MWd/kgU} \end{cases} \quad (\text{A.9})$$

and the fuel burnup during a time-step is described as:

$$Bu^* = 7.435 \times 10^{-13} \rho_{f,i} \Delta Bu \quad (\text{A.10})$$

where

- T = temperature (K),
- $\rho_{f,i}$ = fuel initial density (kg/m^3),
- Bu = total burnup of fuel (MWs/kgU), and
- ΔBu = burnup during a time-step (MWs/kgU).

Comparison of the models is presented in Figure A.2 for fractional volume change due to the solid fission products.

Fractional volume change due to the gaseous fission products is given by:

- MATPRO-11 model

$$\left(\frac{\Delta V}{V}\right)_g = 2.617 \times 10^{-39} (2800 - T)^{11.73} e^{-0.0162(2800-T)} e^{-2.4 \times 10^{-10} \rho_{f,i} Bu} Bu^* \quad (\text{A.11})$$

The above fraction is assumed to be zero greater than $2800K$.

- FRAPCON-4.0 model

$$\left(\frac{\Delta V}{V}\right)_g = \begin{cases} 4.55 \times 10^{-5} T - 4.37 \times 10^{-2}, & 960^\circ < T < 1370^\circ C \\ -4.05 \times 10^{-5} T + 7.40 \times 10^{-2}, & 1370^\circ < T < 1832^\circ C \end{cases} \quad (\text{A.12})$$

Figure A.3 shows the fractional volume change due to the gaseous fission products that is computed from the aforementioned models.

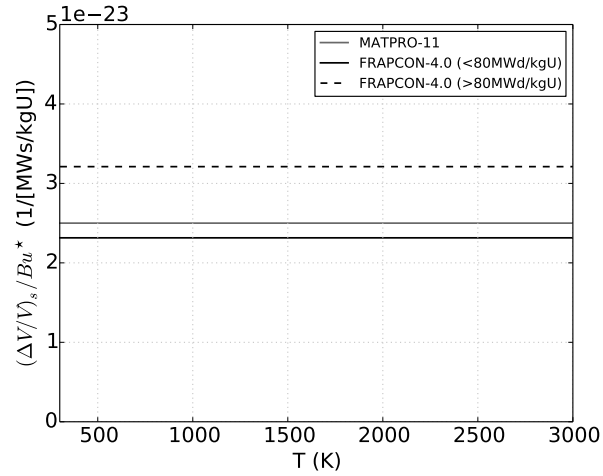


Figure A.2: Model comparison for the fractional volume change due to the solid fission products with respect to temperature.

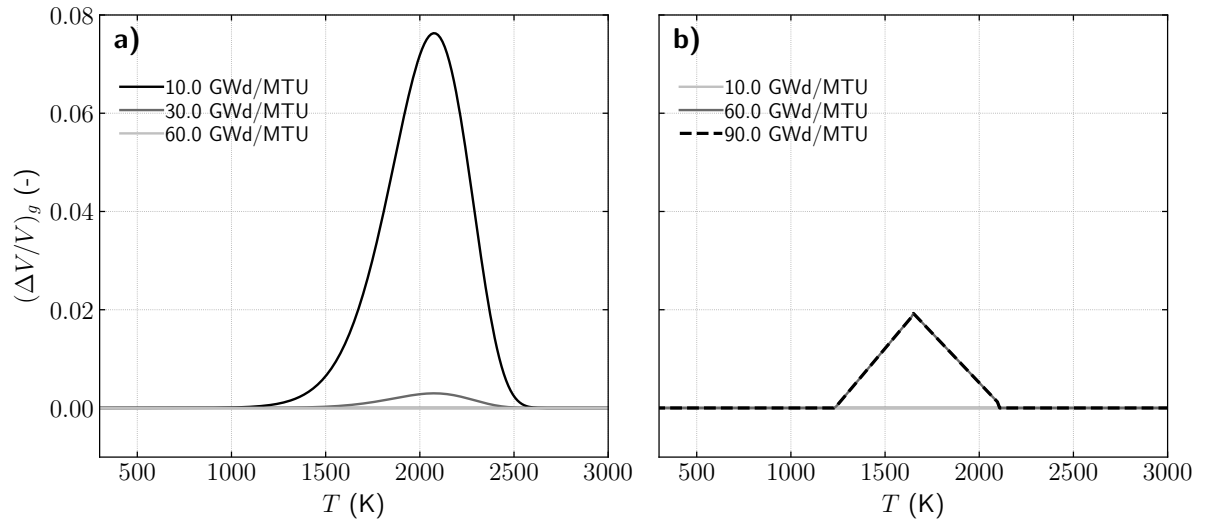


Figure A.3: Model comparison for the fractional volume change due to the gaseous fission products with respect to temperature at various burnups using (a) MATPRO-11 model and (b) FRAPCON model.

A.3 Fuel Irradiation-Induced Densification

The irradiation-induced densification is calculated during the first few thousand hours of water reactor operation for UO_2 and MOX fuels as a function of fuel burnup, temperature, and initial density. The NRC-approved thermal resinter test of 24 hours at 1700 C, or a fuel vendor's NRC-approved resinter test conducted for the specific fuel supplied. Typically, most of the fuel densification occurs relatively quickly. Usually, the densification process is more than 75% complete within the first few thousand MWd/MTU burnup.

MATPRO-11/FRAPCON-4.0 models

Total densification as a function of burnup is given by

$$\frac{\Delta L}{L} = \left(\frac{\Delta L}{L} \right)_m + \exp(-3.0(Bu + B)) + 2.0 \exp(-35.0(Bu + B)) \quad (\text{A.13})$$

where

B = a non-dimensional coefficient that is determined by a numerical algorithm with the boundary condition: $(\Delta L/L) = 0$ when $Bu = 0$.

For $\Delta\rho_{SNTR} = 0.0$ (input), the maximum possible dimension change of fuel due to irradiation is calculated for both models according to:

$$\left(\frac{\Delta L}{L} \right)_m = \begin{cases} -\frac{22.2(100-TD)}{(T_{SNTR}-1453)}, T < 1000K \\ -\frac{66.6(100-TD)}{(T_{SNTR}-1453)}, T \geq 1000K \end{cases} \quad (\text{A.14})$$

For the user-defined resintering density change (i.e., $\Delta\rho_{SNTR} \neq 0.0$), MATPRO-11 model in Eq. A.15a and FRAPCON-4.0 model in Eq. A.15b slightly differentiate from each other.

$$\left(\frac{\Delta L}{L} \right)_m = \begin{cases} -0.00150 \cdot \Delta\rho_{SNTR}, T < 1000K \\ -0.00285 \cdot \Delta\rho_{SNTR}, T \geq 1000K \end{cases} \quad (\text{A.15a})$$

$$\left(\frac{\Delta L}{L_o} \right)_m = \frac{100 \cdot \Delta\rho_{SNTR}}{(3.0 \cdot TD)} \quad (\text{A.15b})$$

where

$(\Delta L/L)_m$ = maximum possible dimension change of fuel due to irradiation (%),
 $\Delta\rho_{SNTR}$ = resintered fuel change (kg/m^3),
 Bu = fuel burnup (MWd/kgU),
 T = fuel temperature (K),
 T_{SNTR} = sintering temperature (K), and
 TD = initial theoretical density (%).

Figure A.4 shows the fractional volume change due to the irradiation-induced densification that is computed from the aforementioned models.

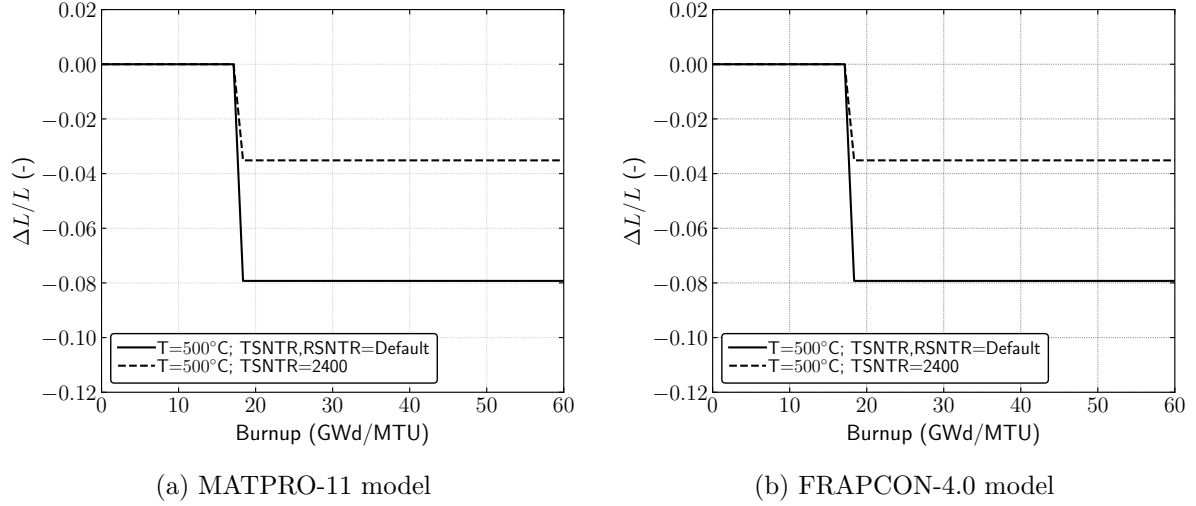


Figure A.4: Model comparison for the fractional volume change due to irradiation-induced densification with respect to the burnup at various temperatures and resintering densities using Eq. A.15.

ESCORE model

Total accrued specific volume change due to densification at a constant temperature operation:

$$\left(\frac{\Delta V}{V}\right) = \Delta\rho_{SNTR} \left[\exp\left(Bu \cdot \frac{\ln(0.010)}{CBu_D}\right) - 1 \right] \quad (\text{A.16})$$

The complete densification typically occurs by about 5,000 MWd/MTU. For temperature-independent densification, empirical constant, C is assumed to be 1.0. For temperature-dependent densification, the constant is calculated as

$$C = \begin{cases} 1.0, & T_f \geq 750^\circ\text{C} \\ 7.2 - \frac{4.3(T_f - 25)}{500}, & T_f < 750^\circ\text{C} \end{cases} \quad (\text{A.17})$$

where

- $\Delta\rho_{SNTR}$ = total amount of densification that can occur as a fraction of theoretical density (%),
- Bu = pellet-average burnup (MWd/MTU),
- Bu_D = burnup at which densification is complete (MWd/MTU), and
- T_f = local fuel temperature ($^\circ\text{C}$).

Figure A.5 shows the fractional volume change due to the irradiation-induced densification that is computed from the ESCORE model.

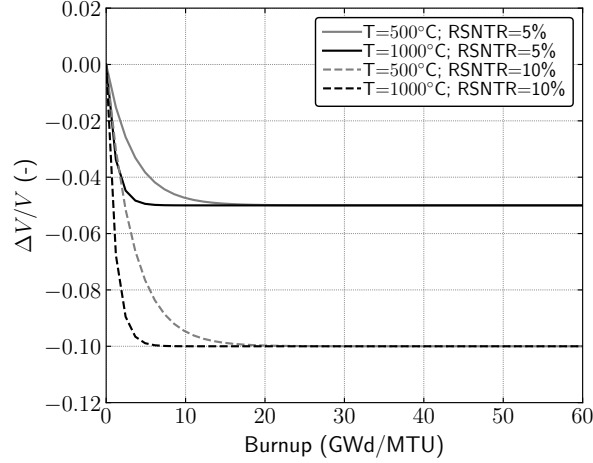


Figure A.5: Model comparison for the fractional volume change due to irradiation-induced densification with respect to the burnup at various temperatures and resintering densities using Eq. A.16.

A.4 Fuel Relocation

The fuel pellet fracture is calculated with a simple empirical fuel relocation model to calculate the percent change in the fuel radius.

FRAPCON-4.0 model

The change in pellet outer diameter as a function of burnup and power is given by

$$\left(\frac{\Delta D}{D}\right) = \begin{cases} 0.055, & Bu < 0.0937 \\ 0.055 + C_R \min(1, [0.5793 + 0.2447 \ln(Bu)]), & \text{otherwise} \end{cases} \quad (\text{A.18a})$$

$$C_R = \begin{cases} 0.345, & q' < 20 \\ 0.345 + \frac{(q'-20)}{200}, & 20 \leq q' \leq 40 \\ 0.445, & q' > 40 \end{cases} \quad (\text{A.18b})$$

where

- $(\Delta D/D)$ = fraction of the gap closure due to relocation to as-fabricated gap closure,
- q' = local power (kW/ft),
- Bu = local burnup (GWd/MTU), and
- C_R = relocation factor (-).

ESCORE model

The change in pellet outer diameter

$$\left(\frac{\Delta D}{D}\right) = 0.80Q \left[\frac{G_t}{D_0}\right] (0.005Bu^{0.3} - 0.20D + 0.3) \quad (\text{A.19a})$$

$$Q = \begin{cases} 0.0 & \text{for } q' \leq 6 \\ (q' - 6)^{1/3} & \text{for } 6 < q' \leq 14 \\ (q' - 10)^{1/2} & \text{for } q' > 14 \end{cases} \quad (\text{A.19b})$$

where

- $(\% \Delta D/D)$ = the percent change in diameter due to relocation (%),
- D_0 = the as-fabricated cold diameter of the fuel pellet (in),
- q' = pellet average linear heat rating (kW/ft),
- Bu_t = pellet average fuel burnup (MWd/MTU), and
- G_t = as-fabricated cold gap diameter (in).

Figure A.6 shows the fractional volume change due to the fuel relocation that is computed from the aforementioned models.

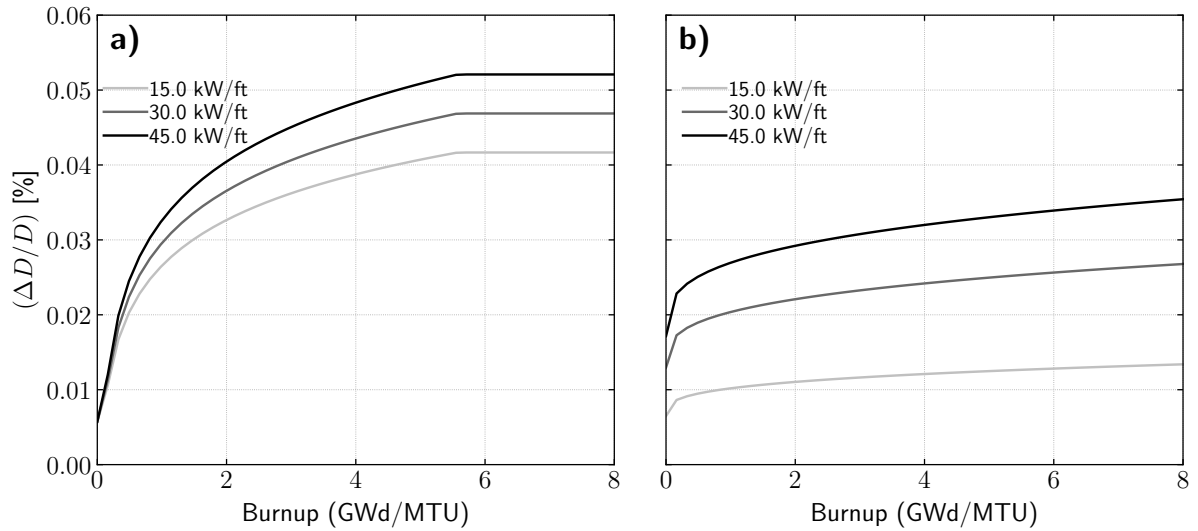


Figure A.6: Model comparison for the fractional volume change due to fuel relocation with respect to the burnup at various linear heat rates using (a) the FRAPCON-4.0 model and (b) the ESCORE model.

APPENDIX

B

RIA TRANSIENT

CTFFuel’s current status on modeling of RIA is examined, which is one of the challenging problems in CASL. Fuel rod behavior during a RIA transient is shown in Figure B.1. CTFFuel is not capable of modeling all features on the figure, yet this is helpful to understand the fuel performance during this transient. This study aims to perform a code comparison to demonstrate how CTFFuel’s transient simulations agree with FRAPTRAN-1.5’s predictions during a RIA transient using the dynamic gap conductance model. These test cases are added to CTFFuel’s test matrix to be used as a reference solution during the code’s ongoing developments. Following section is organized to describe the procedure to create input decks for CTFFuel.

B.1 Approach

Figure B.2 shows schematic illustration of the automated script for the code comparison between CTFFuel and FRAPTRAN-1.5 (the reference code) using the dynamic gap conductance model. FRAPCON is a fuel performance code that calculates steady state response of LWR fuel rods [44]. This code calculates temperature profiles, pressure, and deformation of a fuel rod as functions of time-dependent fuel rod power and coolant boundary conditions. A restart file is generated for FRAPTRAN-1.5 that is a transient code that is designed for simulation of time-dependent rod power scenarios [45]. The reference code’s simulations are obtained and required data for the dynamic gap conductance model in CTFFuel simulations are extracted to create input decks. Then, CTFFuel simulations are run. At the end, both CTFFuel and The reference code’s predictions are compared. A list of fuel rod cases from FRAPTRAN-1.5 integral assessment [9] are tabulated in Table B.1.

It is important to note that the wall temperature is overestimated in CTFFuel’s predictions when setting a constant wall temperature directly from the reference code. Instead, history of

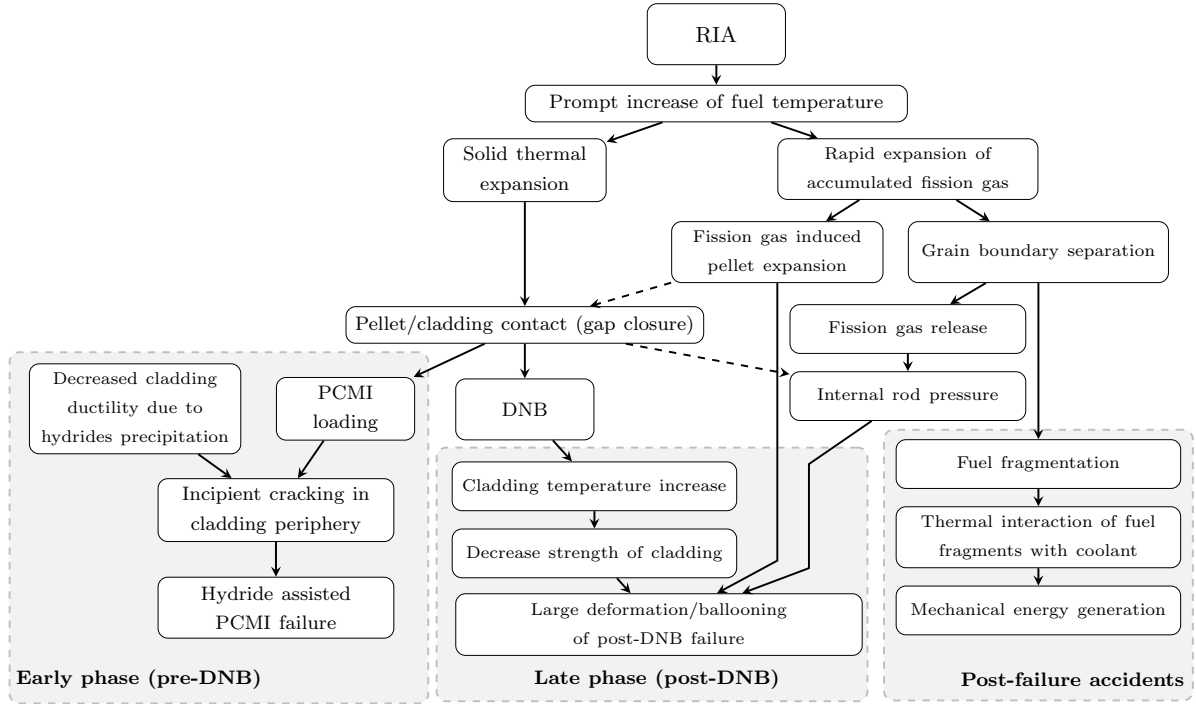


Figure B.1: Schematic illustration of the fuel rod behavior during a RIA transient [36].

Table B.1: List of fuel rod cases used from FRAPTRAN-1.5 integral assessment [9].

Base Irradiation	Transient Reactor	Rod	Source	Rod Type	Fuel Type	Rod Avg. Bu (MWd/kgU)
Gravelines-5	CABRI	NA1	[252]	PWR 17x17	UO ₂	64.0
Gravelines-5	CABRI	NA2	[252]	BR-3	UO ₂	66.0
Gravelines-5	CABRI	NA3	[252]	PWR 17x17	UO ₂	53.8
Gravelines-5	CABRI	NA4	[252]	PWR 17x17	UO ₂	62.0
Gravelines-5	CABRI	NA5	[252]	PWR 17x17	UO ₂	64.0
Gravelines-4	CABRI	NA7	[252]	PWR 17x17	MOX	55.0
Gravelines-5	CABRI	NA8	[252]	PWR 17x17	UO ₂	60.0
St. Laurent B1	CABRI	NA9	[252]	PWR 17x17	MOX	28.1
Gravelines-3 & 2	CABRI	NA10	[252]	PWR 17x17	UO ₂	63.0
Vandellos 2	CABRI	CIP0-1	[253, 254, 255]	PWR 17x17	UO ₂	74.8
Ohi #1	NSRR	HBO-1	[256]	PWR 17x17	UO ₂	50.4
Ohi #1	NSRR	HBO-5	[256]	PWR 17x17	UO ₂	44.0
Ohi #1	NSRR	HBO-6	[256]	PWR 17x17	UO ₂	49.0

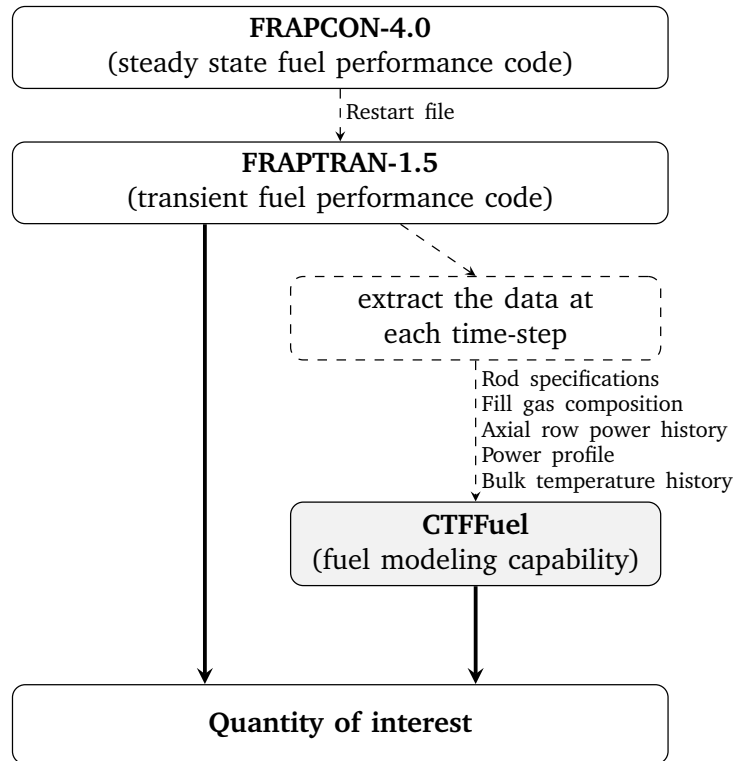


Figure B.2: Illustration of the code comparison between CTFFuel and FRAPTRAN-1.5 for assessment of RIA transient behaviors.

the bulk temperature and heat transfer coefficient are exactly set in the CTFFuel's simulations from the reference code. There should be an infinite bulk heat transfer coefficient when defining a constant wall temperature in CTFFuel. By this way, generated heat can be dissipated away from the fuel rod to the fluid medium. With the specified history of bulk temperature and heat transfer coefficient, the calculated clad outside temperatures in CTFFuel agree perfectly with the reference code's predictions at the clad outside.

The simulations are performed at the base irradiation (i.e., zero burnup), therefore, no effects of thermal degradation are expected to observe on the fuel thermal conductivity. Only thermal expansion model is enabled in the simulations. Radial power distribution and gas composition are assumed to be constant during the transient, which are directly read from the reference code's simulation results.

Preprocessing

This comparison is automated through a Python script that reads the necessary data from the reference code's output file and creates input decks for CTFFuel. For example, the parameters are extracted from the reference code's simulations such as gap thickness, radial and axial temperature predictions, etc. These parameters are used to create input decks for CTFFuel

inputs. Additionally, these values are stored as gold values in csv format.

Processing

CTFFuel inputs are run for the CABRI and Nuclear Safety Research Reactor (NSRR) transient reactors in Table B.1 and the simulation results are acquired in HDF5 formatted outputs.

Postprocessing

Python script to postprocess the data from CTFFuel's HDF5 output files and to compare against the gold values.

B.2 Summary

The code comparison was performed between CTFFuel and FRAPTRAN-1.5 to benchmark transient calculations during a RIA transient. This comparison is automated to reduce possible human errors in the process. From the results, gap thickness results are acceptable as compared to the FRAPTRAN-1.5's predictions. This study constructed a baseline to be used in future codes improvements and/or developments. These test cases are added to the CTFFuel's test matrix along with the Python scripts.

APPENDIX

C

RADIAL POWER DISTRIBUTION

With energy self-shielding of neutrons are more likely absorbed near the fuel surface. Surface layers of the fuel geometrically shields the inner layers from neutron flux, leading to a relatively lower neutron flux inside the fuel rod. Therefore, the neutron flux inside a pellet decreases from the surface to the center due to the self-shielding. Similarly, fission events in the pellets follow this distribution; the highest at the pellet surface due to the additional contribution from the fission of Pu^{239} .

Gadolinium (Gd^{155} and Gd^{157}) is used commonly as a neutron absorber due to its very high neutron absorption cross-section. The radial power profile of Gd-doped UO_2 fuel for LWR conditions is obtained from FRAPCON-4.0 as a function of the normalized radius, $(\frac{r}{R})$, the rod average burnup, Bu , and the gadolinium content, Gd : $f(\frac{r}{R}, Bu, Gd)$ [44]. Variation of the radial power profile is illustrated in Figure C.1 and Figure C.2 and at several burnup levels and Gd concentrations.

Gd-doped fuel has higher self-shielding effect vs. unpoisoned fuel, therefore higher burnout rate at the fuel surface, and depresses the flux through the center of fuel. Once the Gd starts to deplete, the radial power profile of the burnable poison-doped fuel tracks parallel to its unpoisoned equivalent.

This section outlines look-up table concept for correction of fuel temperature profile in neutronics codes to account effects of the varying radial power profile due to the self-shielding effect. Modeling is described firstly. Then, results obtained using the look-up table concept are compared to analytical results as well as sensitivity study to examine how input parameters influence the effective Doppler temperature. Lastly, the results and discussions are summarized.

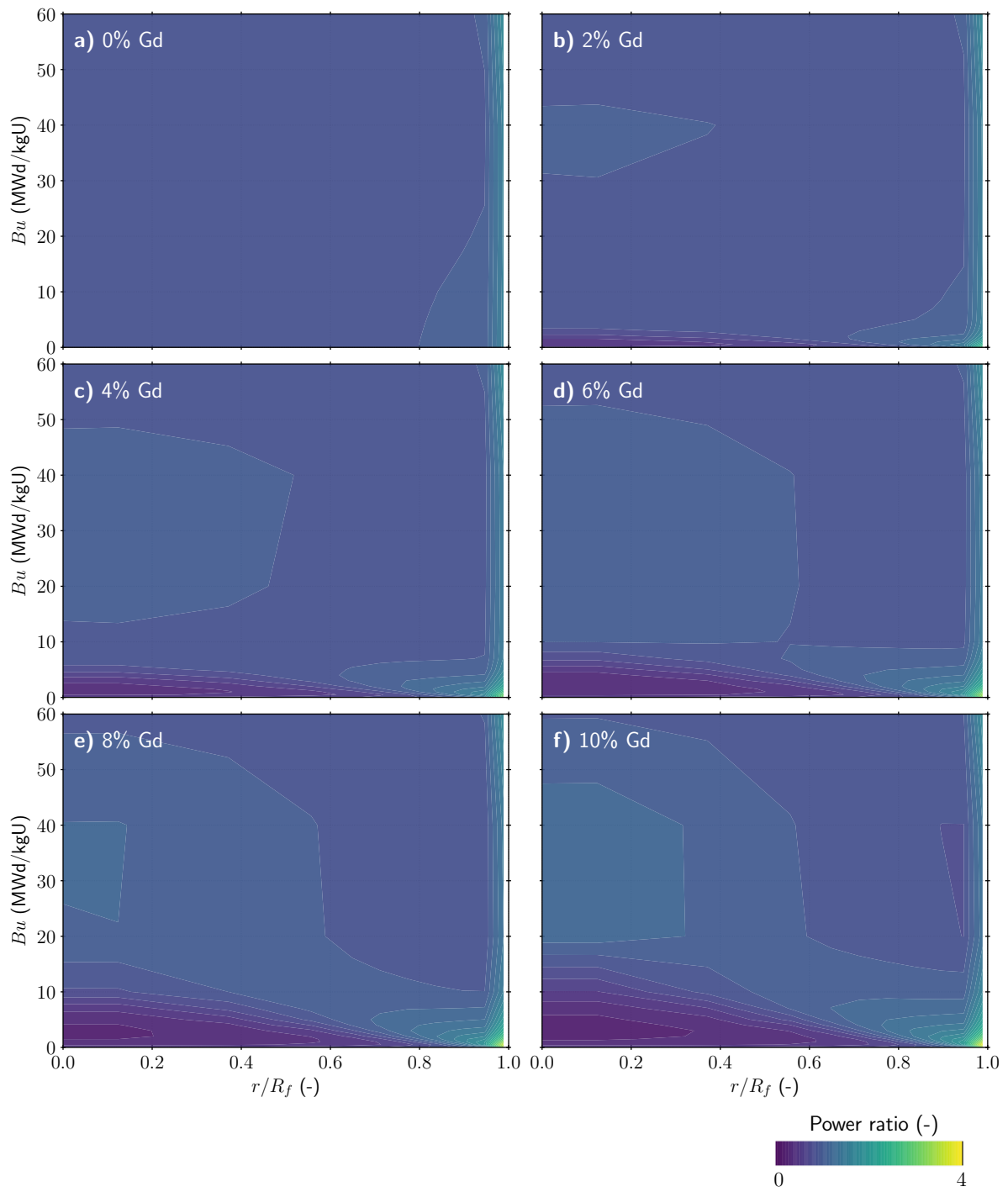


Figure C.1: Contour plots of the radial power distribution as a function of the rod average burnup and the normalized radius for various Gd concentrations.

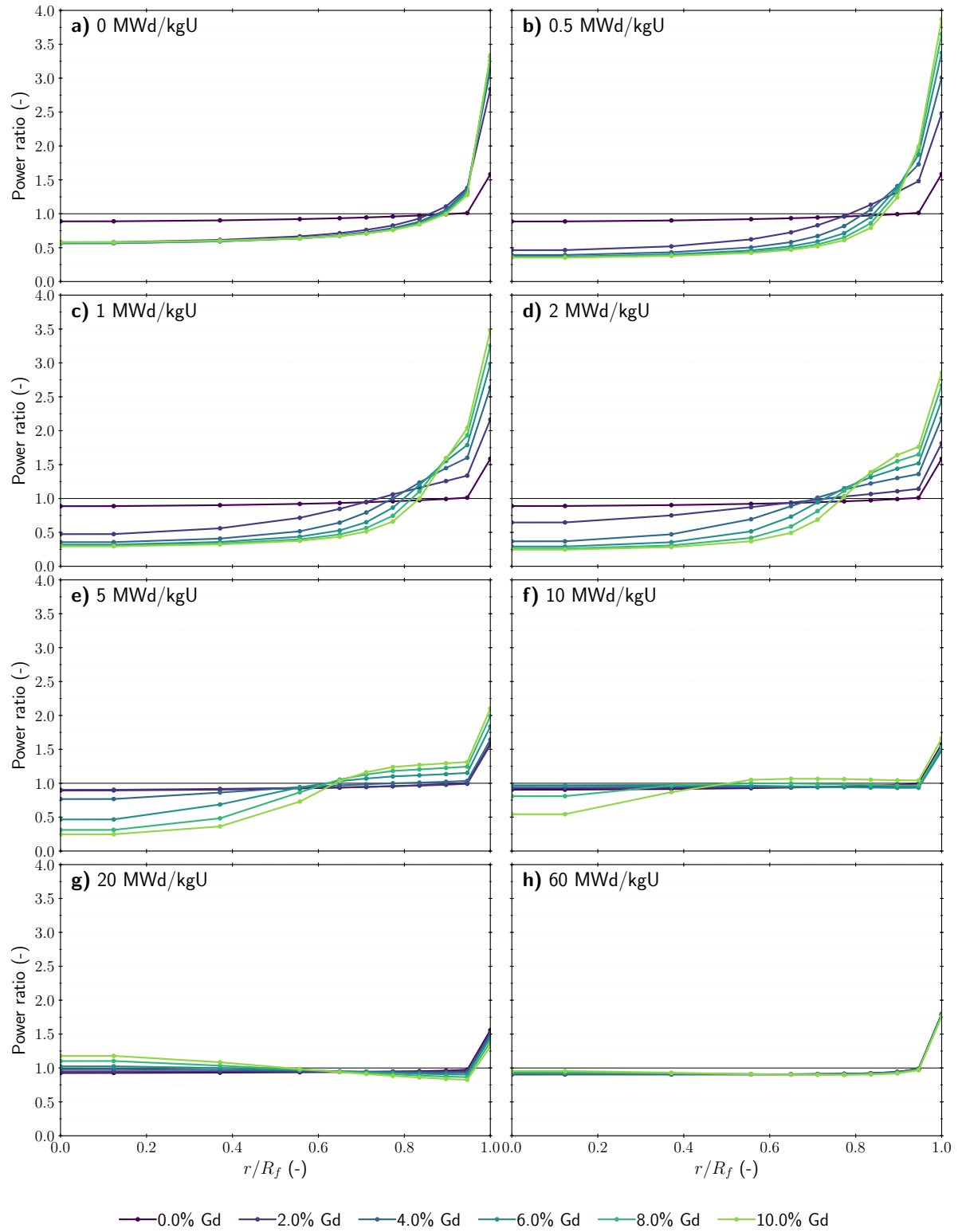


Figure C.2: Evolution of the radial power profile as the fuel burns out for various Gd concentrations.

C.1 Approach

The heat equation in the fuel is given in Eq. 4.4. The heat generation rate, \dot{q} can be as a function of radial position, \vec{r} . However, axial temperature gradient is much smaller than the radial direction in LWR fuel pins. Therefore, the axial conduction term can be neglected in the analysis. In general, changes in thermal conductivity and heat generation rate due to material's transformations are so gradual, so heat conduction process becomes steady-state for fuel element operation at constant power [12].

The temperature profile in the fuel for a known fuel surface temperature, T_{surf} , in Eq. 4.5 is altered to reflect the effects of the self-shielding as

$$T(r) = T_{surf} + \frac{q'_{ax} S_R}{4\pi\lambda_f} \left(1 - \frac{r^2}{R_f^2}\right) \quad (C.1)$$

where

- T_{surf} = fuel surface temperature,
- R_f = fuel radius,
- λ_f = fuel thermal conductivity,
- $S_R = S\left(\frac{r}{R}, Bu, Gd\right)$, flux depression factor, and
- q'_{ax} = linear heat rate at an axial elevation.

The volume averaged fuel temperature is calculated according to

$$\bar{T} = \frac{\int_0^{R_f} T(r) r dr}{\int_0^{R_f} r dr}. \quad (C.2)$$

For a known \bar{T} , the fuel surface temperature can be estimated as

$$T_{surf} = \bar{T} - \frac{q'_{ax}}{2\pi\lambda_f R_f^2} \int_0^{R_f} S_R \left(1 - \frac{r^2}{R_f^2}\right) r dr \quad (C.3)$$

The estimated surface temperature is plugged in Eq. C.3 to obtain the fuel temperature profile. The temperature predictions calculated using look-up tables and CTFFuel predictions agree well as they supposed. Each difference between the table and code result is calculated for i^{th} test and N is the total number of tests. RMSE and rRMSE are calculated as the below. The agreement is found to be within a relative error of 1 K and a rRMSE less than 0.2%.

$$RMSE = \sqrt{\frac{1}{N} \sum_{i=1}^N (T_{table,i} - T_{code,i})^2} \quad (C.4a)$$

$$rRMSE = \sqrt{\frac{1}{N} \sum_{i=1}^N \left(1 - \frac{T_{table,i}}{T_{code,i}}\right)^2} \quad (C.4b)$$

where

- $T_{factor,i}$ = temperature that is calculated using Eq. C.3 and
- $T_{code,i}$ = predicted temperature that is extracted from the CTFFuel output.

C.2 Summary

The self-shielding effect on radial power distribution was studied. Look-up tables were created for correction of fuel temperature profile in neutronics codes to account effects of the varying radial power profile due to the self-shielding effect. A rigorous model was constructed to correction fuel temperature profiles through the flux depression factors. The method was confirmed to be valid and consistent. This concept allows the direct use of analytical solution, room to define different gap heat transfer coefficient and clad thermal conductivity, and can be generated in this format for any fuel type. This study can help to correct fuel temperature profile in MPACT easily prior to enabling data transfer between MPACT-CTFFuel in VERA-CS since flat fuel temperature profile is used in MPACT for feedback calculations.

APPENDIX

D

CTF'S FRICTION FACTOR CORRELATIONS

One of the fundamental models in CTF is that of the frictional pressure drop. It is active for all simulations, both single- and two-phase, over all operating conditions. The model is one of the main components of the pressure drop calculation, which can impact the flow distribution and flow regime in the core. In order to improve the pressure drop calculation in CTF, this work provides an analysis of existing friction modeling options and adds new models. The modeling of frictional pressure drop in the nuclear thermal hydraulics subchannel code, CTF, is improved through the addition of three new modeling options. Two of the new models allow the code to account for the effects of surface roughness and the third enables a user-supplied option. The new friction models were implemented and initially tested in [257].

CTF calculates the pressure drop between two axial cells as a summation of pressure losses due to inertia, acceleration, gravity, wall friction, and form losses. For the scope of this paper, only the pressure loss due to friction is relevant. CTF uses a frictional pressure drop model for single and two-phase flows [258]. The pressure drop per unit length due to the friction between the fluid and a solid structure, $(dP/dx)_{fric}$, is

$$\left. \frac{dP}{dx} \right|_{fric} = \frac{\bar{f}G^2}{2D_h\rho} \Phi^2, \quad (\text{D.1})$$

where

\bar{f} = the effective Darcy friction factor,
 G = the mass flux of the field of interest,
 D_h = the hydraulic diameter,
 ρ = density, and
 Φ = a two-phase multiplier that is only a function of the void fraction, α , and is one for cells with single-phase water.

The friction factor, \bar{f} , is a function of Reynolds number and surface roughness, which is calculated based on the selected friction factor option, which is named **IRFC** in CTF. Various options for calculating the friction factor can be found in the literature. In laminar flow, it is inversely correlated to the Reynolds number according to the Hagen-Poiseuille equation, which is an analytical solution for laminar and incompressible flow for fluid in a smooth pipe [259]. In the transition and turbulent regimes, the friction factor becomes a function of roughness. One of the oldest friction factor correlations that is still commonly used today is the so-called McAdams Correlation, which is based on the work of his student, Koo [260]. Koo gathered a large set of data for smooth and commercially smooth pipes, then combined them into a single correlation. One of the first equations for friction factor in rough pipes was the Colebrook equation, which is an implicit function logarithmically combining approximate solutions for smooth and completely rough turbulent flow [261]. The Colebrook equation is perhaps best known by its graphical representation, which was popularized by Moody in 1944 [262]. It has been common in the literature for researchers to design explicit approximations of Colebrook's equation and assess the accuracy of these approximations [263, 264, 265].

Prior to the work of Toptan [257], CTF had two options for determination of the friction factor. The first—**IRFC=1**—is a model of unknown origin:

$$f = \max\left(\frac{64}{Re}, 1.691Re^{-0.43}, 0.117Re^{-0.14}\right), \quad (\text{D.2})$$

where

Re = the Reynolds number.

This correlation uses a maximum function to continuously transition between a laminar, transition, and turbulent part. The second option—**IRFC=2**—is a modified version of the McAdams correlation.

$$f = \max\left(\frac{64}{Re}, 0.204Re^{-0.2}\right) \quad (\text{D.3})$$

Here, the Hagen-Poiseuille equation is again used for the laminar region and a maximum function is used to ensure that the equation is continuous. Neither of the original CTF correlations account for surface roughness effects. However, varying degrees of roughness can drastically affect the the pressure drop in a nuclear reactor. Not only can materials in the reactor be manufactured with varying degrees of roughness, but the surface topography of the fuel rod can significantly change during reactor operation. For example, chemical deposition on the cladding can lead to Chalk River Unidentified Deposits (CRUD), which significantly increases the surface roughness. Additionally, changes in the cladding—such as cracking—can increase

roughness. Though it is not possible for CTF to account for these changes dynamically, it is important that they can input manually in situations for which they can be a priori estimated.

To account for the important effects of roughness, two correlations were added to CTF: the Zigrang-Sylvester approximation to the Colebrook equation [266] and the Churchill correlation [267]. These are used because they account for the effects of roughness, are well-recognized in the literature, and enable the ability to compare CTF results to other nuclear thermal hydraulic codes, e.g. TRACE [268] and RELAP [269].

The Zigrang-Sylvester approximation to the Colebrook equation—IRFC=3—is

$$f = \max \left(\frac{64}{Re}, \left[-2 \log_{10} \left(\frac{\epsilon}{3.7D} + \frac{2.51}{Re} \left[1.14 - 2 \log_{10} \left(\frac{\epsilon}{D} + \frac{21.25}{Re^{0.9}} \right) \right] \right) \right]^{-2} \right). \quad (\text{D.4})$$

The Churchill correlation—IRFC=4—is

$$f = 8 \left[\left(\frac{8}{Re} \right)^{12} + (a + b)^{-1.5} \right]^{1/12} \quad (\text{D.5a})$$

$$a = \left(2.475 \ln \left[\left(\frac{7}{Re} \right)^{0.9} + \frac{\epsilon}{3.7D} \right]^{-1} \right)^{16} \quad (\text{D.5b})$$

$$b = \left(\frac{3.753 \cdot 10^4}{Re} \right)^{16}. \quad (\text{D.5c})$$

In addition to the two new correlations, an option for a correlation with user-defined parameters is added. This option—IRFC=5—is in a common form of friction factor correlations for the turbulent regime of smooth tubes,

$$f = C_1 + C_2 Re^{C_3} \quad (\text{D.6})$$

There are three constants to be input by the user: C_1 , C_2 , and C_3 . This option allows friction factor estimates to be calibrated to a specific facility or data set. The implementation of the new models is described in the CTF Theory Manual [42]. Instructions for use of the models is in CTF's User Manual [116].

In CTF, an effective roughness is calculated for any subchannel which contacts multiple solid surfaces. Figure D.1 shows three-by-three rod bundle geometry with coolant-centered and rod-centered subchannels. The former is the traditional approach for subchannel analysis [270], whereas the latter has been shown to better predict high-quality flows [271, 272]. For both methods, the subchannels at the edge of the assembly contact both fuel rods and the assembly walls. Since the different rods and walls of the CTF model can have different roughnesses, an effective subchannel roughness is approximated. For each subchannel, the effective roughness is an area-weighted average of the surface roughnesses, which is

$$\bar{\epsilon}_i = \frac{\sum_s \epsilon_s A_s}{\sum_s A_s} \quad (\text{D.7})$$

where

- $\bar{\varepsilon}_i$ = the effective roughness in subchannel i ,
- ε_s = the roughness of the s^{th} surface touching subchannel i , and
- A_s = the area of the s^{th} surface touching subchannel i .

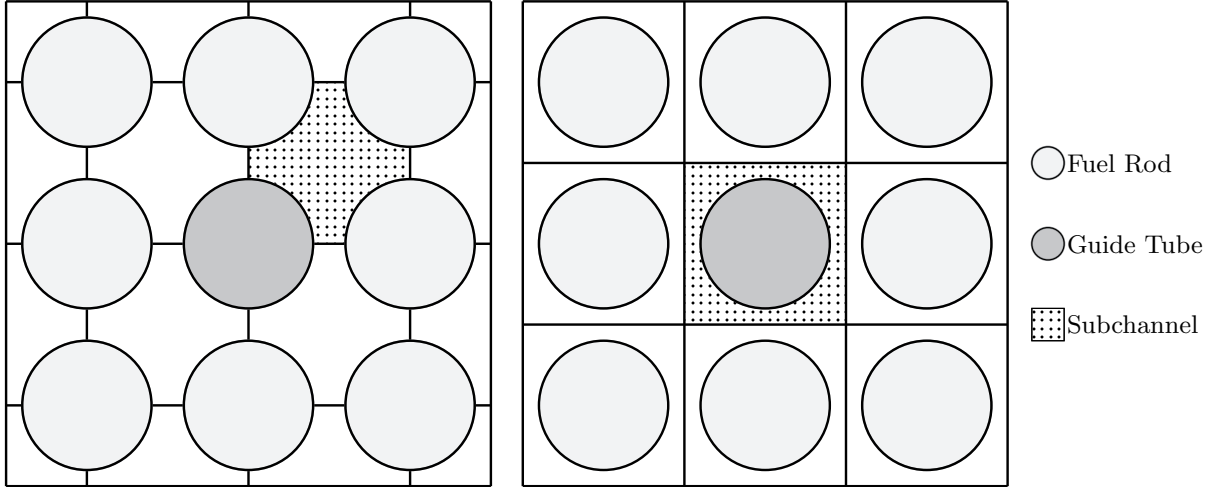


Figure D.1: Three-by-three rod bundle geometry with coolant-centered (left) and rod-centered (right) subchannels.

After the initial implementation of four correlations (Figure D.2), a variety of analyses are performed to test the software quality. First, a series of defect tests are designed for both single- and multi-channel configurations which compare simulated results to approximate solutions. The single-channel tests assess the friction model implementation; a suite of three-by-three bundle tests are used to ensure proper implementation of the roughness averaging scheme. A solution verification test is performed to ensure that the first order numerical scheme in CTF is not significantly disrupted by the friction model. Finally, the wall friction model is validated using both separate and integral effects experimental data. Overall, the software quality, verification, and validation procedure ensures that the new model is coded correctly, that it properly interacts with the rest of CTF, and that it can be used to model real-world data for turbulent single-phase flow. The complete study can be found in Toptan et al. [273].

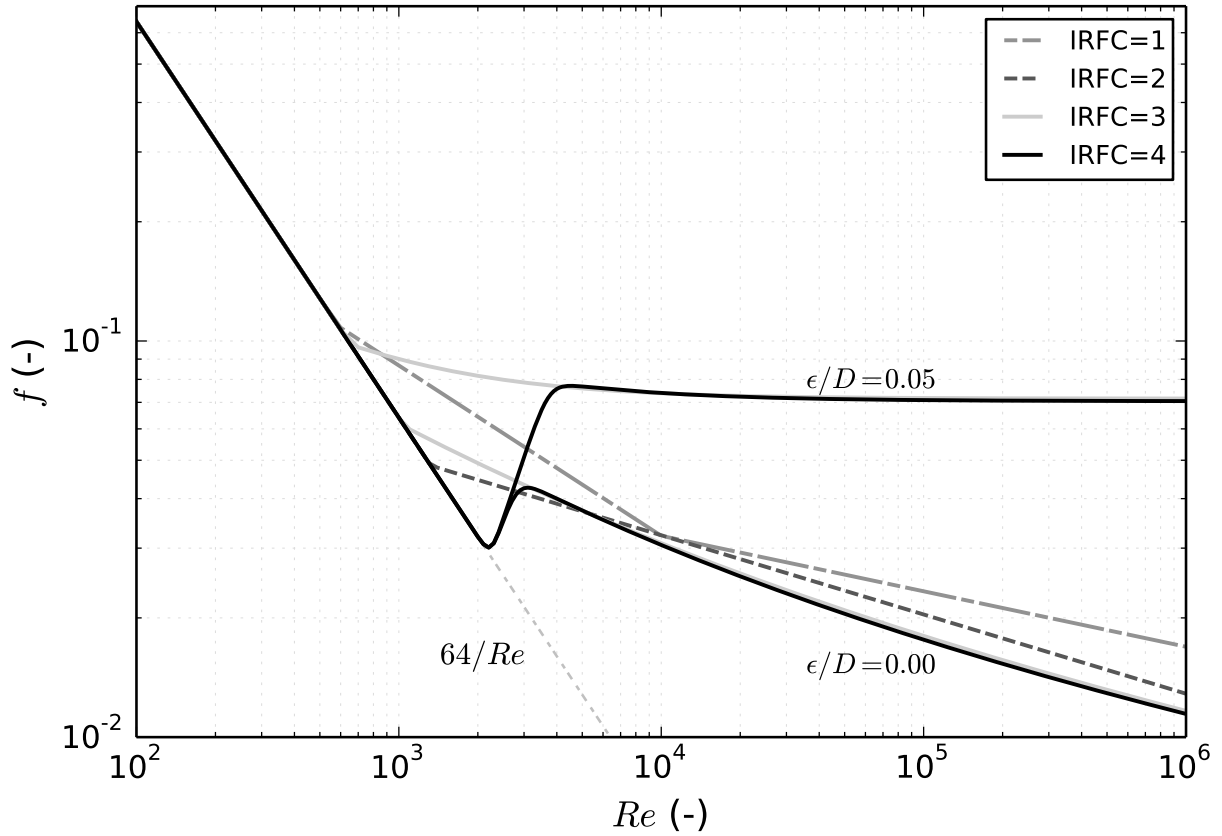


Figure D.2: Comparison of different friction models as coded in CTF. All four options limit to the Hagen-Poiseuille equation for low Reynolds numbers. For the Churchill and Zigrang correlations, the roughness effect is displayed as two extreme values, which are labeled in the figure. Note that the McAdams and Churchill correlations in the code are actually modified versions of their respective namesakes.